

Utah State University

DigitalCommons@USU

All Graduate Theses and Dissertations

Graduate Studies

5-2016

Rayleigh-Scatter Lidar Measurements of the Mesosphere and Thermosphere and Their Connections to Sudden Stratospheric Warmings

Leda Sox
Utah State University

Follow this and additional works at: <https://digitalcommons.usu.edu/etd>



Part of the [Physics Commons](#)

Recommended Citation

Sox, Leda, "Rayleigh-Scatter Lidar Measurements of the Mesosphere and Thermosphere and Their Connections to Sudden Stratospheric Warmings" (2016). *All Graduate Theses and Dissertations*. 5227.
<https://digitalcommons.usu.edu/etd/5227>

This Dissertation is brought to you for free and open access by the Graduate Studies at DigitalCommons@USU. It has been accepted for inclusion in All Graduate Theses and Dissertations by an authorized administrator of DigitalCommons@USU. For more information, please contact digitalcommons@usu.edu.



RAYLEIGH-SCATTER LIDAR MEASUREMENTS OF THE MESOSPHERE AND
THERMOSPHERE AND THEIR CONNECTIONS TO
SUDDEN STRATOSPHERIC WARMINGS

by

Leda Sox

A dissertation submitted in partial fulfillment
of the requirements for the degree

of

DOCTOR OF PHILOSOPHY

in

Physics

Approved:

Vincent B. Wickwar
Major Professor

David Peak
Committee Member

Michael Taylor
Committee Member

Michael Wojcik
Committee Member

Tao Yuan
Committee Member

Mark McLellan
Vice President for Research and
Dean of the School of Graduate Studies

UTAH STATE UNIVERSITY
Logan, Utah

2016

Copyright © Leda Sox 2016

All Rights Reserved

ABSTRACT

Rayleigh-Scatter Lidar Measurements of the Mesosphere and Thermosphere and Their
Connections to Sudden Stratospheric Warmings

by

Leda Sox, Doctor of Philosophy

Utah State University, 2016

Major Professor: Dr. Vincent B. Wickwar
Department: Physics

The Earth's middle atmosphere (10-110 km) has long been a region in which measurement techniques are limited. Many ground-based and remote sensing satellite instruments have been developed over the past several decades, which strive to provide good coverage of this region. However, each of the different techniques has its own measurement limitations in the extent of its coverage in altitude, time, or global-scale. In order for researchers to trace geophysical dynamics and phenomena across the three regions in the middle atmosphere, measurements from many instruments often have to be spliced together. Rayleigh-scatter lidar is a ground-based remote sensing technique that has been used to acquire relative density and absolute temperature measurements throughout the 35-90 km region at several sites for the past four decades. Rayleigh lidars have a unique advantage over many other middle-atmosphere instruments in that their measurements do not have a theoretical limit to their altitude coverage. Their upper altitude limits are only constrained by technological advances in instrumentation and

their lower limits are only constrained by the presence of aerosols (below about 35 km). However, Mie and Raman scatter detectors can be added to extend their measurements down to ground level. The Rayleigh lidar on the campus of Utah State University has recently been upgraded in such a way as to extend its upper altitude limit 25 km higher, into the lower thermosphere. The first year (2014-2015) of data acquired with this new system has been analyzed to obtain temperatures in the 70-115 km region. Numerical experiments were carried out that showed it was possible to compensate for changing atmospheric composition above 90 km with minimal effects on the derived Rayleigh temperatures. These new temperatures were in good agreement with temperatures from the previous version of the system and well-established results of the thermal structure in the mesosphere-lower thermosphere region. Subsequently, the first comparison between collocated Rayleigh and Na lidars, covering identical time periods and altitude ranges, was conducted. An example of the scientific results that can be mined from long-term Rayleigh lidar observations is also given. It establishes the behavior of the midlatitude mesosphere during sudden stratospheric warming events.

PUBLIC ABSTRACT

Rayleigh-Scatter Lidar Measurements of the Mesosphere and Thermosphere and Their
Connections to Sudden Stratospheric Warmings

Leda Sox

The Earth's middle atmosphere is comprised of the stratosphere, mesosphere and thermosphere, from approximately 10 to 110 km, or approximately 6 to 68 miles. An understanding of the dynamics and climatological conditions in this region is of vital importance to the aerospace industry and military, which both launch aircraft and spacecraft into this region, as well as researchers who study climate change and the interactions between the atmosphere and the Earth, oceans, and space.

Measurements of atmospheric properties (density, temperature, and pressure) in this region are relatively difficult to gather as the middle atmosphere's altitudes are both too high for weather balloons to reach and too low for satellite. That is why most instruments that acquire data from the middle atmosphere are of the remote sensing variety. Rayleigh-scatter lidar (light detection and ranging) is a remote sensing technique that is particularly effective at acquiring long-term measurements of the middle atmosphere.

This work focuses on the design and implementation, over one annual cycle, of a unique Rayleigh lidar, which pushes the upper altitude boundary that is typical of such systems. In addition, a study of the connection between Sudden Stratospheric Warmings and the midlatitude mesosphere using a long-term Rayleigh lidar dataset is presented.

This one's for you, Grandpa...

ACKNOWLEDGMENTS

I would like to thank Vince Wickwar for being a great teacher and mentor. I am grateful for your ceaseless support and encouragement as I worked towards my research goals while also helping me grow as a teacher, research mentor, and member of the scientific community. I would also like to thank David Peak, Jan Sojka, Mike Taylor, Mike Wojcik, and Titus Yuan for their invaluable guidance and mentorship throughout the whole graduate school process. Additionally, I would like to thank my coauthors Chad Fish and Joshua Herron for their excellent ideas and feedback.

I am indebted to all the students, past and present, who were involved in the Rayleigh lidar at USU. This dissertation exists purely because I stood on the shoulders of giants, some of whom include: Joshua Herron, Troy Wynn, Marcus Bingham, Lance Petersen, David Barton, Thomas Amely, Ryan Martineau, Bryant Ward, David Moser, Joe Slansky, Preston Hooser, Rebecca Petrick, Patrick Sharp, Jordan Burns, Warren Schweigert, and Luis Navarro. I would also like to thank Neal Criddle, Ivana Molina, and Jinni Meehan for their support through all of the ups and downs.

I would like to thank the Utah NASA Space Grant program, the USU Physics Department, and the Keith Taylor, Howard L. Blood, and Gene Adams scholarship programs for their financial support throughout my graduate school tenure. The upgrades to the Rayleigh lidar were funded by the National Science Foundation, the Space Dynamics Laboratory IR&D program, USU, the USU Physics Department, and personal contributions.

To my parents, thank you for teaching me not to sail where the birds stand.

To Matt, my builder of boats, and Elliot, my light upon the water, thank you for helping me remember this.

Leda Sox

CONTENTS

	Page
ABSTRACT	iii
PUBLIC ABSTRACT	v
DEDICATION	vi
ACKNOWLEDGMENTS	vii
LIST OF TABLES	xi
LIST OF FIGURES	xii
CHAPTER	
1. INTRODUCTION	1
The Earth's Atmosphere	1
Statement of Problem	3
Overview of This Work	6
2. LIDAR AND THE MIDDLE ATMOSPHERE	9
Rayleigh and Resonance Lidar Remote Sensing of the Middle Atmosphere	10
Sudden Stratospheric Warmings	17
References	31
3. HIGH-POWERED, LARGE APERTURE RAYLEIGH-SCATTER LIDAR FOR THE STUDY OF THE MESOSPHERE AND LOWER- THERMOSPHERE	39
Abstract	39
Introduction	40
Rayleigh-Scatter Lidar Theory	41
System Design	44
Data Analysis	54
2014-2015 Observations	67
Discussion	72
Conclusions	75
Acknowledgments	76
References	77
4. COMPARISON OF SIMULTANEOUS RAYLEIGH-SCATTER AND SODIUM RESONANCE LIDAR TEMPERATURE MEASUREMENTS IN THE MESOSPHERE LOWER-THERMOSPHERE REGION FROM A	

SINGLE OBSERVATION SITE	80
Abstract	80
Introduction	81
Description of USU Rayleigh and Na Lidars	84
Observations and Results	88
Discussion	99
Conclusions	105
Acknowledgments	106
References	107
 5. CONNECTION BETWEEN THE MIDLATITUDE MESOSPHERE AND SUDDEN STRATOSPHERIC WARMINGS AS MEASURED BY RAYLEIGH-SCATTER LIDAR	110
Abstract	110
Introduction	111
SSWs and Rayleigh-Scatter Lidar Temperatures from 1993 to 2004	113
Results	118
Discussion	124
Conclusions	127
Acknowledgments	128
References	128
 6. CONCLUSIONS AND FUTURE WORK	132
Conclusions	132
Future Work	135
References	139
 APPENDICES	142
Appendix A	143
Appendix B	180
 CURRICULUM VITAE	188

LIST OF TABLES

Table	Page
2.1 Comparison of Rayleigh-Scatter Lidar System Parameters.....	12
3.1 USU Rayleigh-Scatter Lidar System Parameters.....	45
3.2 Approximate Signal and Background Levels for the USU Rayleigh Lidar.....	53
3.3 Rayleigh Backscatter Cross Section for Four Major Atmospheric Species.....	61
3.4 Seasonal Temperature Average Details	67
4.1 Comparison of Whole-Night Averaged Rayleigh and Sodium Lidar System Parameters	87
4.2 Dates for 2014-2015 Temperature Dataset	88
4.3 Approximate Wave Parameters Obtained from Hourly Temperature Perturbations	100
5.1 List of Major SSWs and USU RSL Data	120

LIST OF FIGURES

Figure	Page
1.1 Diagram of the Earth's atmosphere	2
2.1 Atmospheric features that can be measured with lidar	10
2.2 USU Rayleigh lidar climatological temperature curves.....	13
2.3 Examples of Na resonance fluorescence lidar measurements.....	16
2.4 Example of NASA MERRA reanalysis data used to define SSW events.....	21
2.5 SSW event simulated with the coupled TIME-GCM/CCM3 model	24
2.6 SSW ion temperature differences as measured from Millstone Hill ISR	27
2.7 Northern Annular Mode composites for (a) weak vortex and (b) strong vortex events	28
3.1 Block diagram of the USU Rayleigh lidar	46
3.2 Photograph of Rayleigh lidar telescope cage at the Atmospheric Lidar Observatory on the campus of USU.....	47
3.3 USU Rayleigh lidar telescope cage system.....	48
3.4 Ray tracing geometry of the thin lens approximation of the telescopes	50
3.5 Circuit diagram for custom made voltage divider used to power the ET 9954 PMT	52
3.6 Timing diagram for the Rayleigh lidar	55
3.7 Ratio of lidar signal-to-standard deviation.....	56
3.8 Temperature profile for the all-night average of Rayleigh lidar signal on September 25, 2014.....	59
3.9 MSISe00 model number densities of atmospheric constituents versus altitude for 20 June 2014	60
3.10 Simulation of the effect atomic oxygen has on Rayleigh lidar-measured densities and how to correct for this using the effective cross section.	62
3.11 MSISe00 simulation (for December 31 st) of MMM correction	64

3.12	USU Rayleigh lidar all-night temperature averages for six nights throughout the 2014-2015 year.	65
3.13	Seasonal temperature averages from the 2014-2015 USU Rayleigh lidar campaign	68
3.14	Monthly averaged mesopause temperatures and heights	71
4.1	Summer 2014 temperature-altitude plots for whole-night averages measured using the Rayleigh lidar (green curves) and Na lidar (orange curves)	90
4.2	Same as Figure 4.1, but for the fall 2014 portion of the overlapping dataset.....	91
4.3	Same as Figure 4.1, but for the winter 2014 and spring 2015 portions of the overlapping dataset.....	92
4.4	Same as Figure 4.1, but for the summer 2015 portion of the overlapping dataset.....	93
4.5	Rayleigh and Na lidar temperature time series at 85 km (a), 90 km (b), 95 km (c), 100 km (d), and 105 km (e) along with the differences between the two lidars' temperatures (lower panels, black diamonds)	95
4.6	Correlation coefficients for the two lidar temperature datasets (a) over the 82-100 km altitude range calculated in steps of 1 km and (b) over the whole time series in steps of nights	96
4.7	Temperature profile plots similar to those in Figures 4.1-4.4 except with Na lidar west-pointing beam temperatures (dashed orange curve) and the average of the east and west-pointing beam temperatures (red curve) added	98
4.8	Temperature perturbations (night mean subtracted from hourly means) from Rayleigh lidar data (left panels) and Na lidar data (right panels)	101
5.1	60°-90°N Zonal-mean temperatures (T; black curve) and 60°N zonal-mean zonal winds (u; blue curve) both at 10 hPa from the MERRA database	114
5.2	USU Rayleigh lidar climatology for (a) winter-spring (DJFMA) and (b) summer-fall periods (JJASO).....	118
5.3	USU Rayleigh lidar temperature climatological profiles for a winter night (February 3 rd , blue curve) and a summer night (August 4 th , red curve).....	119

5.4	USU Rayleigh lidar nighttime temperatures for six SSW event periods (a-f)	121
5.5	Temperature difference plots for the six SSW event periods (a-f)	122
5.6	Temperature difference uncertainties for each of the six SSW event periods	124
A.1	Screenshot of the MultiMirror.vi fiber positioning program written in Labview	145
A.2	Screenshot of the Search Pattern.vi fiber alignment search pattern program written in Labview	146
B.1	Copyright permission received for <i>Yuan et al.</i> [2012]	181
B.2	Copyright permission received for <i>Liu and Roble</i> [2002]	182
B.3	Copyright permission received for <i>Goncharenko and Zhang</i> [2008]	183
B.4	Copyright permission received for <i>Baldwin and Dunkerton</i> [2001]	184
B.5	Copyright permission received for <i>Sox et al.</i> [2016]	185
B.6	Permission letter from C. S. Fish to use coauthored paper as Chapter 5	186
B.7	Permission letter from J. P. Herron to use coauthored paper as Chapter 5	187

CHAPTER 1

INTRODUCTION

1. The Earth's Atmosphere

The Earth's Atmosphere is the gaseous layer surrounding the planet retained by gravity, which protects life on Earth by regulating ultraviolet radiation from the sun and temperature. The layers of the atmosphere are typically defined in terms of a change in the temperature gradient with decreasing temperature with altitude defining the troposphere, increasing temperature defining the stratosphere, another decreasing temperature region defining the mesosphere, and another increasing temperature region defining the thermosphere. The ionosphere is the charged part of the atmosphere, which overlaps in altitude with the mesosphere and thermosphere [*Wallace and Hobbs, 1977*].

Starting closest to the surface of Earth, the neutral atmospheric layers moving outward are: the troposphere, stratosphere, mesosphere, thermosphere, and ionosphere, which overlaps with the mesosphere and thermosphere (see Figure 1.1). The transitional regions between each of the neutral layers are given the suffix pause and include the tropopause (between the troposphere and stratosphere), the stratopause (between the stratosphere and mesosphere), and the mesopause (between the mesosphere and thermosphere).

The lower atmosphere is usually defined as including the troposphere and much of the stratosphere, which is the focus of research for the atmospheric science, or meteorology field. Almost all of the atmospheric density and weather events occur in the troposphere (~0-12 km), as well as all commercial air traffic. The stratosphere (~12-50

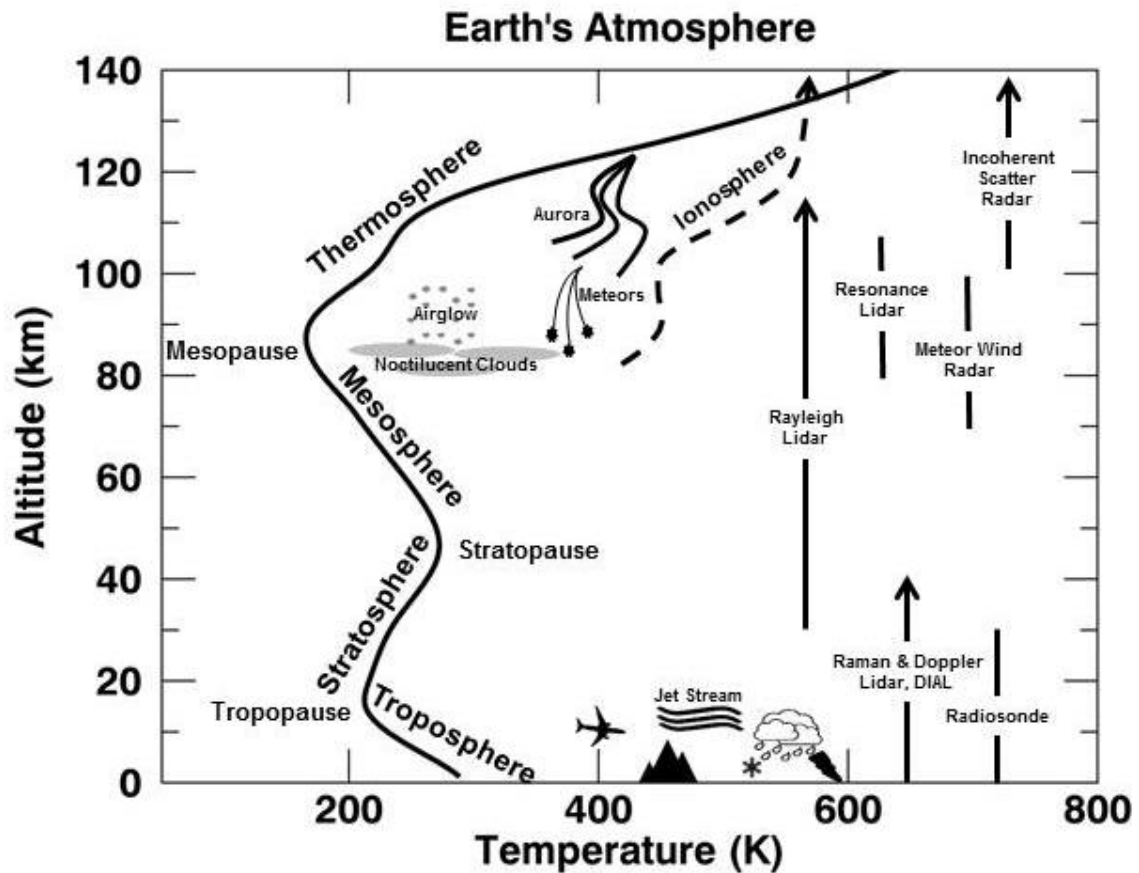


Figure 1.1. Diagram of the Earth's atmosphere. Atmospheric layers are defined by changes in temperature gradient. The temperature curve was produced using the MSISe00 model for June 21st and the location for the Rayleigh lidar facility campus of Utah State University (41.74°N, 111.81°W). Also shown are the altitude ranges of several measurement techniques and notable features. Note that the dashed line only indicates the altitude range of the D and E regions of the ionosphere and does not correspond to ionospheric temperatures.

km) hosts the Earth's ozone layer. The ozone layer absorbs solar radiation, which results in the heating of this region with respect to altitude.

The middle atmosphere includes some of the stratosphere, the mesosphere, and the lower thermosphere, and is the subject of study for researchers in the field of aeronomy. The mesosphere (~50-90 km) is defined by cooling temperature with respect to increasing altitude up to the mesopause (~86 km in summer, ~100 km in winter; *von*

Zahn et al., 1996), which is the coldest place on Earth [*Brasseur and Solomon*, 1984].

The cooling of the mesosphere is associated with radiative cooling from CO₂. This region is also characterized by dynamics (waves, tides, etc.) that can affect change on the general circulation, which affects heating and cooling. In the thermosphere (~100 km and higher), temperatures rise with increasing altitude and can reach an asymptotic value of between 500 K and 2000 K depending on the level of solar activity [*Brasseur and Solomon*, 1984]. The mesosphere and lower thermosphere are host to various dynamics (waves and tides) and phenomena (airglow layers, noctilucent clouds, and aurora; see Figure 1.1 for altitude ranges).

Below about 100 km, the composition of the atmosphere is primarily made up of N₂, O₂, and Ar particles and the mean molecular mass of the atmosphere varies little with altitude due to turbulent mixing. Photodissociation, above 90 km, and diffusive equilibrium, above 100 km, become the dominant processes that cause the mean molecular mass to vary with altitude. For these reasons, the transitional region around 100 km has been given the name turbopause, and the region below it is called the homosphere, and the region above it is called the heterosphere [*Brasseur and Solomon*, 1984].

2. Statement of Problem

Various instruments have been used to make the measurements necessary to define the composition, structure, and dynamics of the atmosphere thus far. The altitude ranges of some of these techniques are given in Figure 1.1. While many of these techniques have been combined in studies concerned with the coupling between the

atmospheric regions, the use a single instrument to simultaneously obtain measurements throughout the entire atmosphere has yet to be achieved.

In the lower atmosphere, measurements of pressure, temperature, and humidity are made by radiosondes, which are attached to unmanned balloons that are launched twice daily from many stations around the world. Data from the North American radiosonde launching sites are collected by the University of Wyoming [University of Wyoming upper air sounding data found at: <http://weather.uwyo.edu/upperair/sounding.html>]. These instruments typically gather data from the ground up to about 30 km where the atmospheric pressure reduces and the balloons expand to a point in which they pop [Dabberdt *et al.*, 2002]. There are also several lidar (light detection and ranging) techniques that are used in the troposphere and stratosphere to make measurements of clouds, aerosols (Rayleigh-Mie lidar), gas concentrations (DIAL), temperature (Raman lidar), and winds (Doppler lidar) [Measures, 1992]. These lidar techniques are limited in altitude range by either their instrumentation (Rayleigh-Mie lidar, Doppler lidar) or the constituents they measure (DIAL, Raman lidar).

Measurements of the middle atmosphere have proved to be more difficult to acquire than those in the lower atmosphere. Sounding rockets made some of the first measurements in this region, though they are limited by high costs for relatively short campaigns. Remote sensing has thus become the preferred technique to measure the middle atmosphere. Instruments on board satellites acquire data with excellent global coverage, but relatively poor spatial resolution and little information regarding time evolution. Ground-based instruments usually give better temporal and spatial resolutions, but again, each technique has its own set of limitations. Airglow instruments

(photometers, imagers, interferometers, and spectrometers) are limited in altitude by the height of the airglow layers (e.g., OH at ~86 km, O (558 nm) at ~97 km, Na at ~ 92 km, and O₂ at ~ 95 km), so while they can capture horizontally varying temperatures and wave structure, they do not provide much information vertically. Resonance lidars obtain measurements over a greater altitude range (~80-105 km) with good temporal and spatial resolution (~minutes to hours and hundreds of meters), but are again limited by the metal layers (e.g., Na, K, Fe, Li, Ca, and Ca⁺) that they measure.

Rayleigh-scatter lidars measure backscatter from atmospheric molecules (N₂, O₂, and Ar), which dominate the atmospheric composition below the turbopause and exist throughout all the regions of the atmosphere. The measured Rayleigh lidar signal is proportional to the combined density of these constituents and thus gives a measure of the relative density of the atmosphere. From the relative density measurements, the absolute temperatures can be derived [*Hauchecorne and Chanin*, 1980]. Like resonance lidars, Rayleigh lidar is capable of making measurements with good temporal (minutes to hours) and spatial resolution (tens to hundreds of meters) at one site. Since Rayleigh lidar systems are limited to one observational site, they provide poor global coverage, as individual instruments. However, networks of Rayleigh lidars could be distributed around the globe to improve this coverage. When it comes to wide-altitude coverage, across all the regions of the atmosphere, Rayleigh lidar has a unique advantage. The upper altitude limit of Rayleigh lidar measurements has only been hindered by instrumentation, in the past. The lower limit of Rayleigh lidar measurements is affected by the presence of aerosols at altitudes below about 30 km that contaminate the Rayleigh signal with signal from Mie scatter. These two signals can be separated, and the Rayleigh lidar

measurements can be extended downward by adding a Raman receiver to existing Rayleigh lidar instruments for scatter from N_2 . Thus, Rayleigh lidar, in theory, has a unique advantage over other instrumentation in its ability to obtain simultaneous measurements from all of the atmospheric regions. The next step is to design and build such an instrument. The first stages in doing so are the subject of most of this dissertation.

3. Overview of This Work

The objectives of this dissertation are to

- 1) Give a detailed description on the design of the recently upgraded, high-power, large-aperture Rayleigh-scatter lidar system, located on the campus of Utah State University. This system is now one of two of the most sensitive Rayleigh lidars in the world, capable of temperature retrievals from the mesosphere-lower thermosphere (MLT) region. Data from the inaugural year of operations with the new USU Rayleigh lidar will show some of the first Rayleigh lidar temperature retrievals from as high as 115 km. These temperature data will be explored and compared with previous measurements made by other techniques in the MLT region.
- 2) Conduct a detailed comparison of the temperature data simultaneously acquired by the collocated USU Rayleigh and sodium (Na) lidars. This will be the first time that measurements throughout one annual cycle will be shown from a Rayleigh and Na lidar operating at the same time, at the same location and covering the same altitude range. Our results will be compared and contrasted with previous climatological

comparisons that were made using lidars from different observational sites and covering a more limited altitude range.

- 3) Present results from the previous USU Rayleigh lidar temperature data set acquired between 1993 and 2004, which shed light on the behavior of the midlatitude mesosphere during sudden stratospheric warming (SSW) events. The Rayleigh lidar observations made during six SSW events throughout this period show that the thermal anomalies seen in the midlatitude mesosphere are consistently stronger in magnitude than previously thought. In fact, the magnitude of the temperature changes seen at our midlatitude site are similar to the magnitudes of the temperature changes seen in the polar mesosphere during SSWs. These results also illustrate the importance of obtaining continuous, long-term measurements using observational instruments like the USU Rayleigh lidar.

The remainder of this dissertation is organized in the following manner: Chapter 2 provides a literature review of the middle and upper atmosphere, the instruments used to measure this region, and the SSW phenomena seen throughout the atmosphere. This literature review will provide the necessary background information for the work presented in the next three chapters. Chapter 3 details the upgrades made to the USU Rayleigh lidar system to convert it to a high-power, large-aperture Rayleigh lidar along with giving a summary of the first year's temperature data obtained with the new system in the MLT region. Chapter 4 provides a comparison between the collocated Rayleigh and Na lidars on the campus of USU. This comparison is the first between these two techniques to show simultaneously acquired temperatures with a complete altitude range overlap. Chapter 5 presents the study of Rayleigh lidar temperature measurements of

midlatitude mesosphere during SSW events between 1993 and 2004. Finally, conclusions and ideas for future work extending these studies will be given in Chapter 6.

References

Brasseur, G., and S. Solomon (1984), *Aeronomy of the Middle Atmosphere*, 441 pp., D. Reidel Publishing Company, Dordrecht, Holland.

Dabberdt, W.F., H. Cole, A. Paukkunen, J. Horhammer, V. Antikainen, and R. Shellhorn (2002), Radiosondes, in *Encyclopedia of Atmospheric Sciences*, vol. 6, edited by J. R. Holton, J. Pyle, J. A. Curry, pp. 1900-1913, Elsevier Science Academic Press, Amsterdam, The Netherlands.

Hauchecorne, A., and M.-L. Chanin (1980), Density and temperature profiles obtained by lidar between 35 and 70 km. *Geophys. Res. Lett.*, 7, 565–568, doi:10.1029/GL007i008p00565.

Measures, R. M. (1992), *Laser Remote Sensing Fundamentals and Applications*, 510 pp., Krieger Publishing Company, Malabar, FL.

von Zahn, U., J. Hoffner, V. Eska, and M. Alpers (1996), The mesopause altitude: Only two distinct levels worldwide?, *Geophys. Res. Lett.*, 23, 3231-3234, doi: 10.1029/96GL03041.

Wallace, J. M., and P. V. Hobbs (1977), *Atmospheric Science an Introductory Survey*, 467 pp., Academic Press Inc., San Diego, CA.

CHAPTER 2

LIDAR AND THE MIDDLE ATMOSPHERE

The Earth's middle atmosphere (roughly 10-110 km) is host to many important atmospheric features including the ozone layer (~20-30 km), the mesopause, which is the coldest part of the whole atmosphere (~85 km or 100 km, depending on season), an overlap with the ionosphere (~70-120 km), metal layers resulting from meteor ablation (~80-110 km), and the turbopause (~110 km) above which turbulent mixing is absent. It is also the region in which phenomena such as airglow, noctilucent clouds, sudden stratospheric warmings, and effects from space weather occur.

These features and phenomena warrant both short- and long-term measurements of parameters such as density, temperature, and winds. These measurements have been conducted over the past several decades with various instruments including: in-situ techniques such as sounding rockets, remote sensing techniques onboard satellites and from ground-based airglow instruments, lidars, and radars.

Lidar is an especially versatile atmospheric measurement technique in that there are many different types of lidar that can measure many different aspects of the atmosphere (e.g., aerosols, clouds, smoke, dust, greenhouse gases, metal atoms, densities, and temperatures) [*Measures*, 1992]. Figure 2.1 shows some examples of the features in the specific atmospheric regions, which can be measured with lidar. In the middle atmosphere, Rayleigh-scatter and resonance lidar are the two predominantly used lidar techniques.

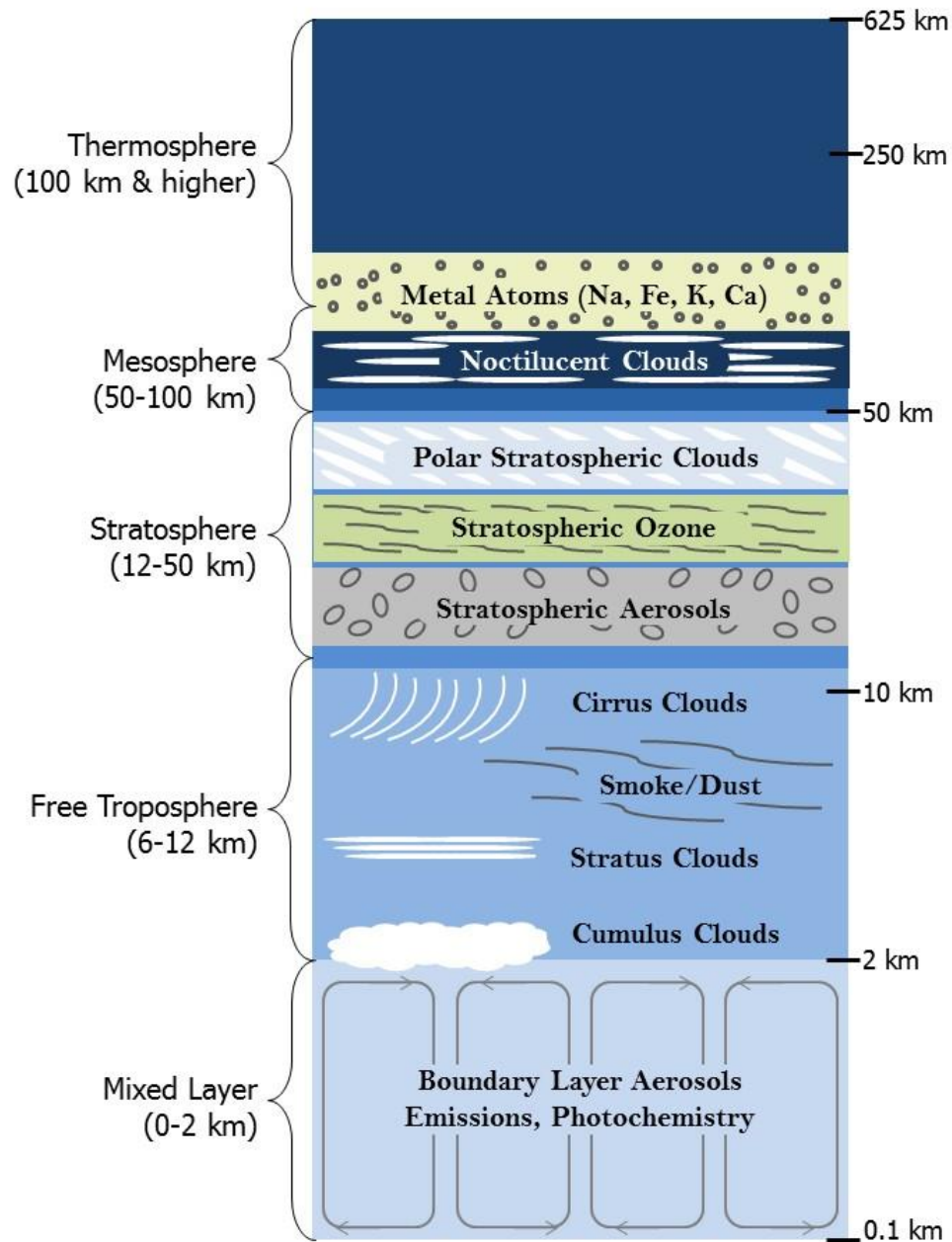


Figure 2.1. Atmospheric features that can be measured with lidar.

1. Rayleigh and Resonance Lidar Remote Sensing of the Middle Atmosphere

Lidar systems remain the most advantageous method for acquiring atmospheric temperature measurements in terms of vertical and temporal resolution. Two of the most widely used lidar techniques for the study of the middle atmosphere are Rayleigh-scatter

lidar and resonance lidar.

1.1. Rayleigh-Scatter Lidar

Employing the Rayleigh-scatter mechanism, where incident light is elastically scattered off of small particles [Measures, 1992] to obtain atmospheric density measurements had been theorized and experimented with long before the advent of lasers or lidar systems [Synge, 1930; Johnson *et al.*, 1939]. The Rayleigh lidar predecessors used pulsed searchlights instead of lasers to transmit incident light, which would then backscatter off of atmospheric molecules and be measured with telescope receivers. Elterman [1953] then used these density measurements to obtain atmospheric temperature profiles. Kent and Wright [1970] applied these methods for deriving atmospheric temperature to the data from one of the first lidar systems and Hauchecorne and Chanin [1980] developed the temperature retrieval explicitly for Rayleigh lidar.

Modern Rayleigh lidar systems measure the backscatter from N₂, O₂, and Ar and from that, obtain relative density and absolute temperature data from about 35 km (below which aerosols are present) up to about 90 km, a limit imposed by most systems' power-aperture product (PAP). Next generation Rayleigh lidars at UWO and USU have higher PAPs (165 W·m² and 206 W·m², respectively). These systems typically use pulsed Nd:YAG lasers (usually operating at 532 nm) as transmitters and large telescopes (~1 m in diameter) to achieve good signal-to-noise ratios at higher altitudes. Examples of some system parameters for a few of the different Rayleigh lidars are given in Table 2.1 (UWO [Sica and Haeefe, 2015]; OHP & TMF [Leblanc *et al.*, 1998]; ALOMAR [von Zahn *et al.*, 2000]; Gadanki [Kishore Kumar *et al.*, 2008]). Figure 2.2 shows some example

Table 2.1. Comparison of Rayleigh-Scatter Lidar System Parameters

System Parameter	USU (1993- 2004)	USU (2014-)	UWO	OHP	ALOMAR	Gadanki	TMF
Emitted λ (nm)	532	532	532	532	532	532	353
Energy (mJ/pulse)	800	1400	1000	300	30	550	50
Power (W)	24 (18)	42	30	17.5	11	11	7.5
Repetition rate (Hz)	30	30	30	50	30	20	150
Aperture Diameter (m)	0.44	2.5	2.65	1.0	1.8	0.75	0.9
PAP (W·m²)	3.6 (2.7)	206	165	13.7	14	4.9	4.8

temperature profiles from the Rayleigh lidar that operated on the campus of Utah State University (USU) between 1993 and 2004. They were taken from the temperature climatology that was created using the 11-year dataset [Herron, 2007] and they show the climatological fall and spring equinoxes, and summer and winter solstices.

By amassing density and temperature measurements, data acquired from Rayleigh lidars can be used to perform many other geophysical studies. Gravity wave analyses can be conducted in which vertical wavelengths, phase speeds, and potential energies are calculated [Gardner *et al.*, 1989; Wilson *et al.*, 1990; Meriwether *et al.*, 1994, Whiteway *et al.*, 1995; Kafle, 2009]. Larger-scale dynamics such as tides [Gille *et al.*, 1991] and planetary waves [Hauchecorne and Chanin, 1983] can also be studied. The stability and

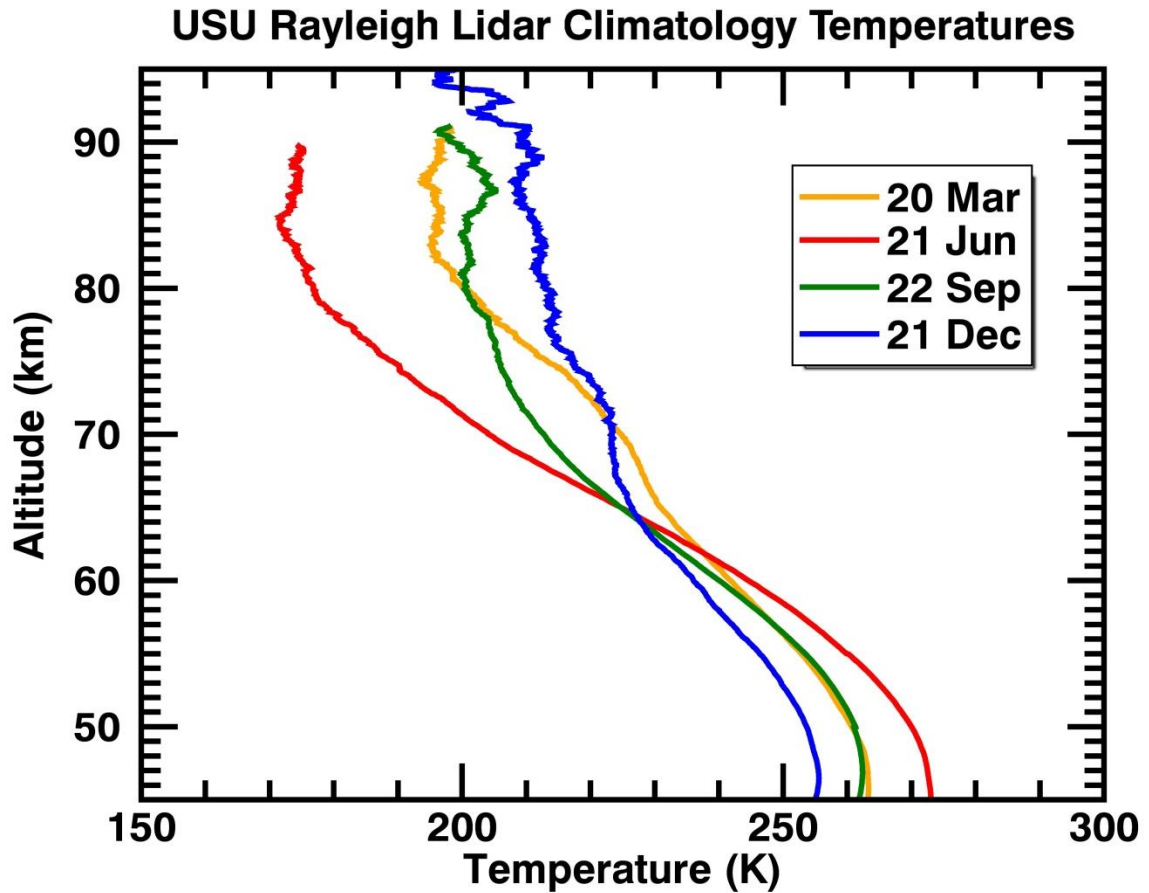


Figure 2.2. USU Rayleigh lidar climatological temperature curves. The USU climatology was created using 11 years of data spanning 1993-2004. The temperature curves depict the climatological spring equinox (orange), summer solstice (red), fall equinox (green), and winter solstice (blue).

ease of use of most Rayleigh lidars allows researchers to make near continuous (though many systems are limited to operating at night) operations over many years. This creates databases of middle atmospheric densities and temperatures that can be used for long-term trend studies [Wynn, 2010; Angot *et al.*, 2012] or can be mined to find occurrences of more anomalous phenomena such as mesospheric inversion layers [Hauchecorne *et al.*, 1987; Whiteway *et al.*, 1995; Irving *et al.*, 2014], noctilucent clouds [Wickwar *et al.*, 2002; Herron *et al.*, 2007], and sudden stratospheric warmings [Hauchecorne and

Chanin, 1983; Angot et al., 2012; Sox et al., 2016a].

While researchers have combined datasets from several different instruments to achieve whole-atmosphere coverage (in the troposphere, stratosphere, mesosphere, and thermosphere) a large-aperture, high-powered Rayleigh lidar has the capability to obtain this same altitude coverage with a single instrument. The robustness and ease of use associated with older Rayleigh lidar systems can scale with the new, larger systems to achieve more cost-effective and continuous data accumulation over all of the atmospheric regions. As mentioned before, the lower altitude limit for Rayleigh lidar systems is determined by the presence of aerosols below about 35 km; however, the upper altitude limit is only determined by the system's instrumentation, often categorized by the power-aperture product figure-of-merit (see Table 2.1), and thus its signal-to-noise ratio at a given height.

Recent improvements to the aforementioned USU Rayleigh lidar have upgraded the existing system to a large-aperture, high-power Rayleigh lidar [*Wickwar et al., 2001; Sox et al., 2016b*]. It is now one of two such systems in the world [*Sica et al., 1995; Sica and Haefele, 2015*]. These two lidars have shown that Rayleigh temperature measurements can extend into the lower thermosphere. In doing so, effects of changing atmospheric composition above 90 km due to photodissociation of O₂ into atomic oxygen and the switch from turbulent mixing to diffusive equilibrium have to be taken into account. Through model studies and our current analysis of the USU Rayleigh lidar data, these effects have been found to be small (~2 K) below 120 km and thus not a limiting factor on the upward extension of Rayleigh lidar measurements [*Argall, 2007; Sox et al., 2016b*]. Another recent development in improving the Rayleigh temperature analysis and

upper altitude limit has been presented in *Sica and Haefele* [2015]. This work replaced the existing Rayleigh temperature retrieval [*Hauchecorne and Chanin*, 1980] with a new technique that uses an optimal estimation method and has the capability to correct for changing atmospheric composition, calculate a more complete error budget, not require a seed temperature at the top of the profile (since the OEM uses an *a priori* temperature profile), and potentially extend the temperature profile even higher in altitude.

1.2. Resonance Fluorescence Lidar

Resonance fluorescence lidar exploits both resonance scattering and laser-induced fluorescence (incident light frequency matched to specific atomic transitions or to electronic transition of an atom, respectively) to measure spectra and Doppler shifts, which can then be used to obtain density measurements of specific atomic species, temperatures, and winds. In resonance scattering, the backscattered light does not change frequency from the incident light. However, in fluorescence, there is a frequency change [*Measures*, 1992]. In the middle atmosphere, the metallic atom layers (Na, Fe, K, Li, Ca, and Ca^+) are typically the source of scatterers for resonance lidar. These metallic layers form from meteor ablation deposits from roughly 80-105 km in the mesosphere-lower thermosphere (MLT) region.

The first lidar measurements of the sodium (Na) layer were made shortly after the tunable dye laser was invented [*Bowman et al.*, 1969]. From there, the first temperature measurements were demonstrated with a Na lidar system by *Gibson et al.* [1979] and then were more routinely acquired with *Fricke and von Zahn* [1985] after the linewidth and frequency stability of dye lasers was improved. Further improvements in laser

technology made Doppler wind measurements possible with Na lidar [Bills *et al.*, 1991]. Daytime measurement capabilities were made possible with the Na lidar technique by the addition of the Faraday filter to an existing system [Chen *et al.*, 1996]. Examples of mean Na density, temperature, and zonal wind profiles are given in Figure 2.3, taken from the Yuan *et al.* [2012b] study, which showed effects from a sudden stratospheric warming in their MLT Na lidar data.

The data acquired with resonance lidar systems has helped explain the behavior of the metal layers [e.g., Megie *et al.*, 1978; Granier *et al.*, 1985; Eska *et al.*, 1998; Plane *et al.*, 1999; Gardner *et al.*, 2011] themselves, as well as the thermal structure of the MLT region [She *et al.*, 2000]. Temperature data from Na and K lidars revealed that the two-level mesopause is characterized by a low (in altitude), cold mesopause in summer and high, warm mesopause in winter [She *et al.*, 1993; von Zahn *et al.*, 1996]. Similar to Rayleigh lidar, resonance lidar data can be further analyzed to study gravity waves [Bossert *et al.*, 2014; Cai *et al.*, 2014; Lu *et al.*, 2015], tidal variations [She *et al.*, 2004;

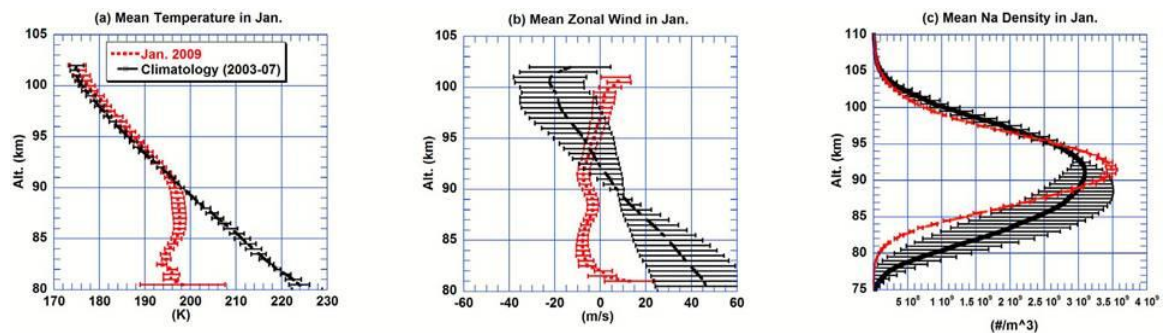


Figure 2.3. Examples of Na resonance fluorescence lidar measurements. The red profiles were obtained during the 2009 sudden stratospheric warming event and show (a) temperature, (b) zonal wind, and (c) Na density. The black profiles show five-year January means. From Yuan *et al.* [2012b]. Reprinted with permission from John Wiley and Sons.

Yuan et al., 2012a], and anomalous phenomena like sudden stratospheric warmings [*Yuan et al.*, 2012b]. Some of the systems that have been running for many years are also starting to provide important information on long-term trends [*She et al.*, 2015]. Though the altitude limits of resonance lidar are bounded by the physical presence of the metal layers, recent findings have shown that these layers, and thus the derived resonance lidar measurements, can, on occasion, extend quite far into the lower thermosphere (the highest recorded case extending to 170 km) [*Lübken et al.*, 2011; *Chu et al.*, 2011; *Friedman et al.*, 2013; *Gao et al.*, 2015; *Raizada et al.*, 2015; *Liu et al.*, 2016].

2. Sudden Stratospheric Warmings

Sudden Stratospheric Warmings (SSWs) and their associated phenomena throughout the atmosphere have been scrupulously studied by nearly every type of scientific group whose main research is in the Earth's atmosphere. The first observation of a SSW was shown in 1952 in *Scherhag* [1952]. The next breakthroughs related to SSWs were focused higher up in the atmosphere with observations of coolings, wind reversals, and stunted gravity wave activity in the upper mesosphere happening on timeframes corresponding to the SSW event. Model studies pushing even further up into the atmosphere predicted warmings in the lower thermosphere, though they were less intense than those in the stratosphere. Most recently, effects of SSWs are being seen in the ion temperatures, total electron content, and ion drifts in the ionosphere. Additionally, SSWs are now being considered for their usefulness in predicting extreme tropospheric weather. While most of these events are well understood in the two polar regions of the Earth, work is now being done to better understand the latitudinal extent of SSWs and

their associated phenomena.

Both Rayleigh and resonance lidar have proven to be exceptional tools to study the SSW phenomena. On their own, some lidar systems can provide the temperature and wind measurements required to define SSWs or they can be used along with data from other instruments or models to give a complete picture of this phenomena [*Hauchecorne and Chanin*, 1983; *Walterscheid et al.*, 2000; *Yuan et al.*, 2012b; *Angot et al.*, 2012; *Sox et al.*, 2016a]. As in the case of the USU Rayleigh lidar, many of these instruments have long-term data sets [*Herron*, 2007], which can be used to study trends in SSWs and their associated events in regions of the atmosphere [*Angot et al.*, 2012; *Sox et al.*, 2016a].

2.1. SSW Definition

SSWs are one of the most carefully studied circulation events in the stratosphere. They are a wintertime, polar phenomenon. The characteristic disturbances of SSWs are a temperature increase averaged over 60°-90° latitude at the 10 hPa level (roughly 32 km) and a weakening of the polar vortex that persists for on the order of a week [*Charlton and Polvani*, 2007]. The polar vortex is a cyclone centered on both of the Earth's poles that is located from the mid troposphere into the stratosphere. A west-to-east circulation driven by zonal winds defines the winter polar vortices.

The major cause of SSWs is considered to be an increase in poleward propagating planetary waves during the winter season [*Matsuno*, 1971]. These planetary waves originate in the troposphere and can propagate vertically into the stratosphere. Many of them are created by the interaction of atmospheric fluid being pushed along from the Coriolis force and the orography of the Earth's surface [*Platzman*, 1968]. Since there is

more planetary wave activity in the northern hemisphere (NH) due to its prevalence of land and orography, more of the SSWs occur in the NH polar region than in the southern hemisphere (SH) polar region.

2.2. Classification of SSWs

Though there are many slight variations from study to study, the classification of types of SSW events described in *Labitzke and Naujokat* [2000] is one of the most widely accepted systems. It defines four different types of SSWs as follows:

- Major. These events involve a temperature increase averaged over the latitudes 60° and poleward at 10 hPa. They also must include a complete reversal of the zonal-mean zonal winds from eastward to westward at 60° at 10 hPa. This creates a complete change in the circulation, or a breakdown, of the polar vortex.
- Minor. These events are the same as major SSWs without the zonal wind field reversal. They often have less intense temperature increases than major SSWs.
- Final. These warmings mark the transition from winter to summer stratospheric circulation in that in the summer, the stratospheric polar vortex switches from an eastward direction to a westward direction. These warmings can either include or not include the zonal wind reversal. However, if they do, the zonal winds usually remain westward as the seasonal transition occurs.
- Canadian. These events take place when the Aleutian anticyclone, which is located in the Northern Pacific, intensifies and moves poleward. These involve warmings over the Canadian Arctic Pole and sometimes, briefly, zonal wind reversals, but never a full breakdown of the polar vortex.

Researchers can use NASA's Modern-Era Retrospective Analysis for Research and Applications (MERRA) [*Rienecker, 2011*] reanalysis data to define individual SSW events. An example of this data is shown in Figure 2.4. The top plot shows several distinct temperature peaks in the 2002-2003 data (red line) that are statistically major deviations from the climatological mean year (thick black line) averaged over 1978-2013. Note that the top plot is an average over 60°-90° N latitude of the zonal mean temperatures. Only the mid-January temperature increase can be accurately identified as a major SSW. Looking at the zonal-mean zonal winds (bottom plot) for 60° N latitude, one can see that the zonal winds become negative around mid-January (vertical blue lines are drawn on both plots for reference). Thus, the only major SSW for winter 2002-2003 occurred in the middle of January, while the late December and late January warmings are classified as minor SSWs.

A further classification system exists to differentiate between the different types of breakdowns that happen in the polar vortex during a major SSW. They include the displacement of the polar vortex off of its location centered at either pole or the splitting of the polar vortex into two different circulation cells. *Charlton and Polvani [2007]* did an extensive study of the characteristics unique to the displaced and the split vortex events. They found that while the temperature increases in the stratosphere were of the same magnitude for both split and displaced polar vortex events, the split events usually were marked with stronger and more sudden wind reversals.

2.3. SSW Lifecycle

By creating a composite SSW event using the average of 39 such individual

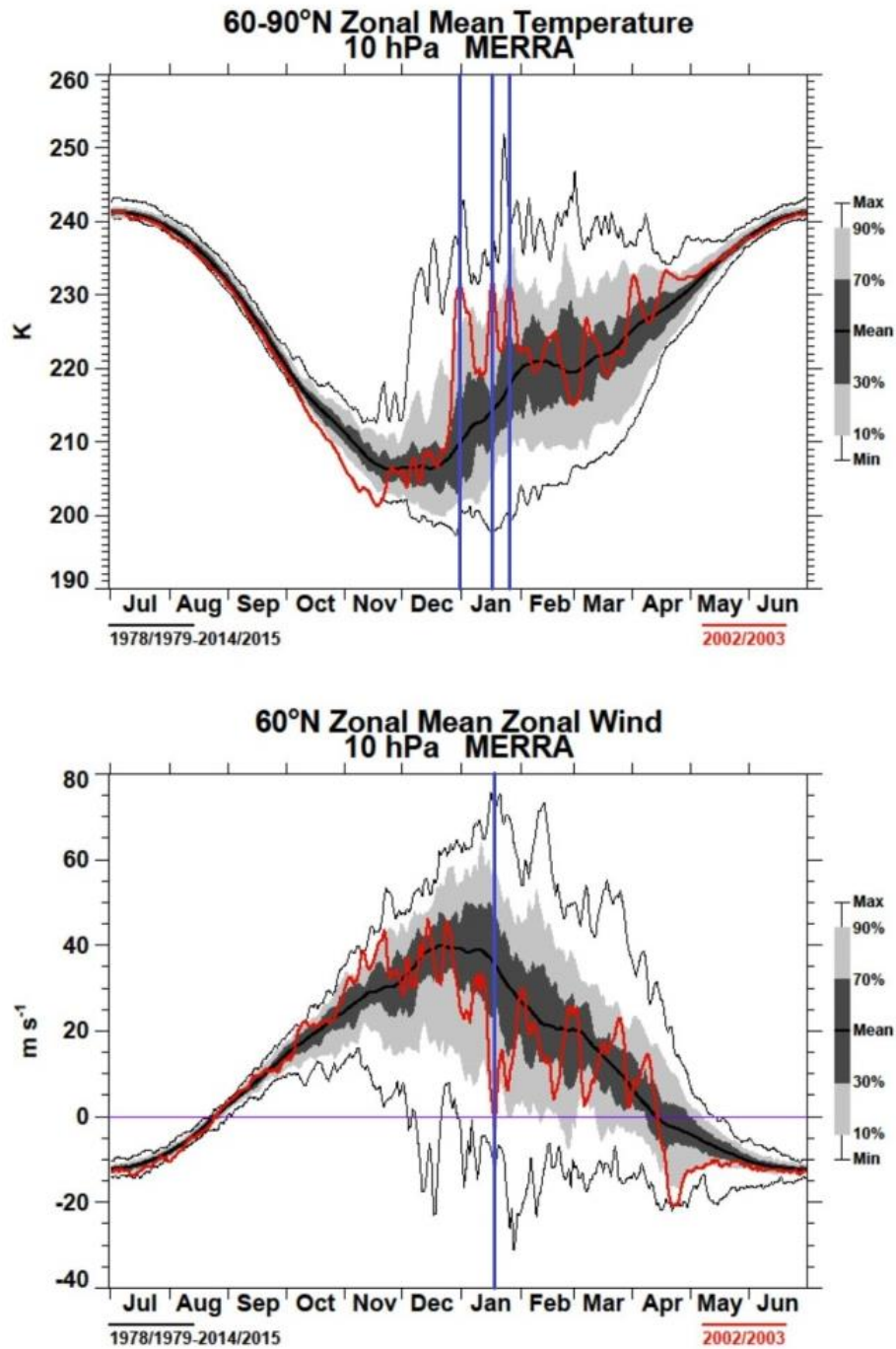


Figure 2.4. Example of NASA MERRA reanalysis data used to define SSW events. The top plot shows zonal mean temperature averaged over 60° -90° N latitude while the bottom plot shows zonal-mean zonal winds at 60° N latitude. For both plots, the red curve denotes values for the 2002-2003 year and the thick black curve denotes climatological values averaged from 1978 to 2015. The vertical blue lines reference minor and major SSWs for that winter.

events from the NCEP-National Center for Atmospheric Research (NCAR) reanalysis dataset, *Limpasuvan et al.* [2004] were able to define the lifecycle common to most SSWs. Three parameters were used to define the lifecycle: (1) zonal-mean zonal wind anomalies, which are negative for anomalously westward winds and positive for eastward winds, (2) zonal temperature anomalies where positive values are warmings and negative values are coolings and (3) the Eliassen-Palm (EP) flux. The EP flux divergence is a measure of planetary wave activity, downward values of EP flux show that planetary wave (PW) activity is going vertically downward in the atmosphere and upward EP flux shows PW activity going upward through the atmosphere. This SSW lifecycle consists of five phases of an 81-day cycle centered on a central date (day 0) including: onset (days -40 to -23), growth (days -22 to -8), maturation (days -7 to +7), decline (days +8 to +22) and decay (days +23 to +40).

2.4. Associated Events in the Mesosphere

Through observations that pushed further up into the atmosphere, a clear picture of associated dynamics in the mesosphere began to take shape in the late 1960s and early 1970s. The mesospheric parameters that were measured to be notably disturbed are temperature, zonal-mean zonal winds, and gravity wave activity.

2.4.1. Mesospheric Coolings

The first observations of temperatures at higher altitudes, coinciding with SSWs, showed coolings in the lower mesosphere, around 60-70 km [*Labitzke*, 1972]. Since then observations have continued to show mesospheric coolings happening either during or slightly before the peak stratospheric warmings. Observations of these mesospheric

coolings have been made with a multitude of instruments [*Labitzke*, 1972; *Whiteway and Carswell*, 1994; *Walterscheid, et al.*, 2000; *Siskind et al.*, 2005; *Hoffmann et al.*, 2007; *Yuan et al.*, 2012b;].

Thorough modeling studies have been able to reproduce these coolings, as well [*Walterscheid et al.*, 2000; *Liu and Roble*, 2002; *Miller et al.*, 2013; *Chandran and Collins*, 2014]. The study done in *Liu and Roble* [2002] is perhaps the most widely referenced model study done on SSWs and their manifestations at higher altitudes. In this study, the authors used the Thermosphere, Ionosphere, Mesosphere, and Electrodynamics General Circulation Model coupled with the Climate Community Model version 3 (TIME-GCM/CCM3) to simulate a zonally averaged minor SSW event and what happens at higher altitudes at similar times. Figure 2.5 shows a comprehensive plot of both temperature change (contour shading) from prior to the SSW to during the peak day of the SSW, as well as the same difference between zonal-mean zonal winds (contour lines). This model study gave mesospheric coolings between 60-110 km and 50°-90° N. It also showed that the mesospheric coolings reached significant values prior to the significant stratospheric warmings. Though, in *Miller et al.* [2013], it was shown through a HAMMONIA model study that the mesospheric coolings' time evolution is very different, zonally. Thus, it is not possible for individual observation stations to predict that an SSW will occur from the preceding mesospheric coolings. An important note is that the *Liu and Roble* [2002] study did not show significant mesospheric coolings reaching into the mid and low latitudes (equatorward of ~60° N latitude). More recent findings have shown that these coolings can reach midlatitudes [*Hauchecorne and Chanin*, 1983; *Hoffmann et al.*, 2007; *Angot et al.*, 2012; *Yuan et al.*, 2012b; *Sox et al.*,

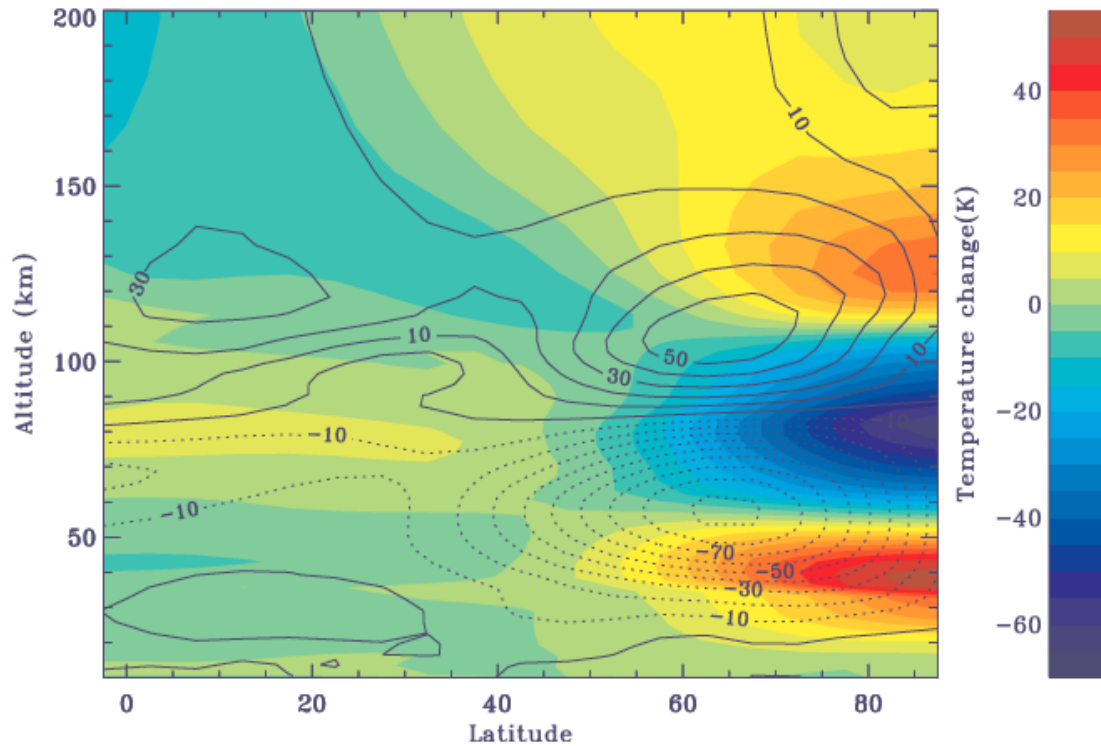


Figure 2.5. SSW event simulated with the coupled TIME-GCM/CCM3 model. The plot shows differences between prior to the simulated SSW and its peak, in zonal-mean temperature (color contours) and zonal-mean zonal winds (line contours in m/s; dotted lines westward direction, solid lines eastward direction). From *Liu and Roble* [2002]. Reprinted with permission from John Wiley and Sons.

2016a].

2.4.2. Mesospheric Zonal-Mean Zonal Wind Reversals

As can also be seen in Figure 2.5, the mesosphere is predicted to experience zonal-mean zonal wind reversals in the same westward direction and magnitude as the zonal wind reversals in the stratosphere during SSW events [*Liu and Roble*, 2002]. In *Hoffmann et al.* [2007], similar MF and meteor wind measurements show corroborative observations, which also show the time evolution of the zonal wind reversals in the mesosphere. What is most interesting in their observations is that the zonal wind reversals

in the mesosphere appear to precede the zonal wind reversals in the stratosphere, which are often used to mark the onset of a SSW event.

2.4.3. Mesospheric Gravity Wave Activity

The sudden westward zonal wind reversals in the stratosphere act as a filter allowing more eastward propagating gravity waves to enter the mesosphere [*Liu and Roble, 2002; Hoffmann et al, 2007; de Wit et al., 2014*]. This is contrary to what happens in the undisturbed winter mesosphere. In the winter stratosphere, the eastward winds block eastward propagating gravity waves through a critical layer interaction. Thus, the waves that make it to the winter mesosphere are normally westward propagating. Additionally, *Whiteway and Carswell [1994]* showed that there are connections between stratospheric warmings and gravity wave breaking near the topmost altitudes of the warmings' vertical extent. At the top of the warming layer, the temperature gradients tended to be equal to the adiabatic lapse rate during the SSW events. When this occurs, convective instability occurs and the gravity waves saturate, depositing their energy and momentum into the local atmosphere.

2.5. Associated Events in the Thermosphere and Ionosphere

2.5.1. Thermospheric Manifestations

Evidence of thermospheric warmings in association with SSWs can be seen in Figure 2.5 taken from the *Liu and Roble [2002]* model study. In the contour plot, the thermospheric warmings extend from about 110-200 km and appear to be less intense than their counterparts in the stratosphere. Though, in *Siskind et al. [2005]*, it is suggested that these thermospheric warmings might reach farther down in altitude, closer to 95-100

km.

2.5.2. Ionospheric Response

The most recent work in conjunction with SSWs has focused on the ionosphere's response to the stratospheric warming events. Ion temperatures from 100-300 were first observed and provided a slightly different picture of the thermosphere-ionosphere region's temperature response to SSWs [*Goncharenko and Zhang, 2008*]. In Figure 2.6 ion temperature differences between a non-warming period, in January 2007, and the SSW that occurred in January 2008 are shown. It was noted in *Goncharenko and Zhang* [2008], that both solar flux and geomagnetic activity were low in January 2008, thus they are not likely causes of the ion temperature change. One can see that a warming exists only in the lower thermosphere, from 100-150 km, unlike in Figure 2.5, where a thermospheric warming is predicted from 110-200 km. In fact, in Figure 2.6, there is another region of cooling from 150-300 km, which the *Liu and Roble* [2002] study did not predict.

Another SSW response in the ionosphere has been measured in total electron content (TEC) measurements made by GPS near the equator. The TEC counts were shown to be strongly disturbed in the daytime ionosphere with a peak about three-four days after the peak of the SSW event. This semidiurnal disturbance was manifested as an enhancement in the equatorial ionization anomaly (EIA) in the morning and a reduction of the EIA in the afternoon (local time of the GPS receivers) [*Goncharenko et al., 2010a; 2010b*]. These measurements were made during periods of low geomagnetic and solar flux activity. Vertical ion drift measurements by the incoherent scatter radar (ISR) at the

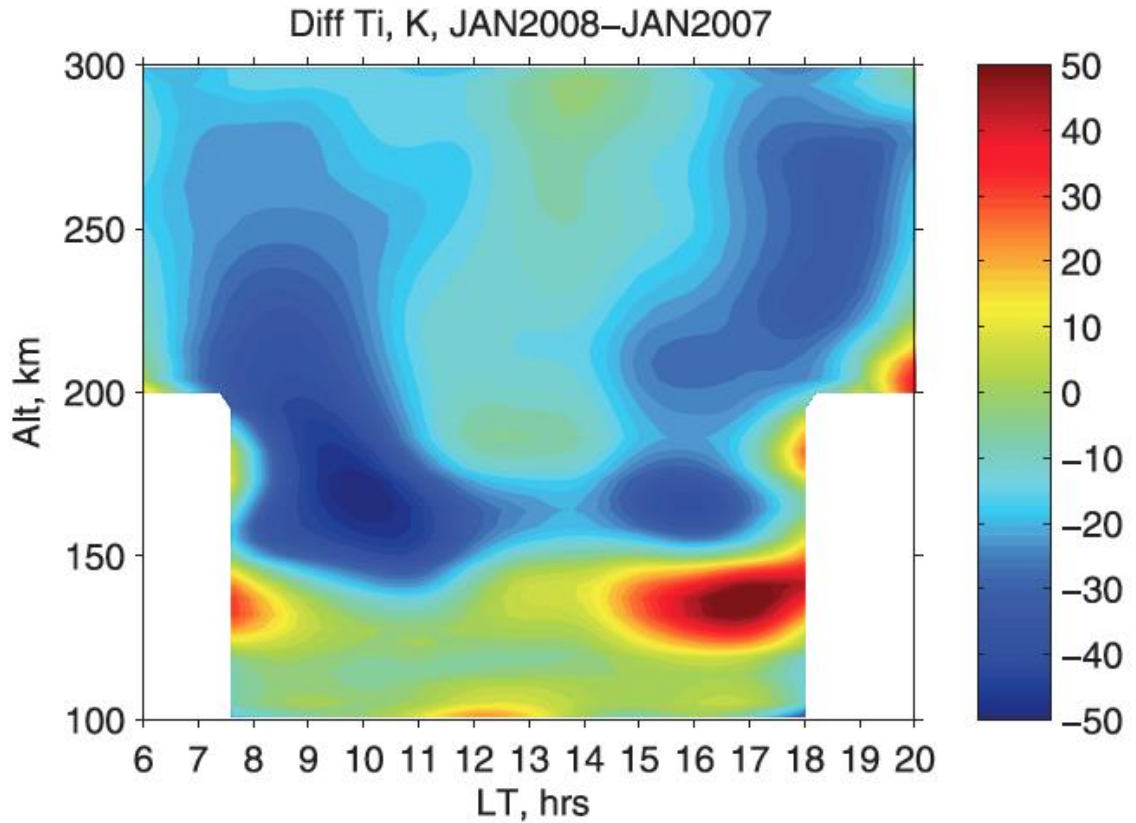


Figure 2.6. SSW ion temperature differences measured with the Millstone Hill ISR. Plot is of differences from a non-warming period and the period during the 2008 SSW. From *Goncharenko and Zhang* [2008]. Reprinted with permission from John Wiley and Sons.

equatorial Jicamarca, Peru station complemented the TEC disturbances. A semidiurnal pattern, with especially enhanced morning ion drifts and strongly suppressed afternoon ion drifts, was observed to be in phase with the TEC disturbances [*Goncharenko et al.*, 2010a].

2.6. Associated Disturbances in the Troposphere

Though connections in the troposphere to SSW events have been known since 1977 [*Quiroz*, 1977], they have recently become more significant as connections to tropospheric weather, which directly affects human life, have been made [*Baldwin and*

Dunkerton, 2001; Thompson et al., 2002]. *Quiroz [1977]* showed observations of a warming in the troposphere lagging a few days behind the warming in the stratosphere. He also noted a cooling in the midlatitude troposphere during the SSW period. Tropospheric connections to SSWs were revisited by *Baldwin and Dunkerton [2001]*. In their study, they established a unique pattern in the Northern Annular Mode (NAM), which gives a relative measure of the strength of the polar vortex in the NH. Figure 2.7 shows the composites of the NAM for both (a) weak polar vortex events (associated with the breakdown of the vortex during SSWs) and (b) strong polar events. The values in

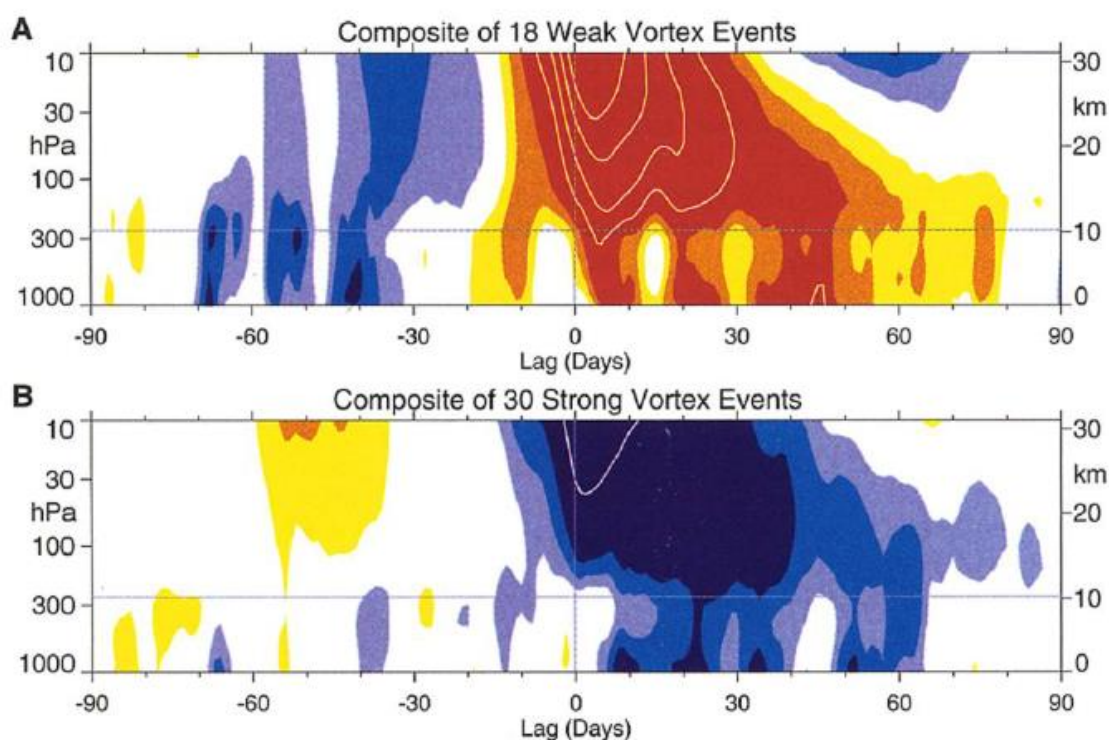


Figure 2.7. Northern Annular Mode composites for (a) weak vortex and (b) strong vortex events. Red contours are negative values of the NAM representative of weak events, while blue contours are positive values and represent strong vortex events. Both composites show a development of anomalous vortex strengths in the stratosphere preceding those in the troposphere. From *Baldwin and Dunkerton [2001]*. Reprinted with permission from AAAS.

these contour plots are nondimensional. Red contours represent negative values of the NAM, which correspond to weak vortex events and the blue contours are positive values, which correspond to strong vortex events. The weak vortex events, which are often common to SSWs in their signature polar vortex breakdowns, have been linked to extreme cold weather conditions in North America, Europe, and Eurasia [Thompson *et al.*, 2002]. An important concept that has come from this work is that the stratosphere could be monitored as a predictor of extreme tropospheric weather events up to two months in advance.

2.7. Southern Hemisphere Stratospheric Warmings

As already mentioned, most of the SSWs happen in the NH polar region. Though there have been many minor SSW events measured in the SH's polar region, only one major SSW has been detected there. The major SH SSW was markedly similar to those measured in the NH stratosphere [Baldwin *et al.*, 2003; Dowdy *et al.*, 2004; Liu and Roble, 2005]. In the SH polar mesosphere, coolings and wind reversals from eastward to westward prior to the SSW are seen in MF radar data and model simulations [Dowdy *et al.*, 2004; Liu and Roble, 2005]. These parameters in the mesosphere and stratosphere were seen to begin to change about one month prior to the SSW and then their altered states intensified with successive PW activity until the major warming in late September 2002 [Liu and Roble, 2005].

A noteworthy consequence of the 2002 SH major SSW is the splitting of the ozone hole in the SH polar stratosphere. Since the breakdown of the polar vortex in the SH SSW event caused the vortex to split into two distinct circulation cells, this meant that

the ozone depletion region also split as they share the same region in the stratosphere [Baldwin *et al.*, 2003]. Their Figure 2.8 depicts the split event in the ozone hole, which happened on September 25, 2002. While the ozone hole did become much smaller during the 2002 SSW, this unusual reduction is not expected to have a lasting effect on the ozone hole.

2.8. Further Questions About SSWs and Associated Phenomena

While so much research across many fields (meteorology, atmospheric science, and aeronomy) has been done to try to gain a complete understanding of SSWs and all of the correlated changes throughout the Earth's atmosphere, there are still many gaps in our understanding of these phenomena. For instance, what happens throughout the atmosphere at mid and low latitudes in conjunction with SSWs could be further explored. While modeling studies such as *Chandran and Collins* [2014] have explored this topic, more observational studies like *Yuan et al.* [2012b], *Angot et al.* [2012] and *Sox et al.* [2016a] are needed to better understand the full latitudinal signatures of SSWs. Following that, observations of the stratospheric, mesospheric, thermospheric and ionospheric disturbances need to be extended over larger longitudinal regions, as were modeled in the *Miller* [2013] study. We also have yet to see if any connections between hemispheres exists during and around SSW events. Finally, our understanding of these phenomena thus far has come to fruition using relatively few observational sites, so improved and further proliferated instrumentation will help us understand even more about these dramatic atmospheric disturbances.

References

- Angot, G., P. Keckhut, A. Hauchecorne, and C. Claud (2012), Contribution of stratospheric warmings to temperature trends in the middle atmosphere from the lidar series obtained at Haute-Provence Observatory (44°N), *J. Geophys. Res.*, *117*, D21102, doi:10.1029/2012JD017631.
- Argall, P. S. (2007), Upper altitude limit for Rayleigh lidar, *Ann. Geophys.* *25*, 19–15, doi:10.5194/angeo-25-19-2007.
- Baldwin, M., T. Hirooka, A. O'Neill, and S. Yoden (2003), Major stratospheric warming in the Southern Hemisphere in 2002: Dynamical aspects of the ozone hole split, *SPARC Newsl.*, *20*, 24–26.
- Baldwin, M. P., and T. J. Dunkerton (2001), Stratospheric harbingers of anomalous weather regimes, *Science*, *294*, 581–584, doi:10.1126/science.1063315.
- Bills, R. E., C. S. Gardner, and S. J. Franke (1991), Na Doppler/temperature lidar: Initial mesopause region observations and comparison with the Urbana medium frequency radar, *J. Geophys. Res.*, *96*(D12), 22701–22707, doi:10.1029/91JD02206.
- Bossert, K., D. C. Fritts, P.-D. Pautet, M. J. Taylor, B. P. Williams, and W. R. Pendleton (2014), Investigation of a mesospheric gravity wave ducting event using coordinated sodium lidar and Mesospheric Temperature Mapper measurements at ALOMAR, Norway (69°N), *J. Geophys. Res.*, *119*, 9765–9778, doi:10.1002/2014JD021460.
- Bowman M. R., A. J. Gibson, and M. C. W. Sandford (1969), Atmospheric sodium measured by a tuned laser radar, *Nature*, *221*, 456–457.
- Cai, X., T. Yuan, Y. Zhao, P.-D. Pautet, M. J. Taylor, and W. R. Pendleton Jr. (2014), A coordinated investigation of the gravity wave breaking and the associated dynamical instability by a Na lidar and an Advanced Mesosphere Temperature Mapper over Logan, UT (41.7°N, 111.8°W), *J. Geophys. Res.*, *119*, 6852–6864, doi:10.1002/2014JA020131.
- Chandran, A., and R. L. Collins (2014), Stratospheric sudden warming effects on winds and temperature in the middle atmosphere at middle and low altitudes: a study using WACCM, *Ann. Geophys.*, *32*, 859–874, doi:10.5194/angeo-32-859-2014.
- Charlton, A. J, and L. M. Polvani (2007), A new look at stratospheric sudden warmings. Part I: Climatology and Modeling Benchmarks, *J. Climate*, *20*, 449–469, doi:10.1175/JCLI3996.1.
- Chen H., M. A. White, D. A. Krueger, and C. Y. She (1996), Daytime mesopause temperature measurements with a sodium-vapor dispersive Faraday filter in a lidar

receiver, *Opt. Lett.*, *21*, 1093–1095, doi:10.1364/OL.21.001093.

Chu, X., Z. Yu, C. S. Gardner, C. Chen, and W. Fong (2011), Lidar observations of neutral Fe layers and fast gravity waves in the thermosphere (110–155 km) at McMurdo (77.8°S, 166.7°E), Antarctica, *Geophys. Res. Lett.*, *38*, L23807, doi:10.1029/2011GL050016.

de Wit, R. J., R. E. Hibbins, P. J. Espy, Y. J. Orsolini, V. Limpasuvan, and D. E. Kinnison (2014), Observations of gravity wave forcing of the mesopause region during the January 2013 major Sudden Stratospheric Warming, *Geophys. Res. Lett.*, *41*, 4745–4752, doi:10.1002/2014GL060501.

Dowdy, A. J., R. A. Vincent, D. J. Murphy, M. T. Tsutsumi, D. M. Riggin, and M. J. Jarvis (2004), The large-scale dynamics of the mesosphere-lower thermosphere during the Southern Hemisphere stratospheric warming of 2002, *Geophys. Res. Lett.*, *31*, L14102, doi:10.1029/2004GL020282.

Elterman, L. (1953), A series of stratospheric temperature profiles obtained with the searchlight technique, *J. Geophys. Res.*, *58*(4), 519–530, doi:10.1029/JZ058i004p00519.

Eska, V., J. Höffner, and U. von Zahn (1998), Upper atmosphere potassium layer and its seasonal variations at 54°N, *J. Geophys. Res.*, *103*(A12), 29207–29214, doi:10.1029/98JA02481.

Fricke, K. H., and U. von Zahn (1985), Mesopause temperature derived from probing the hyperfine structure of the D2 resonance line of sodium by lidar, *J. Atmos. Terr. Phys.*, *47*, 499–512.

Friedman, J. S., X. Chu, C. G. M. Brum and X. Lu (2013), Observation of a thermospheric descending layer of neutral K over Arecibo, *J. Atmos. Sol. Terr. Phys.*, *104*, 253–259.

Gao, Q., X. Chu, X. Xue, X. Dou, T. Chen, and J. Chen (2015), Lidar observations of thermospheric Na layers up to 170 km with a descending tidal phase at Lijiang (26.7°N, 100.0°E), China, *J. Geophys. Res. Space Physics*, *120*, 9213–9220, doi:10.1002/2015JA021808.

Gardner, C. S., M. S. Miller, and C. H. Liu (1989), Rayleigh lidar observations of gravity wave activity in the upper stratosphere at Urbana, Illinois, *J. Atmos. Sci.*, *46*, 1838–1854.

Gardner, C. S., X. Chu, P. J. Espy, J. M. C. Plane, D. R. Marsh, and D. Janches (2011), Seasonal variations of the mesospheric Fe layer at Rothera, Antarctica (67.5°S, 68.0°W), *J. Geophys. Res.*, *116*, D02304, doi:10.1029/2010JD014655.

Gibson, A. J., L. Thomas, and S. K. Battachacharyya (1979), Laser observations of the

ground-state hyperfine structure of sodium and of temperatures in the upper atmosphere, *Nature*, 281, 131–132.

Gille, S. T., A. Hauchecorne, and M. L. Chanin (1991), Semidiurnal and diurnal tidal effects in the middle atmosphere as seen by Rayleigh lidar, *J. Geophys. Res.*, 96, 7579–7587.

Goncharenko, L., and S.-R. Zhang (2008), Ionospheric signatures of sudden stratospheric warming: Ion temperature at middle latitude, *Geophys. Res. Lett.*, 35, L21103, doi:10.1029/2008GL035684.

Goncharenko, L. P., J. Chau, H.-L. Liu, and A. J. Coster (2010a), Unexpected connections between the stratosphere and ionosphere, *Geophys. Res. Lett.*, 37, L10101, doi:10.1029/2010GL043125.

Goncharenko, L. P., A. J. Coster, J. L. Chau, and C. E. Valladares (2010b), Impact of sudden stratospheric warmings on equatorial ionization anomaly, *J. Geophys. Res.*, 115, A00G07, doi:10.1029/2010JA015400.

Granier, G., J. P. Jegou, and G. Megie (1985), Resonant lidar detection of Ca and Ca⁺ in the upper atmosphere, *Geophys. Res. Lett.*, 12, 655–658.

Hauchecorne, A., and M.-L. Chanin (1980), Density and temperature profiles obtained by lidar between 35 and 70 km. *Geophys. Res. Lett.*, 7: 565–568, doi:10.1029/GL007i008p00565.

Hauchecorne, A., and M. L. Chanin (1983), Mid-latitude lidar observations of planetary waves in the middle atmosphere during the winter of 1981–1982, *J. Geophys. Res.*, 88(C6), 3843–3849, doi:10.1029/JC088iC06p03843.

Hauchecorne, A., M. L. Chanin, and R. Wilson (1987), Mesospheric temperature inversion and gravity wave breaking, *Geophys. Res. Lett.*, 14(9), 933–936.

Herron, J.P. (2007), Rayleigh-scatter lidar observations at USU's atmospheric lidar observatory (Logan, UT) — temperature climatology, temperature comparisons with MSIS, and noctilucent clouds, PhD dissertation, 156 pp., Utah State Univ., Logan, UT, <http://digitalcommons.usu.edu/etd/4686>.

Herron J. P., V. B. Wickwar, P. J. Espy, and J. W. Meriwether (2007), Observations of a noctilucent cloud above Logan, Utah (41.7°N, 111.8°W) in 1995, *J. Geophys. Res.*, 112, D19203, doi:10.1029/2006JD007158.

Hoffmann, P., W. Singer, D. Keuer, W. K. Hocking, M. Kunze, and Y. Murayama (2007), Latitudinal and longitudinal variability of mesospheric winds and temperatures during stratospheric warming events, *J. Atmos. Sol. Terr. Phys.*, 69, 2355–2366,

10.1016/j.jastp.2007.06.010.

Irving, B. K., R. L. Collins, R. S. Lieberman, B. Thurairajah, and K. Mizutani (2014), Mesospheric inversion layers at Chatanika, Alaska (65°N, 147°W): Rayleigh lidar observations and analysis, *J. Geophys. Res.*, *119*, 11235–11249, doi:10.1002/2014JD021838.

Johnson, E. A., R. C. Meyer, R. E. Hopkins, and W. H. Mock (1939), The measurement of light scattered by the upper atmosphere from a search-light beam, *J.O.S.A.*, *29*, 512–517.

Kafle, D. N. (2009), Rayleigh-lidar observations of mesospheric gravity wave activity above Logan, Utah, PhD dissertation, 209 pp., Utah State Univ., Logan, UT, <http://digitalcommons.usu.edu/etd/466>.

Kent, G. S., and R. W. Wright (1970), A review of laser radar measurements of atmospheric properties, *J. Atmos. Terr. Phys.*, *32*, 917–943, doi:10.1016/0021-9169(70)90036-X.

Kishore Kumar, G., M. Venkat Ratnam, A. K. Patra, S. Vijaya Bhaskara Rao, and J. Russell (2008), Mean thermal structure of the low-latitude middle atmosphere studied using Gadanki Rayleigh lidar, Rocket, and SABER/TIMED observations, *J. Geophys. Res.*, *113*, D23106, doi:10.1029/2008JD010511.

Labitzke, K. (1972), Temperature changes in the mesosphere and stratosphere connected with circulation changes in winter, *J. Atmos. Sci.*, *29*, 756–766.

Labitzke, K., and B. Naujokat (2000), The lower arctic stratosphere in winter since 1952, *SPARC Newsl.*, *15*, 11–14.

Leblanc, T., I. S. McDermid, A. Hauchecorne, and P. Keckhut (1998), Evaluation of optimization of lidar temperature analysis algorithms using simulated data, *J. Geophys. Res.*, *103*, 6177–6187.

Limpasuvan, V. D., D. W. J. Thompson, and D. L. Hartmann (2004), The life cycle of the Northern Hemisphere sudden stratospheric warmings, *J. Clim.*, *17*, 2584–2596.

Liu, A. Z., Y. Guo, F. Vargas, and G. R. Swenson (2016), First measurement of horizontal wind and temperature in the lower thermosphere (105–140 km) with a Na lidar at Andes Lidar Observatory, *Geophys. Res. Lett.*, *43*, doi:10.1002/2016GL068461.

Liu, H.-L., and R. G. Roble (2002), A study of a self-generated stratospheric sudden warming and its mesospheric-lower thermospheric impacts using the coupled TIME-GCM/CCM3, *J. Geophys. Res.*, *107*(D23), 4695, doi:10.1029/2001JD001533.

- Liu, H.-L., and R. G. Roble (2005), Dynamical coupling of the stratosphere and mesosphere in the 2002 Southern Hemisphere major stratospheric sudden warming, *Geophys. Res. Lett.*, 32, L13804, doi: 10.1029/2005GL022939.
- Lu, X., C. Chen, W. Huang, J. A. Smith, X. Chu, T. Yuan, P.-D. Pautet, M. J. Taylor, J. Gong, and C. Y. Cullens (2015), A coordinated study of 1 h mesoscale gravity waves propagating from Logan to Boulder with CRRL Na Doppler lidars and temperature mapper, *J. Geophys. Res.*, 120, 10006–10021, doi:10.1002/2015JD023604.
- Lübken, F.-J., J. Höffner, T. P. Viehl, B. Kaifler, and R. J. Morris (2011), First measurements of thermal tides in the summer mesopause region at Antarctic latitudes, *Geophys. Res. Lett.*, 38, L24806, doi:10.1029/2011GL050045.
- Matsuno, T. (1971), A dynamical model of the stratospheric sudden warming, *J. Atmos. Sci.*, 28, 1479–1494.
- Measures, R. M. (1992), *Laser Remote Sensing Fundamentals and Applications*, 510 pp., Krieger Publishing Company, Malabar, FL.
- Megie, G., F. Bos, J. E. Blamont, and M. L. Chanin (1978), Simultaneous nighttime lidar measurements of atmospheric sodium and potassium, *Planet. Space Sci.*, 26, 27–35.
- Meriwether, J. W., P. D. Dao, R. T. McNutt, W. Klemetti, W. Moskowitz, and G. Davidson (1994), Rayleigh lidar observations of mesospheric temperature structure, *J. Geophys. Res.*, 99, 16973–16987.
- Miller, A., H. Schmidt, and F. Bunzel (2013), Vertical coupling of the middle atmosphere during the stratospheric warming events, *J. Atmos. Sol. Terr. Phys.*, 97, 11–21, doi: 10.1016/j.jastp.2013.02.008.
- NASA MERRA Database Website: http://acd-ext.gsfc.nasa.gov/Data_services/met/ann_data.html.
- Plane, J. M. C., C. S. Gardner, J. Yu, C. Y. She, R. R. Garcia, and H. C. Pumphrey (1999), Mesospheric Na layer at 40°N: Modeling and observations, *J. Geophys. Res.*, 104(D3), 3773–3788, doi:10.1029/1998JD100015.
- Platzman, G. W. (1968), The Rossby wave, *Q.J.R. Meteorol. Soc.*, 94, 225–248. doi: 10.1002/qj.49709440102.
- Quiroz, R. S. (1977), The tropospheric-stratospheric polar vortex breakdown of January 1977, *Geophys. Res. Lett.*, 4, 151–154.
- Raizada, S., C. M. Brum, C. A. Tepley, J. Lautenbach, J. S. Friedman, J. D. Mathews, F. T. Djuth, and C. Kerr (2015), First simultaneous measurements of Na and K

thermospheric layers along with TILs from Arecibo, *Geophys. Res. Lett.*, *42*, 10106–10112, doi:10.1002/2015GL066714.

Rienecker, M. M., et al. (2011), MERRA: NASA's Modern-Era Retrospective Analysis for Research and Applications, *J. Clim.*, *24*, 3624–3648, doi:10.1175/JCLI-D-11-00015.1.

Scherhag, R. (1952), Die explosionsartigen Stratosphärenerwärmungen des Spätwinters 1952, *Ber. Deut. Wetterdienstes (US Zone)*, *38*, 51–63.

She, C. Y., J. R. Yu, and H. Chen (1993), Observed thermal structure of the midlatitude mesopause, *Geophys. Res. Lett.*, *20*, 567–570, doi: 10.1029/93GL00808.

She, C. Y., S. Chen, Z. Hu, J. Sherman, J. D. Vance, V. Vasoli, M. A. White, J. Yu, and D. A. Krueger (2000), Eight-year climatology of nocturnal temperature and sodium density in the mesopause region (80 to 105 km) over Fort Collins, Co (41°N, 105°W), *Geophys. Res. Lett.*, *27*, 3289–3292, doi:10.1029/2000GL003825.

She, C. Y., et al. (2004), Tidal perturbations and variability in the mesopause region over Fort Collins, CO (41N, 105W): Continuous multi-day temperature and wind lidar observations, *Geophys. Res. Lett.*, *31*, L24111, doi:10.1029/2004GL021165.

She, C.-Y., D. A. Krueger, and T. Yuan (2015), Long-term midlatitude mesopause region temperature trend deduced from quarter century (1990-2014) Na lidar observations, *Ann. Geophys.*, *33*, 363–369, doi:10.5194/angeocom-33-363-2015.

Sica, R. J., S. Sargoytchev, P. S. Argall, E. F. Borra, L. Girard, C. T. Sparrow, and S. Flatt (1995), Lidar measurements taken with a large-aperture liquid mirror. 1. Rayleigh-scatter system. *Appl. Opt.*, *34*(30), 6925–6936, doi: 10.1364/AO.34.006925.

Sica, R. J., and A. Haefele (2015), Retrieval of temperature from a multiple-channel Rayleigh-scatter lidar using an optimal estimation method, *Appl. Opt.*, *54*, 1872–1889, doi: 10.1364/AO.54.001872.

Siskind, D. E., L. Coy, and P. Espy (2005), Observations of stratospheric warmings and mesospheric coolings by the TIMED SABER instrument, *Geophys. Res. Lett.*, *32*, L09804, doi:10.1029/2005GL022399.

Sox, L. S., V. B. Wickwar, C. S. Fish, and J. P. Herron (2016a), Connection between the midlatitude mesosphere and sudden stratospheric warmings as measured by Rayleigh-scatter lidar, *J. Geophys Res.*, *121*, doi:10.1002/2015JD024374.

Sox, L. S., et al. (2016b), Lower thermospheric temperature measurements made by a large-aperture, high-power Rayleigh-scatter lidar, (in preparation) *Geophys. Res. Lett.* or *J. Geophys Res.*

Synge, E. H. (1930), A method of investigating the higher atmosphere, *Phil. Mag.*, 9, 1014–1020.

Thompson, W. J., M. P. Baldwin, and J. M. Wallace (2002), Stratospheric connection to Northern Hemisphere wintertime weather: implications for prediction, *J. Clim.*, 15, 1421–1428.

von Zahn, U., J. Hoffner, V. Eska, and M. Alpers (1996), The mesopause altitude: Only two distinct levels worldwide?, *Geophys. Res. Lett.*, 23, 3231–3234, doi:10.1029/96GL03041.

von Zahn, U., G. von Cossart, J. Fiedler, K. H. Fricke, G. Baumgarten, D. Rees, A. Hauchecorne, and K. Adolfsen (2000), The ALOMAR Rayleigh/Mie/Raman Lidar: objectives, configuration, and performance, *Ann. Geophys.*, 18, 815–833, doi:10.1007/s00585-000-0815-2.

Walterscheid, R. L., G. G. Sivjee, and R. G. Roble (2000), Mesospheric and lower thermospheric manifestations of a stratospheric warming event over Eureka, Canada (80° N), *Geophys. Res. Lett.*, 27, 2897–2900.

Whiteway, J. A., and A. I. Carswell (1994), Rayleigh lidar observations of thermal structure and gravity wave activity in the high arctic during a stratospheric warming, *J. Atmos. Sci.*, 51, 3122–3136.

Whiteway, J. A., A. I. Carswell, and W. E. Ward (1995), Mesospheric temperature inversions with overlying nearly adiabatic lapse rate: An indication of a well-mixed turbulent layer, *Geophys. Res. Lett.*, 22(10), 1201–1204.

Wickwar, V. B., T. D. Wilkerson, M. Hammond, and J. P. Herron (2001), Mesospheric temperature observations at the USU/CASS Atmospheric Lidar Observatory (ALO), *Proceedings of SPIE*, 4153, 272–284, doi:10.1117/12.417056.

Wickwar, V. B., M. J. Taylor, J. P. Herron, and B. A. Martineau (2002), Visual and lidar observations of noctilucent clouds above Logan, Utah, at 41.7°N, *J. Geophys. Res.*, 107, 10.1029/2001JD002280.

Wilson, R., A. Hauchecorne, and M. L. Chanin, (1990), Gravity wave spectra in the middle atmosphere as observed by Rayleigh lidar, *Geophys. Res. Lett.*, 17, 1585–1588.

Wynn, T. A. (2010), Statistical analysis of the USU lidar data set with reference to mesospheric solar response and cooling rate calculation, with analysis of statistical issues affecting the regression coefficients, PhD dissertation, 280 pp., Utah State Univ., Logan, UT.

Yuan, T., C.-Y. She, T. D. Kawahara, and D. A. Krueger (2012a), Seasonal variations of

mid-latitude mesospheric Na layer and its tidal period perturbations based on full-diurnal-cycle Na lidar observations of 2002-2008., *J. Geophys. Res.*, *117*, D11304, doi:10.1029/2011JD017031.

Yuan, T., B. Thuraijah, C.-Y. She, A. Chandran, R. L. Collins, and D. A. Krueger (2012b), Wind and temperature response of midlatitude mesopause region to the 2009 sudden stratospheric warming, *J. Geophys. Res.*, *117*, D09114, doi:10.1029/2011JD017.

CHAPTER 3

HIGH-POWERED, LARGE APERTURE RAYLEIGH-SCATTER LIDAR FOR THE
STUDY OF THE MESOSPHERE AND LOWER-THERMOSPHERE**Abstract**

Rayleigh-scatter lidar (RSL) measurements have provided relative density and absolute temperature measurements of the middle and upper atmosphere (~35-90 km) for over three decades. The data acquired with these instruments have been used to study the thermal structure, dynamics, and long-term trends in these atmospheric regions. Recently, the Rayleigh lidar on the campus of Utah State University (USU; 41.74°N, 111.81°W) has been upgraded to include a greater amount of transmitted power (42 W) and a larger receiving aperture (4.9 m²), which has enabled observations to be made from 70 to up to 115 km. A detailed description of the new system's optical, mechanical and electronic design will be given. The Rayleigh lidar temperature analysis will be described, as well as the changes to this analysis required to compensate for the changing atmospheric composition due to the increasing presence of atomic oxygen, which occurs from photodissociation and the change from a well-mixed atmosphere to one dominated by diffusive equilibrium, starting roughly at 100 km. The data (relative densities and absolute temperatures) collected over the system's inaugural year (summer 2014 to summer 2015) will be presented and compared with the MSISE00 empirical model, as well as climatological data from the original USU RSL system.

1. Introduction

Pulsed-light probing of the Earth's atmosphere, resulting in measurements of density and temperature, has been in practice for over half a century [*Elterman*, 1953]. With the advent of the laser, measurements of Rayleigh scatter off of the molecular middle and upper atmosphere were made possible [*Fiocco and Smullin*, 1963]. Using the Rayleigh-scatter lidar (light detection and ranging) technique as a method for obtaining neutral atmospheric temperatures was pioneered by *Hauchecorne and Chanin*, [1980]. Since then, Rayleigh lidar systems have been used to acquire extensive datasets in the atmospheric region of 30-90 km, which is too high for radiosonde (0-30 km) measurements and too low for meteor wind radar (70-100 km), incoherent scatter radar (from 100 to above 500 km), resonance lidar (80-105 km), and airglow imager (~90 km) measurements. Sounding rockets and satellite remote sensing can cover similar altitude ranges, but lack the temporal coverage that Rayleigh lidars can obtain. While researchers have combined datasets from several of the instruments to achieve whole-atmosphere coverage (in the troposphere, stratosphere, mesosphere and thermosphere) a large-aperture, high-powered Rayleigh lidar has the capability to obtain this same altitude coverage with a single instrument. The robustness and ease-of-use associated with older Rayleigh lidar systems can scale with the new, larger systems to achieve more cost-effective and continuous data accumulation over all of the atmospheric regions.

The Rayleigh lidar that operated on the campus of Utah State University from 1993 to 2004 [*Wickwar et al.*, 2001] has recently undergone major upgrades to transform it into a large-aperture, high-power system. The main upgrades included using two lasers instead of one, which increased the power from about 20 W to 42 W, and four coaligned

1.25 m diameter parabolic mirrors instead of one 44-cm diameter telescope. The larger mirrors increased the total receiving aperture area to 4.9 m^2 . These augmentations to the original Rayleigh lidar made some of the operating and maintenance procedures more complex. Several changes to the optical and electronic systems had to be made to improve the ease of use of the lidar in order for it to be operated by students every clear night.

During the first operational year, from summer 2014 to summer 2015, the upgraded USU Rayleigh lidar acquired nearly 100 nights of relative density and absolute temperature data between the altitudes of 70 and 115 km. This altitude range covers the transition between the mesosphere and lower thermosphere (MLT), which includes the coldest part of the Earth's atmosphere, the mesopause. In this chapter, we will show, for the first time, Rayleigh lidar temperatures in the MLT region for a complete annual cycle.

The remainder of this chapter will be organized as follows: section 2 will review Rayleigh-scatter lidar theory and some of the challenges in extending this technique into the lower thermosphere; section 3 will give a detailed description of the new USU Rayleigh-scatter lidar system; section 4 will explain the data analysis procedures used to reduce the raw lidar signal to temperatures including the additional steps needed to extend the current analysis methods above 90 km; section 5 will review the temperature data obtained over the 2014-2015 year, and section 6 will present a discussion of and conclusions made about the new system and its first year of data in the MLT region.

2. Rayleigh-Scatter Lidar Theory

Rayleigh-scatter lidar systems transmit laser light to induce Rayleigh scattering of

the incident light off of atmospheric molecules. A portion of the backscattered photons are then collected in the system receiver optics. Rayleigh scattering is an elastic scattering process (where there is no energy absorbed by the scattering molecule), which occurs between incident light and particles that are much smaller than the wavelength of the light [Measures, 1992]. In the Earth's middle atmosphere, the dominant Rayleigh scatterers are N₂, O₂, and Ar. Since the backscatter cross section for the Rayleigh process is inversely proportional to λ^4 , these molecules are more effective at scattering shorter wavelengths than long wavelengths. Initially, Rayleigh lidar systems used ruby lasers, which emit light at 694.3 nm [Fiocco and Smullin, 1963], but now the use of the more efficient Nd:YAG laser is preferred. These lasers emit in the infrared at $\lambda=1064$ nm and can be frequency doubled to $\lambda=532$ nm or tripled to $\lambda=355$ nm. While the frequency-tripled mode gives the best backscatter cross section, in practice the frequency-doubled mode in the green at $\lambda=532$ nm is preferred because the visible light makes operations and alignment easier and safer.

The photons that are Rayleigh backscattered per unit time, N , are related to the atmospheric density by the lidar equation [Kent *et al.*, 1967],

$$N = \frac{AQ\sigma_R N_0 T^2 n \delta h}{h^2}, \quad (1)$$

where A is the receiver aperture area, Q is the receiver efficiency, σ_R is the effective Rayleigh backscatter cross section for the atmospheric composition, N_0 is the number of emitted photons per unit time, T is the atmospheric transmission (squared for the roundtrip path through the atmosphere), n is the atmospheric number density, h is the height from the lidar system, and δh is the vertical portion of the atmosphere illuminated

by the laser pulse. Eq. 1 can be rearranged to show atmospheric number density, n , is proportional to lidar signal, N . It follows that the relative density is proportional to Nh^2 .

From here, the calculation can be extended to convert atmospheric density into temperature. This was first applied to the searchlight lidar technique [Elterman, 1953] and then developed by *Hauchecorne and Chanin* [1980] for modern Rayleigh lidar. First, one must assume that the atmosphere is in hydrostatic equilibrium, which mathematically describes the balance between gravity and atmospheric pressure,

$$dp = -mg(h) \frac{n(h)}{N_A} dh, \quad (2)$$

where p is pressure, m is the mean molecular mass (in kg/kmol) of the atmosphere, N_A is the Avogadro constant ($6.022 \times 10^{23} \text{ mol}^{-1}$), and $g(h)$ and $n(h)$ are the gravity and atmospheric number density (in number of particles/m³) given as a function of height, h , (in km). Integrating Eq. 2 from the highest altitude, h_{max} , downward gives

$$p(h_{max}) - p(h) = - \int_h^{h_{max}} n(h')m(h')g(h')dh'. \quad (3)$$

The relationship between pressure, density, and temperature, T , is given by the ideal gas law,

$$p(h) = \frac{n(h)}{N_A} RT(h), \quad (4)$$

where R is the ideal gas constant [8.314 J/(mol·K)]. Substituting Eq. 4 into Eq. 3 gives

$$R \frac{n(h_{max})}{N_A} T(h_{max}) - R \frac{n(h)}{N_A} T(h) = - \frac{1}{N_A} \int_h^{h_{max}} n(h')m(h')g(h')dh'. \quad (5)$$

Rearranging Eq. 5 gives the final Rayleigh lidar temperature integral equation,

$$T(h) = T(h_{max}) \frac{n(h_{max})}{n(h)} + \frac{1}{R} \int_h^{h_{max}} \frac{n(h')}{n(h)} m(h')g(h')dh', \quad (6)$$

where we have modified the calculation given in *Hauchecorne and Chanin* [1980] to

eliminate the pressure terms, similar to *Beissner* [1997] and *Herron* [2007].

It is important to note that σ_R , in Eq. 1, and m , in Eq. 6, are taken to be a constant in practice. This assumption is valid where the atmosphere is a homogeneous mixture of N_2 , O_2 , and Ar, below about 90 km. Above this, photodissociation breaks up O_2 , which, along with diffusive equilibrium, results in a gradual increase in the proportion of atomic oxygen, O, with altitude. The changing atmospheric composition above 90 km was recognized early on as a limiting factor to the Rayleigh lidar technique's upper altitude limit [*Kent and Wright*, 1970]. To go above 90 km, the USU Rayleigh lidar not only had to undergo instrumental improvements, but also, changes to the above calculations in the data reduction, as well. These changes will be described in detail in section 4. It should also be noted that Eq. 6 gives temperatures as a function of a ratio of densities, $n(h_{max})/n(h)$. This relationship allows for the relative density measurements, acquired by the lidar, to be reduced to absolute temperatures. This last detail is why Rayleigh lidar data are typically reported as atmospheric temperatures.

3. System Design

A summary of the USU Rayleigh lidar system parameters is given in Table 3.1 and an overview of the system design is shown in Figure 3.1. In the following subsections, details describing all of the lidar's subsystems (transmitter, timing, telescope, detector, and data acquisition) will be given.

3. 1. Transmitter

The Rayleigh lidar's transmitter (Figure 3.1) is comprised of two Spectra Physics

Table 3.1. USU Rayleigh-Scatter Lidar System Parameters

System Parameter	Value
Emitted laser wavelength	532 nm
Laser energy	1400 mJ/pulse
Total emitted laser power	42 W
Laser repetition rate	30 Hz
Pulse length	7 ns
Beam divergence (after beam expander)	0.125 mrad
Receiving aperture	4.9 m ²
PMT quantum efficiency	15% at 532 nm
Power-Aperture Product	206 W · m ²

GCR-series Nd:YAG lasers. One laser, the GCR-5, emits 600 mJ/pulse at a wavelength of 532 nm and the second, the GCR-6, emits 800 mJ/pulse at 532 nm. Both lasers have been frequency doubled to operate at a wavelength of 532 nm and have a pulse repetition rate of 30 Hz. The laser beams are individually sent through their own transmitter optics, which include dichroics to further eliminate the 1064 nm light and 4x beam expanders to enlarge their beams and reduce the beams' divergence by 4x. After the beam expander, the two beams are reflected from the same 45° mirror, which sends the beams vertically through the roof of the laboratory, through the center of the four-telescope cage, housed on the roof of the observatory building and up into the atmosphere (see Figures 3.1 and 3.3).

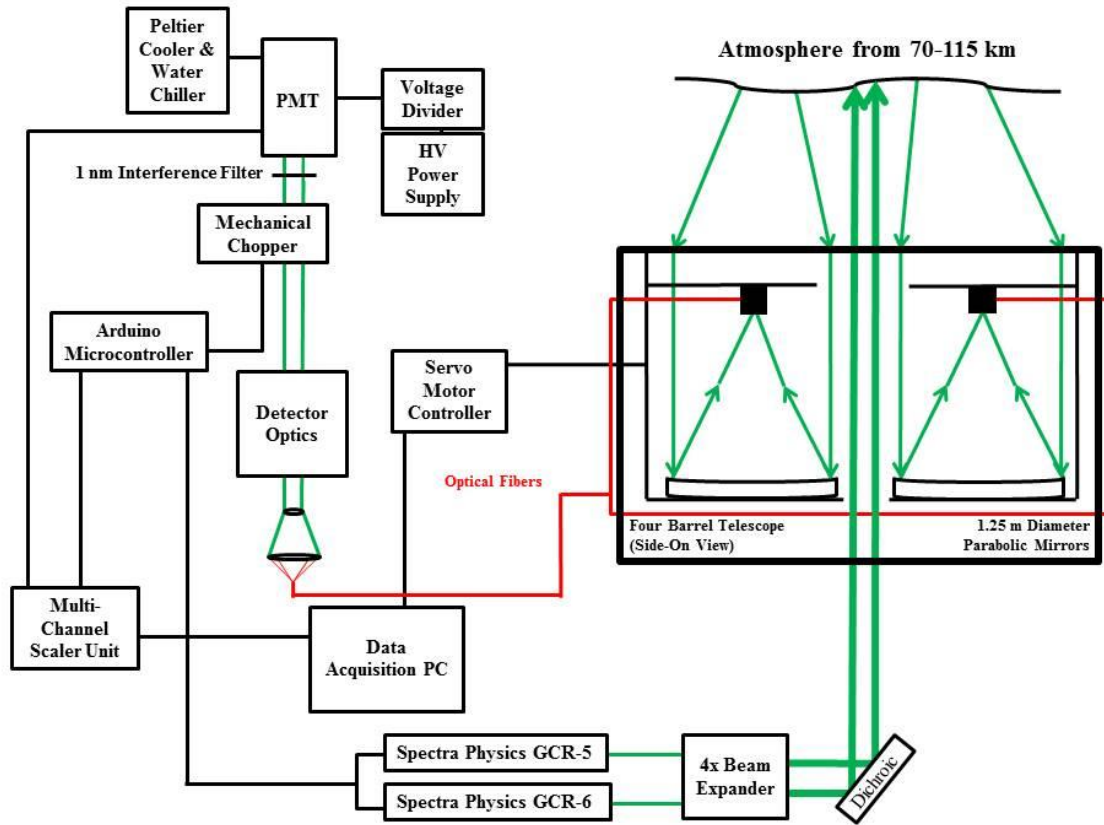


Figure 3.1. Block diagram of the USU Rayleigh lidar. Note that the four-telescope cage is shown in a side-on view, so only two of the four telescopes are visible in this depiction.

3. 2. Telescope

The telescope system (Figures 3.2 and 3.3) is comprised of four individual prime-focus telescopes, each with its own parabolic mirror, all housed in one steel-framed cage, [Wickwar *et al.*, 2001]. Each mirror focuses the return lidar signal directly onto a 1.5 mm diameter Thorlabs optical fiber with numerical aperture of 0.39, which also acts as a field stop. Each mirror is 1.25 m in diameter, and when used together as one receiving aperture, they have an effective collecting area of 4.9 m^2 , which is comparable to a single 2.5 m-diameter mirror. The cost of constructing the telescope system was much lower than the cost would be to build a single mirror telescope with the same size receiving

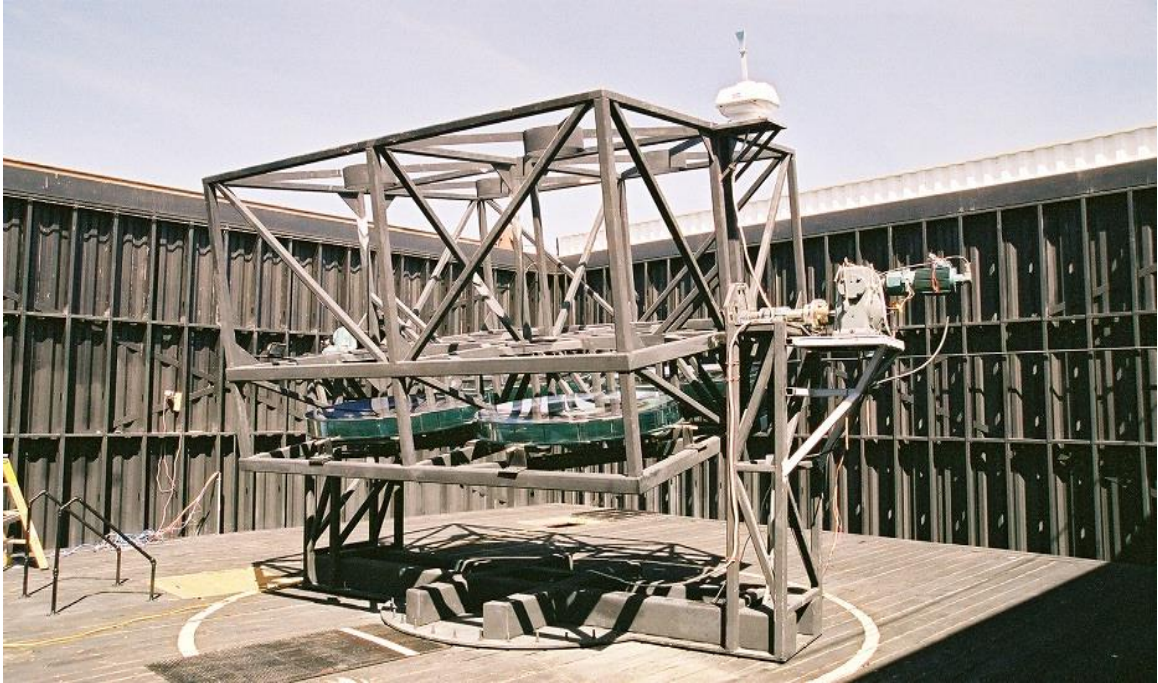


Figure 3.2. Photograph of Rayleigh lidar telescope cage at the Atmospheric Lidar Observatory on the campus of USU.

aperture. Most of the reduced cost was achieved by building four smaller mirrors, rather than one large mirror. The entire cage was designed to have the capability for scanning 540° degrees in azimuth and $\pm 45^\circ$ in zenith angle. For the 2014-2015 year, the telescope was fixed in the zenith position.

Due to the scale of the telescope cage, aligning all four mirrors was initially found to be a very time consuming process. To complete a full alignment procedure, the tilt of each mirror must be adjusted by turning three large bolts attached to three support plates under each mirror. Next, the x -, y -, and z - position of the fiber holder must be aligned. To make this process more efficient, two Thorlabs Z625B motorized actuators were added to each fiber's holder to be able to adjust the fiber in the horizontal plane (x and y directions) parallel to the mirror surface. Labview programs were written to steer the

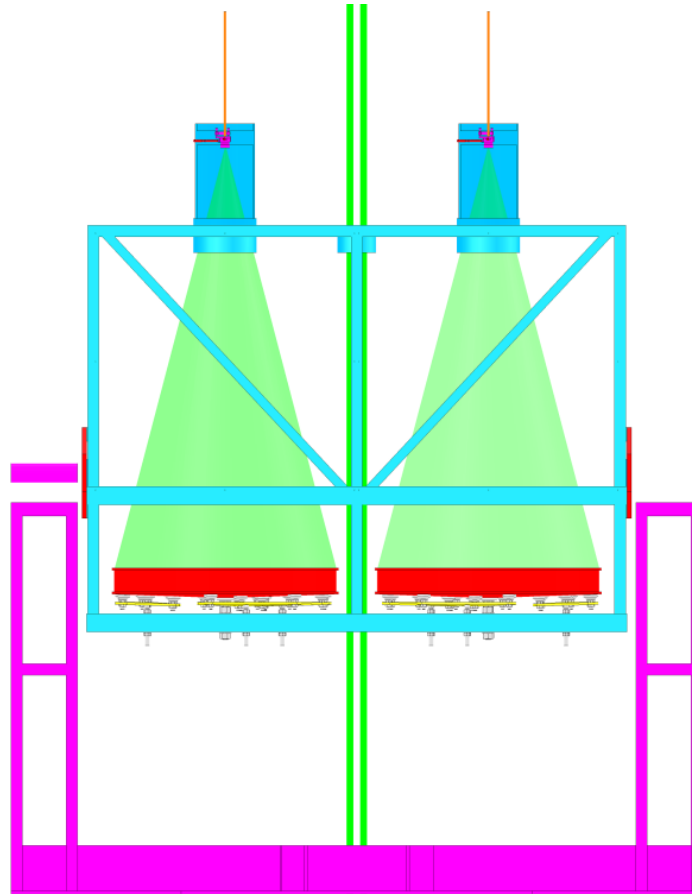


Figure 3.3. USU Rayleigh lidar telescope cage system. Figure shows a side view of the telescope cage (cyan) with the two vertical transmitter beams (green) going through the center of the cage and the returned light (green) being focused by two of the mirrors (red) onto their respective optical fibers (orange). Fiber holders (magenta), actuators (red) and alignment plates (yellow) are the main components used during the alignment procedure.

actuators and also to carry out a search pattern in the horizontal plane to find the optimal position for each fiber, independently. The addition of the actuators and search pattern program shortened the full alignment procedure from one night (~6 hours) per mirror to one night for all four mirrors. A full alignment has been found to be needed approximately every three months, or for every major seasonal (temperature) change.

A rough calculation can be done to show that the telescopes will capture all of the laser spot size at 120 km, an altitude about 5 km higher than the maximum of the 2014-

2015 nighttime averages. To start, the laser beams' have a divergence of 0.5 mrad [Spectra-Physics Lasers, 1991]. This divergence was further reduced by a factor of four using a 4x beam expander (Figure 3.1) to give a final beam divergence, for each laser, of 0.125 mrad. The far-field laser beam's spot size increases linearly with increasing distance from the laser. The half angle beam divergence, θ , is related to the radius of the spot size, h , at a distance, d , from the laser by

$$\sin \theta \approx \theta = \frac{h}{d} \quad (7)$$

for small angles. Since the two laser beams are pointed in the same vertical direction and separated by a small amount (<0.5 in.) on the dichroic shown in Figure 3.1, at large distances from the lasers' spots essentially overlap. For each telescope, the mirror can be approximated as a thin lens as in Figure 3.4. This gives a relationship similar to Eq. 7 where θ is the angular field of view (FOV) of the telescope, d is the focal length of the mirror, and h is the maximum image size the 1.5 mm-diameter optical fiber will allow. The mirrors have a focal length of approximately 93 inches or 2362 mm. This gives a FOV of

$$\theta = \frac{1.5 \text{ mm}}{2362 \text{ mm}} \approx 6.35 \times 10^{-4} \text{ rad} . \quad (8)$$

We reverse this calculation to find the maximum spot size at 120 km, that the FOV of the telescopes would allow,

$$h = \theta d = (6.35 \times 10^{-4} \text{ rad})(1.2 \times 10^5 \text{ m}) \approx 76 \text{ m} . \quad (9)$$

The same calculation can be done to find the laser's spot size at 120 km,

$$h = (1.25 \times 10^{-4} \text{ rad})(1.2 \times 10^5 \text{ m}) \approx 15 \text{ m} . \quad (10)$$

Here we see that the lasers' spot size has less than a quarter the diameter of what the

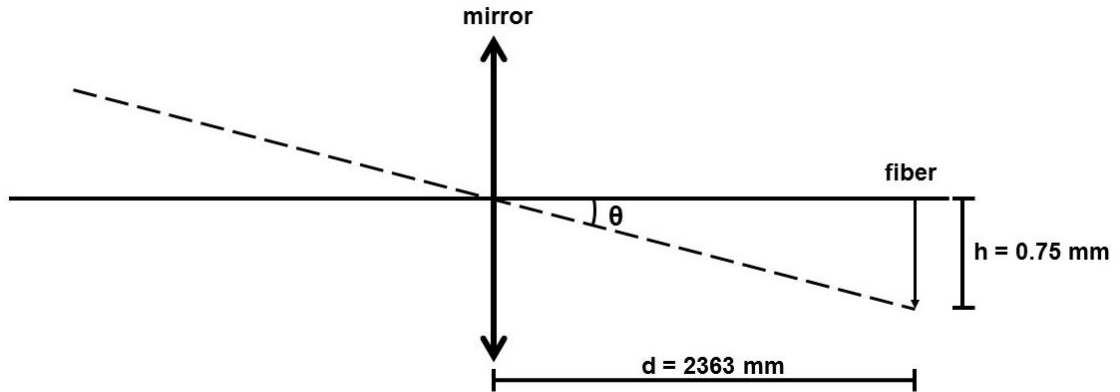


Figure 3.4. Ray tracing geometry of the thin lens approximation of the telescopes.

telescopes' FOV will allow from an image at 120 km.

We can also check that the optical fiber, when placed at the focal point of the mirror, will capture all of the light focused by the mirror. The optical fibers have a numerical aperture (NA) of 0.39 [Thorlabs] and an optical fiber's NA is related to one-half its angular aperture, θ , by,

$$NA = n \sin \theta , \quad (11)$$

where n is the refractive index of the medium at the entrance to the fiber (in this case air $n=1$). Solving Eq. 11 for one-half the angular aperture gives $\theta=0.40$ rad. With the fiber placed at the focal point, f , of the mirror, we can calculate the base diameter, d , of the cone of light that the fiber will accept,

$$d = 2f \sin \theta = 2(2.363 \text{ m}) \sin 0.40 = 1.84 \text{ m} . \quad (12)$$

Thus, the fiber will allow all of the light focused from the 1.25 m-diameter mirror, as well as some extra light scattered around the observatory.

3.3. Detector System

The lidar's photon counting detector system is located inside a light-tight box on

an optical bench in the same room as the laser transmitter system. After the backscattered photons are sent to the four optical fibers, they are combined, optically, at several points in order to take advantage of all four mirror's receiving area. The optical system needed to combine the light from all four fibers is not trivial in design and includes a series of lenses to both combine the four signals and conserve the etendue or throughput $A\Omega$ of the optical system as much as possible. The detector optics place the smallest image possible (~ 2 mm) on the plane of a New Focus (now Newport) optical chopper, which operates at a frequency of 210 Hz, set to block the return signal from altitudes below about 50 km. From there, the return signal goes through a final collimating lens and passes through a narrowband interference filter with a FWHM of 1 nm, centered at 532 nm. After the filter, the return signal enters a Products for Research (PfR) cooled photomultiplier tube (PMT) housing and is incident onto the photocathode of an Electron Tubes (ET) 9954 green sensitive, alkali PMT. The PMT has a quantum efficiency of 15% at 532 nm. Although PMTs with higher quantum efficiency exist, the choice of the ET 9954 was made for its large photocathode size (51 mm), which is able to receive the combined beam (~ 38 mm) from the four fibers. To reduce the noise due to thermionic emission (dark count), the PfR PMT housing is cooled by a combination of a water chiller and a Peltier cooler to about -25° C. High voltage (between -1900 and -2100 VDC) is supplied to the photocathode using a Fluke 415B high-voltage power supply unit (HV PSU). This voltage is then divided across the PMT's 12 dynodes using a custom-made voltage divider (Figure 3.5). The PMT has a gain of 10^6 . With a 3 ns FWHM pulse and 50 Ω impedance in the BNC cable, the output voltage per photon is

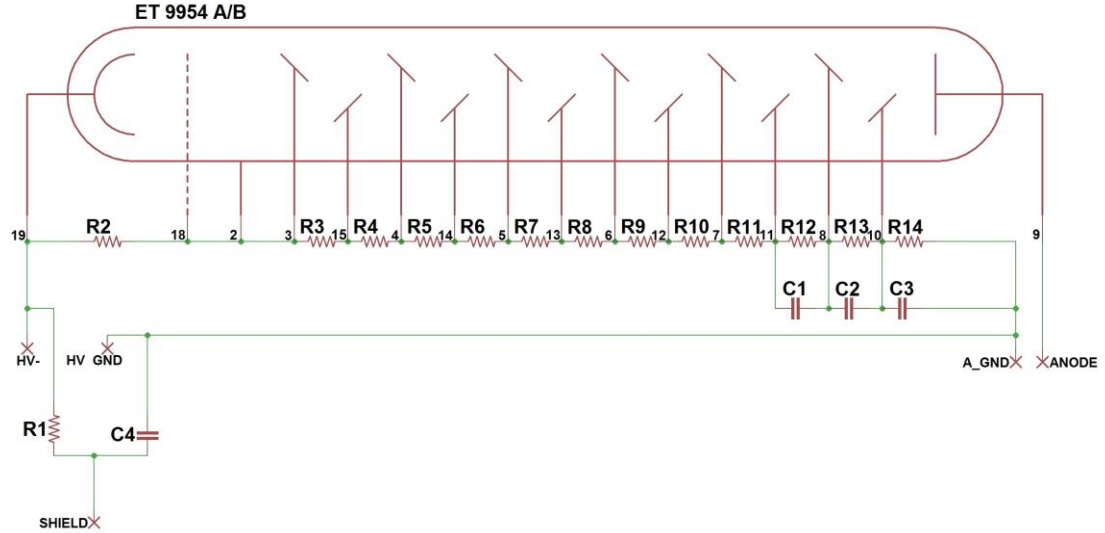


Figure 3.5. Circuit diagram for custom made voltage divider used to power the ET 9954 PMT. All resistors in the dynode chain (R3-R14) have resistances of $R=100\text{ k}\Omega$ with the exception of the modified taper ($R12=R$, $R13=2R$, and $R14=3R$). The remaining components have the following values: $R1=10\text{ M}\Omega$, $R2=220\text{ k}\Omega$, $C1=0.01\text{ }\mu\text{F}$, $C2=0.05\text{ }\mu\text{F}$, $C3=0.1\text{ }\mu\text{F}$, and $C4=0.01\text{ }\mu\text{F}$.

$$V = IR = \frac{(-1.6 \times 10^{-19} \text{ C})(10^6)}{3 \times 10^{-9} \text{ s}} (50 \Omega) = -2.7 \text{ mV} . \quad (13)$$

This voltage is relatively low, so the signal from the PMT anode is sent to an Ortec VT120A Fast-Timing preamplifier with a gain of 200. The use of a preamplifier is recommended when using PMTs as detectors [EG&G Ortec]. The 200x gain was experimentally found to give a better SNR than the 20x gain version of the VT120. The 200x gain brings the output voltage per photon, given in Eq. 13, to -540 mV, which exceeds the discriminator threshold and is well within the signal input range of -5 to +5 V accepted by the MCS [EG&G Ortec].

Typical measured signal, dark count and background (noise due to light sources such as stars, the moon and city lights, and dark count) levels are given in Table 3.2. Note that these count rates do not exceed the approximate 1 MHz count rate of the PMT before

Table 3.2. Approximate Signal and Background Levels for the USU Rayleigh Lidar

Signal type	1-year average (MHz)	1-year average (counts per 2 min integration)	Signal dependent upon
Signal (at 70 km)	0.640	575	Laser power, number of lasers used, telescope area used, atmospheric transmission, and cloud cover
Background noise + dark count (averaged from 189 to 339 km)	0.022	20	light pollution, and phase of the moon
Dark count* (no light on tube)	0.006-0.022	6-20	Which ET 9954 PMT was used, cooling temperature

*Dark count was measured independently only during testing and different for each of the three different ET 9954 PMTs used for the 2014-2015 run.

it goes nonlinear, which results in undercounting of photons.

3.4. Data Acquisition System

The negative pulse output of the PMT and preamplifier combination is sent to an Ortec Turbo Multichannel Scaler (MCS) and is recorded as a function of time. A voltage discriminator inside the MCS sets a voltage threshold of -0.0708 V, a value experimentally found to give the best signal-to-noise ratio, and counts any pulses more negative than this threshold into 14,000 altitude bins each 37.5 m (250 ns) long. The data are integrated for two minutes, then sent to a PC using the provided Ortec MCS software. A MCS job file program (Appendix A) runs continuously to record two-minute profiles throughout the night.

3.5. Timing System

The timing of the lidar system is controlled by an Arduino Duemilanove microcontroller board, which is based on the ATmega168 microcontroller, which has a clock speed of 16 MHz. The input to the Arduino is supplied by the chopper controller running at 210 Hz. The chopper input is divided by 7 to supply a 30 Hz signal to the laser's flashlamps after a delay chosen to prevent PMT saturation from low-altitude signal. The Q-switch of each laser is fired with a 62-ns offset from one another after a delay, which was chosen to maximize both lasers' power output. A start pulse is sent to the MCS to initiate data recording from the PMT, coincident with the first Q-switch firing. A timing diagram is given in Figure 3.6 and the Arduino timing code can be found in Appendix A.

4. Data Analysis

The USU Rayleigh lidar group uses the temperature integral equation, given in section 2, to reduce raw lidar signal to atmospheric temperatures. The raw lidar signal is averaged over a given time interval (usually either one hour or a whole night) and converted to relative densities that are then used in the temperature calculation. A Hamming filter with a FWHM of 2 km is applied to smooth the data in the vertical direction. The 2-km window width was chosen to match the Na lidar smoothing width for the comparison between the two lidars, which will be discussed in Chapter 4. To begin the temperature calculation an initial, or seed temperature must be given at the highest altitude. This altitude can vary from night to night, depending on the length of the observation, laser power, atmospheric transmission, and the atmospheric number density.

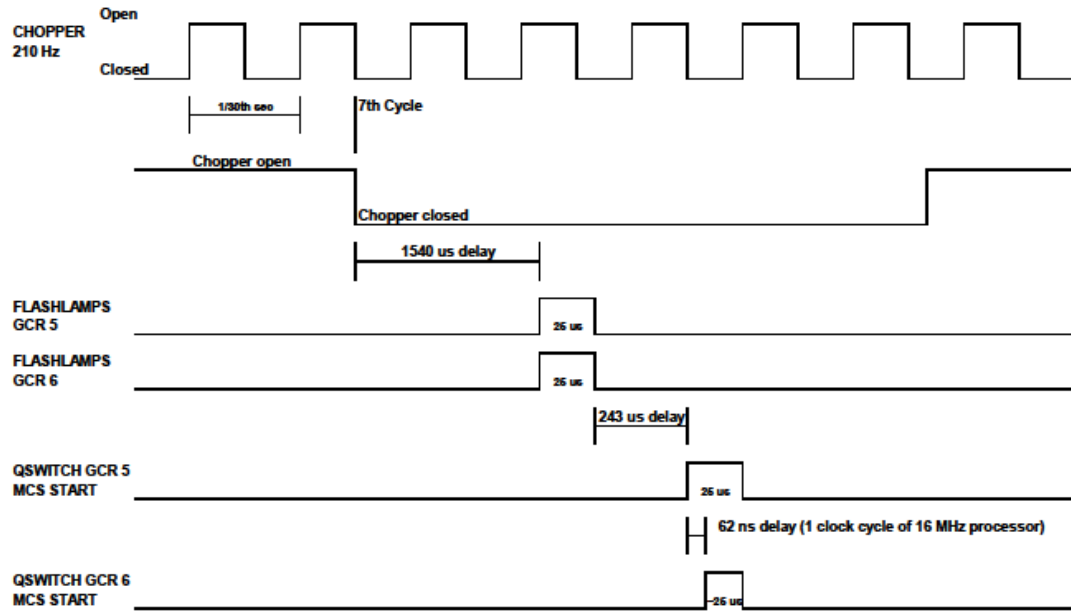


Figure 3.6. Timing diagram for the Rayleigh lidar. The lidar timing is controlled with an Arduino Duemilanove microcontroller board. The mechanical chopper provides the input to the board, which generates the firing commands for the two lasers' flashlamps, Q-switches and the start signal for the MCS after the 7th falling edge of the chopper signal. A delay of $1540 \mu\text{s}$ after the chopper closes was chosen to provide the best blocking of low-altitude signal. A delay of $243 \mu\text{s}$ after the falling edge of the flashlamp pulses was experimentally found to give the most power output from the lasers' pulses. The flashlamp and Q-switch pulse widths were chosen to be $25 \mu\text{s}$ based on the recommendation from *Spectra-Physics Lasers* [1991].

For this study, the seed temperature was taken from the Mass Spectrometer Incoherent Scatter (MSISe00) empirical model [Picone *et al.*, 2002]. The highest altitude is calculated statistically for each night as where the averaged lidar signal drops below 16 times its standard deviation. An example of the signal-to-standard deviation ratio is given in Figure 3.7 for the night of July 20, 2014. In the plot, one can see that the value of 16 makes a good cutoff value in that this value is reached right before the signal becomes indiscernible from the noise. In this plot, the background subtracted signal is used, as opposed to the signal plus background that is measured by the system, thus the noise

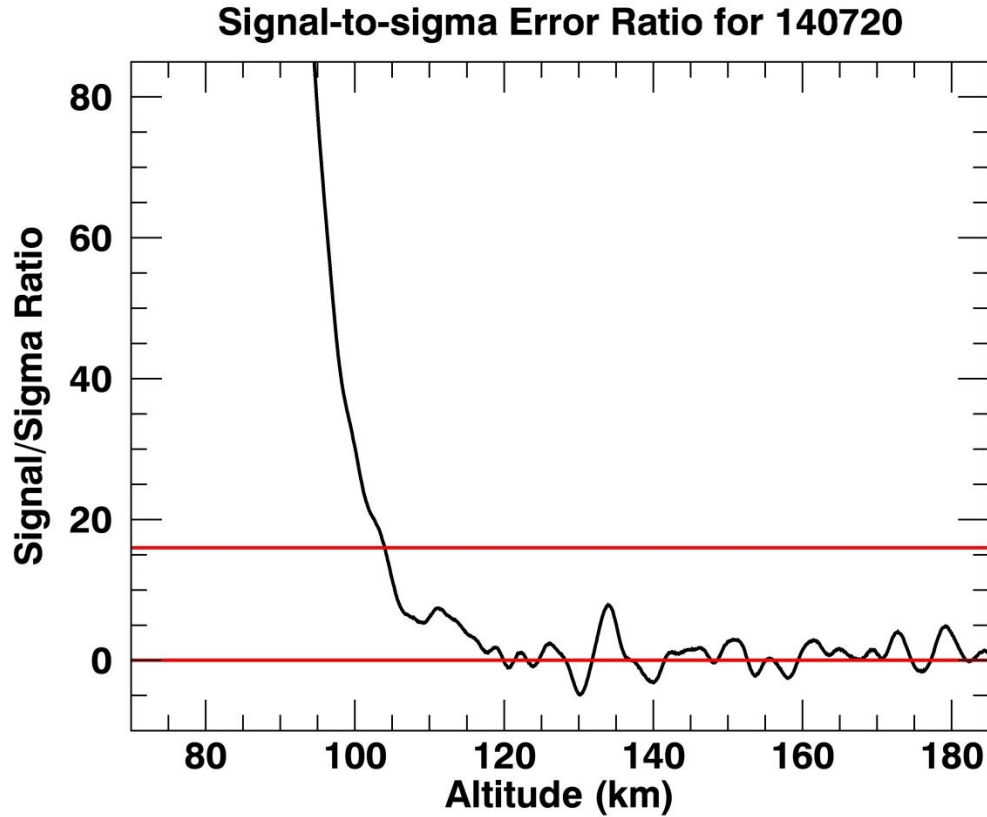


Figure 3.7. Ratio of lidar signal-to-standard deviation. From all-night average calculated from July 20, 2014 data. Red horizontal lines indicate where the ratio is equal to zero and sixteen.

level is centered at zero. For estimated signal and background levels, refer to Table 3.2.

4.1. Error Calculations

There are two main sources of error in the Rayleigh lidar temperature reduction: the random error from the lidar measurements (photon counting) and the systematic error from the initial temperature guess. The measured lidar signal includes both the true lidar signal, S , and a constant background, or noise, signal, N . The MCS is set to record data out to about 525 km and the chopper remains fully open until about 400 km. Although there is hardly any lidar signal to be measured out to these altitudes, the high-altitude data

is used for calculating an average background value. For the data reported in this paper, the background value is found by averaging the measured signal from bin number 5000 to 9000 (or roughly 189 to 339 km). To get the true lidar signal, the background value is subtracted from the entire measured lidar signal profile,

$$S = (S + N) - N . \quad (14)$$

The measured lidar signal follows Poisson statistics, which describes an experiment made of random, independent events (e.g., photon counting). In Poisson statistics, the standard deviation of a measurement, x , is the square root of that measurement, \sqrt{x} . It then follows, from the propagation of error through Eq. 14, that the standard deviation for the true lidar signal, at a height, h , calculated from a measured signal averaged over J time bins and smoothed vertically with a 2 km FWHM Hamming window and a background value averaged over J time bins and K altitude bins is

$$\sigma_{\langle \bar{S} \rangle_h} = \sqrt{\frac{1}{Jf_{107}^2} \{ \sum_{i=1}^{107} F_i^2 \langle S + N \rangle_J \} + \frac{1}{JK} \langle \langle N \rangle \rangle_{KJ}} , \quad (15)$$

where F_i^2 / f_{107}^2 are the normalized Hamming coefficients calculated at each point, i . With each altitude bin being 37.5 m, this gives the full Hamming window using 107 points a full width of approximately 4 km. The height, h , indicates the altitude in the middle of the window at point 54. The temperature standard deviation, due to the random measurement error, will be given by

$$\sigma_{T_h} = \sqrt{T_h^2 \left(\frac{\sigma_{n_h}}{n_h} \right)^2 + [\sigma_{T_{h_{max}}}^2 + T_{h_{max}}^2 \left(\frac{\sigma_{n_{h_{max}}}}{n_{h_{max}}} \right)^2] e^{\frac{-2(h_{max}-h)}{H}}} \quad (16)$$

through error propagation of Eq. 15 through the temperature calculation given in Eq. 6.

Here, T_h is the calculated temperature, n_h is the calculated density, and σ_{n_h} is the

measurement error given in Eq. 15, all at a specific height bin, h . The values with h_{max} in the subscript refer to the values at the highest altitude. H is the atmospheric scale height, which is assumed to be a constant 7 km in our calculations. The uncertainty in the seed temperature, $\sigma_{T_{h_{max}}}$, is typically unknown, so the second term in Eq. 16 is assumed to be zero, in practice. This assumption is a valid approximation since the multiplication by the exponential causes both the second and third terms in Eq. 16 to decrease rapidly with decreasing altitude. The complete derivations of Eqs. 15 and 16 are given in *Herron* [2007], although here, Eq. 15 has been modified from their Eq. 2.6.17, which was calculated for a rectangular smoothing window, to include the effect of the Hamming smoothing.

From Eq. 16, one can see that the effect of the seed temperature, $T_{h_{max}}$, decreases exponentially as one steps down in altitude. Figure 3.8 illustrates this by showing three different temperature profiles for the night of September 25, 2014. The black curve gives temperatures calculated using the MSISe00 seed temperature at 109 km and the two red dashed curves give temperatures calculated using the MSISe00 seed temperature ± 20 K at 109 km. This plot emphasizes that even if the seed temperature guess were 20 K off from the actual atmospheric temperature, after about 20 km, the integration converges to the same temperature profile. In Figure 3.8 the differences between the original curve and the ± 20 K curves become less than 1 K at 93 km, which is only 16 km below the top altitude.

4.2. Effects of Changing Atmospheric Composition in MLT Region

Inherent in the Rayleigh lidar temperature retrieval method is the assumption that

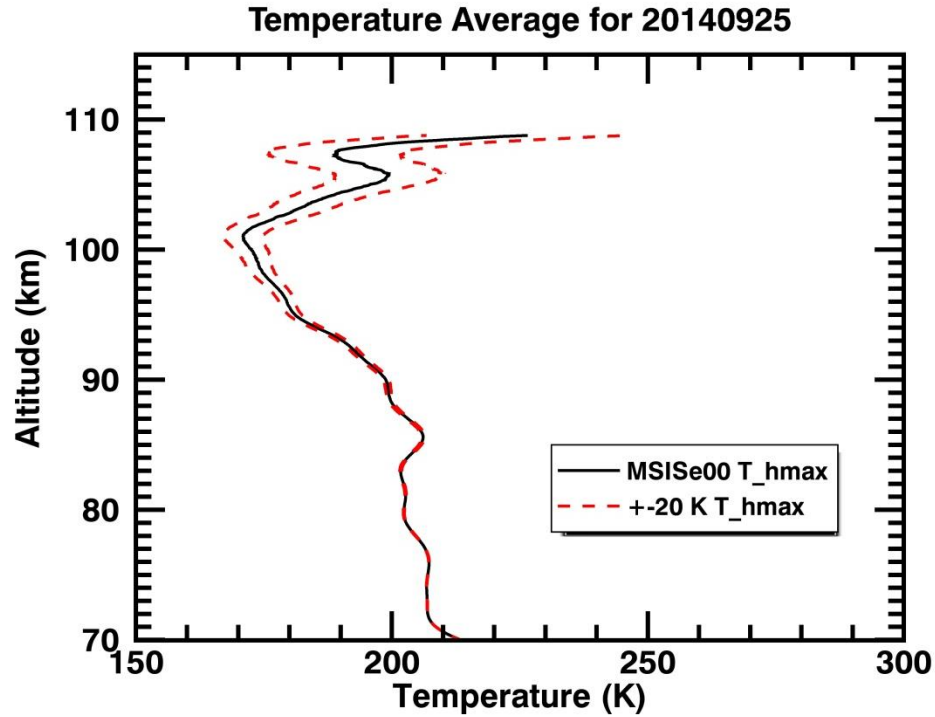


Figure 3.8. Temperature profile for the all-night average of Rayleigh lidar signal on September 25, 2014. The solid black curve gives the temperature using the MSISe00 supplied seed temperature of 225 K. The red dashed curves show temperatures calculated with seed temperatures that are 205 K and 245 K.

the neutral atmosphere is dominated by a turbulently mixed combination of molecular nitrogen (N_2), oxygen (O_2), and atomic argon (Ar), which is a good assumption up to about 90 km. This assumption allows one to take the Rayleigh-backscatter cross section (RBCS) and mean molar mass (MMM) to be constant over the altitude range of the Rayleigh lidar measurements, which previously did not extend much above 90 km. However, above 90 km, photodissociation and diffusive equilibrium break up molecular oxygen, which increases the proportion of atomic oxygen along in the atmospheric mixture of N_2 , O_2 , and Ar (see Figure 3.9). Due to this change in atmospheric composition, the temperature retrieval method used for new USU Rayleigh lidar

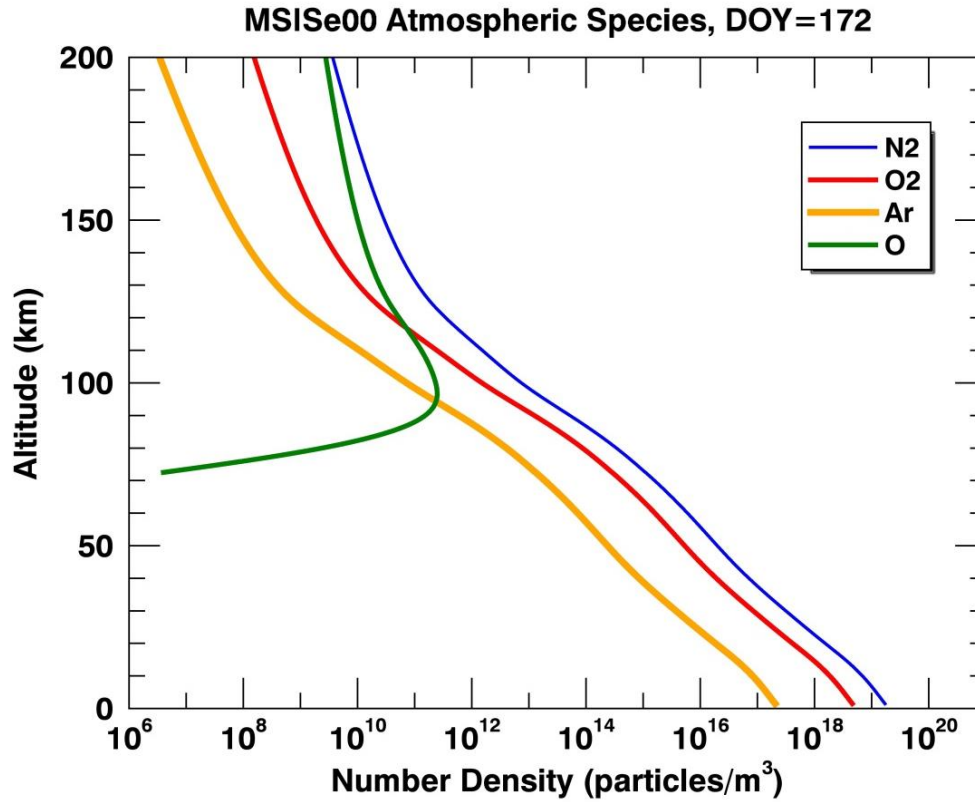


Figure 3.9. MSISe00 model number densities of atmospheric constituents versus altitude for 20 June 2014.

measurements above 100 km has to be examined. *Argall* [2007] explored the effects of changing atmospheric composition on the Rayleigh lidar temperature retrieval technique using simulated data from the MSIS model and found that correcting for these effects did not show an appreciable difference when the resulting temperature curves are initiated at about 120 km and below. In the following, we will develop a similar set of corrections to make to the Rayleigh lidar temperature retrieval using MSISe00 model data and then apply these corrections to actual lidar data acquired at USU. We will still assume that hydrostatic equilibrium still dominates over diffusive equilibrium, thus Eq. 2 will still be valid with the following modifications made to account for atomic oxygen.

To account for the change in atmospheric composition, the lidar signal, N , measured by a Rayleigh lidar system and given in Eq. 1 will have to be broken into a sum with each term including the individual atmospheric species' number densities, n_i , which will then each be multiplied by their own RBCSs, σ_i . To simulate the signal that the lidar would measure using MSISe00, N_{sim} , we can approximate the lidar signal as a function of height using

$$N_{sim}(h) = \sigma_{N_2} n_{N_2}(h) + \sigma_{O_2} n_{O_2}(h) + \sigma_{Ar} n_{Ar}(h) + \sigma_O n_O(h) , \quad (17)$$

where the RBCS values are taken from *Argall*, [2007] and given in Table 3.3. The MSISe00 model number densities are given by the blue curves in Figure 3.10 and the simulated lidar signal, scaled to the total number density, is given by the red curves. One can see that these two sets of curves begin to diverge around 90 km, which illustrates how the lidar signal will slightly underestimate the actual atmospheric number density above this altitude. To correct for this underestimation, the lidar signal can be divided by the effective cross section given by

$$\sigma_{eff} = \frac{\sum_i \sigma_i n_i}{\sum_i n_i} , \quad (18)$$

where the subscript denotes each atmospheric species. The dotted gold curves in Figure

Table 3.3. Rayleigh Backscatter Cross Section for Four Major Atmospheric Species

Atmospheric Species	Cross-section ($\times 10^{-32} \text{ m}^2 \text{sr}^{-1}$)
Molecular nitrogen, N_2	6.29
Molecular oxygen, O_2	5.20
Atomic argon, Ar	5.26
Atomic oxygen, O	1.1

MSISe00 Number Density vs Simulated Lidar Density

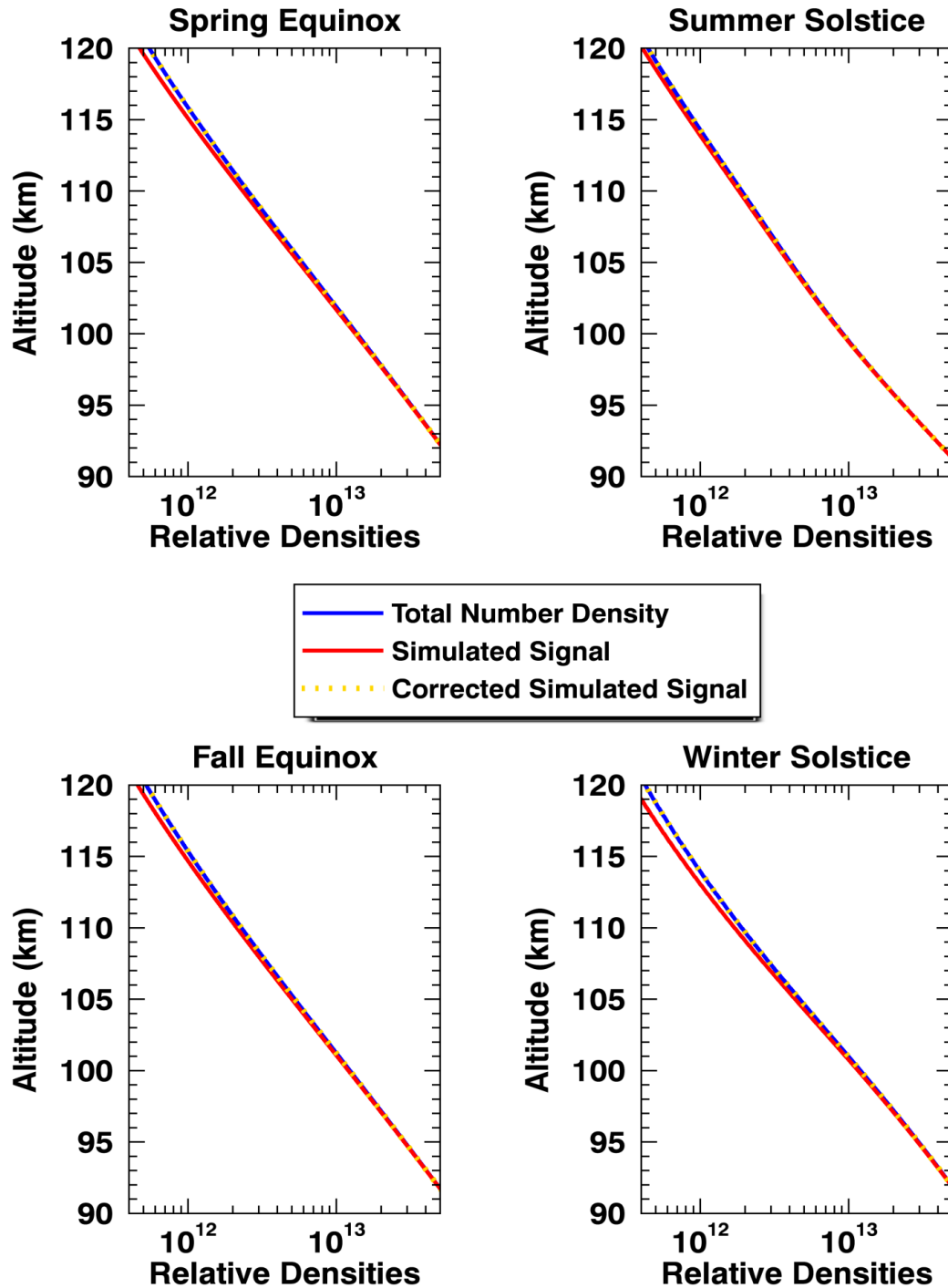


Figure 3.10. Simulation of the effect atomic oxygen has on Rayleigh lidar-measured densities and how to correct for this using the effective cross section. Lidar density (red) and corrected lidar density (dotted gold) were normalized to the MSIS number density (blue) at 70 km.

3.10 give the simulated lidar density divided by Eq. 18. These curves match the actual atmospheric number density given by the blue curves, showing that this is an accurate correction to the simulated lidar-measured densities. To apply this correction to the densities measured by the USU Rayleigh lidar, we use the RBCS values from Table 3.3 and the number densities, n_i , from the MSISe00 model to calculate Eq. 18. This gives

$$n_{measured} = \frac{N_{measured} \times r^2}{\sigma_{eff}}, \quad (19)$$

where $N_{measured}$ is the whole-night averaged lidar signal profile, r is the range from the lidar, and $n_{measured}$ is the density calculated from the lidar signal, which is normalized to unity at 70 km before it is input into the temperature algorithm.

The second correction for changing atmospheric composition involves the atmospheric MMM. In the traditional Rayleigh lidar temperature calculation (Eq. 6), the mean molecular mass is assumed to be a constant value of 28.951 kg/kmol, which is a weighted average calculated under the assumption that the atmosphere up to 90 km is constant mixture of 78.08% N₂, 20.95% O₂, and 0.93% Ar [Goody, 1995]. However, above 90 km, the volume ratios of the individual constituents change as the atomic oxygen proportion increases. Thus, the existing Rayleigh lidar temperature calculation must be amended to include a changing MMM with height. The MMM profile is calculated using both the total number density and individual species' number densities as provided by the MSISe00 model and is given by

$$M(h) = \frac{n_{N_2}(h)}{n_{tot}(h)}(28.014) + \frac{n_{O_2}(h)}{n_{tot}(h)}(31.998) + \frac{n_{Ar}(h)}{n_{tot}(h)}(39.948) + \frac{n_O(h)}{n_{tot}(h)}(15.999), \quad (20)$$

where the atomic masses of the four species are in units of kg/kmol. Figure 3.11 shows the effect of using Eq. 20 in place of a constant MMM value in Eq. 6. In this plot, the

blue curve gives the MSISe00 derived temperatures, the red curve gives the temperatures calculated using the simulated lidar signal in Figure 3.11 (dotted gold curves) input into Eq. 6 with constant MMM value, and the dotted gold curve gives the temperatures calculated with the constant MMM value replaced by Eq. 20.

The RBCS and MMM corrections were made to the existing Rayleigh lidar temperature retrieval described in Section 2 and applied to some of the 2014-2015 USU Rayleigh lidar data. The results are shown in Figure 3.12. In these plots, both the

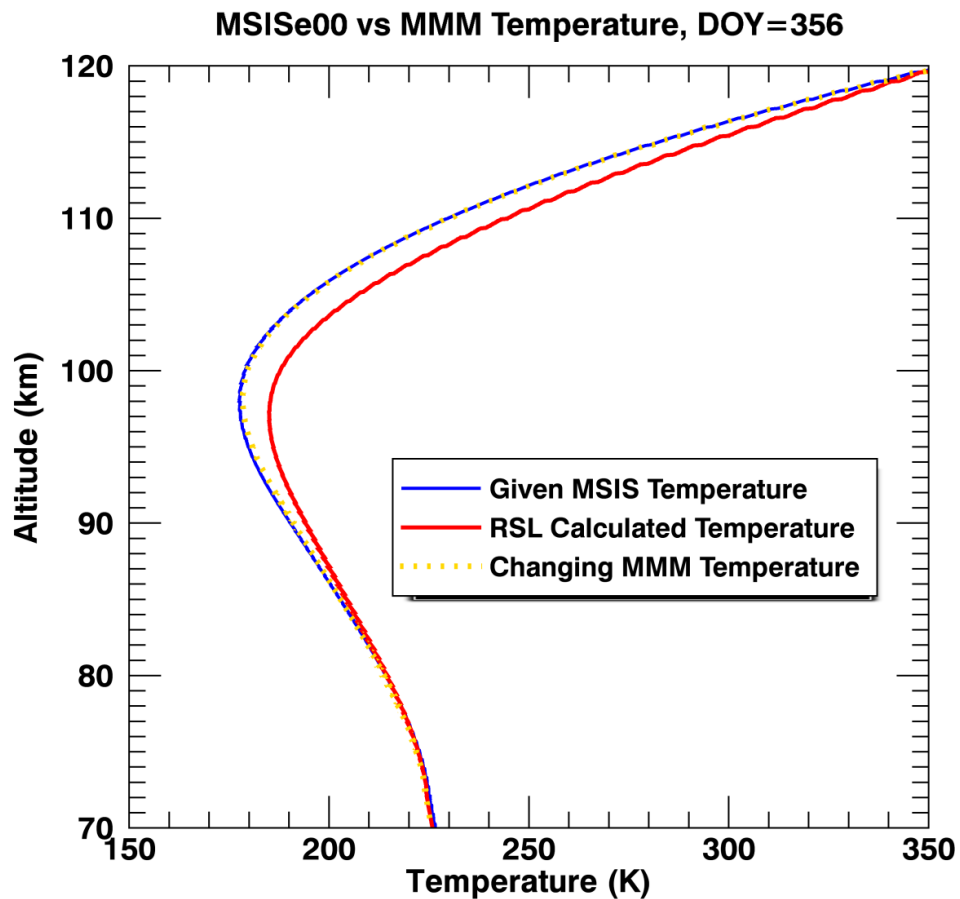


Figure 3.11. MSISe00 simulation (for December 31st) of MMM correction. The effect that decreasing MMM with altitude has on the Rayleigh lidar temperature calculation (red) and how to correct for this using a profile for MMM that changes with height (dotted gold) are shown.

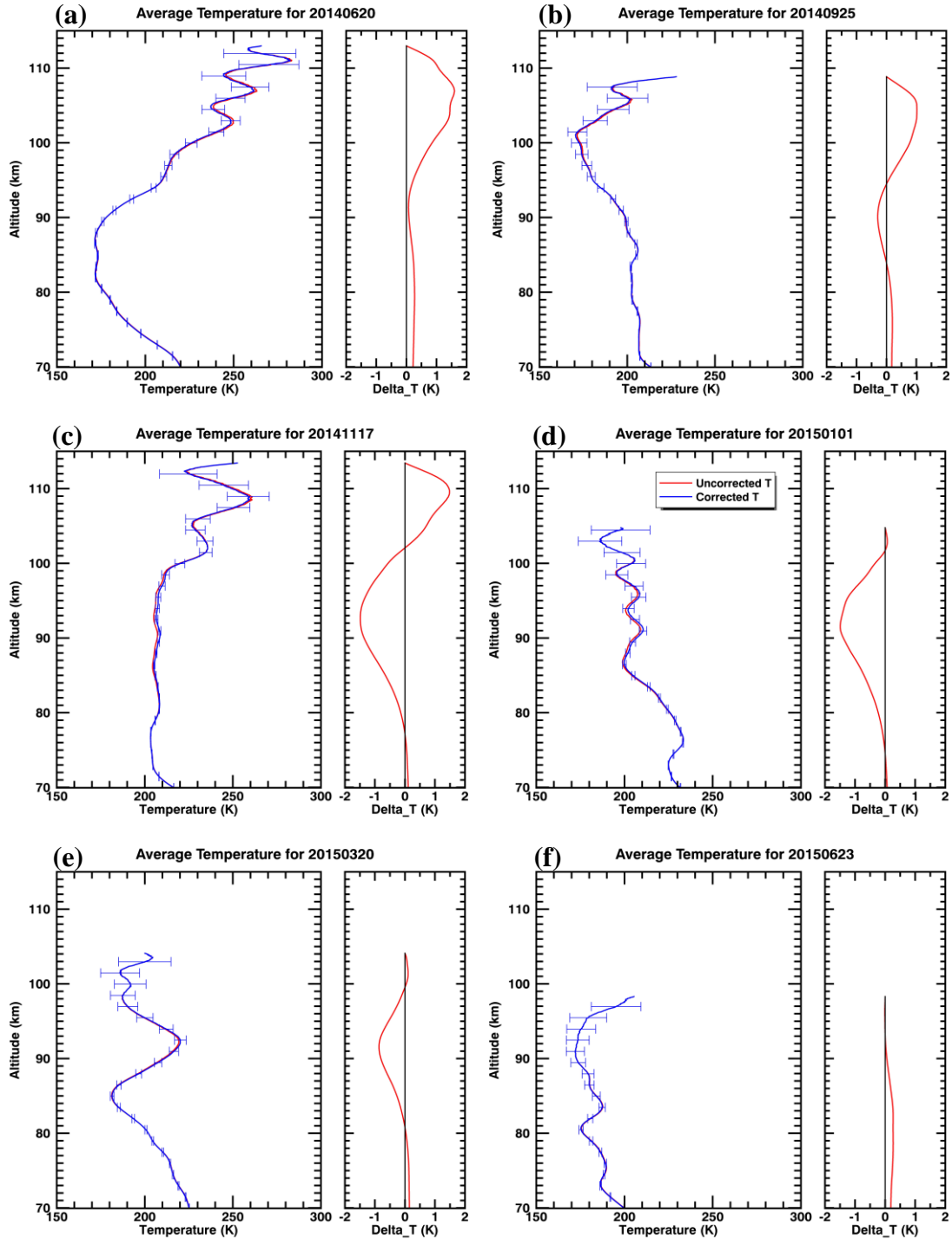


Figure 3.12. USU Rayleigh lidar all-night temperature averages for six nights throughout the 2014-2015 year. Both the uncorrected (constant RBCS and MMM; red curve) and corrected (RBCS and MMM changing with altitude; blue curve) temperatures are shown, as well as the differences, $T_{\text{uncorrected}} - T_{\text{corrected}}$, (right panels). Error bars shown are the same for both the corrected and uncorrected temperatures.

corrected and uncorrected whole-night average temperatures are shown (left panels), along with the differences between the two curves (right panels). The dates for the six nights' averages in Figure 3.12 were chosen to show a broad cross section of the year, the nights closest to the solstices and equinoxes, and nights when a relatively high upper altitude limit was achieved. The same seed temperature from the MSISe00 model was used to initialize both the corrected and uncorrected temperature calculations, which causes the two curves to artificially agree at the topmost altitudes for each nights' average. However, one can see that there is a small difference between the corrected and uncorrected temperatures when the integration is initiated above about 100 km, Figure 3.12 (a–e), and hardly any when initiated below 100 km, Figure 3.12 (f), which agrees with what is shown in *Argall* [2007]. One also can note that, in keeping with Figure 3.10, there is a bigger difference between the uncorrected and corrected temperatures in the winter when the MSISe00 composition change is greatest [Figure 3.12 (d-e)]. Figure 3.12 (c) illustrates the combination of these two effects, and thus, the largest in this set of temperature curves.

Overall, when the RBCS and MMM are both allowed to vary with altitude, the effect on the existing Rayleigh lidar temperature retrieval method appears to be small with a maximum of about 2 K difference between the temperatures corrected for changing RBCS and MMM and those that assumed a constant RBCS and MMM. This shows that pushing the Rayleigh technique up to 115-120 km and correcting for composition change does not give a big difference between corrected and uncorrected temperatures. If we pushed higher (up to 140 km), *Argall* [2007] showed that correcting the temperatures would become more important.

5. 2014-2015 Observations

In this section, a summary of the temperature data collected with the new USU Rayleigh-scatter lidar, during its inaugural 2014-2015 year, will be given. Special attention will be paid to the seasonal trends seen in the Rayleigh lidar data and how they compare with existing theory and observations in the MLT region.

5.1. Seasonal Temperature Averages

Seasonal (summer, fall, winter, and spring) temperature averages were calculated using the all-night averages from the periods listed in Table 3.4 and are shown in Figure 3.13 (a-d). The individual seasonal curves are plotted along with the all-night averages used in the seasonal calculation. Seasonal curves from the original Rayleigh lidar climatology (1993-2004) are calculated by averaging the 15th from each month listed in Table 3.4 and are also plotted in Figure 3.13 (a-d), for comparison. Since the climatology was averaged using a 31-day sliding boxcar average, the 15th from each month in the climatology gives the monthly average. Seasonal averages from the MSISe00 model are also calculated by averaging the 15th of each month listed in Table 3.4. Finally, Figure

Table 3.4. Seasonal Temperature Average Details

Season	Months	Number of Nights	Avg. Hours per Night
Summer	JJA	48	3.4
Fall	SON	25	6.6
Winter	DJF	9	4.1
Spring	MAM	16	4.7

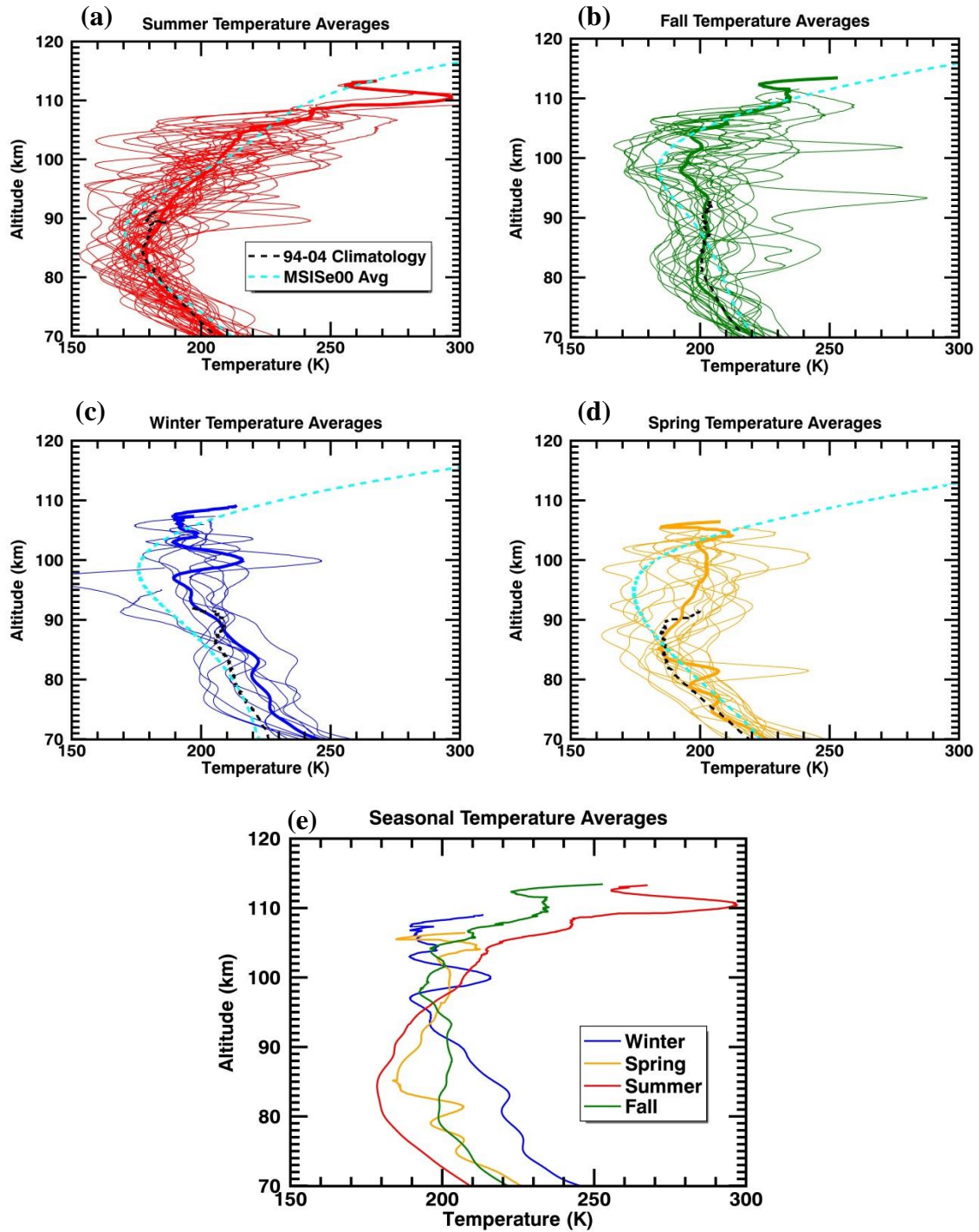


Figure 3.13. Seasonal temperature averages from the 2014-2015 USU Rayleigh lidar campaign. Summer, winter, spring, and fall averages are shown in the thick, solid curves in (a)-(d), and thin, solid curves show the all-night averages used to calculate the seasonal averages. Dashed, black curve shows the seasonal average from the original Rayleigh lidar climatology, and the dashed cyan curve shows the MSISe00 seasonal average. All four seasonal 2014-2015 averages are plotted together in (e).

3.13 (e) plots the four seasonal averages from the 2014-2015 Rayleigh lidar dataset together to highlight the changes in temperature structure in the MLT region from season to season.

The two seasons with the most whole-night temperature curves (summer and fall) show the best agreement with both the USU climatology and the MSISe00 model. This is to be expected because the climatology and MSISe00 model represent the average temperature structure rather than day-to-day variability. Summer, fall, and spring averages show very good agreement with the USU climatology in their overlapping altitude region. The winter average, however, is about 10 K warmer than the climatology throughout most of the overlapping altitude region. All of the seasonal averages appear to have warmer mesopauses than the MSISe00 model by about 10-20 K. The agreement between the seasonal averages and the MSISe00 model curves above 100 km is somewhat artificial because the MSISe00 temperatures were used as the seed temperature for all of the whole-night average temperature calculations. It is interesting to note that in the winter average, both the climatology and the MSISe00 temperatures show the best agreement and the seasonal average differs by about 10-15 K, from 70-105 km, from these two curves, unlike in the other three seasons where the climatology and seasonal averages agree more with one another than the MSISe00 curve. The seasonal winter average agrees quite well, however, with the winter average, from another midlatitude lidar dataset, shown in *She et al.* [1993]. Though it should be noted, that the *She et al.* [1993] definition of the seasons is about one month earlier than the season definitions given in Table 3.4.

The four 2014-2015 seasonal averages are plotted together in Figure 3.13 (e) to

better highlight the seasonal temperature changes in the MLT region throughout the year. The most pronounced seasonal change is the transition of the mesopause in both altitude and temperature. In the spring and summer, the mesopause, which is the transitional region between the mesosphere and thermosphere and also the coldest part of the Earth's atmosphere, is low in altitude and cold. In the fall and winter, the mesopause raises in altitude and temperature [von Zahn *et al.*, 1996]. The seasonal averages calculated with the new USU Rayleigh lidar data show this expected transition with the summer and spring mesopause heights being about 83-85 km and around 100 km in the fall and winter, though the latter two averages show less clear mesopause structure due to what appears to be wave activity in the mesopause region. In temperature, the mesopause is the coldest in the summer at about 170 K, warms in the fall to about 192 K, cools slightly in the winter to about 190 K, and then cools again in the spring to 188 K.

5.2. Monthly Mesopause Averages

To further explore the seasonal evolution of the mesopause, we define the mesopause as the point where the temperatures are at their lowest for each night's temperature profile and average all of these temperatures and their respective altitudes together on a monthly basis. Figure 3.14 shows the monthly averages of both mesopause temperature and height. One can see that the mesopause is at its lowest altitude (82 km) and has a relative minimum temperature (174 K) in June. The mesopause remains low and cold through the summer and then rises and warms in the fall and winter, reaching a maximum temperature in November (199 K) and a maximum height (107 km) in February.

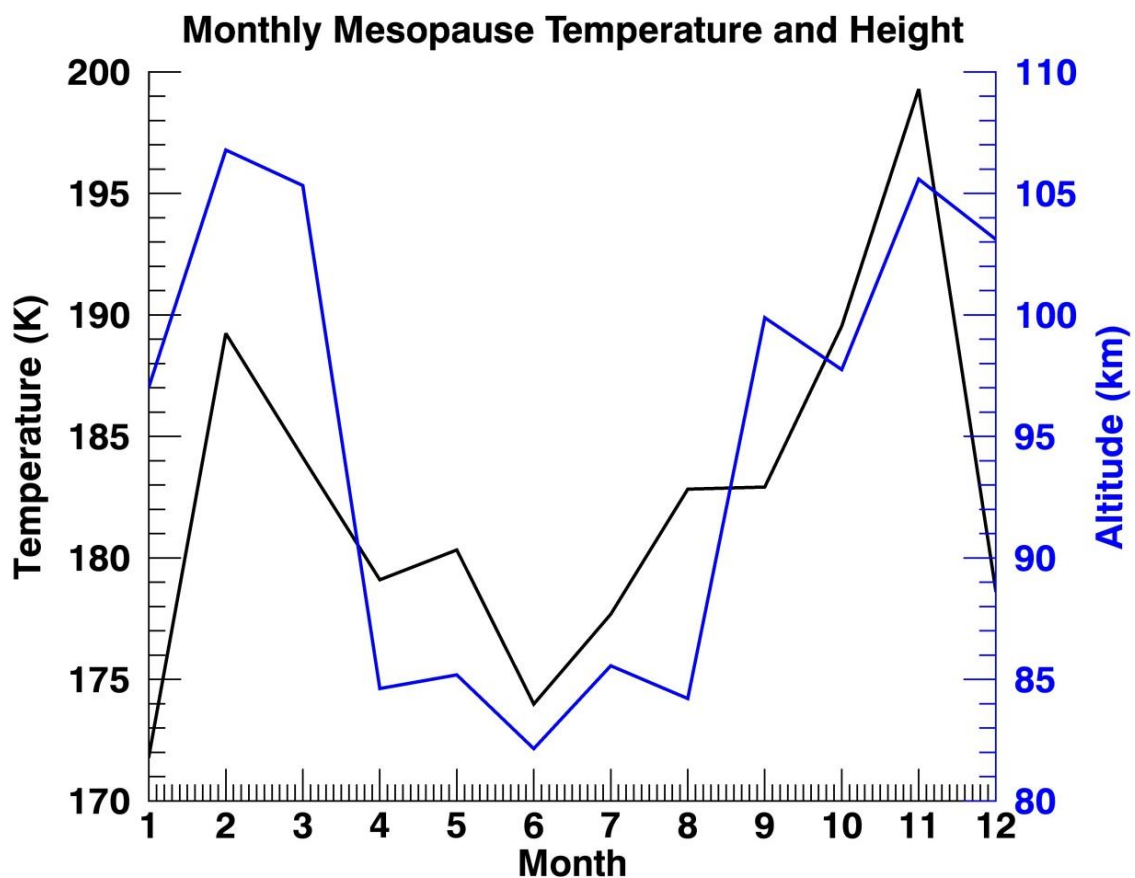


Figure 3.14. Monthly averaged mesopause temperatures and heights. Mesopause temperatures shown in black and mesopause altitudes shown in blue.

The overall pattern of a cold, low mesopause in spring and summer and a warm, high mesopause in fall and winter agrees well with previous studies [*She et al.*, 1993; *von Zahn et al.*, 1996; *Plane et al.*, 1999; *States and Gardner*, 2000]. However, the behavior in December and January does not agree with the normal seasonal change of the mesopause region. The mesopause heights in December (103 km) and January (97 km) are relatively low, compared with the other month's averages, while the temperatures are quite low in December (179 K) and even reach a global minimum in January (172 K).

This anomalous behavior could be explained by the fact that there was a minor

sudden stratospheric warming (SSWs) during the time of the sparse December and January observations, which were only comprised of four consecutive nights from December 31, 2014 to January 3, 2015. SSWs, which are a polar winter stratosphere phenomena that have connected anomalies at all latitudes and throughout all the atmospheric regions [see Chapter 2, Section 3], manifest in the midlatitude mesosphere as a temporary switch from winter thermal and circulation conditions to summer conditions [Sox *et al.*, 2016]. The mesopause heights and temperatures in December and January appear to exemplify this phenomenon as they take on values expected for the summer season.

6. Discussion

The temperature results presented in Section 5 agree well with the previous results from the version of the USU Rayleigh lidar that ran from 1993 to 2004 [Herron, 2007], as well as modeling based on observations of the MLT using sodium (Na) resonance lidar [She *et al.*, 1993; von Zahn *et al.*, 1996; Plane *et al.*, 1999; States and Gardner, 2000]. The consistency of our results with both the previous Rayleigh lidar system and Na lidar studies gives confidence in our Rayleigh lidar measurements, which are some of the first to be extended into the lower thermosphere. The new USU Rayleigh lidar's higher observational range necessitates measurement comparisons with resonance lidar systems, which cover the MLT region, unlike most Rayleigh lidars. Chapter 4 presents just such a comparison using a subset of the 2014-2015 Rayleigh data which overlapped with observations from the Na lidar collocated on the campus of USU.

The design of the USU Rayleigh lidar can also be compared with other lidar

systems. The power-aperture product (PAP) represents a figure of merit to describe the relative sensitivity of a given lidar system. Extending the system's measurement range into the lower thermosphere was primarily achieved by increasing the area of the receiving aperture (primary mirror in the telescope) and increasing the amount of emitted laser power, which in turn further increased the PAP of the USU system.

Wickwar et al. [2001] summarizes some system parameters and PAP values for seven different Rayleigh lidars located around the world, including the original USU system (their Table 2). The high-power, large-aperture USU Rayleigh lidar has a PAP of 206 Wm^2 , which is about 76 times greater than the original USU system and about 26 times greater than the Rayleigh system with the highest PAP in the *Wickwar et al.* [2001] summary. Absent from this summary, however, is the Purple Crow Rayleigh lidar system operated by a group at the University of Western Ontario (UWO). This system uses a 30 W, 30 Hz, Nd:YAG laser transmitter, operated at 532 nm [*Sica and Haefele*, 2015] and a 2.65 m diameter liquid mercury mirror [*Sica et al.*, 1995], which together give it a PAP value of about 165 Wm^2 . With a higher PAP value, the USU Rayleigh lidar can be expected to obtain temperature measurements from slightly higher in the atmosphere than the UWO Rayleigh system. To the best of our knowledge, this has been found to be true in that the temperatures presented in this work extend up to about 5 km higher than those reported by the UWO group using the temperature retrieval described in Section 2 [*Sica et al.*, 1995; *Argall and Sica*, 2007; *Sica and Haefele*, 2015].

The group at UWO has, however, recently developed a new technique for retrieving Rayleigh lidar temperatures using an optimal estimation method [OEM; *Sica and Haefele*, 2015], which has allowed them to account for changing RBCS and MMM

and with more confidence in the uncertainty calculations, to extend the Rayleigh temperatures higher in altitude. Applying this new technique to the USU Rayleigh lidar could be beneficial in several ways: correcting for changing atmospheric composition could be achieved without relying on model calculations, the effects of a seed temperature would be lessened (since the OEM uses an *a priori* temperature profile), and potentially the temperature profile could be extended higher in altitude.

Returning to the design and engineering of the USU Rayleigh lidar, there are several key features of the system, which make it a good candidate to be used as a basis for future lidar designs, and also a few shortcomings, which could be improved with future systems. Two of the key strengths of this particular system are its ruggedness and relative ease of use. Compared with the dye laser transmitters in most resonance lidar systems, the solid state Nd:YAG lasers are much easier and cheaper to maintain and operate. The large glass mirrors in the receiving telescope are also easier and more cost effective to maintain than the comparably sized liquid mercury mirror at UWO. Operating the system is relatively easy, as well, and can be reliably carried out by a single trained undergraduate student. Additionally, the Rayleigh lidar technique can be extended down in altitude, with the use of more PMT detector channels to account for the dynamic range of the atmosphere, to as low as 30 km, where the aerosol cross section becomes large leading to significant Mie scattering. A system like the one at USU can measure Raman scatter of the 532-nm transmitted light from N₂ molecules at 607 nm [Measures, 1992], which could then be used in the Klett inversion technique [Klett, 1981]. This would allow one to retrieve temperatures in a region where both Mie and Rayleigh scattering exist. These additions to the system could allow the USU Rayleigh lidar to

obtain a single temperature profile simultaneously from almost the entire atmosphere (15-115 km). Such altitude coverage could only be achieved with the Rayleigh-Mie-Raman lidar technique, which is limited by technology, as opposed to the resonance lidar techniques, which are limited by the existence of the individual metal layers in the MLT region. The addition of a second detector channel, to bring the USU Rayleigh observational lower limit down to 35 km has already been completed and now is in the testing phase.

The complexity of using multiple components in both the transmitter and receiver is a drawback of the system—maintaining two lasers instead of one and aligning four telescopes instead of one adds to both the cost of and time spent maintaining the overall system. However, these drawbacks can be mitigated in the development of new Rayleigh lidars. The combination of a single, larger telescope mirror and a PMT with higher quantum efficiency (e.g. the Hamamatsu H7421-40 module, which has 40% quantum efficiency at 532 nm) could achieve the same, if not better, measurements than our current system, while still using the same laser technology (which has not made any appreciable advances). Such a system would physically be smaller and easier to maintain and operate, which could be advantageous for applications where a mobile Rayleigh lidar is required or simply a more rugged system is needed for placement in remote observing locations.

7. Conclusions

For the first time, Rayleigh scatter lidar temperatures have been reported into the lower thermosphere, up to about 115 km. This was achieved by redesigning and

upgrading the original USU Rayleigh lidar system, which operated from 1993 to 2004, and transforming it into a high-power, large-aperture Rayleigh lidar. The details of this upgrade were extensively described in this work. In summary, the upgrade includes the use of an additional laser, the construction of a four-barrel telescope cage system and new detector optics design. Careful attention was paid in amending the existing Rayleigh lidar temperature retrieval method to account for changing atmospheric composition above 90 km. A summary of the data acquired in the system's inaugural 2014-2015 operational year was presented by exploring the seasonal behavior of the MLT thermal structure. The new USU Rayleigh lidar temperature measurements were seen to agree well with previous observations in this region made with both Rayleigh and Na resonance lidar techniques. Finally, the advantages in building, operating and maintaining the USU Rayleigh lidar were explored, as well as future improvements that are either currently underway or are planned to be added to the system.

Acknowledgments

The original Rayleigh lidar was initially upgraded to the much more sensitive configuration with funds from NSF, AFOSR, and USU. The system was further upgraded to bring it on line with funds provided by the Space Dynamics Laboratory Internal Research and Development program, USU, the USU Physics Department, and personal contributions. Engineering support for these latter upgrades was provided by Matthew Emerick, Thomas Amely, and Ryan Martineau. The Rayleigh data presented in this paper were acquired through the dedicated efforts of many student operators including: David Barton, David Moser, Bryant Ward, Joe Slansky, Preston Hooser,

Rebecca Petrick, Patrick Sharp, Luis Navarro, Jordan Burns, and Warren Schweigert. L.

Sox was supported by the Utah NASA Space Grant Consortium and the Howard L.

Blood, Keith Taylor, and Gene Adams graduate physics scholarships.

References

Argall, P. S. (2007), Upper altitude limit for Rayleigh lidar, *Ann. Geophys.* 25, 19–15.

Argall, P. S., and R. J. Sica (2007), A comparison of Rayleigh and sodium lidar temperature climatologies, *Ann. Geophys.*, 25, 27–33, doi:10.5194/angeo-25-27-2007.

Beissner, K. C. (1997), Studies of mid-latitude mesospheric temperature variability and its relationship to gravity waves, tides, and planetary waves, PhD dissertation, 186 pp., Utah State Univ., Logan, UT, <http://digitalcommons.usu.edu/etd/4687>.

EG&G Ortec, *Turbo-MCS with Companion Software A67-BI User's Manual*.

Elterman, L. (1953), A series of stratospheric temperature profiles obtained with the searchlight technique, *J. Geophys. Res.*, 58(4), 519–530, doi:10.1029/JZ058i004p00519.

Fiocco G., and L. D. Smullin (1963), Detection of scattering layers in the upper atmosphere (60–140 km) by optical radar, *Nature*, 199, 1275–1276, doi:10.1038/1991275a0.

Goody, R. (1995), *Principles of Atmospheric Physics and Chemistry*, 325 pp., Oxford University Press, New York, NY.

Hauchecorne, A., and M. -L. Chanin (1980), Density and temperature profiles obtained by lidar between 35 and 70 km. *Geophys. Res. Lett.*, 7: 565–568, doi:10.1029/GL007i008p00565.

Herron, J. P. (2007), Rayleigh-Scatter Lidar Observations at USU's Atmospheric Lidar Observatory (Logan, UT) — Temperature Climatology, Temperature Comparisons with MSIS, and Noctilucent Clouds, PhD dissertation, 156 pp., Utah State Univ., Logan, UT, <http://digitalcommons.usu.edu/etd/4686>.

Kent, G. S., B. R. Clemesha, and R. W. Wright (1967), High altitude atmospheric scattering of light from a laser beam, *J. Atmos. Terr. Phys.*, 29, 169–181, doi:10.1016/0021-9169(67)90131-6.

Kent, G. S., and R. W. Wright (1970), A review of laser radar measurements of atmospheric properties, *J. Atmos. Terr. Phys.*, 32, 917–943, doi:10.1016/0021-

9169(70)90036-X.

Klett, J. D. (1981), Stable analytical inversion solution for processing lidar returns, *Appl. Opt.*, *20*, 211–220, doi:10.1364/AO.20.000211.

Measures, R. M. (1992), *Laser Remote Sensing Fundamentals and Applications*, 510 pp., Krieger Publishing Company, Malabar, FL.

Picone, J. M., A. E. Hedin, D. P. Drob, and A. C. Aiken (2002), NRLMSISE-00 empirical model of the atmosphere: Statistical comparisons and scientific issues, *J. Geophys. Res.*, *107*(A12), 1468, doi:10.1029/2002JA009430.

Plane, J. M. C., C. S. Gardner, J. Yu, C. Y. She, R. R. Garcia, and H. C. Pumphrey (1999), Mesospheric Na layer at 40°N: Modeling and observations, *J. Geophys. Res.*, *104*(D3), 3773–3788, doi:10.1029/1998JD100015.

She, C. Y., J. R. Yu, and H. Chen (1993), Observed thermal structure of the midlatitude mesopause, *Geophys. Res. Lett.*, *20*, 567–570, doi: 10.1029/93GL00808.

Sica, R. J., S. Sargoytchev, P. S. Argall, E. F. Borra, L. Girard, C. T. Sparrow, and S. Flatt (1995), Lidar measurements taken with a large-aperture liquid mirror. 1. Rayleigh-scatter system. *Appl. Opt.*, *34*(30), 6925–6936, doi: 10.1364/AO.34.006925.

Sica, R. J., and A. Haefele (2015), Retrieval of temperature from a multiple-channel Rayleigh-scatter lidar using an optimal estimation method, *Appl. Opt.*, *54*, 1872–1889, doi: 10.1364/AO.54.001872.

Sox, L. S., V. B. Wickwar, C. S. Fish, and J. P. Herron (2016), Connection between the midlatitude mesosphere and sudden stratospheric warmings as measured by Rayleigh-scatter lidar, *J. Geophys Res. Atmos.*, *121*, 4627–4636, doi:10.1002/2015JD024374.

Spectra-Physics Lasers (1991), *Quanta-Ray GCR-3 and GCR-4 Pulsed Nd:YAG Laser* Mountain View, CA.

States, R. J., and C. S. Gardner (2000), Temperature structure of the mesopause region (80–105 km) at 40°N latitude, 1, Seasonal variations, *J. Atmos. Sci.*, *57*, 66–77, doi:10.1175/1520-0469(2000)057<0066:TSOTMR>2.0.CO;2.

Thorlabs FT1.5EMT Hard Cladding Fiber: <https://www.thorlabs.us/thorproduct.cfm?partnumber=FT1.5EMT&pn=FT1.5EMT#4562>.

von Zahn, U., J. Hoffner, V. Eska, and M. Alpers (1996), The mesopause altitude: Only two distinct levels worldwide?, *Geophys. Res. Lett.*, *23*, 3231–3234, doi: 10.1029/96GL03041.

Wickwar, V. B., T. D. Wilkerson, M. Hammond, and J. P. Herron (2001), Mesospheric temperature observations at the USU/CASS Atmospheric Lidar Observatory (ALO), *Proceedings of SPIE*, 4153, 272–284, doi:10.1117/12.417056.

CHAPTER 4

COMPARISON OF SIMULTANEOUS RAYLEIGH-SCATTER AND SODIUM
RESONANCE LIDAR TEMPERATURE MEASUREMENTS IN THE MESOSPHERE-
LOWER THERMOSPHERE REGION FROM A SINGLE OBSERVATION SITE**Abstract**

There are relatively few instruments that have the capabilities to make near continuous measurements of the mesosphere-lower-thermosphere (MLT) region. Rayleigh-scatter and resonance lidars, particularly sodium resonance lidar, have been the two dominant ground-based techniques for acquiring mesosphere and MLT vertical temperature profiles, respectively, for more than two decades. With these measurements, the dynamics (gravity waves and tides), and long-term temperature trends (upper atmosphere cooling) of the MLT region can be studied. The USU campus hosts a unique upper atmospheric observatory, which houses both a high-power, large-aperture Rayleigh-scatter lidar and a sodium (Na) resonance lidar. For the first time, we will present coordinated, night-time averaged temperatures, overlapping in observational range (80-110 km), from the two lidars. This overlap has been achieved through upgrades to the existing USU Rayleigh lidar which elevated its observational range from 45-90 km to 70-115 km, making it one of two Rayleigh lidars in the world that can extend into the thermosphere, and by a relocation of the Colorado State Na lidar to the USU campus. The comparison of the two sets of temperature measurements is important because the two lidar techniques derive temperature profiles using different observational techniques and analysis methods, each of which are based on different sets of physical assumptions and

theories. Furthermore, previous climatological comparisons between Rayleigh and Na lidar, in the 80-90 km range, have suggested that significant temperature differences exist between the two techniques. This comparison aims to extend this comparison by exploring possible temperature effects in the 80-110 km range from simultaneous observations with the two different techniques.

1. Introduction

The mesosphere and lower thermosphere (MLT) region of the Earth's upper atmosphere (~45-120 km) is host to many important atmospheric features and phenomena, which warrant both short- and long-term measurements of parameters such as density, temperature, and winds. These measurements have been conducted over the past several decades with various instruments including: in-situ techniques such as sounding rockets, remote sensing techniques from satellites, ground-based airglow instruments, and lidars.

Lidar systems remain the most advantageous method for acquiring temperature measurements in terms of vertical and temporal resolution. Two of the most widely used lidar techniques for the study of the upper atmosphere are Rayleigh-scatter lidar and sodium (Na) resonance lidar. Rayleigh lidar systems measure elastic backscatter from neutral N₂, O₂, Ar, and O particles in the atmosphere. Rayleigh lidar backscatter measurements give relative density profiles, which are then used to calculate absolute temperature profiles. Na lidar measures resonant scatter from sodium atoms, which form a layer in the 80-105 km region of the atmosphere where meteors typically ablate. With proper design, Na lidars can measure thermal broadening and Doppler shifts of the laser-

induced fluorescent Na spectrum. From this, Na density, temperature, and winds can be deduced.

Long-term observations of the middle atmosphere and MLT at several lidar sites have resulted in climatological studies of the temperature structure in this region [Hauchecorne *et al.*, 1991; Leblanc *et al.*, 1998; She *et al.*, 2000; States and Gardner, 2000; Argall and Sica, 2007; Herron, 2007; Yuan *et al.*, 2008]. The Rayleigh and Na lidar facilities used in these studies each underwent a great deal of testing through model simulations (Rayleigh) or analyses of atomic physics (Na), which gave researchers confidence in the techniques, separately. However, the two techniques have yet to be compared with one another using simultaneous, collocated observations. Two of these climatological studies compared results from the two lidar techniques [Leblanc *et al.*, 1998; Argall and Sica, 2007]. The first study used data sets from Rayleigh lidars located at the Observatoire d'Haute-Provence (OHP; 43.6°N, 5.4°E) and Centre d'Essais des Landes (CEL; 44.3°N, 1.2°W), the Table Mountain Facility (TMF; 34.4°N, 117.7°W), and the Mauna Loa Observatory (MLO; 19.5°N, 155.5°W) and the Na lidar at Colorado State University (CSU; 41°N, 105°W) [Leblanc *et al.*, 1998]. The second study compared datasets with the large-aperture Rayleigh lidar at the Purple Crow Lidar site (PCL; 42.5°N, 81.2°W) in Canada and the aforementioned OHP and CEL lidars in France and Na lidars at both CSU and Urbana, Illinois (URB; 40°N, 88°W) [Argall and Sica, 2007]. Both studies showed good agreement between Rayleigh datasets at similar latitudes, but less agreement between the Rayleigh and sodium datasets.

The Rayleigh lidar system located on the campus of Utah State University (USU; 41.74°N, 111.81°W), has recently gone through a series of major upgrades in order to

raise its observational range from 45-95 km to 70-115 km. These upgrades included employing two lasers, instead of one, to achieve greater transmitted power and increasing the receiving area of the system's telescopes from 0.15 m² to 4.9 m². This resulted in an increase in the power-aperture product (PAP), or lidar system figure of merit, of the USU system from 2.7 W·m² to 206 W·m². By extending the USU Rayleigh lidar's altitude range farther into the MLT region, significant overlap with the typical observational range of Na lidar systems (~80-105 km) has been achieved. The only other Rayleigh system with a comparable PAP is the PCL Rayleigh system, though they reported slightly less overlap with the Na lidar range [Argall and Sica, 2007].

In 2010, the CSU Na lidar system was moved to the same site on the USU campus as the Rayleigh lidar system. By summer 2014, both lidar systems were independently making regular observations with occasional concurrent nocturnal observations. This work focuses on 19 simultaneous observations made by the two lidar systems between summer 2014 and summer 2015. To the best of our knowledge, this is the first time a significant number of simultaneous, collocated Rayleigh and Na lidar measurements, taken over the same altitude range, have been presented.

The remainder of this paper is organized as follows: in section 2 technical descriptions of both the Rayleigh and Na lidar systems at USU will be given as well as explanations of their respective data sets and data analysis methods, in section 3 the temperature results from the two systems will be compared in several ways, and finally in sections 4 and 5, respectively, a discussion and conclusions from this comparison will be presented.

2. Description of USU Rayleigh and Na Lidars

2.1. USU Rayleigh Lidar System and Data Analysis Description

The large-aperture, high-power Rayleigh lidar began operating at the Atmospheric Lidar Observatory on the campus of USU during the summer of 2014 [Sox *et al.*, 2016]. It employs both a Spectra Physics GCR-5 and GCR-6 series Nd:YAG laser that transmit 18 W (600 mJ per pulse) and 24 W (800 mJ per pulse), respectively for a total output power of 42 W and energy per pulse of 1400 mJ. Both lasers are frequency doubled to operate at a wavelength of 532 nm and have a pulse repetition rate of 30 Hz (the two lasers' pulses being offset by 62 ns). The telescope receiver is comprised of four parabolic primary mirrors, each 1.25 m in diameter, each focusing directly onto the optical fiber. The signals from the four fibers are then combined, optically, and sent to an Electron Tubes 9954 series photomultiplier tube (PMT). The low-altitude signal and background are reduced by a mechanical chopper and 1-nm interference filter placed in front of the PMT. A more detailed list of the Rayleigh lidar's system parameters is given in Table 4.1. The raw signal profiles are recorded, using a multichannel scaler unit, with a time resolution of two minutes. In altitude, the raw signal is binned in 250 ns, or 37.5 m, intervals. However, in post processing, a Hamming filter with a 2 km FWHM is applied in the vertical direction and, for this study, the data are averaged over either one-hour periods or the whole-night observing period common to both lidar systems.

The Rayleigh lidar data were used to calculate absolute temperatures using a modified version of the method described in *Hauchecorne and Chanin* [1980], [Beissner, 1997; Herron, 2007]. This method uses the proportionality between lidar signal and relative atmospheric density to calculate absolute temperatures under the assumption that

the measured part of the atmosphere is in hydrostatic equilibrium. This results in an integral equation, which is calculated going down in altitude and requires an initial condition, or a seed temperature, at the highest altitude. The influence of this seed temperature decreases exponentially as one goes down in altitude, having little to no effect about 15-20 km from the top altitude. For this study, the seed temperature is taken from the Na lidar temperature profile, except when the Rayleigh lidar temperatures start at a higher altitude. In these cases, the seed temperature is taken from the Mass Spectrometer Incoherent Scatter (MSISE00) empirical model [Picone *et al.*, 2002].

The Rayleigh lidar's upper altitude limit, for each night's average, is chosen to be where the Rayleigh signal is twenty times its standard deviation. Several factors determine how good the signal-to-standard deviation ratio is at a given height for each observed night, including: length of the observation, laser power, how many lasers are used (maximum of two), how many mirrors are used (maximum of four), atmospheric transmission, and neutral number density. Depending mostly on the number of hours in each night's average and how many lasers and mirror are used, the upper altitude limit would vary from 100-115 km, but reached 107 km, on average.

2.2. USU Na lidar System and Data Analysis Description

The configuration of the Na lidar and subsequent data analysis used to acquire Na lidar temperatures presented in this paper are explained in detail by Krueger *et al.* [2015]. In short, the USU Na lidar employs a CW dye laser, frequency locked at the Na D_{2a} line, whose light is then sent through a dual acousto-optic modulator (AOM), which allows the laser's frequency to also be shifted up and down periodically relative to the Na D_{2a} line.

Each of these three frequencies ($D_{2a}+630$ MHz, D_{2a} , $D_{2a}-630$ MHz) is sent through a pulsed dye laser amplifier, which turns the CW beam into laser pulses that are transmitted to the atmosphere at a repetition rate of 50 Hz. The transmitted beam is split into a three-beam pointing configuration, which then necessitates three telescope receivers, one for each returned signal, in order to determine line-of-sight winds along with Na density and temperature. The collision frequency, between the Na atoms and neutral molecules, is great enough that the Na and neutral temperatures are assumed to be the same [Krueger *et al.*, 2015]. With the insertion of a Faraday filter [Chen *et al.*, 1996], the Na lidar is also able to make daytime observations. However, in this study only the nighttime data was used in order to overlap with the Rayleigh lidar's measurements. The Na lidar data are recorded with a 1 μ s, or 150 m, bin size and a one-minute time resolution. A Hanning filter is then applied with a 2 km FWHM window in the vertical direction and the data were averaged in time over both one-hour and whole-night periods.

The three-frequency measurement allows the Na lidar to be able to detect Doppler shifts and Doppler broadening of the mesospheric Na atom's laser-induced fluorescence spectrum. The Na lidar temperature deduction uses the relationship between the three frequencies of the returned signal and the detailed shape of the Na spectrum to relate lidar signal to atmospheric temperatures and winds [She *et al.*, 2015; Krueger *et al.*, 2015].

Parameters from both the Rayleigh and Na lidar systems are given in Table 4.1 for comparison. In the MLT, the Na density is many (~ 9) orders of magnitude lower than the neutral (N_2 , O_2 , and Ar) density. However, the Na cross section per steradian, for $\lambda_{Na}=589$ nm, is some 17 orders of magnitude greater than the Rayleigh backscatter cross

Table 4.1. Comparison of Whole-Night Averaged Rayleigh and Sodium Lidar System Parameters

System Parameter	Rayleigh Lidar	Na Lidar
Emitted laser wavelength (nm)	532	589 \pm v
Laser energy (mJ/pulse)	1400	20-30 (per transmitted v)
Total transmitted laser power (W)	42	~1 (per transmitted v)
Laser rep. rate (Hz)	30	50
Transmitted beam divergence (mrad)	0.125	0.8
Receiving aperture (m ²)	4.86 (4 mirrors)	0.45(1 mirror)
Vertical resolution after smoothing (km)	2	2
Maximal altitude range (km)	70-114	76-114
Estimated error at top (K)	19	10
Estimated error at midrange (~93 km; K)	1.1	0.3
Estimated error at bottom (K)	0.1	10

section for $\lambda_{\text{Ray}} = 532 \text{ nm}$ [Kent and Wright, 1970; Measures, 1992]. The net effect being that the Na resonance scattering is about eight orders of magnitude more efficient than the Rayleigh scattering. For this reason, the Na lidar is able to obtain good signal levels in the MLT region using much less transmitted power and much smaller receiving aperture area than the Rayleigh lidar. The Na lidar's overall measurement range is limited by the Na layer, which is, on average, located between 80-105 km [Yuan *et al.*, 2012], with some sporadic events, at low geomagnetic latitudes, reaching up to 140 and 170 km [Liu *et al.*, 2016; Gao *et al.*, 2015]. The Rayleigh lidar's measurement range is only

limited by the advances required in instrumentation (laser power, telescope size, and detector sensitivity) to achieve an appropriate level of signal-to-noise, which decreases exponentially with altitude as the molecular density in the atmosphere decreases and by range-squared from the laser.

3. Observations and Results

Between summer 2014 and summer 2015, there were 19 nights (see Table 4.2) when the two lidars made simultaneous measurements throughout the night (at least four hours). The overlap in the two lidars' measurements is relatively small due to the different observational schedules that are employed by each group. Since the Na lidar can observe over full diurnal cycles, the Na lidar group typically conducts campaigns once a

Table 4.2. Dates for 2014-2015 Temperature Dataset

Index Number	Date (YYMMDD)	Index Number	Date (YYMMDD)
0	140620	17	141029
1	140702	18	141104
2	140717	19	141106
3	140722	20	141108
4	140723	21	141109
5	140724	36	150328*
10	140912	37	150414
11	140913	41	150610
12	140925*	42	150618
13	140926*		

*Dates closest to fall and spring equinoxes.

month for three-five days and nights. Since the Rayleigh lidar cannot currently operate in the daytime, the Rayleigh group aims to observe over every clear night throughout the year. The difference in observational schedules allows the two lidar systems' dataset to complement each other well, but also means simultaneous measurements are infrequent unless deliberately planned.

3.1. Nightly Average Temperature Profile Comparison

Whole-night averages of temperature were calculated for each lidar's dataset. The averages are at least four hours long and the beginning and end times for each lidar are within two minutes of one another. Temperature profiles from each lidar along with a profile from the MSIS00 model were plotted for each night in Figures 4.1-4.4. The error bars plotted with the Rayleigh and sodium curves were calculated by propagating the measurement error (from photon counting) through each lidar's respective temperature reduction process. Each set of plots represents a different seasonal period.

Often, the best agreement between the two sets of lidar temperatures is found between about 85 and 95 km in altitude (Figures 4.1-4.4). There are significant differences of up to 30-80 K [see Figure 4.1 (a), (b) and (d), Figure 4.2 (a), Figure 4.3 (c), and (d)] between the two sets of temperatures above these altitudes on many nights and occasionally there are less significant differences of up to 16 K below 92 km. The largest temperature differences occur at higher altitudes (above 100 km) and typically result in Rayleigh lidar temperatures being warmer than Na lidar temperatures. There is also a difference in the structure of the temperature profile at these higher altitudes where the Rayleigh temperatures show stronger and more distinct wave structure than the Na

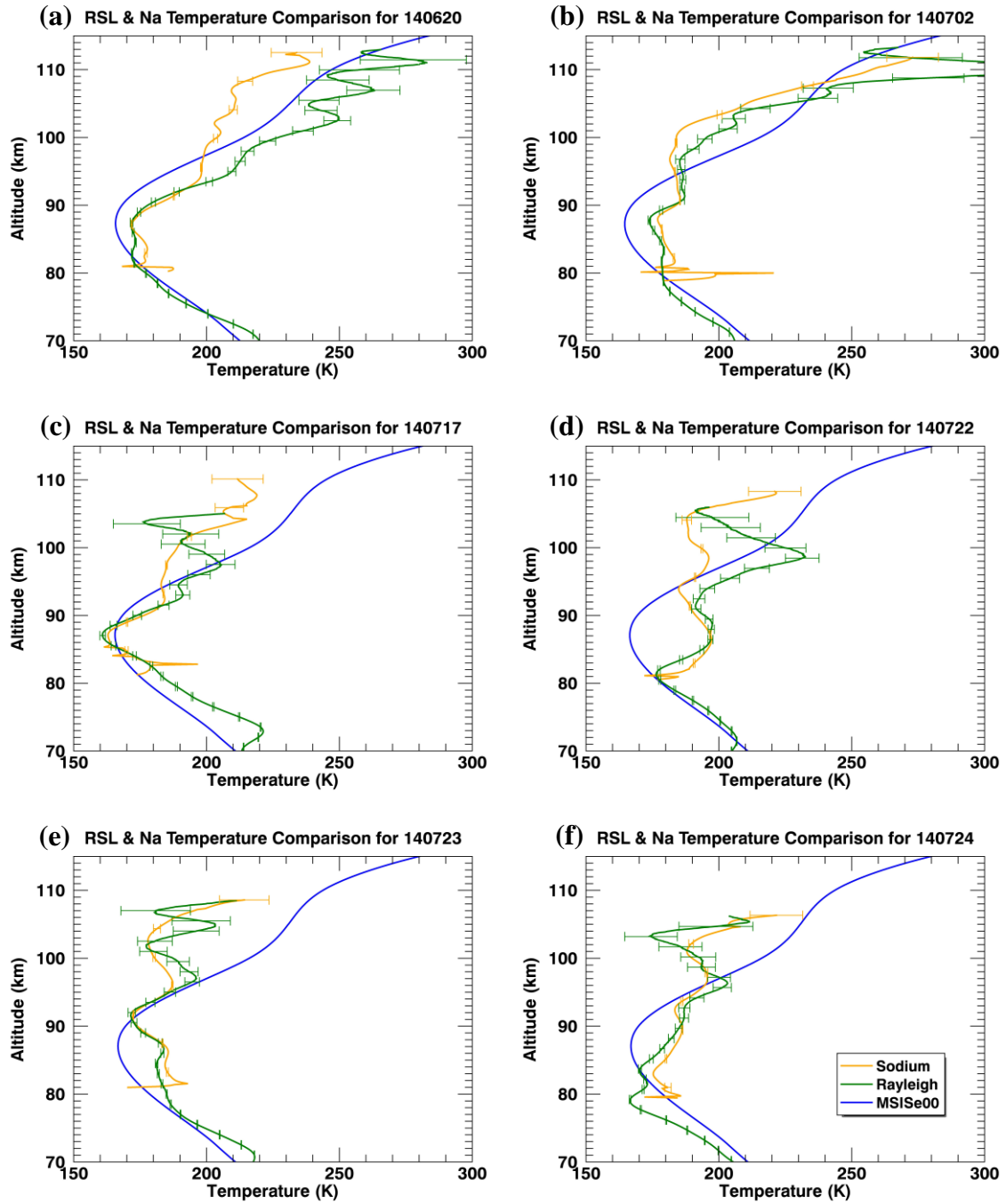


Figure 4.1. Summer 2014 temperature-altitude plots for whole-night averages measured using the Rayleigh lidar (green curves) and Na lidar (orange curves). MSISe00 model temperatures (blue curves) for each date at 6 UT are also given.

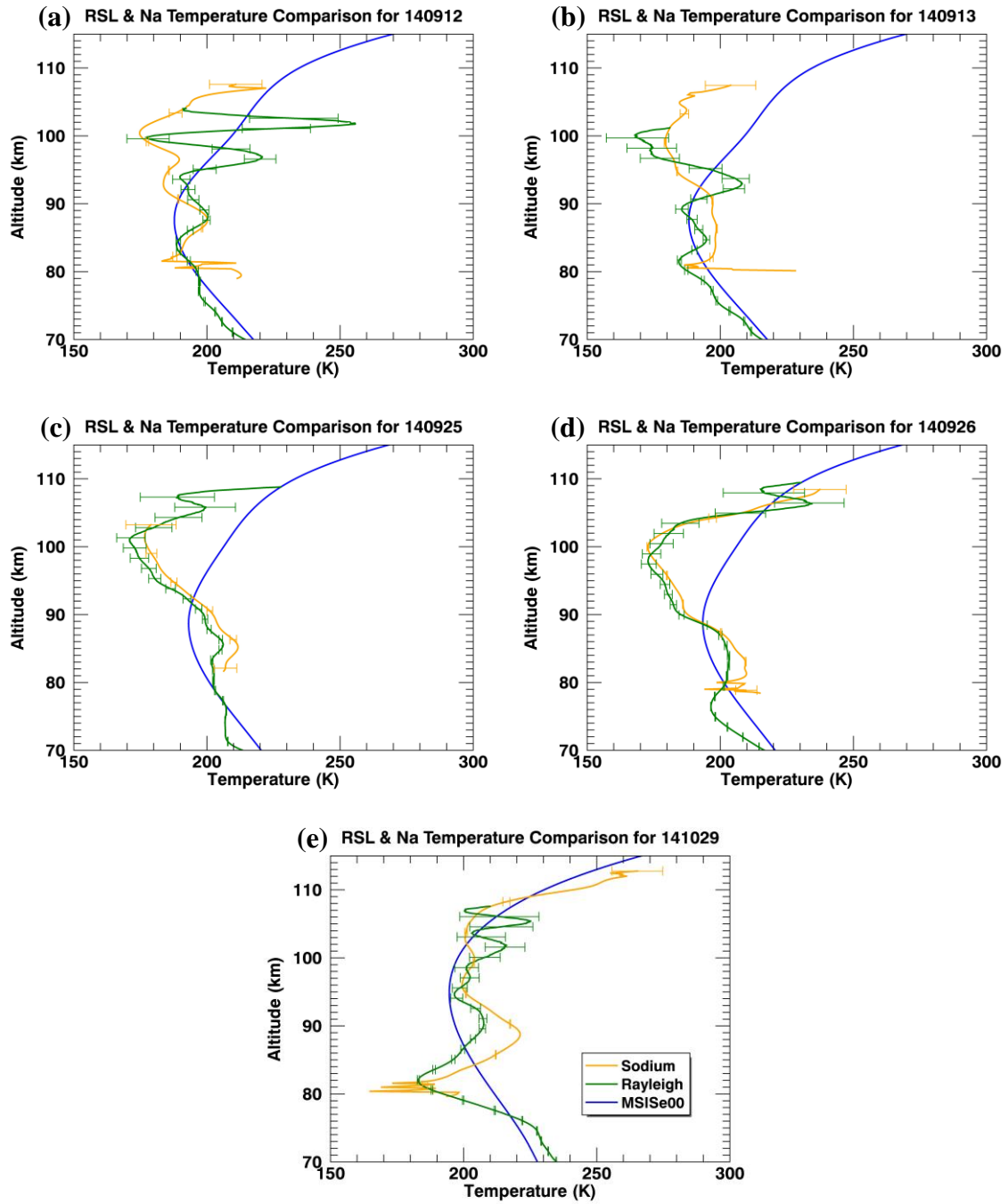


Figure 4.2. Same as Figure 4.1, but for the fall 2014 portion of the overlapping dataset.

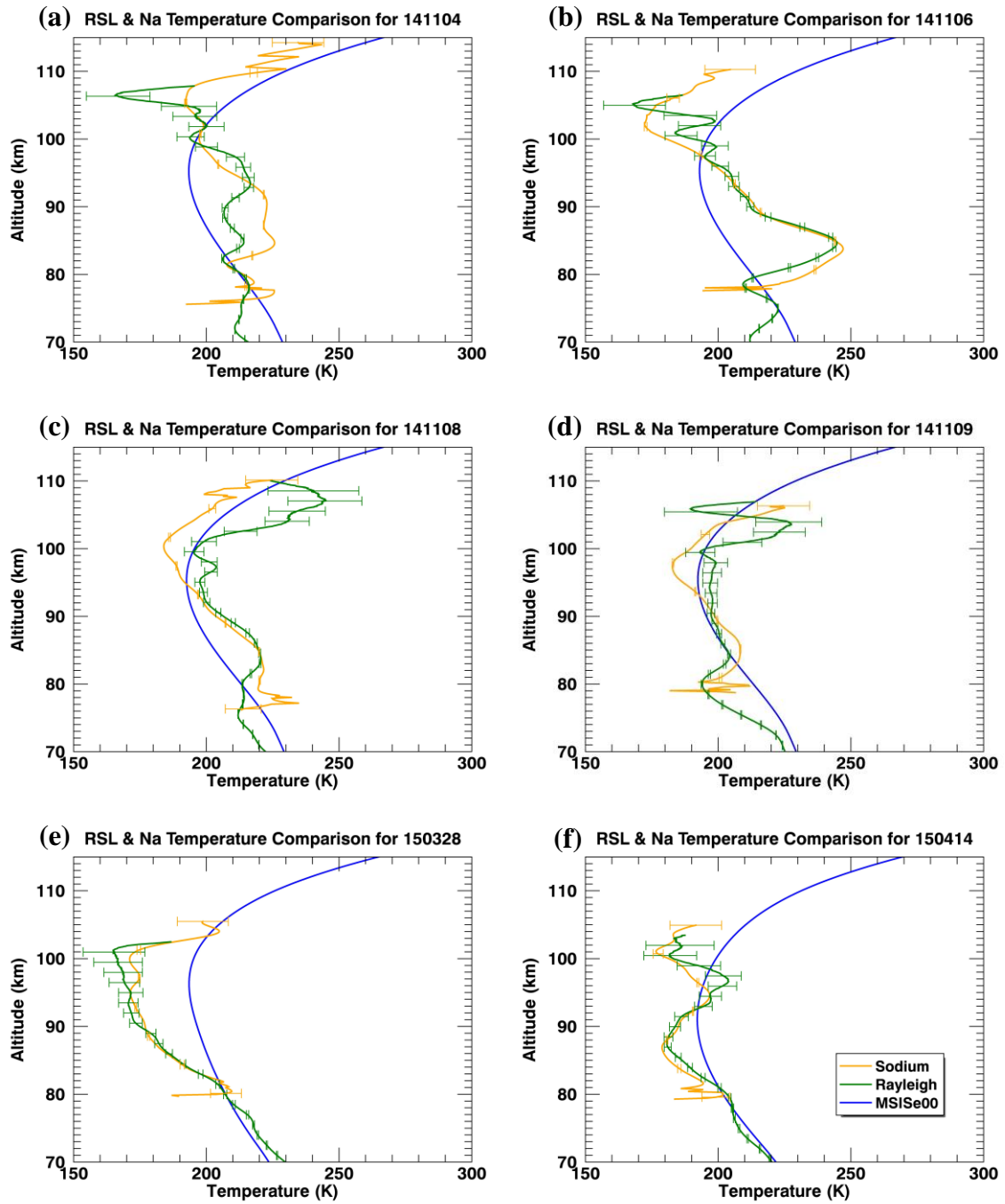


Figure 4.3. Same as Figure 4.1, but for the winter 2014 and spring 2015 portions of the overlapping dataset.

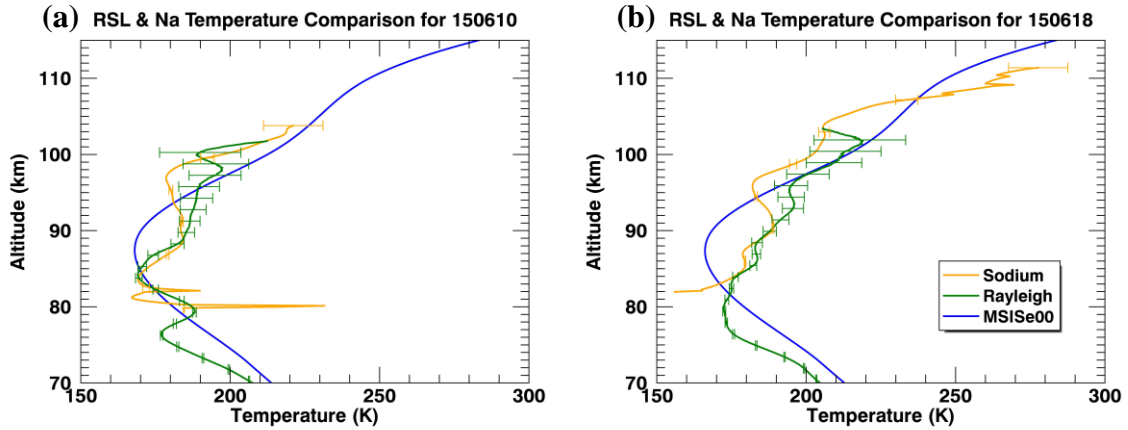


Figure 4.4. Same as Figure 4.1, but for the summer 2015 portion of the overlapping dataset.

temperatures. For the lower altitude differences, the Na lidar temperatures are typically warmer than the Rayleigh temperatures. The nights with the best agreement between the two lidars' temperatures, over the entire altitude range (between 80-110 km, depending on the night), happen to also be close to the fall (23 September 2014) and spring (20 March 2015) equinoxes, as seen, respectively, in Figures 4.2 (c and d) and Figure 4.3 (d).

The two lidars' temperatures agree much better with one another than they do with the MSIS00 model temperatures. For the most part, if one lidar's temperature profile is either warmer or colder than the MSIS00 temperatures, then the other lidar's temperatures behave the same way. There are a few exceptions, though, as in Figure 4.1 (d), 4.2 (a), and 4.3 (c). In all of these cases, above 90 km, the Na temperatures are colder than MSIS00 temperatures, whereas Rayleigh temperatures are warmer. While the structure of the lidars' temperature profiles are roughly similar to the MSIS00 structure, there are a few cases where the lidars' mesopauses are at different altitudes than the MSIS00 mesopause [Figure 4.2 (all), 4.3 (a), (b), and (c), and Figure 4.4 (all)].

The differences between the two lidars' temperature profiles seem to have both a seasonal dependence (best agreement close to equinoxes) and a possible dependence on lidar technique (Na temperatures warmer at lower altitudes, Rayleigh temperatures warmer at higher altitudes and stronger wave activity appearing in the Rayleigh temperatures). In subsection 3.2., we will investigate the possible seasonal dependence and in subsection 3.3., we will explore some differences in the two techniques.

3.2. Seasonal Temperature Comparison

To better compare the two lidar datasets, seasonally, the temperatures from each lidar, at a given altitude, were plotted in a time series in the upper panels of Figure 4.5. Though the overlapping lidar dataset covers one annual cycle, the data coverage over winter 2014-2015 is sparse. In order to show gaps in the data but still keep the plots visually legible, an indexing system was applied to the actual calendar dates when the lidar observations were made. The dates and their respective indices are given in Table 4.2. Differences between the two lidars' temperatures are shown in the lower panels of Figure 4.5. In Figure 4.5 (e), the lack of a Rayleigh lidar data point indicates when the Rayleigh lidar temperatures started at an altitude lower than 105 km.

The time series plots show that at and below 90 km, the Rayleigh temperatures were generally colder than the Na temperatures (on average about 1.5 K). At 95 km and above, the Rayleigh temperatures are generally warmer than the Na temperatures (on average about 13 K). This agrees with the behavior seen in the largest temperature differences in Figures 4.1-4.4. Looking at the lower panels of Figure 4.5, there does not appear to be a strong seasonal dependence in the difference between the two temperature

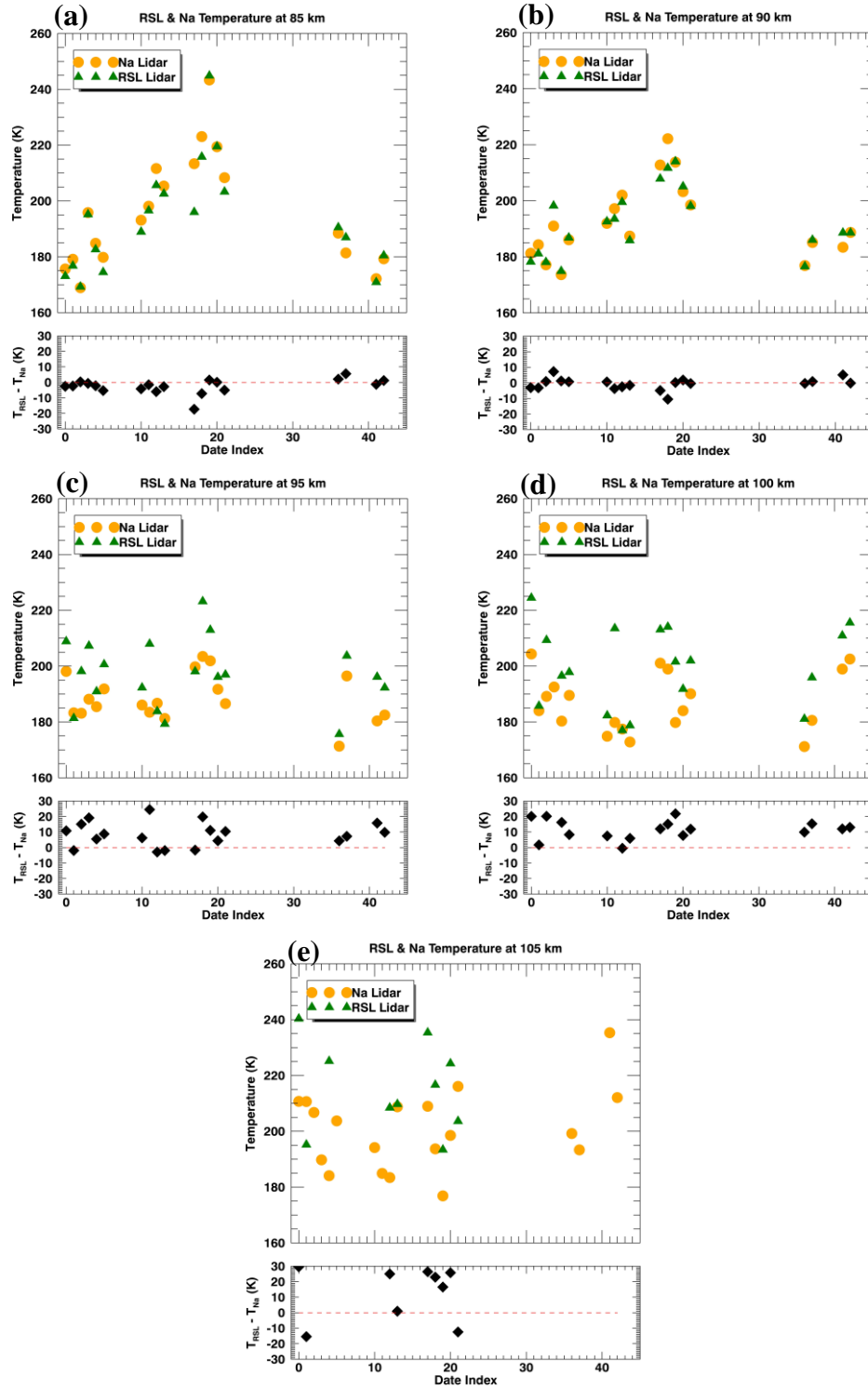


Figure 4.5. Rayleigh and Na lidar temperature time series at 85 km (a), 90 km (b), 95 km (c), 100 km (d), and 105 km (e) along with the differences between the two lidars' temperatures (lower panels, black diamonds). The relationship between date index and calendar date given in Table 4.2.

datasets, at all altitudes. Rather, there is a dependence on altitude with the most agreement (smallest differences) occurring at lower altitudes and the least agreement (largest differences) at higher altitudes.

Correlation coefficients were calculated for the dataset in two different ways.

Figure 4.6 (a) shows the Pearson correlation coefficients between the two lidars' sets of temperatures from 82-100 km in 1 km steps. Figure 4.6 (b) shows the Pearson correlation coefficients between the two lidars' temperatures over the 82-100 km range in steps of nights, plotted with the same date indices as given in Table 4.2. Before calculating the correlation coefficients, the temperature profiles from each lidar for each night were rebinned to give them approximately a 1 km resolution. The plots in Figure 4.6 corroborate the altitude dependence of the lidar temperature's agreement, as opposed to a seasonal dependence, as shown in Figure 4.5. The best agreement [correlation coefficient greater than 0.9, Figure 4.6 (a)] being over the 82-92 km range for the whole dataset, with less agreement at altitudes above 92 km. The occurrence of slightly higher coefficient

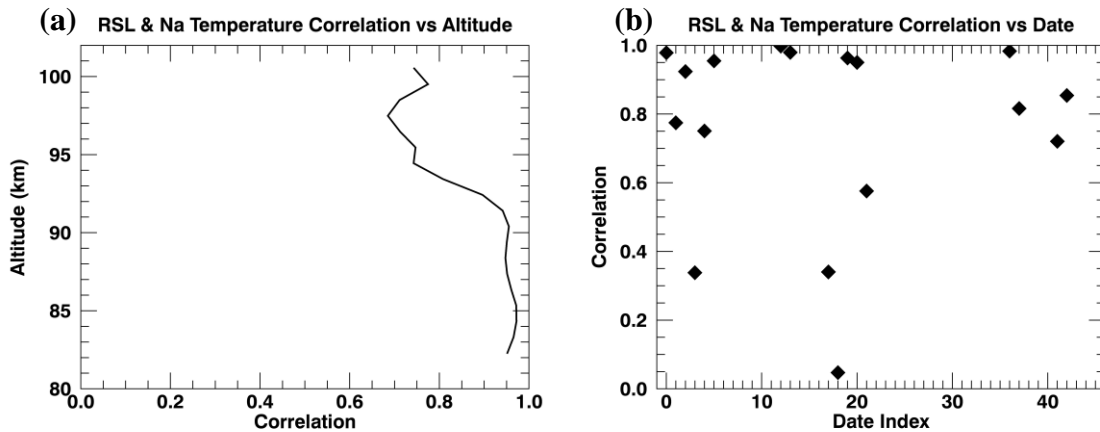


Figure 4.6. Correlation coefficients for the two lidar temperature datasets (a) over the 82-100 km altitude range calculated in steps of 1 km and (b) over the whole time series in steps of nights.

values in Figure 4.6 (a) at the highest altitudes is somewhat artificial due to the use of Na temperatures as Rayleigh seed temperatures for some nights. Over the whole 82-100 km range, the two lidar datasets do not show as much agreement with only about half of the 19 nights having correlation that coefficients at or above 0.9 [Figure 4.6 (b)].

3.3. Lidar Technique Comparison

One possible explanation for the differences between the two techniques is that the beam-pointing geometries are different. The Rayleigh lidar transmits in the vertical, whereas the Na lidar typically operates with a three-beam pointing configuration: one beam pointing to the east (20° off-zenith), one to the west (20° off-zenith) and one to the north (30° off-zenith). This configuration enables the determination of wind speeds. All the data shown in the previous section were acquired using the east-pointing Na lidar beam. At higher altitudes (~ 110 km), this would separate the two lidar beams by about 40 km in the horizontal east-west direction. In the MLT region, large amplitude (~ 20 K) waves exist [Herron *et al.*, 2007], which could account for the differences seen in the two temperature datasets. (Additionally, transmitted beam divergence would cause the diameter of the Na lidar beam at about 110 km to be about 88 m wide and the Rayleigh beam to be about 14 m wide, but these distances are negligible compared to the beam separations).

West-pointing beam data from the Na lidar was only available on 11 of the 19 overlapping nights. Figure 4.7 shows four temperature profile plots with similar curves as Figures 4.1-4.4, except with curves added for the Na west-pointing beam temperatures and the average of the east and west beam temperatures. These four nights were chosen to

show nights when the Rayleigh and Na temperatures had large differences [Figure 4.7 (a) and (c)], a night when the two sets of temperatures agreed well [Figure 4.7 (b)] and a night when the east- and west-pointing beam temperatures disagreed the most [Figure 4.7 (d)]. Error bars have been removed to make the plots more visually legible, but the west-pointing beam temperature error bars are similar to the east-pointing beam error bars seen in Figures 4.1-4.4. From Figure 4.7, one notes that the differences between the east- and west-beam Na temperatures are not very significant (at most about 15 K on one night). It

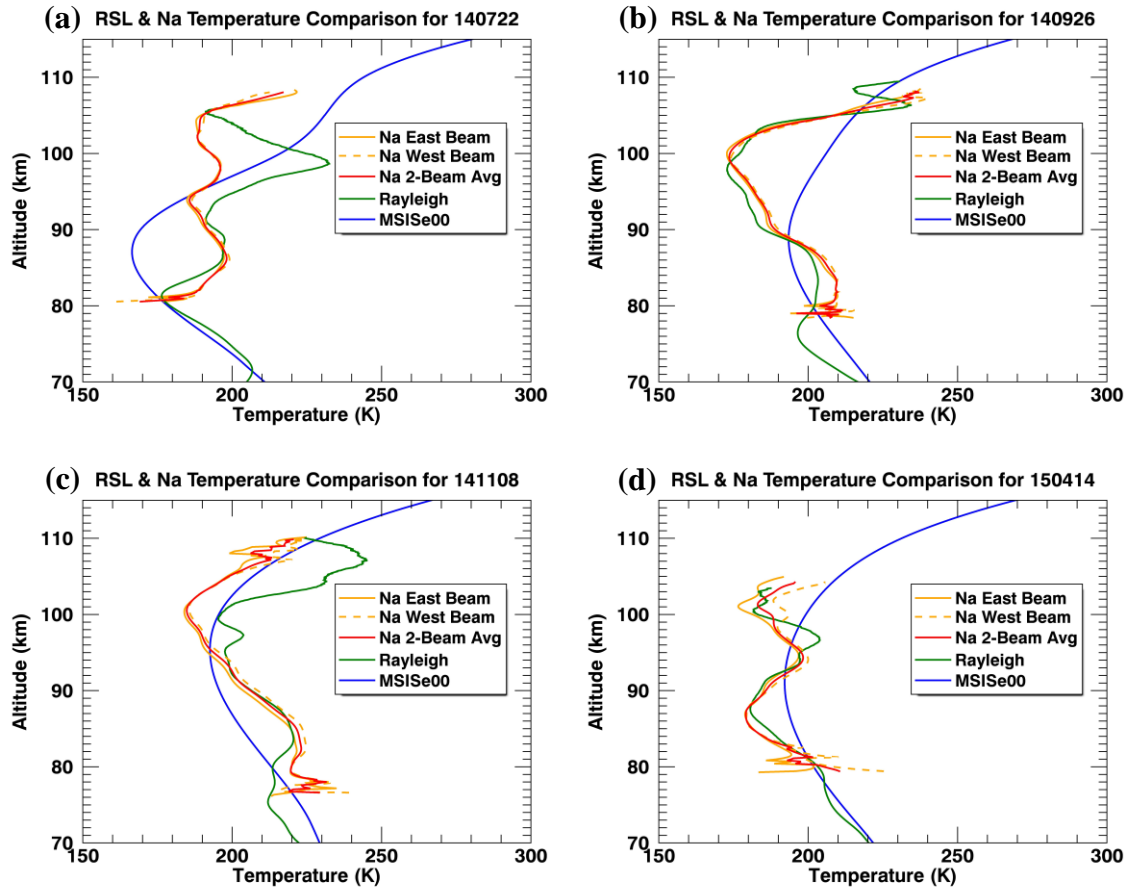


Figure 4.7. Temperature profile plots similar to those in Figures 4.1-4.4, except with Na lidar west-pointing beam temperatures (dashed orange curve) and the average of the east and west-pointing beam temperatures (red curve) added.

is also noted that these differences do not, in general, account for the differences in temperatures between the Na and Rayleigh lidar. In the two cases where taking the average of the east and west beam Na data does give better agreement with Rayleigh temperatures, from ~85-90 km in Figure 4.7 (c) and from ~100-105 km in Figure 4.7 (d), there are still significant differences (up to about 45 K) in the two lidars' temperatures at other altitudes. From the four representative plots we have shown here, it is clear that the pointing direction of the Na lidar does not greatly affect the temperature profiles, and thus, does not explain the large differences between the two.

Hourly temperature perturbations were calculated from both lidars' temperature measurements for four nights from the 2014-2015 year and are shown in Figure 4.8. These four nights were chosen to give examples of strong wave activity throughout the different seasons. To calculate the perturbations, each lidars' whole-night average was subtracted from each lidars' respective hourly average. The two lidars' hourly temperature perturbations display very similar structure. The lidars capture the same wave parameters, which are given in Table 4.3 for the four selected nights. While there are differences in absolute temperature between the two lidars' measurements, the fact that the temperature perturbations measured by each lidar are strikingly similar shows that the two different lidar techniques are capable of capturing the same atmospheric dynamics and also that the two lidars are not measuring different portions of the same wave structure.

4. Discussion

The Rayleigh lidar temperatures are shown to be colder than those of the Na lidar

Table 4.3. Approximate Wave Parameters Obtained from Hourly Temperature Perturbations

Date (YYMMDD)	Amplitude (K)	<u>Rayleigh Lidar</u>		<u>Na Lidar</u>	
		Period (hour)	Phase Velocity (km/hr)	Period (hour)	Phase Velocity (km/hr)
140702	15	>7	2.5	>7	2.5
140925	20	9.5	5.5	>10	9.5
141108	30	11	2.25	11.5	2
150414	10	4	5.5	4.75	6.25

between 85 and 90 km [Figure 4.5 (a) and (b) and many curves in Figures 4.1-4.4]. A similar observation was made by *Argall and Sica* [2007] using climatological data from different sites. Without simultaneous measurements, they compared Rayleigh and Na lidar climatologies from several different sites at roughly the same latitude, but several hundred kilometers apart in longitude, over a smaller overlapping altitude range of about 80-95 km. They found that on average, the Rayleigh temperatures were 7 K cooler. While our data show the Rayleigh temperatures being colder at these altitudes, our difference is much less—having an average of only about 1.5 K. *Leblanc et al.* [1998] showed an earlier comparison of Rayleigh (OHP & CEL) and Na (CSU) lidar climatologies. The overlapping altitude region between the Rayleigh and Na lidars in *Leblanc et al.* [1998] was shifted downward, compared to the *Argall and Sica* [2007] study. Nonetheless,

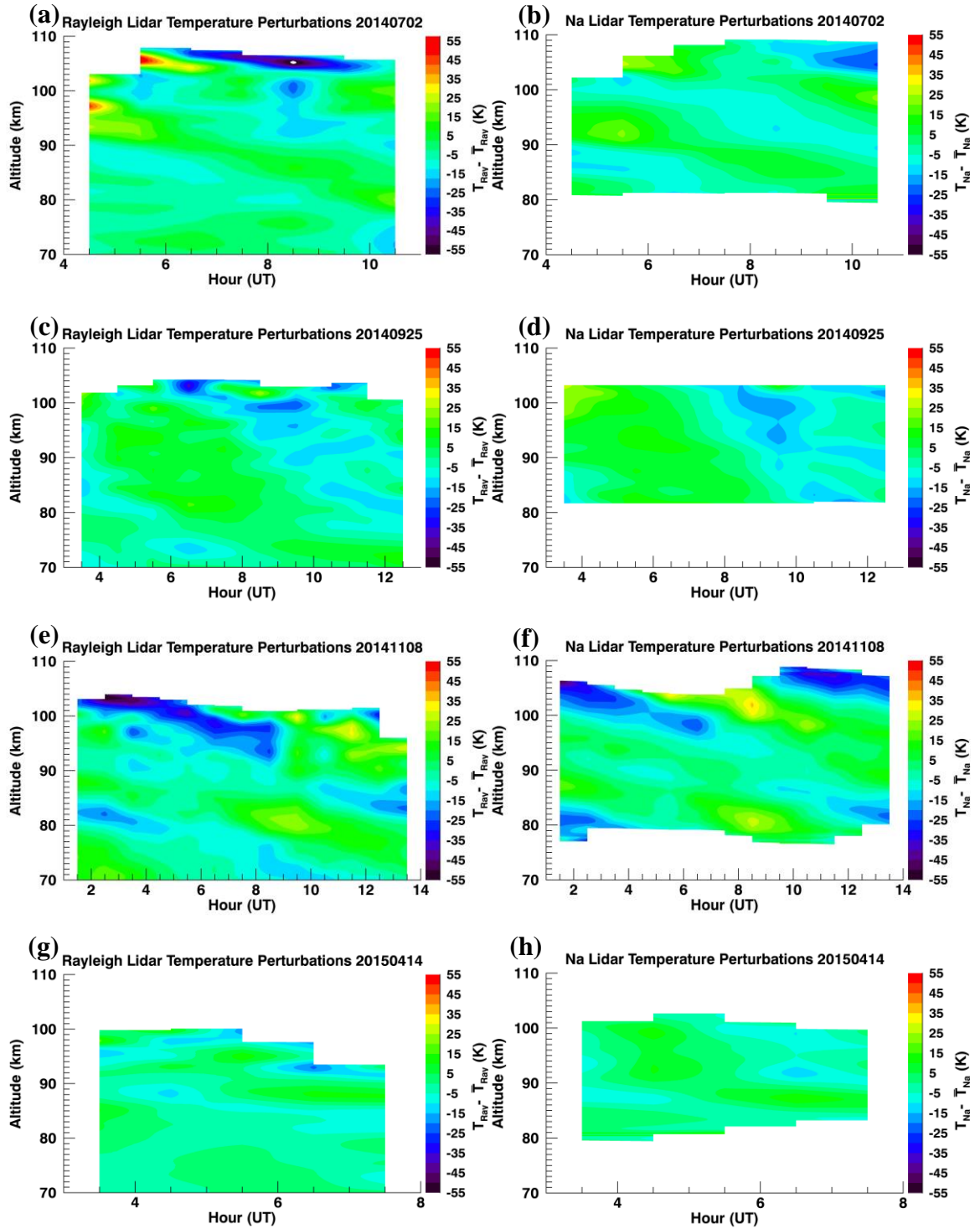


Figure 4.8. Temperature perturbations (night mean subtracted from hourly means) from Rayleigh lidar data (left panels) and Na lidar data (right panels).

Leblanc et al. [1998] again showed that the Rayleigh temperatures were colder than the Na temperatures in the 80-88 km region (their Figure 1). From 82-88 km, the Rayleigh temperatures were 2-6 K colder than the Na temperatures, which is between what we observe at USU and what was shown in the *Argall and Sica* [2007] study. Between 80-82 km, the *Leblanc et al.* [1998] shows that the difference between the two lidars' temperatures becomes even greater with the Rayleigh temperatures being between 8-14 K colder than the Na temperatures. This is a much larger difference than what is presented in our study. At 95 km and above, our data shows that the Rayleigh temperatures are on average increasingly warmer as one goes up in altitude, reaching an average maximum temperature difference of about 16 K at 105 km [Figure 4.5 (c)-(e)]. This result cannot be compared with the previous studies since their overlapping measurements did not extend this high in altitude.

Leblanc et al. [1998] suggested that the differences in Rayleigh and Na lidar climatologies could be explained by their choice of taking the Rayleigh initialization information (either temperature or pressure) from the CIRA-86 model [*Fleming et al.*, 1990]. In *Argall and Sica* [2007], the use of initialization information from a model causing the difference between the two lidar temperature climatologies was dispelled by using the CSU Na temperatures as seed temperatures for the PCL Rayleigh lidar temperatures and still observing large differences between the two lidars' climatologies. From there, *Argall and Sica* [2007] went on to suggest that the difference in the two climatologies could be caused by the geographical separation of the Rayleigh and Na lidar sites. They argued that the distance between the lidar sites could allow for changes in planetary or gravity wave activity which could explain the differences that they saw

between the Rayleigh and Na climatologies. From what we have found, this could have been the case in their studies between about 83 and 92 km, as the differences between the two sets of temperatures are much smaller in our study, which eliminated the geographical separation of the lidar sites.

What now comes into question is the reason for the large temperature differences between the two USU lidar instruments at altitudes above 95 km, where previous studies did not reach in their overlapping measurements. The choice of Rayleigh seed temperature seems to not affect these differences since we use either the Na or MSISe00 temperatures and the magnitude of temperature difference can be large or small regardless of seed temperature choice. Again, geographical distance is not a factor here since the two lidars are located about 5 m apart at the same ground-based observatory and the Rayleigh and Na beams are 40 km apart at 110 km altitude due to the beam-pointing geometry described above. This separation is not likely the reason for these temperature differences because the east- and west-pointing Na beams, which are 80 km apart at that altitude, have practically the same temperatures.

From these simultaneous and collocated observations at USU, one can begin to question differences in the two lidar techniques, themselves. It is known that at altitudes above about 90 km, molecular oxygen (O_2) experiences photodissociation and the proportion of atomic oxygen (O) increases gradually with altitude. The effect of changing composition on Rayleigh backscatter cross section (RBCS) and mean molecular mass (MMM) might affect the Rayleigh temperature calculation, which usually assumes constant RBCS and MMM throughout the measurement region. However, the effects of changing RBCS and MMM on the Rayleigh lidar temperature data reduction have been

studied using both models [Argall, 2007] and measurements [Sox *et al.*, 2016]. They only change the Rayleigh lidar temperatures by at most 2 K in the 85-115 km region. This temperature difference is negligible when compared to the tens of kelvin difference seen between the Na and Rayleigh temperatures. However, more can be done in exploring composition change effects on the Rayleigh temperatures (i.e., experiment with different model values for atomic oxygen density).

In the region of the Na layer, there was shown to be weak anticorrelation between Na density and temperatures above 96 km possibly due to ion-molecule chemistry [Plane *et al.*, 1999]. Since the Rayleigh lidar is insensitive to Na atoms and ions, this Na chemistry might be a factor that affects Na temperatures but not Rayleigh temperatures. However, it is assumed, as long as the Na atom collision rate is high, that temperatures derived from the broadening of the Na spectrum are equal to the neutral temperature.

While the mechanism causing the differences between the two lidars' temperatures has yet to be explained, there are a few clues that may prove helpful in working towards a solution. The first is that the Rayleigh temperatures appear to show stronger wave activity in the whole-night averages (i.e., larger wave amplitudes, more distinguishable waves) than the Na temperatures [see Figure 4.1 (a), (d-f), Figure 4.2 (a), (b), and (e), Figure 4.4 (b)], especially at altitudes above 100 km. A second clue is that the best agreement, at all altitudes, between the two datasets occurs on dates closest to the equinoxes. A third clue is that the differences between the two temperatures change sign depending on altitude, or in other words, the Rayleigh temperatures tend to be warmer at higher altitudes (above 95 km) and colder at lower altitudes (below 90 km) compared to the Na temperatures.

5. Conclusions

We have presented a comparison of simultaneous temperatures acquired by Rayleigh-scatter and sodium resonance lidars collocated in the same observatory on the campus of USU and covering the same altitude range (~80-110 km). Several conclusions can be reached through this work:

- Our simultaneous, collocated Rayleigh and Na lidar measurements have corroborated the previous climatological comparisons [*Leblanc et al., 1998; Argall and Sica, 2007*] in the 80-95 km region by showing that the Rayleigh temperatures were on average colder than the Na temperatures (by about 1.5 K).
- Above 95 km, we have shown new results that were not possible in previous studies, which did not extend this high, one being that the Rayleigh temperatures are much warmer (~13 K) than the Na temperatures in this region.
- The Rayleigh lidar temperatures show stronger and more distinct wave activity than the Na temperatures above about 100 km.
- The best agreement, throughout the entire 80-110 km range between the two techniques' temperatures, occurs on the nights, albeit only two, closest to the equinoxes.

To attempt to explain the observed differences between the two techniques' temperatures, instrument configurations were brought into question. The west- and east-pointing laser beam configurations of the Na lidar give approximately the same temperature profiles, meaning that the comparisons between Rayleigh and Na temperatures are independent of the pointing direction of the Na lidar. This confirms that

the discrepancies between the two temperature sets do not arise from each lidar measuring, for instance, different portions of the same wave structure. To further confirm this, hourly temperature perturbations showed that the two lidars measured the same wave parameters.

Though the causes for the differences in temperature at the high and low ends of the Na and Rayleigh lidar overlapping altitudes are left to be explained, there are some clues that can be further explored. These include the apparent wave activity seen in the Rayleigh, but not the Na temperatures, the agreement during the equinox periods, and the change in sign of the temperature differences based on altitude.

Continued observations from the two collocated lidars will probably shed light on these unanswered questions. Ideally, enough simultaneous data will be collected from the two USU lidars to obtain good coverage throughout all months in order to further explore the day-to-day and seasonal differences between the two systems' deduced temperatures.

Acknowledgments

The original Rayleigh lidar was initially upgraded to the much more sensitive configuration with funds from NSF, AFOSR, and USU. The system was further upgraded to bring it on line with funds provided by the Space Dynamics Laboratory Internal Research and Development program, USU, the USU Physics Department, and personal contributions. Engineering support for these latter upgrades was provided by Matthew Emerick, Thomas Amely, and Ryan Martineau. The Rayleigh data presented in this paper were acquired through the dedicated efforts of many student operators including: David Barton, David Moser, Bryant Ward, Joe Slansky, Preston Hooser,

Rebecca Petrick, Patrick Sharp, Luis Navarro, Jordan Burns, and Warren Schweigert. The Na lidar was supported under NSF AGS grant number 1135882. The Na data presented in this paper were acquired through the dedicated efforts of many student operators including Xuguang Cai and Neal Criddle.

References

- Argall, P. S. (2007), Upper altitude limit for Rayleigh lidar, *Ann. Geophys.* 25, 19–15, doi:10.5194/angeo-25-19-2007.
- Argall, P. S., and R. J. Sica (2007), A comparison of Rayleigh and sodium lidar temperature climatologies, *Ann. Geophys.*, 25, 27–33, doi:10.5194/angeo-25-27-2007.
- Beissner, K. C. (1997), Studies of mid-latitude mesospheric temperature variability and its relationship to gravity waves, tides, and planetary waves, PhD dissertation, 186 pp., Utah State Univ., Logan, UT, <http://digitalcommons.usu.edu/etd/4687>.
- Chen H., M. A. White, D. A. Krueger, and C. Y. She (1996), Daytime mesopause temperature measurements with a sodium-vapor dispersive Faraday filter in a lidar receiver, *Opt. Lett.*, 21, 1093–1095, doi:10.1364/OL.21.001093.
- Fleming, E. L., S. Chandra, J. J. Barnett, and M. Corney (1990), COSPAR International Reference Atmosphere, Chapter 2: Zonal mean temperature, pressure, zonal wind and geopotential height as functions of latitude, *Adv. Space Res.*, 10, 11–59, doi:10.1016/0273-1177(90)90386-E.
- Gao, Q., X. Chu, X. Xue, X. Dou, T. Chen, and J. Chen (2015), Lidar observations of thermospheric Na layers up to 170 km with a descending tidal phase at Lijiang (26.7°N, 100.0°E), China, *J. Geophys. Res. Space Physics*, 120, 9213–9220, doi:10.1002/2015JA021808.
- Hauchecorne, A., and M.-L. Chanin (1980), Density and temperature profiles obtained by lidar between 35 and 70 km. *Geophys. Res. Lett.*, 7: 565–568, doi:10.1029/GL007i008p00565.
- Hauchecorne, A., M.-L. Chanin, and P. Keckhut (1991), Climatology and trends of the middle atmospheric temperature (33–87 km) as seen by Rayleigh lidar over the south of France, *J. Geophys. Res.*, 96(D8), 15297–15309, doi:10.1029/91JD01213.
- Herron, J. P. (2007), Rayleigh-Scatter Lidar Observations at USU’s Atmospheric Lidar Observatory (Logan, UT) — Temperature Climatology, Temperature Comparisons with

MSIS, and Noctilucent Clouds, PhD dissertation, 156 pp., Utah State Univ., Logan, UT, <http://digitalcommons.usu.edu/etd/4686>.

Herron, J. P., V. B. Wickwar, P. J. Espy, and J. W. Meriwether, 2007: Observation of a noctilucent cloud above Logan, Utah (41.7°N, 111.8°W) in 1995, *J. Geophys. Res.*, *112*(D19203), 10.1029/2006JD007158.

Kent, G. S. and R. W. Wright (1970), A review of laser radar measurements of atmospheric properties, *J. Atmos. Terr. Phys.*, *32*, 917–943, doi:10.1016/0021-9169(70)90036-X.

Krueger, D. A., C. Y. She, and T. Yuan (2015), Retrieving mesopause temperature and line-of-sight wind from full-diurnal-cycle Na lidar observations, *Appl. Opt.*, *54*, 9469–9489, doi:10.1364/AO.54.009469.

Leblanc, T., I. S. McDermid, P. Keckhut, A. Hauchecorne, C. Y. She, and D. A. Krueger (1998), Temperature climatology of the middle atmosphere from long-term lidar measurements at middle and low latitudes, *J. Geophys. Res.*, *103*(D14), 17191–17204, doi:10.1029/98JD01347.

Liu, A. Z., Y. Guo, F. Vargas, and G. R. Swenson (2016), First measurement of horizontal wind and temperature in the lower thermosphere (105–140 km) with a Na lidar at Andes Lidar Observatory, *Geophys. Res. Lett.*, *43*, 2374–2380, doi:10.1002/2016GL068461.

Measures, R. M. (1992), *Laser Remote Sensing Fundamentals and Applications*, 510 pp., Krieger Publishing Company, Malabar, FL.

Picone, J. M., A. E. Hedin, D. P. Drob, and A. C. Aiken (2002), NRLMSISE-00 empirical model of the atmosphere: Statistical comparisons and scientific issues, *J. Geophys. Res.*, *107*(A12), 1468, doi:10.1029/2002JA009430.

Plane, J. M. C., C. S. Gardner, J. Yu, C. Y. She, R. R. Garcia, and H. C. Pumphrey (1999), Mesospheric Na layer at 40°N: Modeling and observations, *J. Geophys. Res.*, *104*(D3), 3773–3788, doi:10.1029/1998JD100015.

She, C. Y., S. Chen, Z. Hu, J. Sherman, J. D. Vance, V. Vasoli, M. A. White, J. Yu, and D. A. Krueger (2000), Eight-year climatology of nocturnal temperature and sodium density in the mesopause region (80 to 105 km) over Fort Collins, CO (41°N, 105°W), *Geophys. Res. Lett.*, *27*, 3289–3292, doi:10.1029/2000GL003825.

She, C. Y., H. Chen, and D. A. Krueger (2015), Optical processes for middle atmospheric Doppler lidars: Cabannes scattering and laser-induced resonance fluorescence, *J. Opt. Soc. Am. B*, *32*, 1575–1592, doi:10.1364/JOSAB.32.001575.

Sox, L. S., et al. (2016), Lower thermospheric temperature measurements made by a large-aperture, high-power Rayleigh-scatter lidar, (in preparation) *Geophys. Res. Lett.* or *J. Geophys Res.*

States, R. J., and C. S. Gardner (2000), Temperature structure of the mesopause region (80-105 km) at 40°N latitude, 1, Seasonal variations, *J. Atmos. Sci.*, 57, 66–77, doi:10.1175/1520-0469(2000)057<0066:TSOTMR>2.0.CO;2.

Yuan, T., C.-Y. She, D. A. Krueger, F. Sassi, R. Garcia, R. G. Roble, H.-L. Liu, and H. Schmidt (2008), Climatology of mesopause region temperature, zonal wind, and meridional wind over Fort Collins, Colorado (41°N, 105°W), and comparison with model simulations, *J. Geophys. Res.*, 113, D03105, doi:10.1029/2007JD008697.

Yuan, T., C.-Y. She, T. D. Kawahara, and D. A. Krueger (2012), Seasonal variations of mid-latitude mesospheric Na layer and its tidal period perturbations based on full-diurnal-cycle Na lidar observations of 2002-2008., *J. Geophys. Res.*, 117, D11304, doi:10.1029/2011JD017031.

CHAPTER 5

CONNECTION BETWEEN THE MIDLATITUDE MESOSPHERE AND SUDDEN
STRATOSPHERIC WARMINGS AS MEASURED BY RAYLEIGH-SCATTER
LIDAR ¹**Abstract**

While the mesospheric temperature anomalies associated with Sudden Stratospheric Warmings (SSWs) have been observed extensively in the polar regions, observations of these anomalies at midlatitudes are much more sparse. The Rayleigh-scatter lidar system, which operated at the Center for Atmospheric and Space Sciences on the campus of Utah State University (41.7°N, 111.8°W), collected a very dense set of observations, from 1993 through 2004, over a 45-90 km altitude range. This paper focuses on Rayleigh lidar temperatures derived during the six major SSW events that occurred during the 11-year period when the lidar was operating, and aims to characterize the local response to these midlatitude SSW events. In order to determine the characteristics of these mesospheric temperature anomalies, comparisons were made between the temperatures from individual nights during a SSW event and a climatological temperature profile. An overall disturbance pattern was observed in the mesospheric temperatures associated with SSW events, including coolings in the upper

¹ This chapter was published in *Journal of Geophysical Research-Atmospheres*: Sox, L. S., V. B. Wickwar, C. S. Fish, and J. P. Herron (2016), Connection between the midlatitude mesosphere and sudden stratospheric warmings as measured by Rayleigh-scatter lidar, *J. Geophys Res.*, 121, doi:10.1002/2015JD024374. Copyright 2016 by the American Geophysical Union (AGU). Reproduced with permission of AGU (see Appendix B).

mesosphere and warmings in the upper stratosphere and lower mesosphere, both comparable to those seen at polar latitudes.

1. Introduction

Sudden stratospheric warmings (SSWs) are major disturbances in the polar region of the winter hemisphere that are defined by changes in stratospheric temperature and circulation. They were first observed in 1952 via radiosonde [Scherhag, 1952; Labitzke and van Loon, 1999] and are characterized by a temperature increase of tens of degrees Kelvin, averaged over 60°-90° latitude at 10 hPa (roughly 32 km), and a weakening of the polar vortex that persists for the order of a week at 60° and 10 hPa level [Charlton and Polvani, 2007].

The term *sudden stratospheric warming*, although the accepted term, can be misleading. SSW effects on middle atmosphere temperature and circulation have lifetimes of 80 days [Limpasuvan *et al.*, 2004], and thus are not very *sudden*. Their effects have been seen throughout the entire atmospheric column [Baldwin and Dunkerton, 2001; Labitzke, 1972; Whiteway and Carswell, 1994; Siskind *et al.*, 2005; Walterscheid *et al.*, 2000; de Wit *et al.*, 2014; Laskar and Pallamraju, 2014; Hoffmann *et al.*, 2007; Chau *et al.*, 2010; Goncharenko *et al.*, 2010], and thus are not limited to just the *stratosphere*. They can also manifest as temperature decreases in other parts of the globe and atmosphere and thus are not only characterized by *warmings* [Labitzke, 1972; Liu and Roble, 2002; Whiteway and Carswell, 1994; Siskind *et al.*, 2005; Walterscheid *et al.*, 2000; Quiroz, 1977].

The mechanism for generating SSWs involves an increase in planetary wave

(PW) activity in the upper troposphere and lower stratosphere, which then propagates upward in the stratosphere and then dissipates in a wave-mean flow interaction with the polar vortex [Matsuno, 1971]. Planetary waves, or Rossby waves, are the class of atmospheric wave that have the largest horizontal wavelengths and result from the pole-to-pole potential vorticity gradient created by the Earth's rotation [Holton, 2004; Andrews *et al.*, 1987]. The polar vortex is a cyclone centered on the Earth's wintertime pole and is characterized by strong eastward zonal winds. The increased PW activity leads to increased PW breaking [McIntyre and Palmer, 1983] in the polar stratosphere and the deposition of the PW's westward momentum in the polar vortex. This weakens the polar vortex, and in the case of major SSWs, reverses the zonal wind direction to westward. The reversal of the stratospheric jet allows more eastward propagating gravity waves (GWs) to travel up into the mesosphere where, under normal winter conditions, westward propagating GWs dominate [Liu and Roble, 2002; Yamashita *et al.*, 2010; Thuraijajah *et al.*, 2014; de Wit *et al.*, 2014]. The atypical wintertime GW filtering and the resulting dominance of eastward GWs induce an equatorward circulation in the mesosphere, similar to what it is in summer, which leads to the cooling of the upper polar mesosphere. Mesospheric coolings of tens of degrees have been observed in the polar regions for several decades [Labitzke, 1972; Whiteway and Carswell, 1994; Walterscheid *et al.*, 2000; Azeem *et al.*, 2005]. However, at midlatitudes there were shown to be only small deviations (less than 10 K) from normal wintertime temperatures in the mesosphere [Angot *et al.*, 2012; Chandran and Collins, 2014; Liu and Roble, 2002]. Case studies have challenged this notion by reporting mesospheric coolings at midlatitude sites that have magnitudes of up to 30 K [Hauchecorne and Chanin, 1983; Yuan *et al.*, 2012]. This

study aims to further challenge the notion that the midlatitude stratosphere and mesosphere are unaffected during sudden stratospheric warmings by giving a climatological context using 11 years' worth of Rayleigh-scatter lidar temperatures from a midlatitude site.

This paper is organized as follows. In section 2 the methodology for classifying SSWs and the instrument and data descriptions of the USU Rayleigh lidar system are given. Section 3 shows the results from the USU Rayleigh lidar temperature dataset. Finally, sections 4 and 5 (respectively) present a discussion of and conclusions about the results presented in the paper.

2. SSWs and Rayleigh-Scatter Lidar Temperatures from 1993 to 2004

2.1. Classification of SSW Events

This study looks exclusively at major, northern hemisphere SSWs. We selected major SSWs using the same method as in *Charlton and Polvani* [2007]. Here, we use NASA's Modern-Era Retrospective Analysis for Research and Applications (MERRA) reanalysis dataset [*Rienecker et al.*, 2011] to select the SSWs which meet the two defining criteria of major SSWs: (1) a large deviation from the mean of the temperatures zonally-averaged from 60° to 90° N at the 10 hPa pressure level and (2) a reversal of the zonal-mean winds from eastward to westward at 60° N and at the 10 hPa pressure level. Figure 5.1 shows the MERRA temperatures, zonal winds and planetary wave zonal number 1 (PW1) amplitudes of the geopotential height for the six major SSWs between 1993-2004, during which there were observations made by the Rayleigh-scatter lidar (RSL) on the campus of Utah State University (USU) (described in the following section

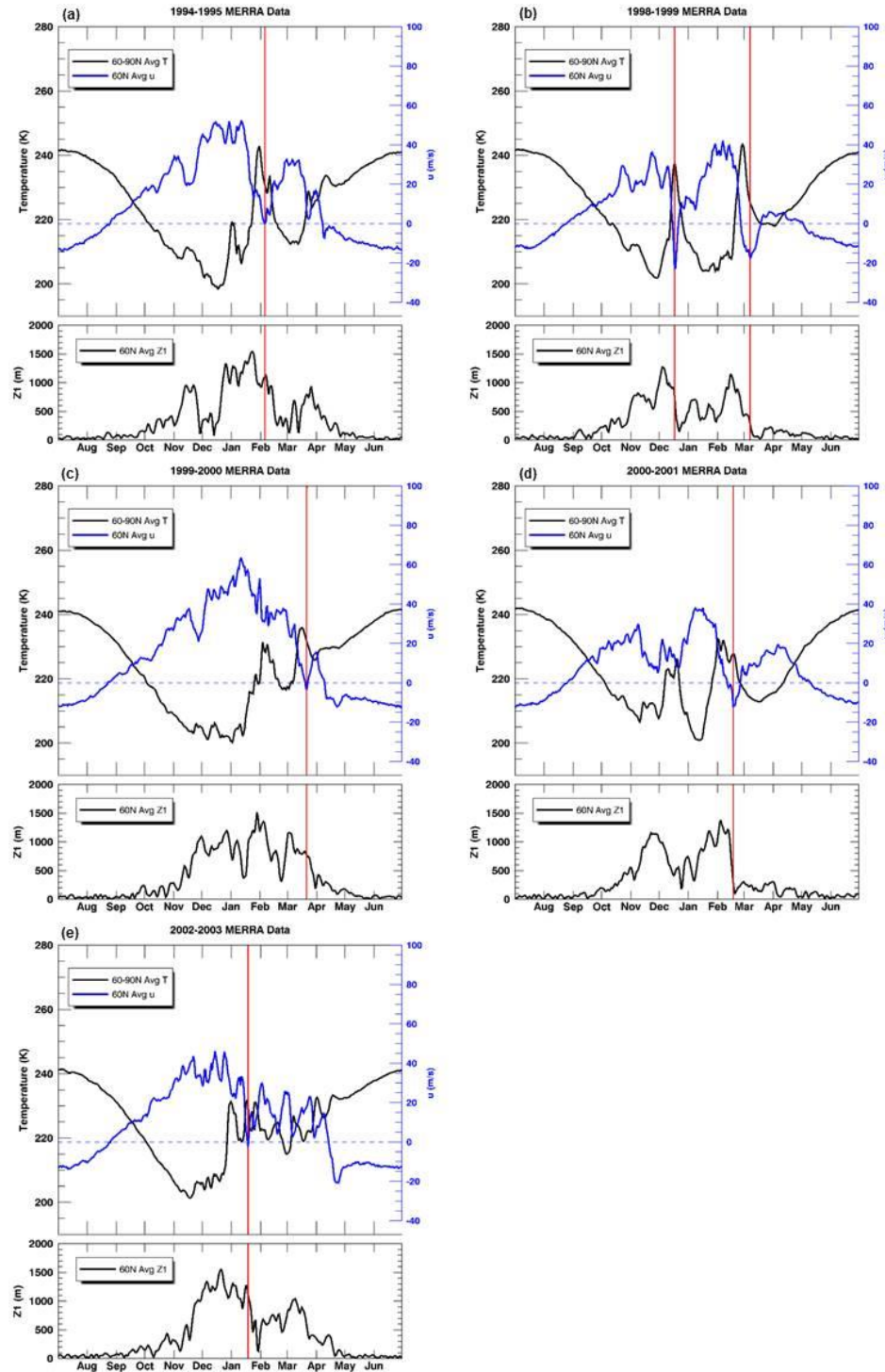


Figure 5.1. 60°-90°N zonal-mean temperatures (T; black curve) and 60°N zonal-mean zonal winds (u; blue curve) both at 10 hPa from the MERRA database. Six SSW events between 1993 and 2004 are given (a-e). Red vertical lines mark peak dates. Note that the 1998-1999 winter had two SSW events. The bottom panels show the PW1 amplitudes (Z1) of geopotential height zonally averaged around 60°N as a function of time.

of this paper). There were eight major SSW events that occurred between 1993 and 2004 and the USU RSL dataset overlapped with six of them. Additionally, to make the distinction between major SSWs and final warmings, events were only selected in which the zonal winds reversed back to eastward for at least two weeks prior to their seasonal reversal to westward in spring. An example of this can be seen in Figure 5.1 (c) during the March 2000 SSW when the zonal winds switch back to westward for 17 days before they make their seasonal reversal to eastward in early April.

2.2. 1993-2004 USU RSL Temperature Data

A RSL operated at the Atmospheric Lidar Observatory on the campus of USU (41.7°N, 111.8°W) from 1993 to 2004 [*Herron, 2007; Wickwar et al., 2001*]. It employed either a Spectra Physics GCR-5 or GCR-6 Nd:YAG laser to transmit 18 W (600 mJ per pulse) or 24 W (800 mJ per pulse), respectively. Both lasers operated at a wavelength of 532 nm and pulse repetition rate of 30 Hz. The receiver was comprised of a 44-cm diameter Newtonian telescope that was optically coupled to an Electron Tubes 9954 series photomultiplier tube (PMT). The low-altitude signal was reduced by a mechanical chopper and by electronically gating the PMT. The lidar's raw signal profiles were recorded, using a multichannel scaler unit, with a time resolution of two minutes. In altitude, the raw signal was binned in 250 ns, or 37.5 m, intervals. However, in post-processing, a boxcar average was applied to the time-averaged signal with a 3-km window. In this study, the signal was also time-averaged over the entire night, for each given night. This results in a variable number of hours in each night's average. The mean number of hours per night in each nighttime average in this study is 6.5 hours. The

gating of the PMT was set so that the tube would be fully on at altitudes of 38 km and higher. The upper altitude limit, for each night's average, was chosen to be where the lidar signal was twenty times its standard deviation. Several factors determine how good the signal-to-standard deviation ratio was at a given height for each observed night, including: length of the observation, laser power, atmospheric transmission, and neutral number density. Depending mostly on the number of hours in each night's average, the upper altitude limit would vary from 80-95 km, but reached 90 km on most nights [Herron, 2007].

The USU RSL data were used to calculate absolute temperatures using a modified version of the method described in *Hauchecorne and Chanin*, [1980], [Beissner, 1997; Herron, 2007]. This method relies on the proportionality between lidar signal and relative density, which is then related to absolute temperature using the ideal gas law and the assumption that the measured portion of the atmosphere is in hydrostatic equilibrium. The RSL temperature integral requires a seed temperature at the highest altitude, which is used as an initial condition for the downward integration. In this study the seed temperature values were taken from the climatology of the sodium resonance lidar, formerly at Colorado State University [She *et al.*, 2000], for nights when the lidar data reached 83 km and above. For nights when the USU RSL data did not reach 83 km, a combination of the MSISE90 [Hedin, 1991] empirical model and the CSU climatology was used.

The CSU temperatures were chosen as a seed temperature source due to the fact that the two lidars' datasets overlapped both temporally and in altitude, and because the CSU lidar site was close in latitude and longitude (40.6° N, 105° W) to the USU lidar site.

While choice of a seed temperature can introduce a systematic source of error at the upper RSL altitudes, its effect becomes exponentially smaller as one continues the temperature integration downward in altitude. If one supplies seed temperatures that are ± 20 K different from the initial seed temperature at the top altitude, then by 15 km lower, the differences in the temperature curves go down to ± 1 K and continue decreasing thereafter as the altitude decreases. In addition to the systematic seed temperature error, there is also a random error from photon counting that is propagated through the temperature calculation. Again, these errors decrease significantly with decreasing altitude as the signal-to-standard deviation ratio increases rapidly with decreasing altitude. For the purpose of this study, the temperatures reported above about 80 km should be conservatively considered.

A temperature climatology was calculated using over 800 nights (over 5000 hours) of data collected with the USU RSL from 1993 to 2004. The climatology averaged the nighttime temperatures over a window 31 nights wide, centered on each night, and 11 years deep. Figure 5.2 gives the winter-to-spring (December-April) and summer-to-fall (June-October) portions of the climatology.

The climatology shows the expected seasonal change in mesospheric temperatures that range from about 170 K in the upper mesosphere to 270 K in the lower mesosphere during the summer months and then range from 205 K in the upper mesosphere to 250 K in the lower mesosphere during the winter months. Figure 5.3 shows example temperature profiles from the winter (Feb 3rd) and summer (Aug 4th) portions of the climatology. The choice of Feb 3rd and Aug 4th as representative climatological dates will be further discussed in the following section. For the remainder

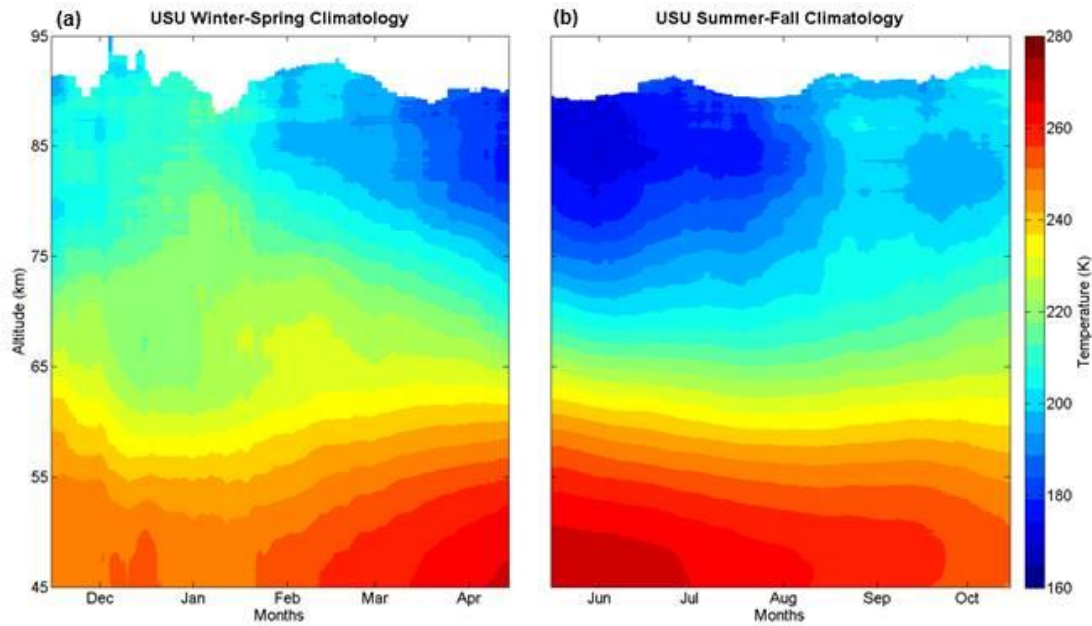


Figure 5.2. USU Rayleigh lidar climatology for (a) winter-spring (DJFMA) and (b) summer-fall periods (JJASO). The climatology was calculated using nighttime temperature measurements from 1993 to 2004.

of this paper, the winter temperature range will reference the 170-270 K range and the summer temperature range will reference the 205-250 K range.

There are also two notable cold temperature minima anomalies in the USU climatology, one occurring from about 60-75 km lasting from December to January and another from about 73-87 km lasting from mid-September to mid-October. The first minimum is likely a signature from SSWs since the RSL data overlapping with SSW events were included in the calculation of the climatology. Also, there is a corresponding warming in the upper stratosphere (45-50 km) during this same period. The second minimum is an interesting feature that has yet to be fully explained.

3. Results

There were six major SSW events that occurred between 1993 and 2004 during

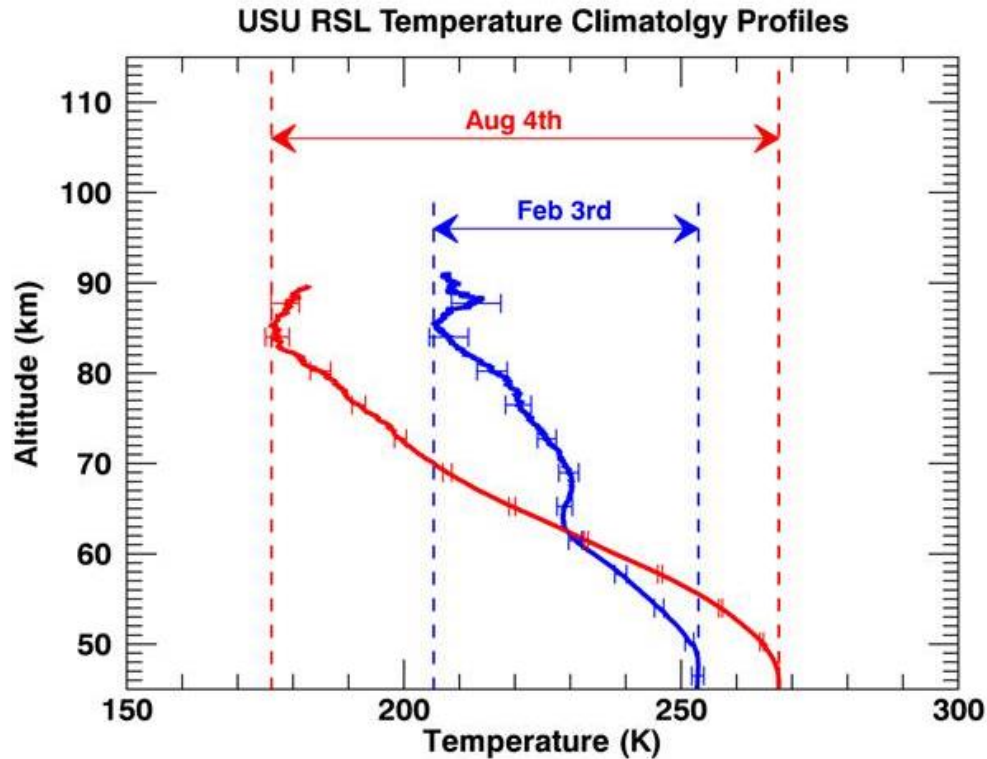


Figure 5.3. USU Rayleigh lidar temperature climatological profiles for a winter night (February 3rd, blue curve), and a summer night (August 4th, red curve). The minimum and maximum of each curve defines the representative winter temperature range (205-250 K) and summer temperature range (170-270 K). Error bars shown are the RMS standard deviation of the mean for each climatological profile.

which there were USU RSL observations. Table 5.1 lists the six SSW periods along with their peak dates [*Limapsuvan et al.*, 2004], or the date on which the zonal-mean zonal winds were at the maximum westward value. The dates for ± 40 days from the peak date are also given, along with the number of nighttime RSL observations for the event period. USU RSL temperatures for each of the six SSW event periods are shown in Figure 5.4. The nighttime averaged RSL temperatures were smoothed with a window of five days to emphasize the temporal structure. Peak dates for each event are denoted by a red vertical line. The color bars for each of the plots in Figure 5.4 have the same scale as the

Table 5.1. List of Major SSWs and USU RSL Data

SSW Event	Peak Date	– 40 Days	+ 40 Days	Nights of USU RSL Data
Jan-Feb 1995	05 Feb 1995	28 Dec 1994	17 Mar 1995	26
Dec 1998- Jan 1999	17 Dec 1998	07 Nov 1998	26 Jan 1999	19
Feb-Mar 1999	07 Mar 1999	26 Jan 1999	16 Apr 1999	29
Mar-Apr 2000	21 Mar 2000	10 Feb 2000	30 Apr 2000	9
Jan-Mar 2001	17 Feb 2001	08 Jan 2001	29 Mar 2001	26
Jan-Feb 2003	18 Jan 2003	10 Dec 2002	27 Feb 2003	17

climatology in Figure 5.2. In all of the plots, Figure 5.4 (a-f), the temperatures switch from the climatology's winter temperature range to its summer temperature range (Figure 5.3) during the SSW. This results in a warming of the upper stratosphere and lower mesosphere (45-65 km) and a cooling of the upper mesosphere (65-90 km). For the Jan-Apr 1999 [Figure 5.4 (c)] and Jan-Feb 2003 [Figure 5.4 (f)] events, this switch from winter-to-summer conditions happens prior to the peak date. For the Nov 1998-Jan 1999 [Figure 5.4 (b)] and Jan-Mar 2001 [Figure 5.4 (e)] events, this switch happens after the peak date. The Dec 1994-Mar 1995 [Figure 5.4 (a)] and Mar-Apr 2000 [Figure 5.4 (d)] events do not have good RSL data coverage around the peak dates, but one can see that the switch to summer-like conditions has happened in the days following the peak date.

Another salient feature in these temperature plots is that the cooling of the upper mesosphere consistently precedes the peak date of the stratospheric wind reversal [Figure 5.4 (b, c, e, and f)]. In two cases, the cooling of the upper mesosphere even precedes the warming of the lower mesosphere [Figure 5.4 (b & e)].

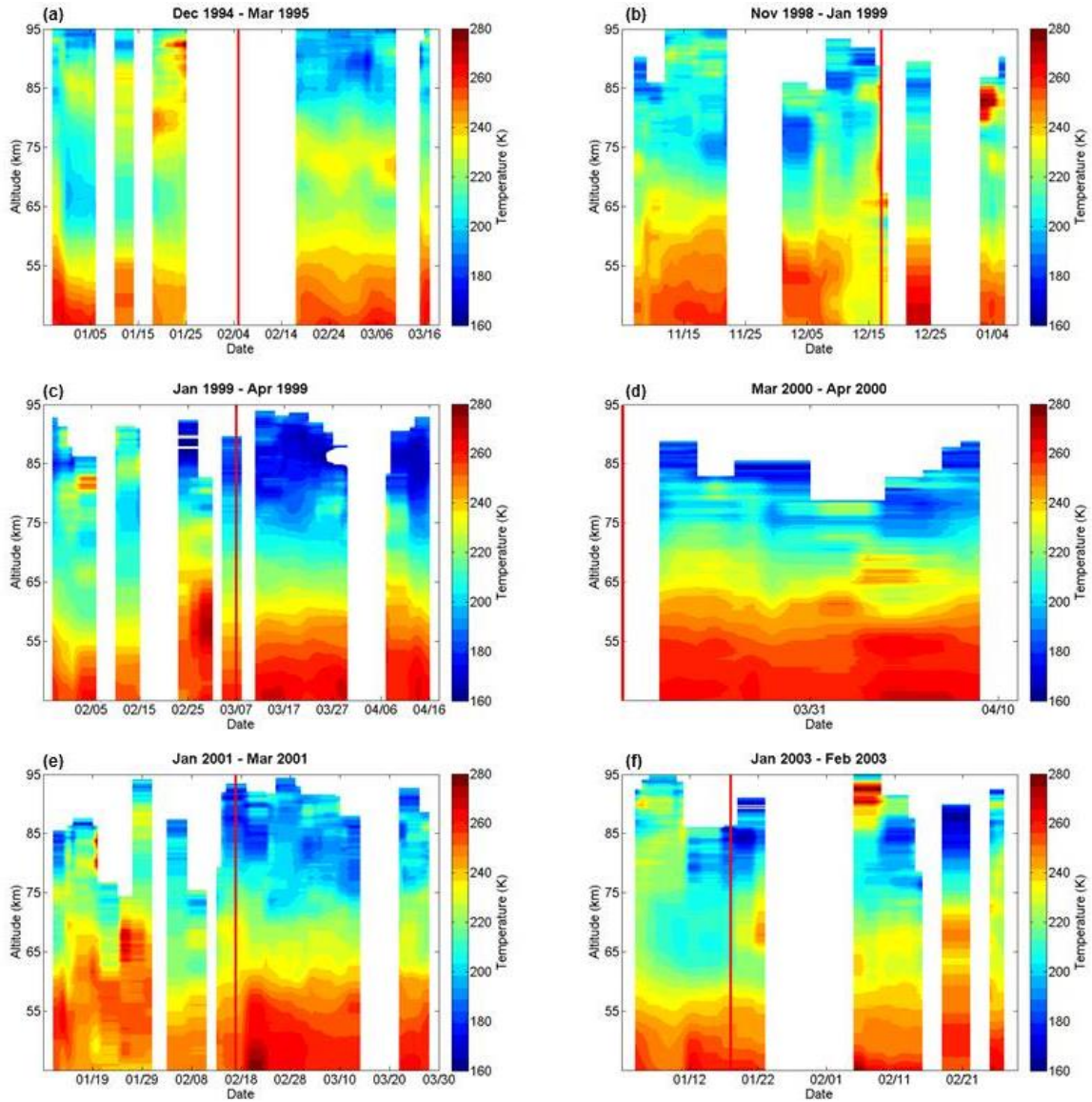


Figure 5.4. USU Rayleigh lidar nighttime temperatures for six SSW event periods (a-f). Red vertical lines mark peak dates. Color bars are on the same scale as in Figure 5.2.

To better define the upper mesosphere coolings and lower mesosphere warmings, temperature difference plots [Figure 5.5 (a-f)] were created by subtracting the climatological February 3rd profile from each nighttime temperature profile during each of the six SSW events. February 3rd was chosen because it was in the middle of the

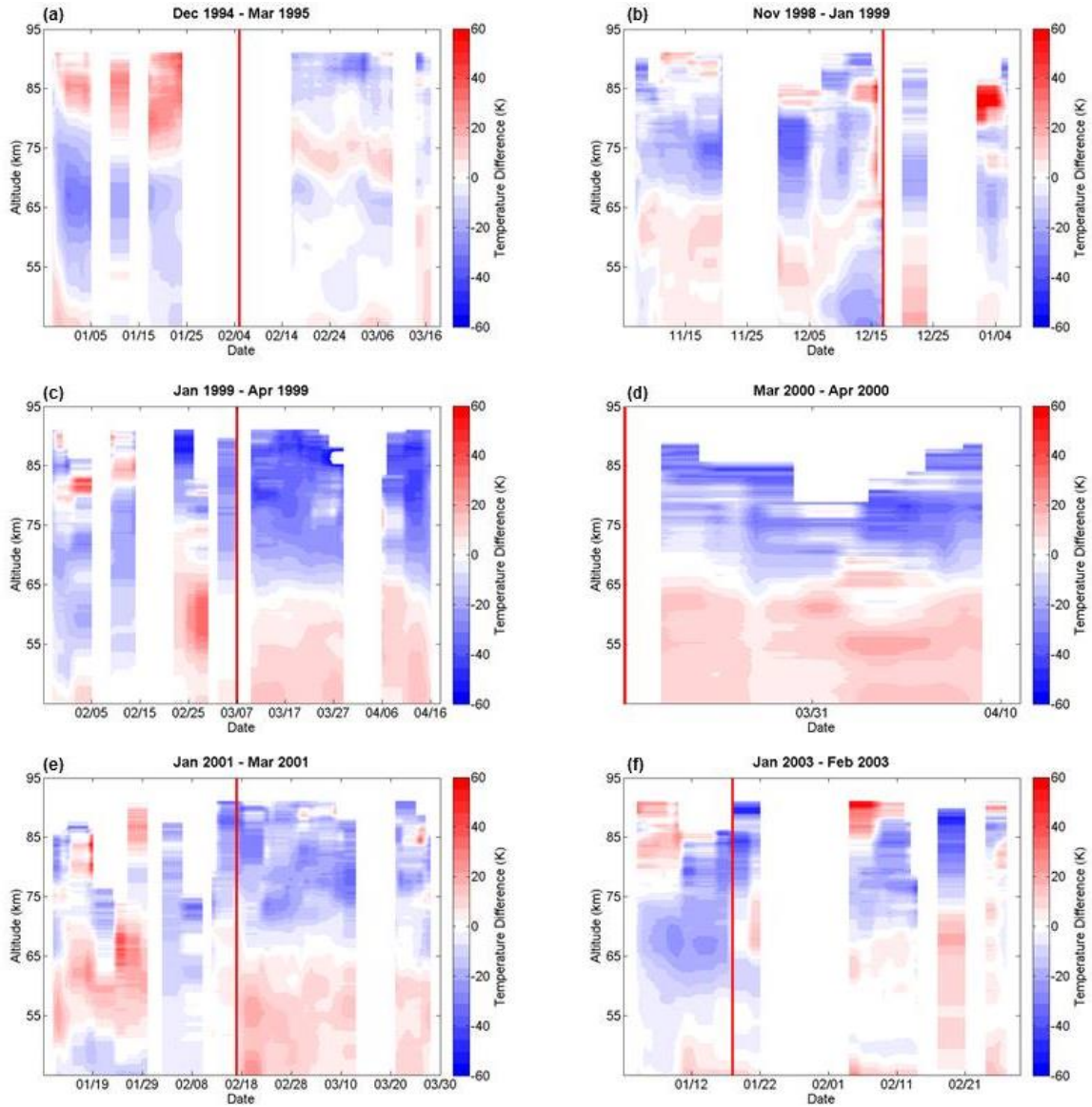


Figure 5.5. Temperature difference plots for the six SSW event periods (a-f). Red vertical lines mark peak dates.

climatological period of interest [Figure 5.2 (a)]. However, because the temperature climatology was averaged with at 31-day sliding window, the February 3rd profile is really an average from January 19th to February 18th, which makes it more representative of winter climatological temperatures, overall. A climatological profile was chosen as opposed to a profile preceding the SSW or an average of winter nights' temperatures

when there was no SSW, due to lack of data consistently acquired during these two periods.

In Figure 5.5, the dominant vertical pattern, that occurs near the peak date and continues for several weeks after, is made up of warmings in the upper stratosphere and lower mesosphere (45-65 km) and coolings in the upper mesosphere (65-90 km) [as seen in Figure 5.5(b-f)]. This pattern supports the switch in Figure 5.4 from winter-to-summer temperatures and assigns magnitudes to these mesospheric temperature anomalies. The coolings typically decrease by -30 or -40 K and the warmings increase by $+30$ K. One extreme warming at the end of February 1999 attained a relative change of $+40$ K [Figure 5.5 (c)] and corresponded to what appears to be an elevated stratopause event (elevated in both temperature and altitude). Unlike previously reported elevated stratopause events in the arctic [Chandran *et al.*, 2013], this event occurred prior to the peak of the SSW. The uncertainty for the temperature differences (Figure 5.5), as a function of altitude and time, for each event, are given in Figure 5.6. The temperature difference uncertainties, $\sigma_{D_{ij}}$, are calculated as

$$\sigma_{D_{ij}} = \sqrt{\sigma_{T_{ij}}^2 + \bar{\sigma}_{C_i}^2},$$

where $\sigma_{T_{ij}}$ is the standard deviation, based on Poisson statistics, of the temperatures for an individual night j at altitude i , and $\bar{\sigma}_{C_i}$ is the RMS standard deviation of the mean of the temperature climatology [see error bars in Figure 5.3] for the February 3rd climatological profile at altitude i .

It should be noted that these uncertainties are overestimated, because the variable smoothing from one to five days was not taken into account. For the most part, the

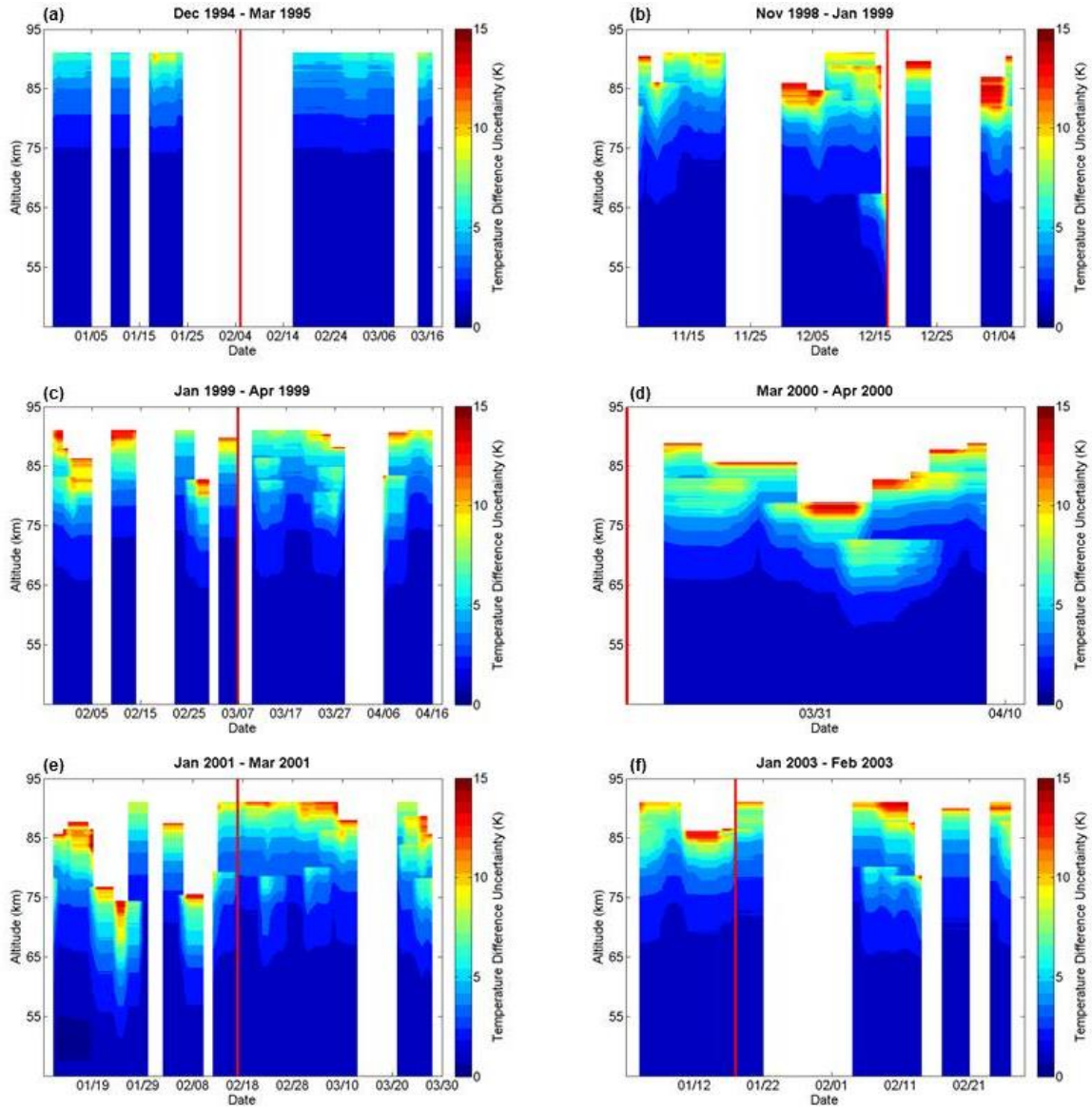


Figure 5.6. Temperature difference uncertainties for each of the six SSW event periods. Red vertical lines mark peak dates.

uncertainty is between 1 and 10 K. This indicates that the consistent 20 to 40 K temperature differences shown in Figure 5.5 are statistically significant.

4. Discussion

The first midlatitude mesospheric temperature anomalies during a minor SSW

event were shown with lidar observations made by *Hauchecorne and Chanin*, [1983] at the Observatoire d'Haute Provence (OHP; 44°N, 6°E). Their study showed a cooling of the low to mid mesosphere (50-70 km) of more than -20 K and a warming in the mid to upper stratosphere (30-45 km) also of about $+20$ K. Decades later, negative temperature anomalies in the tens of degrees at midlatitudes (54°N and 41° N) were observed higher into the mesosphere (80-90 km) [*Hoffmann et al.*, 2007; *Yuan et al.*, 2012]. Our observations agree in magnitude (maximum temperature anomaly of about -30 or -40 K at 80-90 km) with the anomalies presented in these case studies. They also manifest during all of the SSW periods in which there are overlapping USU RSL measurements. The observations presented in this paper suggest that these strong temperature changes at midlatitudes in the mesosphere are not limited to singular case studies, but rather occur consistently during most, if not all major SSW events.

While our observations from a single site do not capture the full longitudinal variability at midlatitudes during SSWs, our results do show a consistent mesospheric warming and cooling pattern during every observed event (in the 11-year observational period, there were eight major SSWs and the USU RSL dataset overlapped with all but two of these events). Furthermore, the magnitudes of these warmings and coolings are especially strong in magnitude, when compared with other midlatitude studies. Two model studies [*Chandran and Collins*, 2014; *Liu and Roble*, 2002], show zonal mean, SSW-induced temperature anomalies at roughly 42°N, which are significantly smaller in magnitude (up to ± 10 K) than our temperature difference results (up to ± 40 K). The RSL at OHP showed composite temperature anomalies for 13 SSW winters [*Angot et al.*, 2012], which gave significantly different results from what is presented in this paper. For

the 20 days preceding the SSW event and about 10 days after, they showed coolings down to about -10 K in the upper mesosphere and warmings in the upper stratosphere and lower mesosphere up to about $+15$ K. These anomalies are again significantly smaller in magnitude than our results and also do not persist for as long after the peak day of the SSW. The discrepancy in magnitude between the USU RSL temperature anomalies and those presented in the aforementioned studies could be a signature of the longitudinal variability in the SSW event, itself. However, the fact that (a) temperature anomalies of about the same strength are shown during every observed SSW event, without much variation between the years and (b) that the PW1 amplitudes in the upper stratosphere greatly decrease after the peak dates of all six SSW events (Figure 5.1 bottom panels) suggests that the magnitudes of the temperature anomalies seen at the USU RSL are not strictly a longitudinally based phenomena. To fully examine the longitudinal variability of these temperature anomalies, coordinated measurements amongst several individual sites spaced around the same latitude circle are needed.

Several studies have noted that observed anomalies in the mesosphere occur prior to the warming and wind reversal in the stratosphere [*Walterscheid et al.*, 2000; *Azeem et al.*, 2005; *Hoffmann et al.*, 2007; *Yuan et al.*, 2012]. While our observations do show the mesospheric coolings consistently precede the wind reversal peak, they do not always precede the warmings in the upper stratosphere/lower mesosphere (45-50 km) measured by our lidar. Figures 5.3 (b & e) do show two cases of mesospheric coolings preceding both the wind reversal peak and the warming at lower altitudes. For two other cases, [Figure 5.3 (c and f)], the mesospheric coolings happen prior to the peak wind reversal, but do not precede the lower mesospheric warming. These results indicate that

mesospheric coolings do not always precede stratospheric warmings at midlatitudes.

5. Conclusions

The midlatitude mesosphere's thermal structure during SSW events was studied using the USU RSL temperature data from 1993-2004. The RSL dataset overlapped with six of the eight major SSWs that occurred during the 11-year period. Careful attention was paid in determining each of the SSW events in the polar stratosphere using NASA MERRA zonal mean temperatures and zonal winds both at the 10 hPa level and in defining the peak date of the wind reversal. From there, available USU RSL temperature profiles were presented for ± 40 days around the peak date. These nighttime profiles were then compared with a wintertime climatological profile.

From this comparison, we saw that the thermal structure of the midlatitude mesosphere switches from winter (170-270 K) to summer (205-250 K) conditions in the span of only a few days around the peak date and persists for several days thereafter. Temperature deviations from the climatological February 3rd profile showed that this switch resulted in warmings of the lower mesosphere up to +40 K and coolings in the upper mesosphere of down to -40 K. These magnitudes are consistent with the midlatitude case study results and are comparable with the temperature deviations typically seen in the polar mesosphere.

It has been noted in the past that mesospheric coolings have preceded stratospheric warmings. However, in the data presented here, this pattern was not seen throughout all of the events, only two of the six. However, it is important to note that strong upper mesospheric coolings did exist during all of the observed SSW periods. In

the past, case studies have suggested strong temperature changes at latitudes similar to the northern Utah USU RSL site. Our work clearly demonstrates a pattern of mesospheric connection that consistently extends down to the USU site at 42°N latitude during major SSW events.

Acknowledgments

MERRA data is available at http://acd-ext.gsfc.nasa.gov/Data_services/met/ann_data.html. USU RSL data are available from the authors upon request. The RSL data collection was supported by the National Science Foundation under grant numbers ATM-9203034, ATM-9302118, ATM-9714789, and ATM-01234145. L. S. was supported through the Utah NASA Space Grant Consortium grant number 120845 and by USU. Special thanks go to the dedicated student lidar operators.

References

- Andrews, D. G., J. R. Holton, and C. B. Leovy (1987), *Middle Atmosphere Dynamics*, 489 pp., Academic Press.
- Angot, G., P. Keckhut, A. Hauchecorne, and C. Claud (2012), Contribution of stratospheric warmings to temperature trends in the middle atmosphere from the lidar series obtained at Haute-Provence Observatory (44°N), *J. Geophys. Res.*, *117*, D21102, doi:10.1029/2012JD017631.
- Azeem, S. M. I., E. R. Talaat, G. G. Sivjee, H.-L. Liu, and R. G. Roble (2005), Observational study of the 4-day wave in the mesosphere preceding the sudden stratospheric warming events during 1995 and 2002, *Geophys. Res. Lett.*, *32*, L15804, doi:10.1029/2005GL023393.
- Baldwin, M. P., and T. J. Dunkerton (2001), Stratospheric harbingers of anomalous weather regimes, *Science*, *294*, 581–584.
- Beissner, K. C. (1997), Studies of mid-latitude mesospheric temperature variability and its relationship to gravity waves, tides, and planetary waves, PhD dissertation, 186 pp..

Utah State Univ., Logan, UT, <http://digitalcommons.usu.edu/etd/4687>.

Chandran A., R. L. Collins, R. R. Garcia, D. R. Marsh, V. L. Harvey, J. Yue, and L. de la Torre (2013), A climatology of elevated stratopause events in the whole atmosphere community climate model, *J. Geophys. Res.*, *118*, 1234–1246, doi:10.1002/jgrd.50123.

Chandran, A., and R. L. Collins (2014), Stratospheric sudden warming effects on winds and temperature in the middle atmosphere at middle and low altitudes: a study using WACCM, *Ann. Geophys.*, *32*, 859–874, doi:10.5194/angeo-32-859-2014.

Charlton, A. J., and L. M. Polvani (2007), A New Look at Stratospheric Sudden Warmings. Part I: Climatology and Modeling Benchmarks, *J. Clim.*, *20*, 449–469, doi:<http://dx.doi.org/10.1175/JCLI3996.1>.

Chau, J. L., N. A. Aponte, E. Cabassa, M. P. Sulzer, L. P. Goncharenko, and S. A. González (2010), Quiet time ionospheric variability over Arecibo during sudden stratospheric warming events, *J. Geophys. Res.*, *115*, A00G06, doi:10.1029/2010JA015378.

de Wit, R. J., R. E. Hibbins, P. J. Espy, Y. J. Orsolini, V. Limpasuvan, and D. E. Kinnison (2014), Observations of gravity wave forcing of the mesopause region during the January 2013 major Sudden Stratospheric Warming, *Geophys. Res. Lett.*, *41*, 4745–4752, doi:10.1002/2014GL060501.

Goncharenko, L. P., J. L. Chau, H.-L. Liu, and A. J. Coster (2010), Unexpected connections between the stratosphere and ionosphere, *Geophys. Res. Lett.*, *37*, L10101, doi:10.1029/2010GL043125.

Hauchecorne, A., and M. L. Chanin (1980), Density and temperature profiles obtained by lidar between 35 and 70 km, *Geophys. Res. Lett.*, *7*, 565–568.

Hauchecorne, A., and M. L. Chanin (1983), Mid-latitude lidar observations of planetary waves in the middle atmosphere during the winter of 1981-1982, *J. Geophys. Res.*, *88*(C6), 3843–3849, doi:10.1029/JC088iC06p03843.

Hedin, A. E. (1991), Extension of the MSIS thermosphere model into the middle and lower atmosphere, *J. Geophys. Res.*, *96*(A2), 1159–1172.

Herron, J. P. (2007), Rayleigh-scatter lidar observations at USU's atmospheric lidar observatory (Logan, UT) — temperature climatology, temperature comparisons with MSIS, and noctilucent clouds, PhD dissertation, 156 pp., Utah State Univ., Logan, UT, <http://digitalcommons.usu.edu/etd/4686>.

Hoffmann, P., W. Singer, D. Keuer, W. K. Hocking, M. Kunze, and Y. Murayama (2007), Latitudinal and longitudinal variability of mesospheric winds and temperatures

during stratospheric warming events, *J. Atmos. Sol. Terr. Phys.*, *69*, 2355–2366, doi:10.1016/j.jastp.2007.06.010.

Holton, J. R. (2004), *An Introduction to Dynamic Meteorology*, 535 pp., Academic Press.

Labitzke, K. G. (1972), The interaction between stratosphere and mesosphere in winter, *J. Atmos. Sci.*, *29*, 1395–1399.

Labitzke, K. G., and H. van Loon (1999), *The Stratosphere: Phenomena, History and Relevance*, 189 pp., Springer.

Laskar, F. I., and D. Pallamraju (2014), Does sudden stratospheric warming induce meridional circulation in the mesosphere thermosphere system? *J. Geophys. Res.*, *119*, 10133–10143. doi:10.1002/2014JA020086.

Limpasuvan, V., D. J. Thompson, and D. L. Hartmann (2004), The life cycle of the northern hemisphere sudden stratospheric warmings, *J. Clim.*, *17*, 2584–2596.

Liu, H.-L., and R. G. Roble (2002), A study of a self-generated stratospheric sudden warming and its mesospheric–lower thermospheric impacts using the coupled TIME-GCM/CCM3, *J. Geophys. Res.*, *107*(D23), 4695, doi:10.1029/2001JD001533.

Matsuno, T. (1971), A dynamical model of the stratospheric sudden warming, *J. Atmos. Sci.*, *28*, 1479–1494.

McIntyre, M. E., and T. N. Palmer (1983), Breaking planetary waves in the stratosphere, *Nature*, *305*, 593–600.

Quiroz, R. S. (1977), The tropospheric–stratospheric polar vortex breakdown of January 1977, *Geophys. Res. Lett.*, *4*, 151–154.

Rienecker, M. M., et al. (2011), MERRA: NASA’s Modern-Era Retrospective Analysis for Research and Applications, *J. Clim.*, *24*, 3624–3648.

Scherhag, R. (1952), Die explosionsartigen Stratosphärenwärmungen des Spätwinters, *Ber. Dtsch. Wetterdienst (US Zone)*, *6*, 51–63.

She, C. Y., S. Chen, Z. Hu, J. Sherman, J. D. Vance, V. Vasoli, M. A. White, J. R. Yu, and D. A. Krueger (2000), Eight-year climatology of nocturnal temperature and sodium density in the mesopause region (80 to 105 km) over Fort Collins, CO (41° N, 105° W), *Geophys. Res. Lett.*, *27*, 3289–3292.

Siskind, D. E., L. Coy, and P. Espy (2005), Observations of stratospheric warmings and mesospheric coolings by the TIMED SABER instrument, *Geophys. Res. Lett.*, *32*, L09804, doi:10.1029/2005GL022399.

Thurairajah, B., S. M. Bailey, C. Y. Cullens, M. E. Hervig, and J. M. Russell III (2014), Gravity wave activity during recent stratospheric sudden warming events from SOFIE temperature measurements, *J. Geophys. Res.*, *119*, 8091–8103, doi:10.1002/2014JD021763.

Walterscheid, R. L., G. G. Sivjee, and R. G. Roble (2000), Mesospheric and lower thermospheric manifestations of a stratospheric warming event over Eureka, Canada (80° N), *Geophys. Res. Lett.*, *27*, 2897–2900.

Whiteway, J. A., and A. I. Carswell (1994), Rayleigh lidar observations of thermal structure and gravity wave activity in the high arctic during a stratospheric warming, *J. Atmos. Sci.*, *51*, 3122–3136.

Wickwar, V. B., T. D. Wilkerson, M. Hammond, and J. P. Herron (2001), Mesospheric temperature observations at the USU/CASS Atmospheric Lidar Observatory (ALO), *Proceedings of SPIE*, *4153*, 272–284, doi:10.1117/12.417056.

Yamashita, C., H.-L. Liu, and X. Chu (2010), Responses of mesosphere and lower thermosphere temperatures to gravity wave forcing during stratospheric sudden warming, *Geophys. Res. Lett.*, *37*, L09803, doi:10.1029/2009GL042351.

Yuan, T., B. Thurairajah, C.-Y. She, A. Chandran, R. L. Collins, and D. A. Krueger (2012), Wind and temperature response of midlatitude mesopause region to the 2009 Sudden Stratospheric Warming, *J. Geophys. Res.*, *117*, D09114, doi:10.1029/2011JD017142.

CHAPTER 6

CONCLUSIONS AND FUTURE WORK

1. Conclusions

The development and construction of a high-power, large-aperture Rayleigh-scatter lidar system have been completed on the campus of Utah State University. The first full year of observations using this unique lidar system was made between summer 2014 and summer 2015. These observations showed, for the first time, Rayleigh-scatter lidar temperatures extending into the lower thermosphere, up to about 115 km, for one full annual cycle. The new Rayleigh lidar's instrumentation was described in detail in this work, but in brief, included two Nd:YAG, pulsed lasers transmitting at a wavelength of 532 nm and repetition rate of 30 Hz, which are used as a single transmitter with an average power output of 42 W and a four-barrel telescope cage system which gives an effective receiving area of 4.9 m². By increasing these system parameters, compared to the previous USU Rayleigh lidar and similar systems, the sensitivity of the instrument increased, which allowed for more signal to be obtained from higher altitudes.

The classical Rayleigh lidar temperature retrieval method [*Hauchecorne and Chanin*, 1980] assumed that both the Rayleigh backscatter cross section and the atmospheric mean molecular mass do not change with altitude, which is a good assumption at altitudes below 90 km, where photodissociation of O₂ has not become significant and diffusive equilibrium has not become the dominant process affecting vertical distribution. By extending Rayleigh lidar measurements above 90 km, the effects of changing atmospheric composition had to be explored. The MSISe00 model [*Picone et*

al., 2002] was used to develop the corrections to the existing temperature calculation and then these corrections were applied to the 2014-2015 data. A very small change (at most 2 K) between the corrected and uncorrected temperatures was found.

The 2014-2015 Rayleigh lidar temperature data was summarized by calculating seasonal averages, using the individual whole-night averages, which were shown to agree well with climatological data from the previous incarnation of the USU Rayleigh lidar in the two systems' overlapping region (70-90 km). The expected seasonal variability in the MLT region (coldest temperatures in the summer, warmest temperatures in the winter [Herron, 2007]) was seen in the 2014-2015 dataset. This was further explored by specifically examining the monthly averages of the mesopause height and temperature, which showed the known behavior of the mesopause being low and cold in the spring and summer and high and warm in the fall and winter [She *et al.*, 1993; von Zahn *et al.*, 1996; Plane *et al.*, 1999; States and Gardner, 2000]. Although, possible effects from a sudden stratospheric warming (SSW) event might have disrupted the normal winter behavior.

These initial comparisons of the new Rayleigh lidar with its predecessor and other techniques provided the basis for conducting a detailed comparison between this system and the collocated sodium (Na) lidar system. This comparison between the Rayleigh and Na lidar techniques was the first of its kind to examine temperatures from the two lidars that were acquired over simultaneous time periods, at the same observational site and covering the same altitude range (~80-110 km). While the overlapping dataset was small (19 nights), it did cover one annual cycle summer 2014-2015.

The comparison showed that the two different lidars' temperatures agreed the most in the 85-95 km region and that there were a few interesting features in the

differences between the two temperature sets. The differences in our two temperature sets were consistent with the differences seen in previous studies which compared climatologies from Rayleigh and Na lidars at different sites with a more limited overlapping altitude range (80-95 km) [*Leblanc et al.*, 1998; *Argall and Sica*, 2007]. These lower altitude differences were relatively small (~ 1.5 K for our study, 2-7 K in the climatological studies) and the Rayleigh lidar temperatures were uniformly colder than the Na temperatures. Our comparison extended above the previous studies in altitude, which gave new comparison results. Above 95 km, in both summer and winter, the differences between the two lidars' temperatures was much larger (~ 13 K) and the sign of the difference changed (compared with the lower altitudes) meaning that the Rayleigh temperatures tended to be warmer than the Na temperatures. Also, at altitudes above 95 km, the Rayleigh lidar temperature profiles showed more distinct and larger amplitude wave structures than the Na profiles. Contrary to the above, a finding that stood out was that the best agreement between the two sets of temperatures, across the whole 80-110 km altitude range, occurred on the dates closest to the fall and spring equinoxes.

Turning to the dataset acquired with the previous version of the USU Rayleigh lidar, which operated between 1993 and 2004, temperature anomalies observed in the midlatitude mesosphere (45-90 km) were shown to be connected to six major SSW events. The major SSW events, which occur when temperatures averaged between 60° and 90° latitude increase, and zonal winds averaged around the 60° latitude line reverse from eastward to westward, were identified using the NASA MERRA reanalysis data. From there, the whole-night averaged Rayleigh temperatures were examined by looking at their time evolution over ± 40 days from the maximum wind reversal date. The general

pattern showed that the temperature ranges near the peak dates resembled the temperature range from a climatological summer night (170-270 K), rather than the expected winter night's temperature range (205-250 K). To identify regions of relative cooling and warming, compared with normal winter temperatures, a winter climatological profile was subtracted from the individual night's averages during each event. These temperature differences showed a vertical pattern of warmings (up to about 40 K) in the upper stratosphere and lower mesosphere (45-65 km) and coolings (down to about -40 K) in the upper mesosphere (65-90 km). Temperature anomalies of these magnitudes had previously been seen in the polar mesosphere and in a few case studies of individual events in the midlatitude mesosphere, but had yet to be shown consistently during every observed SSW event over more than a decade.

Along with presenting observations that further elucidate the current understanding of the global SSW phenomena, this study also gives an example of the types of scientific results that can be mined from long observational data sets, such as the 1993-2004 USU Rayleigh lidar temperature data. This illustrates the significance of developing new and improved ground-based instrumentation capable of acquiring these long-term, near continuous datasets [*Rishbeth et al.*, 1993]. The coupling between the stratosphere and mesosphere presented here also indicates a need for more simultaneous measurements across all the atmospheric regions.

2. Future Work

There are many ways in which to build on the work presented in this dissertation in both instrumentation and scientific study. The results showing the behavior of the

midlatitude mesosphere during SSWs could be extended into the lower thermosphere with more wintertime measurements using the new USU Rayleigh lidar. Previous model studies [*Liu and Roble*, 2002] and observations [*Siskind et al.*, 2005; *Goncharenko and Zhang*, 2008] show that there is a secondary warming in the lower thermosphere during SSW events. Measurements from the USU Rayleigh lidar could be used to explore the equatorward extent of the thermospheric warmings using methods similar to those presented in Chapter 5. The USU climatology used in the midlatitude mesosphere study would have to be replaced by some other baseline dataset, which would act as the normal conditions that the anomalous SSW event behavior would be compared to.

The differences between the Rayleigh and Na lidar temperatures need to be further explored in order to develop a good explanation as to their cause. Making more simultaneous measurements with the two different lidars will help with this. Additionally, increasing the density of simultaneous measurements throughout the annual cycle, will provide more information regarding the observed seasonal variability of the differences between the two sets of temperatures. A thorough review of the assumptions and analyses that each technique uses to calculate temperatures could also shed some light on the cause of the differences. For example, one could experiment with the magnitude of the proportion of atomic oxygen used in the Rayleigh temperature reduction to see if changing composition has an effect on the two lidars' differences. For the large temperature differences above 95 km, one can use data from satellites to add to the comparison. Using temperature data acquired in the lower thermosphere from satellites as the seed temperature for the Rayleigh lidar temperature integral calculation could also reduce the error in the topmost altitudes of the Rayleigh lidar temperatures. The USU

Optical Profiling of the Atmospheric Limb (OPAL) CubeSat, which will be launched in 2017, could be a source for Rayleigh seed temperatures as it will cover the 90-140 km altitude range [Marchant *et al.*, 2014] using O₂ airglow observations. Additionally, the new optimal estimation method (OEM) developed for Rayleigh lidar temperature retrievals by Sica and Haefele [2015] can be applied to the USU Rayleigh lidar data. This analysis technique has the potential to improve the USU MLT temperature dataset by correcting for changing atmospheric composition without relying on model calculations, not requiring a seed temperature at the top of the profile (since the OEM uses an *a priori* temperature profile), and potentially extending the temperature profile higher in altitude.

While this work presented the first successful results from the new high-power, large-aperture Rayleigh, there is still much that can be done to augment the new system as one works toward building a single lidar system capable of simultaneously observing the whole atmosphere. The first step would be to extend the current system's measurements downward in altitude, until the point (about 30 km) where the Rayleigh technique is impeded by Mie scattering off of aerosols. The instrumentation for this next step has already been developed and built by a group of USU students and is currently in the testing phase [Elliott *et al.*, 2016] The student group used the smaller telescope from the previous USU Rayleigh lidar system, and coupled another PMT and MCS unit to the telescope receiver, in conjunction with the current laser transmitters to obtain first light from about 35-80 km. To extend the measurements further downward, two more PMT detectors would have to be added, one to measure the signal from Rayleigh and Mie scatter in the ~15-60 km range and the second to measure Raman scatter from N₂ at 607 nm, which is required for the Klett algorithm [Klett, 1981] that will be used to separate

the Rayleigh and Mie signals in order to obtain temperatures in the region containing aerosols. This last step would transform the current Rayleigh lidar into a Rayleigh-Mie-Raman (RMR) scatter lidar. Another straightforward improvement to the system would be to replace the current PMT receiver (Electron Tubes 9954 with 15% quantum efficiency at 532 nm) with PMT with greater quantum efficiency (e.g., a Hamamatsu H7421-40 PMT, with 40% quantum efficiency at 532 nm). This final step would enable for the temperature measurements to be pushed even further into the lower thermosphere (at least to 120 km).

Other than having extensive altitude coverage, a whole-atmosphere lidar system would enable many sophisticated comparisons and scientific studies. For example, data from the lower altitudes could be compared with data from reanalysis models, which typically do not reach much above 45 km. Thesis work has already begun to make temperature comparisons at 45 km between the previous Rayleigh lidar results and the reanalysis models [*Moser et al.*, 2015]. By having part of the full altitude range overlap with reanalysis models and radiosonde data, the relative density measurements acquired by the RMR lidar could be calibrated with model or observational data to obtain absolute densities from the stratosphere up into the lower thermosphere. This would provide very useful information to both neutral and ionospheric models [e.g., MSISe00 (*Picone et al.*, 2002) and GAIM (*Scherliess et al.*, 2006)] and also the neutral models used for satellite drag calculations in the thermosphere [e.g., JB2008 (*Bowman et al.*, 2008)]. Again, this study has already begun, using reanalysis model data at 45 km to provide an absolute density calibration for the 1993-2004 Rayleigh lidar data throughout the mesosphere [*Barton et al.*, 2015]. Returning to SSW events, measurements from a whole atmosphere

lidar could allow for the temperature anomalies associated with these events to be simultaneously observed in multiple atmospheric regions. To the best of our knowledge, the closest to these types of observations that researchers have gotten has been achieved by splicing together data from various instruments [Alpers *et al.*, 2004] or through correlative studies.

References

- Alpers, M., R. Eixmann, C. Fricke-Begemann, M. Gerding, and J. Höffner (2004) Temperature lidar measurements from 1 to 105 km altitude using resonance, Rayleigh, and rotational Raman scattering, *Atmos. Chem. Phys.*, 4, 793–800, doi:10.5194/acp-4-793-2004.
- Argall, P. S., and R. J. Sica (2007), A comparison of Rayleigh and sodium lidar temperature climatologies, *Ann. Geophys.*, 25, 27–33, doi:10.5194/angeo-25-27-2007.
- Barton, D. L., Wickwar, V. B., Herron, J. P., Sox, L., and Navarro, L. A. (2015), Mesospheric neutral densities derived from Rayleigh lidar observations at Utah State University, *EPJ Web of Conferences*, 119, 13006, doi:<http://dx.doi.org/10.1051/epjconf/201611913006>.
- Bowman, B. R., W. K. Tobiska, F. A. Marcos, C. Y. Huang, C. S. Lin, and W. J. Burke (2008), A new empirical thermospheric density model JB2008 using new solar and geomagnetic indices, paper presented at AIAA/AAS Astrodynamics Specialist Conference, Honolulu, HI, 18 August.
- Elliott, S., B. Ward, B. Lovelady, J. Gardiner, L. Priskos, M. T. Emerick, and V. B. Wickwar (2016), Reestablishing observations throughout the mesosphere with the ALO-USU Rayleigh-scatter lidar, poster presented at Joint CEDAR-GEM Workshop, Santa Fe, NM, 22 June, http://digitalcommons.usu.edu/atmlidar_post/25.
- Goncharenko, L., and S. -R. Zhang (2008), Ionospheric signatures of sudden stratospheric warming: Ion temperature at middle latitude, *Geophys. Res. Lett.*, 35, L21103, doi:10.1029/2008GL035684.
- Hauchecorne, A. and M. -L. Chanin (1980), Density and temperature profiles obtained by lidar between 35 and 70 km. *Geophys. Res. Lett.*, 7: 565–568, doi:10.1029/GL007i008p00565.
- Herron, J. P. (2007), Rayleigh-scatter lidar observations at USU's atmospheric lidar

observatory (Logan, UT) — temperature climatology, temperature comparisons with MSIS, and noctilucent clouds, PhD dissertation, 156 pp., Utah State Univ., Logan, UT, <http://digitalcommons.usu.edu/etd/4686>.

Klett, J. D. (1981), Stable analytical inversion solution for processing lidar returns, *Appl. Opt.*, 20, 211–220, doi:10.1364/AO.20.000211.

Leblanc, T., I. S. McDermid, P. Keckhut, A. Hauchecorne, C. Y. She, and D. A. Krueger (1998), Temperature climatology of the middle atmosphere from long-term lidar measurements at middle and low latitudes, *J. Geophys. Res.*, 103(D14), 17191–17204, doi:10.1029/98JD01347.

Liu, H.-L. and R. G. Roble (2002), A study of a self-generated stratospheric sudden warming and its mesospheric-lower thermospheric impacts using the coupled TIME-GCM/CCM3, *J. Geophys. Res.*, 107(D23), 4695, doi:10.1029/2001JD001533.

Marchant, A., M. Taylor, C. Swenson, and L. Scherliess (2014), Hyperspectral limb scanner for the OPAL mission, paper presented at the 28th Small Satellite Conference, Logan, UT.

Moser, D. K., V. B. Wickwar, L. Navarro, D. Barton, and J. Herron (2015), Comparing Rayleigh lidar and assimilative model temperatures at 45 km, poster presented at CEDAR Workshop, Seattle, WA, 23 Jun.

Picone, J. M., A. E. Hedin, D. P. Drob, and A. C. Aiken (2002), NRLMSISE-00 empirical model of the atmosphere: Statistical comparisons and scientific issues, *J. Geophys. Res.*, 107(A12), 1468, doi:10.1029/2002JA009430.

Plane, J. M. C., C. S. Gardner, J. Yu, C. Y. She, R. R. Garcia, and H. C. Pumphrey (1999), Mesospheric Na layer at 40°N: Modeling and observations, *J. Geophys. Res.*, 104(D3), 3773–3788, doi:10.1029/1998JD100015.

Rishbeth, H., D. M. Willis, and A. Hewish (1993), Long-term solar terrestrial monitoring, *Eos Trans. AGU*, 74, 313–320.

Scherliess, L., R. W. Schunk, J. J. Sojka, D. C. Thompson, and L. Zhu (2006), Utah State University global assimilation of ionospheric measurements gauss-markov kalman filter model of the ionosphere: model description and validation, *J. Geophys. Res.*, 111, A11315, doi:10.1029/2006JA011712.

She, C. Y., J. R. Yu, and H. Chen (1993), Observed thermal structure of the midlatitude mesopause, *Geophys. Res. Lett.*, 20, 567–570, doi: 10.1029/93GL00808.

Sica R. J., and A. Haeferle (2015), Retrieval of temperature from a multiple-channel Rayleigh-scatter lidar using an optimal estimation method, *Appl. Opt.*, 54, 1872–1889,

doi: 10.1364/AO.54.001872.

Siskind, D. E., L. Coy, and P. Espy (2005), Observations of stratospheric warmings and mesospheric coolings by the TIMED SABER instrument, *Geophys. Res. Lett.*, *32*, L09804, doi:10.1029/2005GL022399.

States, R. J., and C. S. Gardner (2000), Temperature structure of the mesopause region (80–105 km) at 40°N latitude, 1, Seasonal variations, *J. Atmos. Sci.*, *57*, 66–77, doi:10.1175/1520-0469(2000)057<0066:TSOTMR>2.0.CO;2.

von Zahn, U., J. Hoffner, V. Eska, and M. Alpers (1996), The mesopause altitude: Only two distinct levels worldwide?, *Geophys. Res. Lett.*, *23*, 3231–3234, doi: 10.1029/96GL03041.

APPENDICES

APPENDIX A

USU RAYLEIGH LIDAR OPERATIONAL AND DATA ANALYSIS CODE

A. 1. Lidar Arduino Timing Program

The following code controls the timing of the lidar system when it is in its night time operational mode. This software runs the Arduino Duemilanove microcontroller board.

```
// USU RMR Lidar "Green Beam" Timing Control Program
// Version PROTOTYPE 2.2 Oct 29 2012
// Written by Matthew Emerick 2012
// Last edited by 29OCT2012

// Connections:
// CHOP ARD2
// FL6 ARD3
// FL5 ARD4
// QS6 ARD5
// QS5 ARD6
// PMT1 ARD7

volatile int count = 0;
void setup(){
  DDRD = 0b11111000;      //PINS 3,4,5,6,7 OUTPUTS
}
void loop(){
  attachInterrupt(0, counter, RISING);
  if(count == 7)
  {
    noInterrupts();        //CRITICAL TIMING BEGINS
    delayMicroseconds(1950); //FL SYNC
    PORTD = 0b00011000;    //FL6+FL5 HI
    delayMicroseconds(25);  //FL LENGTH
    PORTD = 0b00000000;    //FL6+FL5 LO
    delayMicroseconds(243); //QS STD DELAY
    PORTD = 0b01000000;    //QS5 HI
    PORTD = 0b01100000;    //QS5 HI
    delayMicroseconds(25);  //QS LENGTH
    PORTD = 0b00000000;    //QS6+QS5+MCS LO
    //delayMicroseconds(350); //PMT DELAY
    //PORTD = 0b10000000;    //PMT1 HI
    interrupts();          //CRITICAL TIMING ENDS
    //delayMicroseconds(3000); //PMT1 LENGTH
    //PORTD = 0b00000000;    //PMT1 LO
    count=count-7;
  }
}
```

```

}
void counter(){
    count = count + 1;
}

```

A. 2. Multi-Channel Scalar Job File

The following code gives an example of a job file that runs the Ortec Turbo Multi-channel scalar (MCS) unit in the lidar's night time operational mode. The job file controls the continuous recording of the lidar's 2-minute raw data (photocount) profiles throughout the night. A job file is created for each night and records the raw data files in a folder titled with the night's date in Universal Time (UTC) in YYMMDD format. Both .mcs binary and ASCII file types are recorded for each 2-minute profile. The code below is taken from the night of September 12, 2014.

```

SET_MCS 1
ENABLE_DISCRIMINATOR
SET_DISCRIMINATOR_EDGE 1
SET_DISCRIMINATOR -0.0708
SET_TRIGGER 1
SET_MODE_ACQUIRE 0
SET_DWELL_TIME 250E-9
SET_PASS_LENGTH 14000
SET_PRESET_PASS 3600
CLEAR
START
LOOP 900
    WAIT
    FILL_BUFFER
    SET_MCS 1
    CLEAR
    START
    SET_MCS 0
    DESCRIBE_SAMPLE "Rayleigh EMI9954 PMT -1950V DISC= -71mV sample #???"
    DESCRIBE_HARDWARE "Text for Hardware Description Rayleigh2"
    SAVE "c:\MCS Data\20140912\20140912 Rayleigh Data???.MCS"
    EXPORT "c:\MCS Data\20140912\20140912(High Altitude) Rayleigh Data???.Asc"
    SET_MCS 1

```

END_LOOP

A. 3. Optical Fiber Steering and Search Labview Programs

Labview virtual instrument (VI) programs were written by Ryan Martineau to control the Thorlabs Z625B motorized actuators (2 actuators for each of the 4 fibers, thus 8 total) that align the optical fibers at each prime focus of each of the four telescope mirrors.

The MultiMirror.vi program is used to manually steer each of the Thorlabs actuators (Figure A.1). The Search Pattern.vi (Figure A.2) program conducts a spiral search around a specified center point with specified step sizes (maximum 4 mm in any

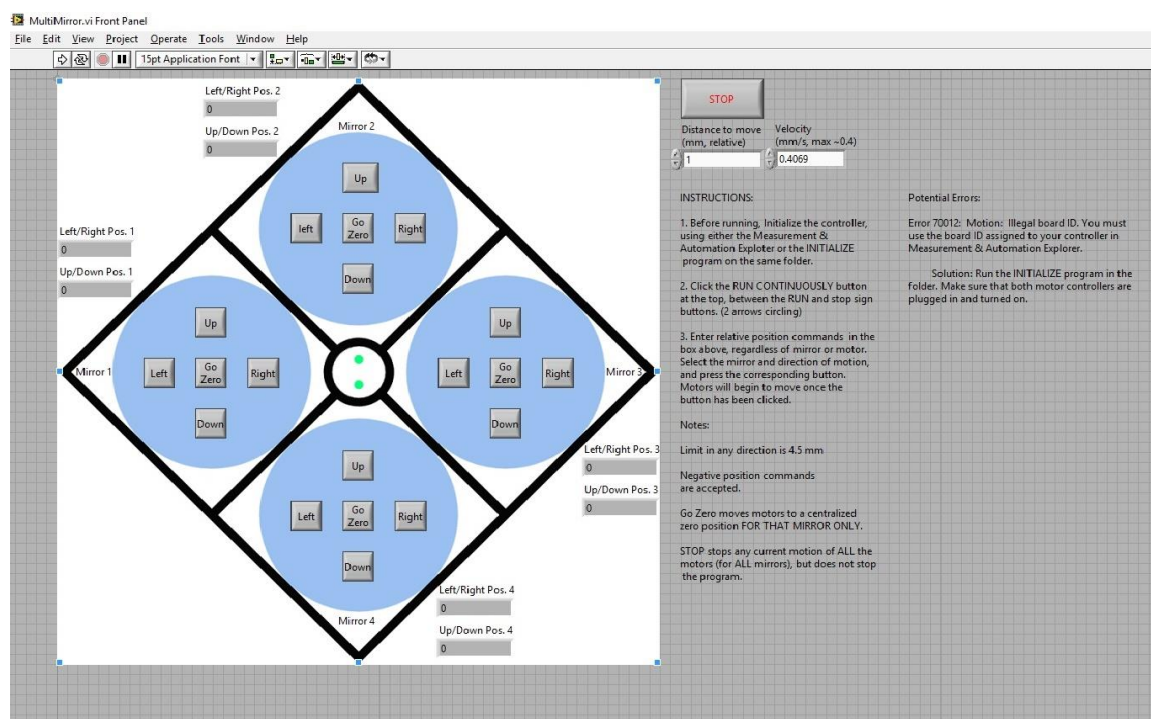


Figure A.1. Screenshot of the MultiMirror.vi fiber positioning program written in Labview. Step size (in mm) and velocity (in mm/s) specified on the right. Each of the four fibers can be steered in four different directions with a maximum of 4 mm in each direction.

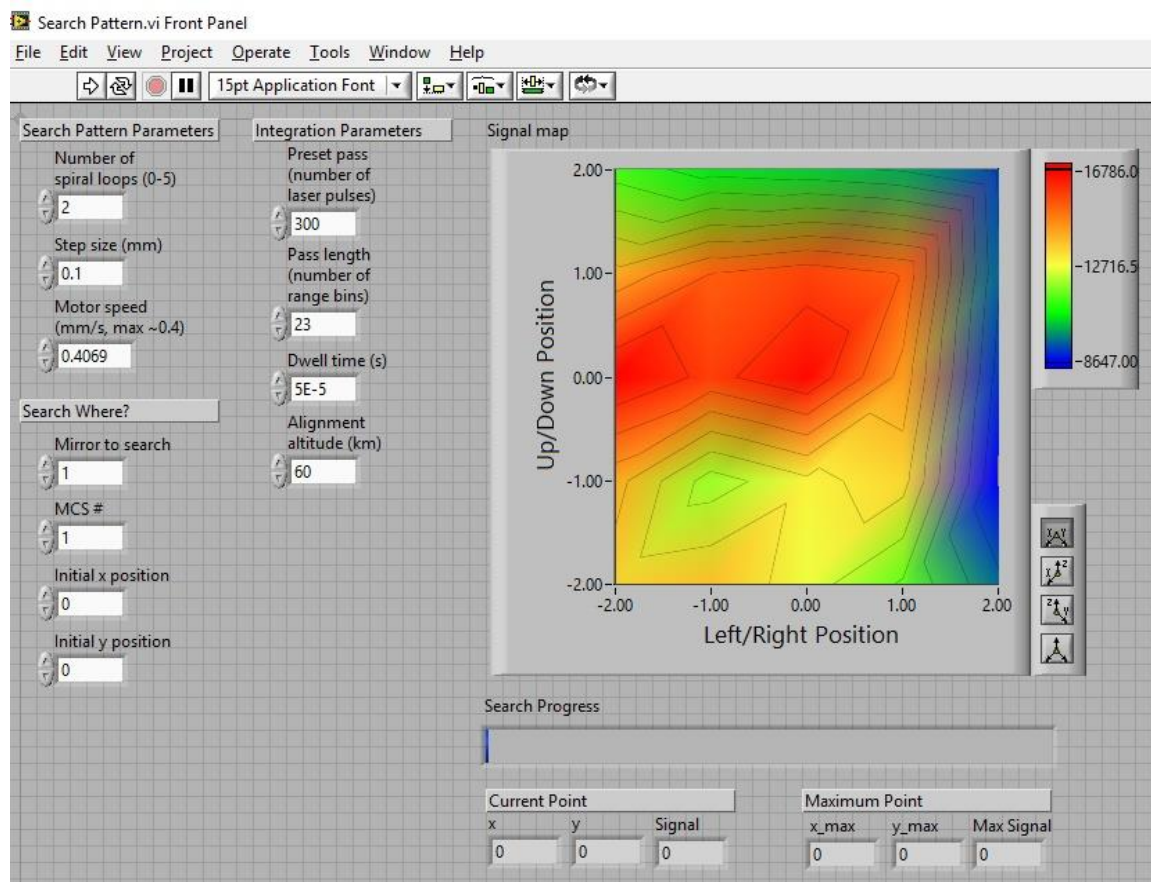


Figure A.2. Screenshot of the Search Pattern.vi fiber alignment search pattern program written in Labview. Parameters to set are shown on the left with the contour plot window on the right, which shows the position that gives the maximum count rate at the end of the search (in red). Below the contour plot, the count rates at each step are given as the search progresses.

direction) at a specified alignment altitude (usually 60 km). Once the optimal alignment position is found it is recorded and each night, the fibers are sent to a mechanically defined zero position. Then, at the beginning of each night, the fibers are steered back to the optimal position using MultiMirror.vi. Realignment using Search Pattern.vi is conducted whenever the system is suspected to be out of alignment (i.e. low signal, seasonal change, significant time lapses between lidar runs, etc.).

A.4. Temperature Reduction Program in Interactive Data Language

The USU Rayleigh lidar temperature reduction was written in the Interactive Data Language (IDL) programming language. The main program 'newreduction.pro' calls several subroutines which calculate gravity ('gravity.pro') and mean molecular mass vectors ('mmmvector.pro'), with respect to altitude. Other subroutines calculate the statistics, which determine the measurement uncertainty and maximum altitude for each night ('signal.pro'), convert the average photon counts to density ('newdensity.pro') and then finally calculate the temperature and temperature error bars ('temperature.pro').

A.4.1. Newreduction.pro

PRO NEWReduction

;Created by Leda Sox, April 2014

;Define constants

MMM = 28.951 ;28.9415 ;AVERAGE MEAN MOLECULAR MASS

RRR = 8.31432 ;IDEAL GAS CONSTANT

GEOLAT = 41.74 ;LATITUDE OF THE SYSTEM

GEOLONG = -111.81 ;LONGITUDE OF THE SYSTEM

fitbin = 1826 ;bin number corresponding to 70 km

LENGTH = 14000 ;total number of altitude bins for the arrays

ALTRES = 0.0375 ;height in km of one range bin

ALTPROF = FINDGEN(LENGTH)*ALTRES+1.466+(ALTRES/2.0) ;altitude profile (in km)

 ;starting at height of the observatory = 1.466 km

RANGE = FINDGEN(LENGTH)*ALTRES+(ALTRES/2.0) ;range profile in km

BKHI = 9000 ;upper bin number for the background calculation

BKLO = 5000 ;lower bin number for the background calculation

;Date in YYMMDD format to find file directory for a night's data

date = " ;set 'date' to be a string

print,'Date in YYMMDD format?'

read,date

dayofyear,date,doy,strdoy ;run dayofyear program to get 3-digit day of year,DOY

year = strmid(date,0,2) ;decatenate the 2 year digits from 'date'

month = strmid(date,2,2) ;decatenate the 2 month digits from 'date'

```

day = strmid(date,4,2) ;decatenate the 2 day digits from 'date'
timestring = '20'+year+month+day ;put date in YYYYMMDD format
print,timestring

;Give option to manually input T_i value, rather than take from MSIS
naanswer = 'N'
;print,'Manually input T_i (y/n)?'
;read,naanswer

;Date in YYDDD format to give as an input to runnrlmsise00.pro
YYDDD = long(strcompress(year+strdoy,/remove_all))
print,'YYDDD= ',yyddd

;Give year the full four digits
if (year ge '93') then begin
    lonyear = long(strcompress('19'+year,/remove_all))
endif else begin
    lonyear = long(strcompress('20'+year,/remove_all))
endelse

;calculate the mean molecular mass array and effective cross section array
mvector,yyddd,mvector,EffCrossSection

;Calculate average signal profile and measurement error w/ boxcar smoothing

Signal,TIMESTRING,FITBIN,ALTPROF,DATA,AVGSIGNAL,TOPBIN,H_i,bkhi,bklo
,sigma,$
    signaltosigma,hannsignal,AVGBACK

;Calculate average signal profile and measurement error w/ Hamming smoothing
hammSignal,TIMESTRING,FITBIN,ALTPROF,DATA,hammAVGSIGNAL,hammSIG
MA,$
    hammsignaltoSIGMA,hammTOPBIN,hammH_i,bkhi,bklo,HAMMAVGBACK

;Calculate average signal profile and measurement error w/ Hanning smoothing
hanningSignal,TIMESTRING,FITBIN,ALTPROF,DATA,hannAVGSIGNAL,hannSIGM
A,$
    hannsignaltoSIGMA,hannTOPBIN,hannH_i,bkhi,bklo,HANNAVGBACK

;'Y' if you want the option to manually change the topbin
topchange = 'n'
if topchange eq 'y' or 'Y' then begin
    print,'New topbin? '

```

```

read,topbin
h_i = altprof(topbin)
endif

;Print some values for night-to-night comparison
PRINT,'Bckgnd subtracted signal at 60 km = ',AVGSIGNAL[1560]
PRINT,'Bckgnd subtracted signal at 70 km = ',AVGSIGNAL[1826]
PRINT,'TOPBIN= ',TOPBIN
print,'boxcar H_i (km)= ',H_i
print, ' Hamming H_i= ',hammh_i
print, ' Hanning H_i= ',hannh_i
signalmax = max(avgsignal)
PRINT
dataprof = data[1,*]
datamax = max(dataprof)
print,'max photocount of one profile= ',datamax
print,'photocount at 70km = ', hammapvgsignal(1832)
lowavg = total(avgsignal[0:493])/(494)
print, 'Avg signal from 0 to 20 km = ',lowavg

;Find linear fit to the signal-to-sigma profile to flag for data quality
ENDBIN = 10500
STARTBIN = TOPBIN+200
linfit = linfit(altprof[topBIN:ENDBIN],signaltosigma[topBIN:ENDBIN],yfit=fit)
LAST = ENDBIN-topBIN
SLOPE = (FIT(LAST)-FIT(0))/(ALTPROF(LAST)-ALTPROF(0))
if (slope LT -0.02) or (slope GT 0.02) THEN BEGIN
  SigQual = 'BAD'
  print, 'Signal Quality = ',SigQual
  print, 'Slope from H_i to 395 km = ',Slope
endif else begin
  SigQual = 'GOOD'
  print, 'Signal Quality = ',SigQual
  print, 'Slope from H_i to 395 km = ',slope
endelse

;Calculate signal-to-noise ratio compare with signal-to-sigma ratio
SNR,TIMESTRING,FITBIN,ALTPROF,smoothdata,background,SNR_TOPBIN,SNR_H
_i,bkhi,$
  bklo,SNRTEST
;print, '16 Standard Deviation Method H_i = ',h_i
;print, 'SNR Less than 2.0 Method H_i = ',SNR_h_i

;Calculate density with boxcar signal

```

```

NEWDENSITY,LENGTH,EffCrossSection,ALTRES,FITBIN,AVGSIGNAL,DENSITY,
$
    crossdensity
;Calculate density with hamming signal

NEWDENSITY,LENGTH,EffCrossSection,ALTRES,FITBIN,hammavgSIGNAL,hamm
DENSITY,$
    hammcrossdensity
;Calculate density with hanning signal

NEWDENSITY,LENGTH,EffCrossSection,ALTRES,FITBIN,hannavgSIGNAL,hannDE
NSITY,$
    hanncrossdensity
;Calculate linear fit to density
linfitdensity = linfit(altprof[bklo:bkhi],density[bklo:bkhi],yfit=fit)

;Create MSISe00 temperature profile for plotting comparison
MSIS_t=fltarr(length)
for i=0,length-1 do begin
    runnrlmsise00,YYDDD,altprof[i],GEOLAT,GEOLONG,D,T,IYD
    MSIS_t[i]=t(0)
endfor

;Select MSISe00 temperature for seed temperatures
T_I  = MSIS_T[TOPBIN]
hammT_I = MSIS_T[hammTOPBIN]
hannT_I = MSIS_T[hannTOPBIN]
PRINT,'T_i = ',string(t_i)+' K'

;If manual T_i is selected it is read-in here
if (naanswer eq 'y') or (naanswer eq 'Y') then begin
    print, 'What is the temperature at ', hannh_i, ' ?'
    read,hannT_i
endif

;Calculate gravity profile
GRAVITY, GEOLAT, GEOLONG, LENGTH, ALTRES, GNEW

;Calculate temperature and errors for boxcar signal
NEWTEMPERATURE,mmm,rrr,altres,length,altprof,sigma,fitbin,topbin,t_i,gnew,$
    density,TEMPERATURE,TEMPERR,tempa,tempb
;Calculate temperature and errors for hamming signal
NEWTEMPERATURE,mmm,rrr,altres,length,altprof,hammsigma,fitbin,hammtopbin,$
    hammt_i,gnew,hammdensity,hammTEMPERATURE,hammTEMPERR,$

```

```

        hammtempa,hammtempb
;Calculate temperature and errors for hanning signal
NEWTEMPERATURE,mmm,rrr,altres,length,altprof,hannsigma,fitbin,hanntopbin,$
        hannt_i,gnew,hanndensity,hannTEMPERATURE,hannTEMPERR,$
        hanntempa,hanntempb
;Calculate temperature and errors for boxcar signal and changing MMM
mmmtemperature,mvector,rrr,altres,length,altprof,fitbin,topbin,t_i,gnew,$
        crossdensity,SIGMA,MMMTEMP,MMMTEMPERR
;Calculate temperature and errors for hamming signal and changing MMM
mmmtemperature,mvector,rrr,altres,length,altprof,fitbin,hammtopbin,HAMMt_i,$

gnew,hammcrossdensity,hammsigma,hammMMMTEMP,hammMMMTEMPERR
;Calculate temperature and errors for hanning signal and changing MMM
mmmtemperature,mvector,rrr,altres,length,altprof,fitbin,hanntopbin,HANnt_i,$
        gnew,hanncrossdensity,hannsigma,hannMMMTEMP,hannMMMTEMPERR

;Calculate the difference between MSIS T_i profile and T_i+20 profile
hammtemp_20 = hammtemperature-hammtempb
;Calculate differences between constant and changing MMM temperatures
temp_diff   = temperature-mmmtemp
hammtemp_diff = hammtemperature-hammmmmtemp

;Print max and min boxcar temperature
maxtemp = max(temperature,/nan)
mintemp = min(temperature,/nan)
print,'Tmax = ',max(temperature,i,/nan)
print,'at ',altprof(i)
print,'Error bar at H_i = ',temperr(topbin-1)

;Print the max value from hamming temperatures
print,'Max Hamming temperature = ', max(hammtemperature,maxindex,/nan),$
        ' at ',altprof(maxindex)
print,maxindex

;Print the max and min of the constant and changing MMM temperature diffs
print,'T_diffmax = ',max(temp_diff,i,/nan), 'at ',altprof(i)
print,'T_diffmin = ',min(temp_diff,i,/nan), 'at ',altprof(i)

;Calculate temperature profiles minus and plus temperature errors
temperr_plus = dblarr(length)
temperr_minus = dblarr(length)
temperr_plus = temperature+temperr
temperr_minus = temperature-temperr

;Print different temperature values throughout the temp. profile

```

```

answer = 'n'
if (answer 'y') then begin
  print,'T at 115 km ', temperature(3027)
  print,'T at 105 km ', temperature(2760)
  print,'T at 95 km ', temperature(2494)
  print,'T at 85 km ', temperature(2227)
endif

;Create string values of h_i and t_i
H = strcompress(string(h_i),/remove_all)
T = strcompress(string(t_i),/remove_all)

DOY      = STRDOY
TOPTEMP  = T_i
hammTOPTEMP = hammT_i
hannTOPTEMP = hannT_i
Hdiff    = Hanntemperature-hammtemperature
;difference between hamming and hanning smoothed temperatures

;Save data in .dat files-----
if (naanswer EQ 'y') OR (NAANSWER EQ 'Y') then begin
  save,SigQual,slope,DOY,ALTPROF,BKHI,BKLO,fitbin,DATA,MSIS_T,$

  AVGSIGNAL,SIGNALTOSIGMA,TOPTEMP,DENSITY,TEMPERATURE,T
  EMPERR,$
  MMMTEMP,MMMTEMPERR,$

  hammAVGSIGNAL,hammSIGNALTOSIGMA,hammTOPTEMP,hamm
  DENSITY,$

  hammTEMPERATURE,hammTEMPERR,hammMMMTEMP,hammMMMTEMPERR,
  $

  hannAVGSIGNAL,hannSIGNALTOSIGMA,hannTOPTEMP,hannDENSIT
  Y,$
  hannTEMPERATURE,hannTEMPERR,hannMMMTEMP,hannMMMTEMPERR,$
  filename='c:\Users\Leda\IDLWorkspace83\Default\NewData\'+'timestring+$
  \''+date+'nahmax.DAT'
endif else begin
  save,SigQual,slope,DOY,ALTPROF,BKHI,BKLO,fitbin,DATA,MSIS_T,$

  AVGSIGNAL,SIGNALTOSIGMA,TOPTEMP,DENSITY,TEMPERATURE,T
  EMPERR,$
  MMMTEMP,MMMTEMPERR,$

```

```

hammAVGSIGNAL,hammSIGNALTOSIGMA,hammTOPBIN,hammTOPTEMP,hamm
DENSITY,$

```

```

hammTEMPERATURE,hammTEMPERR,hammMMMTEMP,hammMMMTEMPERR,
$

```

```

hannAVGSIGNAL,hannSIGNALTOSIGMA,hannTOPBIN,hannTOPTEMP,hannDENSI
TY,$

```

```

hannTEMPERATURE,hannTEMPERR,hannMMMTEMP,hannMMMTEMPERR,$ratur
e,$

```

```

    hammtemperror,hammMMMtemp,hammMMMTEMPERR,msis_t,$
    filename='c:\Users\Leda\IDLWorkspace83\Default\NewData\'+'timestring+$
    \'+'date+'.DAT'
endelse

```

```

;Save temperatures in text file-----
writecol,timestring+'temperatureavg.txt',altprof,temperature,temperr

```

```

;Begin plotting-----
plotanswer = 3

```

```

props = { xrange:[150,400],yrange:[altprof(fitbin),115],$
          xtitle:'Temperature (K)',ytitle:'Altitude (km)',thick:2,$
          FONT_SIZE:16, font_style:'bold',ythick:3,xthick:3,$
          FONT_NAME:'Helvetica',XTICKINTERVAL:50}

```

```

;Create a profiles of ones and zeros with length=length
ones = fltarr(length)+1
zeros = fltarr(length)+0

```

```

;-----
;Plot average signal profile
;-----

```

```

p1 = plot(altprof,avgsignal,$
          title=date+' Average Background-Subtracted Signal',$
          ytitle='Photon Counts',xtitle='Altitude (km)',xrange=[0,550],$
          yrange=[-50,signalmax+5],thick=2)
p2 = plot(altprof,zeros,/overplot,thick=2,color='red')

```

```

;-----
;Temperature Plots with and without changing MMM

```



```

;-----
if (plotanswer eq 0) then begin
  W = WINDOW(DIMENSION=[800,700],$
    title=' Average Temperature for '+TIMESTRING, FONT_SIZE=18,$
    font_style='bold')
  P1 = plot(HAMMTEMPERATURE[fitbin:topbin],ALTPROF[fitbin:topbin],$
    color='RED',_extra=props,/CURRENT,POSITION=[.1,.1,.65,.9])
;Plot error bars
  FOR i=fitbin,topbin-1,40 DO BEGIN
    Pe = errorplot(hammtemperature[i:i],altprof[i:i],hammtemperror[i:i],$
      zeros[i:i],overplot=1,thick=2)
    Pe.thick=3
    Pe.errorbar_capsize=0.2
    Pe.errorbar_color='red'
  ENDFOR

  p2 = plot(HAMMMMMtemp[fitbin:hammtopbin],ALTPROF[fitbin:hammtopbin],$
    color='blue',/overplot,THICK=2)
  P1.NAME = 'Uncorrected T'
  P2.NAME = 'Corrected T'
  legend=legend(target=[P1,p2],position=[280,86],/data,font_style='bold',$
    font_size=14)

  P3 = plot(HAMMTEMP_diff[fitbin:hammtopbin],ALTPROF[fitbin:hammtopbin],$
    yrange=[altprof(fitbin),115],xrange=[-2,2],color='red',$
    xtitle='Delta_T (K)',THICK=2,xminor=1,$
    ytitle='Altitude (km)',FONT_SIZE=16, font_style='bold',$
    ythick=3,xthick=3,FONT_NAME='Helvetica',/CURRENT,$
    POSITION=[.7,.1,.95,.9])
  ax = P3.AXES
  ax[1].showtext = 0

  p4 = plot(zeros[fitbin:hammtopbin],ALTPROF[fitbin:hammtopbin],$
    color='black', overplot=1,thick=2)
endif
writecol,'tempmatch.txt',altprof,hammtemperature,hammmmmtemp,hammtemp_diff

;-----
;Temperature Plots with +or- 20 K seed temp
;-----

if (plotanswer eq 1) then begin
  P1 = plot(hammTEMPERATURE[fitbin:hammtopbin-1],$
    ALTPROF[fitbin:hammtopbin-1],color='BLACK',$

```

```

        title='Average Temperature for '+TIMESTRING,_extra=props)
p2 = plot(hammtempa[fitbin:hammtopbin-1],altprof[fitbin:hammtopbin-1],$
        /overplot,color = 'red',linestyle=2,thick=2)
p3 = plot(hammtempb[fitbin:hammtopbin-1],altprof[fitbin:hammtopbin-1],$
        /overplot,color = 'red',linestyle=2,thick=2)

p1.name = 'MSISe00 T_hmax'
p2.name = '+-20 K T_hmax'
L1      = legend(target=[P1,p2],position=[285,85],/data,font_style='bold')

p4 = plot(hammtemp_20[fitbin:hammtopbin-1],ALTPROF[fitbin:hammtopbin-1])
p5 = plot(ones,altprof,color='red',linestyle=2,/overplot,yrange=[70,115])
ENDIF

;-----
;Temperature Plots with mmmtemp/msis and Error bars
;-----

if (plotanswer eq 2) then begin
W = WINDOW(DIMENSION=[900,900]);title='Night of '+month+'/' +day+'/' +YEAR,
P1 = plot(TEMPERATURE[fitbin:topbin-1],ALTPROF[fitbin:topbin-1],$
        xrange=[150,300],yrange=[altprof(fitbin),115],color='red',$
        title='Average Temperature for '+TIMESTRING,$
        xtitle='Temperature (K)',ytitle='Altitude (km)',thick=2,$
        FONT_SIZE=16,font_style='bold',XTICKINTERVAL=50,/CURRENT,$
        POSITION=[.1,.1,.65,.9])
p2 = plot(mmmtemp[fitbin:topbin],altprof[fitbin:topbin],/overplot,$
        color = 'blue',thick=2,/current)
FOR i=fitbin,topbin-1,40 DO BEGIN
P3 = errorplot(temperature[i:i],altprof[i:i],temperror[i:i],zeros[i:i],$
        overplot=1,thick=2)
        ;This will plot an error bar on each data point.
P3.thick=3
P3.errorbar_capsize=0.2
P3.errorbar_color='black'
ENDFOR
p4 = plot(temp_diff[fitbin:topbin-1],altprof[fitbin:topbin-1],/CURRENT,$
        POSITION=[.7,.1,.95,.9],title='Temperature Difference',$
        xtitle='$\Delta$ T (K)',xrange=[-2,2],$
        yrange=[altprof(fitbin),115],thick=2,FONT_SIZE=16,$
        font_style='bold',XTICKINTERVAL=1)
p5 = plot(zeros[fitbin:topbin-1],altprof[fitbin:topbin-1],/CURRENT,$
        /overplot,color='red',thick=2)
ax = p4.AXES
ax[1].showtext = 0

```

```

endif

;-----
;Temperature Plots with boxcar smoothed signal, HAMMING and HANNING smoothed
;signal
;-----

if (plotanswer eq 3) then begin
  W = WINDOW(DIMENSION=[800,700],$
    title=' Average Temperature for '+TIMESTRING, FONT_SIZE=18,$
    font_style='bold')
  P1 = plot(TEMPERATURE[fitbin:topbin-1],ALTPROF[fitbin:topbin-1],$
    color='black',thick=2,_extra=props,/CURRENT,POSITION=[.1,.1,.65,.9])
  p2 = plot(hammTEMPERATURE[fitbin:hammtopbin-
1],ALTPROF[fitbin:hammtopbin-1],$
    /overplot,thick=2,color = 'RED')
  p3 = plot(haNNTEMPERATURE[fitbin:hammtopbin-1],ALTPROF[fitbin:hammtopbin-
1],$
    /overplot,thick=2,color = 'BLUE')
  FOR i=fitbin,hammtopbin-1,40 DO BEGIN
    P4 = errorplot(haNNtemperature[i:i],altprof[i:i],haNNtemperr[i:i],$
      zeros[i:i],overplot=1,thick=2)
    P4.thick=3
    P4.errorbar_capsize=0.2
    P4.errorbar_color='BLUE'
  ENDFOR

  p1.name = 'Boxcar smooth'
  p2.name = 'Hamming smooth'
  p3.name = 'Hanning smooth'
  L1 = legend(target=[P1,p2,p3],position=[285,85],/data)
endif

p5 = plot(Hdiff[fitbin:hammtopbin],ALTPROF[fitbin:hammtopbin],$
  yrange=[altprof(fitbin),115],xrange=[-20,20],color='red',$
  xtitle='Delta_T (K)',THICK=2,xminor=1,$
  ytitle='Altitude (km)',FONT_SIZE=16, font_style='bold',$
  ythick=3,xthick=3,FONT_NAME='Helvetica',/CURRENT,$
  POSITION=[.7,.1,.95,.9])
ax = P5.AXES
ax[1].showtext = 0
p6 = plot(zeros[fitbin:hammtopbin],ALTPROF[fitbin:hammtopbin],color='black',$
  overplot=1,thick=2)

;-----
; Boxcar smoothed Temperature plots with error bars

```

```

;-----
if (plotanswer eq 5) then begin
  P1 = plot(TEMPERATURE[fitbin:topbin-1],ALTPROF[fitbin:topbin-1],$
    xrange=[150,300],yrange=[altprof(fitbin),115],color='red',$
    title='Average Temperature for '+TIMESTRING,$
    xtitle='Temperature (K)',ytitle='Altitude (km)',thick=2,$
    FONT_SIZE=16,font_style='bold',XTICKINTERVAL=50)
  FOR i=fitbin,topbin-1,40 DO BEGIN
    P3 = errorplot(temperature[i:i],altprof[i:i],temperror[i:i],zeros[i:i],$
      overplot=1,thick=2)
    P3.thick=3
    P3.errorbar_capsize=0.2
    P3.errorbar_color='black'
  ENDFOR
endif

;-----
;Temperature Plots with HAMMING smoothed signal, changing MMM and error bars
;-----
STRHAMMT_I = STRING(HAMMT_I)
STRHAMMH_I = STRING(ALTPROF(HAMMTOPBIN))

if (plotanswer eq 6) then begin
  P1 = plot(hammMMMtemp[fitbin:topbin-1],ALTPROF[fitbin:topbin-1],$
    color='black',title='Average Temperature for '+timestring,$
    thick=2,_extra=props)
  FOR i = hammtopbin-1,fitbin,-40 DO BEGIN
    P2 = errorplot(hammMMMtemp[i:i],altprof[i:i],hammtemperror[i:i],$
      zeros[i:i],overplot=1,thick=2)
    P2.thick=3
    P2.errorbar_capsize=0.2
    P2.errorbar_color='BLACK'
  ENDFOR
  t1 = TEXT(230,83,'H_i ='+strhammh_i+' km',FONT_SIZE=14,$
    FONT_NAME='Helvetica',/data)
  t2 = TEXT(231,80,'T_i ='+strhammt_i+' K',FONT_SIZE=14,$
    FONT_NAME='Helvetica',/data)
  coords = [[225, 78],[290, 78], [290,87], [225, 87]]
  SQUARE = POLYGON(coords, TARGET=mglobe, /DATA,
    FILL_BACKGROUND=0,$
    COLOR='BLACK', THICK=2)
endif

;-----

```

```

;Plots temperatures using Hanning vs Hamming smoothed signal
;-----
if (plotanswer eq 7) then begin

P1 = plot(HAMMMMMtemp[fitbin:hammtopbin],ALTPROF[fitbin:hammtopbin],$
  color='RED',_extra=props,title='Average Temperature for '+TIMESTRING)
;Plot error bars
FOR i=fitbin,topbin-1,40 DO BEGIN
  Pe = errorplot(hammmmmtemp[i:i],altprof[i:i],hammmmmTEMPERR[i:i],$
    zeros[i:i],overplot=1,thick=2)
  Pe.thick=3
  Pe.errorbar_capsize=0.2
  Pe.errorbar_color='red'
ENDFOR

p2 =
plot(HAnnMMMtemp[fitbin:hanntopbin],ALTPROF[fitbin:hanntopbin],color='blue',$
  /overplot,THICK=2)
P1.NAME = 'Hamming'
P2.NAME = 'Hanning'
legend=legend(target=[P1,p2],position=[280,86],/data,font_style='bold',$
  font_size=14)
endif
;-----
;END PLOTTING
;-----

END

```

A.4.2. Mvector.pro

PRO mvector,YYDDD,mvector,EffCrossSection

;Created by Leda Sox, 2015

```

GEOLAT      = 41.74 ;LATITUDE OF THE SYSTEM
GEOLONG     = -111.81 ;LONGITUDE OF THE SYSTEM
altres      = 0.0375
length      = 14000
altprof     = FINDGEN(length)*ALTRES+1.466+(ALTRES/2.0)
MVECTOR     = FLTARR(LENGTH)
EffCrossSection = FLTARR(LENGTH)

density     = fltarr(length)

```

```

He      = fltarr(length)
O       = fltarr(length)
N2      = fltarr(length)
O2      = fltarr(length)
Ar      = fltarr(length)
rho     = fltarr(length)
H       = fltarr(length)
N       = fltarr(length)
Oanom   = fltarr(length)
Tn      = fltarr(length)
temperature = fltarr(length)
tempdiff = fltarr(length)

```

```

for i=0,length-1 do begin
  runnrlmsise00,yyddd,altprof[i],GEOLAT,GEOLONG,D,T
  He[i] = d(0)
  O[i]  = d(1)
  N2[i] = d(2)
  O2[i] = d(3)
  Ar[i] = d(4)
  rho[i] = d(5)
  H[i]  = d(6)
  N[i]  = d(7)
  Oanom[i] = d(8)
  Tn[i] = t(0)
endfor

```

```

density = N2+O2+Ar+O

```

```

;Create a mmm vector
hed = fltarr(length)
Od  = fltarr(length)
N2d = fltarr(length)
O2d = fltarr(length)
Ard = fltarr(length)
Hd  = fltarr(length)
Nd  = fltarr(length)
oanomd = fltarr(length)

```

```

for bin=0,length-1 do begin
  hed(bin) = he(BIN)/density(BIN)
  Od(bin)  = o(BIN)/density(BIN)
  N2d(bin) = N2(BIN)/density(BIN)
  O2d(bin) = O2(BIN)/density(BIN)
  Ard(bin) = Ar(BIN)/density(BIN)

```

```

Hd(bin)  = H(BIN)/density(BIN)
Nd(bin)  = N(BIN)/density(BIN)
oanomd(bin) = Oanom(BIN)/density(BIN)
endfor

mVECTOR = (Od*15.999)+(N2d*(14.007*2))+(O2d*(15.999*2))+(Ard*39.948)
          ;+(Hd*1.008)+(Nd*14.007)+(OanomD*15.999)+(hed*4.003)

EffCrossSection = ((6.29E-32)*N2+(5.20E-32)*O2+(5.62E-32)*Ar+(1.1E-
32)*O)/density

END

```

A.4.3. Signal.pro

```

PRO
Signal,TIMESTRING,FITBIN,ALTPROF,DATA,AVGSIGNAL,TOPBIN,HMAX,bkhi,
bklo,$
    sigma,sigaltosigma,hannsignal,AVGBACKGROUND

;Created by Leda Sox April 2014

; print,'Background Threshold (in photon counts):'
; read,backthresh
backthresh=100
BKHI = 9000
BKLO = 5000
THRESHOLD = 1/16. ;1.0/16.0 ;Sigma-to-signal ratio
AVGBINS = 81.0 ;NUMBER OF RANGE BINS TO AVERAGE OVER (josh's value
was 81.0)

cd = 'c:\Users\Leda\IDLWorkspace83\Default\NewData\' + timestring
cd,cd
restore,timestring+'data.sav'

Year = strmid(timestring,0,4)
month = strmid(timestring,4,2)
day = strmid(timestring,6,2)

width = (size(data))(1)
length = (size(data))(2)
print,'Number of 2 mins= ',width

```

```

;For low-altitude Rayleigh system-----
for i=0,width-1 do begin
    maxsig = max(data(i,*),/nan)
    for j=360,length-1 do begin
        if (data(i,j) eq maxsig) then begin
            ; print,'Max signal at ',altprof(j),' km in profile #',i
        endif
    endfor
endfor
;-----

background = dblarr(width)
adata      = dblarr(length)
avgdata    = dblarr(length)
sigma_2    = dblarr(length)
avgsignal  = dblarr(length)
sigma      = dblarr(length)
signaltosigma = dblarr(length)
hannsignal = dblarr(length)

;;BACKGROUND CALCULATION
FOR i=0,width-1 do begin
    background(i) = double(TOTAL(data[i,BKLO:BKHI])/(BKHI-BKLO+1.0))

    if (background(i) gt backthresh) then begin
        print,'Profile number where background is above threshold = ',i+1,background(i)
    endif
    if (background(i) lt 1) then begin
        ; print,'Profiles where background is LT 1 = ',i+1,background(i)
    endif
    for j = 1800,length-1 do begin ; for j = 0,length-1 do begin
        if (data[i,j] ge 2000) and (j gt 225) then begin ;10000
            print,'Spike in profile # ',i+1, ' at', altprof(j)
        endif
        if (data[i,j] ge 20) and (j gt 2493) then begin
            ;print,'Spike in profile # ',i+1, ' at', altprof(j)
        endif
    endfor
    if (data[i,1826] le 100) and (background[i] le 100) then begin
        ; print,'Low signal in profile # ',i+1
    endif
endfor

```



```

backmin = strcompress(string(min(background,/nan)),/remove_all)
backmax = strcompress(string(max(background,/nan)),/remove_all)
print,'Back min = ',backmin
print,'Back max = ', backmax

profnumber = findgen(width)+1

p = plot(background,$
    title='Background Values Through the Night '+TIMESTRING,$
    ytitle='Background Value',xtitle='2 Minute Profile Number',$
    YRANGE=[0,250])
t1 = TEXT(.45,.4, 'Max Background = '+backmax, FONT_SIZE=14,$
    FONT_NAME='Helvetica')
t2 = TEXT(.45,.35, 'Min Background = '+backmin, FONT_SIZE=14,$
    FONT_NAME='Helvetica')
avgbackground = double(total(background(*),/nan)/width)
PRINT,'Average Background Value= ',avgbackground

;;ALL-NIGHT AVERAGE
for j=0,length-1 do begin
    avgdata(j) = double(total(data[*],j),/nan)/width)
endfor

BKGND=STRING(LONG(AVGBACKGROUND))
PCNTS=STRING(LONG(AVGDATA[1560]))
uplimit = background+5.0

;;ERROR CALCULATION
sigma_back = DOUBLE(SQRT((AvgBackground/(width*(BKHI-BKLO+1))))))
sigma_2 = double((Avgdata/(Avgbins*width))+(AvgBackground/$
    (width*(BKHI-BKLO+1))))

;;BACKGROUND SUBTRACT
backsubtract = double(Avgdata-(AvgBackground))

;----Testing: ADDING OSCILLATIONS TO THE SIGNAL-----
oscillation = fltarr(length)

for i = 0, length-1 do begin
    oscillation = cos((1/100)*i);0.5*avgbackground*cos((1/7)*i)
endfor

oscanswer = 1
if (oscanswer eq 1) then begin
    backsubtract = backsubtract*oscillation

```

```

;backsubtract = double(Avgdata-(AvgBackground))
endif
;-----

;;SMOOTHING OF DATA

avgSIGNAL=double(smooth(backsubtract,avgbins,/edge_truncate))

;-----
;(LS OCT 30 2015) Hanning filter smoothing instead of boxcar
dumsignal = fltarr(length)
pts      = 107 ;Full window width (217 pts*0.0374 km = 8 km, 107 pts for 4 km)

start = fix((pts-1)*0.5) ; first point that is averaged
stop  = (length -1) - start ; last point that is averaged

w_k = HANNING(pts, ALPHA=0.54) ;0.54 = HAMMING
normw_k = w_k / TOTAL (w_k)

FOR ji = start,stop do begin;length-start-1 DO BEGIN
  FOR jk = 0,pts-1 DO BEGIN
    Dumsignal(ji) = double(Dumsignal(ji)+normw_k(jk)*backsubtract(ji-start+jk))
  endfor
endfor

for i = 0,start do begin
  dumsignal(i) = backsubtract(i)
endfor

for i = stop,length-1 do begin
  dumsignal(i) = backsubtract(i)
endfor

hannsignal = dumsignal

backvector = fltarr(length)
backvector(*) = avgbackground
zeros      = fltarr(length)
zeros(*)   = 0.

P1 = PLOT(Altprof,backsubtract,TITLE='Averaged Data '+timestring,$
  ytitle='Photon Counts',xtitle='Altitude (km)',$,
  yrange=[-20,AVGBACKGROUND+15],xrange=[70,350],thick=2)
p2 = plot(altprof,avgsignal,color='orange',/overplot,thick=2)
p3 = plot(altprof,hannsignal,color='blue',/overplot,thick=2,linestyle=2)

```

```

p4 = plot(altprof,backvector,color='red',/overplot,thick=2)
p5 = plot(altprof,zeros,color='red',/overplot,thick=2)
P2.NAME = 'Boxcar'
p3.name = 'Hamming'
legend=legend(target=[P2,p3],position=[300,AVGBACKGROUND+10],/data)

writocol,timestring+'datasmooth.txt',altprof,avgdata, backsubtract,$
    avgsignal,hannsignal
;-----

maxsignal = max(avgsignal)

for j = 0,length-1 do begin
    if (avgsignal[j] eq maxsignal) then begin
        print,'Max signal = ',maxsignal, ' at', altprof(j)
    endif
endfor

;;STANDARD DEVIATION
sigma      = SQRT(sigma_2)/AvgSignal
signalto sigma = double(AvgSignal/(SQRT(sigma_2)))

FOR START=fitbin, 4227 DO BEGIN
    ERROR  = TOTAL(sigma[START-5:START+5])/11.0
; ERROR  = sigma(START)
    TOPBIN = START
    IF (ERROR GE (THRESHOLD)) THEN BEGIN
        START=4227
    ENDIF
ENDFOR
HMAX=altprof(topbin)

writocol,'oldERRORCALC.txt',altprof,avgdata,sigma_2,sigma

END

```

A.4.4. Hammsignal.pro

```

PRO
hammSignal,TIMESTRING,FITBIN,ALTPROF,DATA,hammAVGSIGNAL,hammSIG
MA,$
    hammsignaltoSIGMA,hammTOPBIN,hammHMAX,bkhi,bklo,
AVGBACKGROUND

```

; Created by Leda Sox, Dec 2015

```
;print,'Background Threshold (in photon counts):'
;read,backthresh
backthresh = 100
```

```
BKHI = 9000
BKLO = 5000
THRESHOLD = 1.0/16. ;1/16, Signal to noise ratio
AVGBINS = 81.0 ;NUMBER OF RANGE BINS TO AVERAGE OVER (josh's value
was 81.0)
```

```
cd = 'c:\Users\Leda\IDLWorkspace83\Default\NewData\' + timestring
cd,cd
restore,timestring+'data.sav'
```

```
Year = strmid(timestring,0,4)
month = strmid(timestring,4,2)
day = strmid(timestring,6,2)
```

```
width = (size(data))(1)
length = (size(data))(2)
print,'Number of 2 mins= ',width
```

```
avgdata = dblarr(length)
hammavgdata = dblarr(length)
hammsigma_2 = dblarr(length)
hammavgsignal = dblarr(length)
hammsignaltosigma = dblarr(length)
hammsigma = dblarr(length)
hammsignal = dblarr(length)
```

```
::ALL-NIGHT AVERAGE
for j=0,length-1 do begin
  avgdata(j) = double(total(data[* ,j],/nan)/width)
endfor
```

```
;-----
; Hamming filter smoothing over signal range
dumsignal = fltarr(length)
dumsigerr = fltarr(length)
pts = 109;217
```

```

start = fix((pts-1)*0.5)    ; first point that is averaged
stop  = (length -1) - start ; last point that is averaged

w_k = HANNING(pts, ALPHA=0.54) ; 0.54 = HAMMING
normw_k = w_k / TOTAL (w_k)

FOR ji = start,stop do begin;length-start-1 DO BEGIN
  FOR jk = 0,pts-1 DO BEGIN
    Dumsignal(ji)= double(Dumsignal(ji) + normw_k(jk) * avgdata(ji-start+jk))
    Dumsigerr(ji)= double(Dumsigerr(ji) + normw_k(jk)^2 * avgdata(ji-start+jk))
  endfor
endfor

for i = 0,start do begin
  dumsignal(i) = avgdata(i)
endfor

for i = stop,length-1 do begin
  dumsignal(i) = avgdata(i)
endfor
hammavgdata[0:bklo-(pts/2)] = dumsignal[0:bklo-(pts/2)]
hammavgdata[1+bklo-(pts/2):length-1] = avgdata[1+bklo-(pts/2):length-1]

; Background Calculation-----
avgbackground = double(TOTAL(hammavgdata[BKLO:BKHI])/(BKHI-BKLO+1.0))
PRINT,'Hamming Background= ',avgbackground

;Background subtraction-----
hammavgsignal = hammavgdata-avgbackground

;;ERROR CALCULATION
for j = 0,length-1 do begin
  hammsigma_2[j] = double(((dumsigerr[j]/(width)))+(AvgBackground/(width*(BKHI-
BKLO+1))))
endfor

;;STANDARD DEVIATION
hammsigma = double(SQRT(hammsigma_2)/hammAvgSignal)
hammsignaltosigma = double(hammAvgSignal/(SQRT(hammsigma_2)))

FOR START=fitbin, 4227 DO BEGIN
  ERROR = TOTAL(hammsigma[START-5:START+5])/11.0
; ERROR = sigma(START)

```

```

    hammTOPBIN = START
    IF (ERROR GE (THRESHOLD)) THEN BEGIN
        START=4227
    ENDIF
ENDFOR
    hammHMAX=altprof(hammtopbin)

END

```

A.4.5. Hanningsignal.pro

```

PRO
hanningSignal,TIMESTRING,FITBIN,ALTPROF,DATA,hannAVGSIGNAL,hannSIGM
A,$

```

```

hannsignaltoSIGMA,hannTOPBIN,hannHMAX,bkhi,bklo,AVGBACKGROUND

```

```

; Created by Leda Sox, April 2016

```

```

;print,'Background Threshold (in photon counts):'
;read,backthresh
backthresh = 100

```

```

BKHI = 9000
BKLO = 5000
THRESHOLD = 1.0/16. ;1/16, Signal to noise ratio
AVGBINS = 81.0 ;NUMBER OF RANGE BINS TO AVERAGE OVER (josh's value
was 81.0)

```

```

cd = 'c:\Users\Leda\IDLWorkspace83\Default\NewData\' + timestring
cd,cd
restore,timestring+'data.sav'

```

```

Year = strmid(timestring,0,4)
month = strmid(timestring,4,2)
day = strmid(timestring,6,2)

```

```

width = (size(data))(1)
length = (size(data))(2)
print,'Number of 2 mins= ',width

```

```

avgdata = dblarr(length)

```

```

hannavgdata    = dblarr(length)
hannsigma_2    = dblarr(length)
hannavgsignal  = dblarr(length)
hannsignaltosigma = dblarr(length)
hannsigma      = dblarr(length)
hannsignal     = dblarr(length)

;;ALL-NIGHT AVERAGE
for j=0,length-1 do begin
    avgdata(j) = double(total(data[* ,j],/nan)/width)
endfor

;-----
; Hamming filter smoothing over signal range
dumsignal = fltarr(length)
dumsigerr = fltarr(length)
pts       = 109;217

start = fix((pts-1)*0.5) ; first point that is averaged
stop  = (length -1) - start ; last point that is averaged

w_k = HANNING(pts, ALPHA=0.5) ;0.54 = HAMMING, 0.50 = HANNING
normw_k = w_k / TOTAL (w_k)

FOR ji = start,stop do begin;length-start-1 DO BEGIN
    FOR jk = 0,pts-1 DO BEGIN
        Dumsignal(ji)= double(Dumsignal(ji) + normw_k(jk) * avgdata(ji-start+jk))
        Dumsigerr(ji)= double(Dumsigerr(ji) + normw_k(jk)^2 * avgdata(ji-start+jk))
    endfor
endfor

for i = 0,start do begin
    dumsignal(i) = avgdata(i)
endfor

for i = stop,length-1 do begin
    dumsignal(i) = avgdata(i)
endfor
hannavgdata[0:bklo-(pts/2)] = dumsignal[0:bklo-(pts/2)]
hannavgdata[1+bklo-(pts/2):length-1] = avgdata[1+bklo-(pts/2):length-1]

; Background Calculation-----
avgbackground = double(TOTAL(hannavgdata[BKLO:BKHI])/(BKHI-BKLO+1.0))
PRINT,'Hamming Background= ',avgbackground

```

```

;Background subtraction-----
hannavgsignal = hannavgdata-avgbackground

;;ERROR CALCULATION
for j = 0,length-1 do begin
  hannsigma_2[j] = double((dumsigerr[j]/(width))$
    +(AvgBackground/(width*(BKHI-BKLO+1))))
endfor

;;STANDARD DEVIATION
hannsigma      = double(SQRT(hannsigma_2)/hannAvgSignal)
hannsignalstosigma = double(hannAvgSignal/(SQRT(hannsigma_2)))

FOR START=fitbin, 4227 DO BEGIN
  ERROR = TOTAL(hannsigma[START-5:START+5])/11.0
  hannTOPBIN = START
  IF (ERROR GE (THRESHOLD)) THEN BEGIN
    START=4227
  ENDIF
ENDFOR
hannHMAX=altprof(hanntopbin)

END

```

A.4.6. Snr.pro

```

PRO
SNR,TIMESTRING,FITBIN,ALTPROF,smoothdata,background,TOPBIN,HMAX,bkhi,
bklo,$
  SNRTEST

```

;Created by Leda Sox April 2014

```

BKHI=9000
BKLO=5000
THRESHOLD = 2.0 ;Signal to noise ratio
AVGBINS = 81.0 ;NUMBER OF RANGE BINS TO AVERAGE OVER (josh's value
was 81.0)

```

```

cd = 'c:\Users\Leda\IDLWorkspace83\Default\NewData\' +timestring

```



```

cd,cd
restore,timestring+'data.sav'

Year = strmid(timestring,0,4)
month = strmid(timestring,4,2)
day = strmid(timestring,6,2)

width = (size(data))(1)
length = (size(data))(2)
; print,'Number of 2 mins= ',width

avgdata = dblarr(length)

;;ALL-NIGHT AVERAGE
for j=0,length-1 do begin
  avgdata(j) = double(total(data[*,j])/width)
endfor

background = double(total(avgdata[bklo:bkhi])/(bkhi-bklo+1.0))

backsubtract = avgdata-background
smoothdata = smooth(backsubtract,avgbins,/edge_truncate)
SNRTEST = SMOOTHDATA/BACKGROUND
FOR i=fitbin, 4227 DO BEGIN
  SNR = smoothdata(i)/background
  TOPBIN = i
  IF (SNR LT (THRESHOLD)) THEN BEGIN
    I=4227
  ENDIF
ENDFOR

HMAX=altprof(topbin)

;writecol,'c:\Users\Leda\IDLWorkspace83\Default\NewData\' + timestring + '\' + timestring + '
SNR.txt',ALTPROF,SMOOTHDATA,SNRTEST

END

```

A.4.7. Newdensity.pro

```

PRO
newdensity,LENGTH,EffCrossSection,ALTRES,FITBIN,AVGSIGNAL,DENSITY,cros

```

sdensity

;Created by Leda Sox April 2014

RANGE = FINDGEN(LENGTH)*ALTRES+(ALTRES/2.0)
 DENSITY = AVGSIGNAL*RANGE*RANGE ;SINGAL*R^2 GIVES A
 RELATIVE DENSITY PROFILE

NORMFACTOR = DENSITY[FITBIN] ;FITBIN IS THE POINT WE ARE
 NOMALIZING THE DENSITY TO 1 AT
 DENSITY = DENSITY/NORMFACTOR

crossdensity = (AVGSIGNAL*RANGE*RANGE)/EffCrossSection
 crossNORMFACTOR = crossDENSITY[FITBIN]
 crossDENSITY = crossDENSITY/crossNORMFACTOR

END

A.4.8. Runnrlmsise00.pro

PRO RunNRLMSISE00,yyddd,Hmax,GEOLAT,GEOLONG,D,T,iyd

;Created by Leda Sox April 2014

;Inputs
 iyd = YYDDD
 GEOLONG = 360.0+GEOLONG
 hour = 6.
 sec = hour*3600.
 aflux1 = 150.0
 dflux1 = 150.0
 ap = fltarr(7)
 ap = 4.0
 ;ap(0) = 4.
 ;ap(1) = 4.
 mass = 48L
 LST1 = (hour)+(geolong/15.)

;OUTPUTS
 d = FLTARR(9)
 ;d(0) = Helium number density [He]
 ;d(1) = Atomic Oxygen number density [O]

```

;d(2) = Molecular Nitrogen number density [N2]
;d(3) = Molecular Oxygen number density [O2]
;d(4) = Argon number density [Ar]
;d(5) = Total mass density [rho_total]
;d(6) = Hydrogen number density [H]
;d(7) = Atomic Nitrogen number density [N]
;d[8] = Anomalous Oxygen [O*]

t    = FLTARR(2)
;t[0] = Temperature at altitude (K)
;t[1] = Exospheric Temperature (K)

dllpath = 'C:\Users\Leda\IDLWorkspace83\Default\msis02_scaled1_x64.dll'
result = call_external(dllpath,'msis2002',iyd,sec, Hmax, GEOLAT, GEOLONG, lst1,$
                        aflux1, dflux1,ap, mass, d, t)
t=t[1]

END

```

A.4.9. Gravity.pro

PRO GRAVITY,GEOLAT,GEOLONG,LENGTH,ALTRES,GNEW

```

;Created by Josh Herron
;-----
gm          =      3986004.418e8
omega =      7292115.0e-11
a          =      6378137.0
b          =      6356752.3142
e          =      8.1819190842622e-2
EE         =      5.2185400842339e5
k          =      0.00193185265241
m          =      0.00344978650684
f          =      1/298.257223563
gge        =      9.7803253359
ggp        =      9.8321849378
phi        =      GeoLat*!DTOR
si         =      atan(((1-f)^2)*tan(phi))
lambda=    GeoLong*!DTOR
alpha  =    phi-si
ho      =    1460
N       =    a/sqrt(1-e*e*sin(phi)*sin(phi))
gnew    =fltarr(length)

```

```

FOR i=0, length-1 DO BEGIN
  h      =      1460+altres*1000.0*i
  x      =      (N+h)*cos(phi)*cos(lambda)
  y      =      (N+h)*cos(phi)*sin(lambda)
  z      =      ((b*b)/(a*a)*N+h)*sin(phi)
  u      =      sqrt((1.0/2.0)*(x*x+y*y+z*z-
EE*EE)*(1.0+sqrt(1.0+4.0*EE*EE*z*z/(x*x+y*y+z*z-EE*EE)^2)))
  beta   =      atan(z*sqrt(u*u+EE*EE)/(u*sqrt(x*x+y*y)))
  w      =      sqrt((u*u+EE*EE*sin(beta)*sin(beta))/(u*u+EE*EE))
  q      =      (1.0/2.0)*((1.0+3.0*u*u/(ee*ee))*atan(EE/u)-
3.0*u/EE)
  qo     =      (1.0/2.0)*((1.0+3.0*b*b/(ee*ee))*atan(EE/b)-
3.0*b/EE)
  qp     =      3.0*(1.0+u*u/(ee*ee))*(1.0-u/ee*atan(ee/u))-1.0
  gu     =      (-
1.0/w)*(gm/(u*u+ee*ee)+(omega*omega*a*a*ee*qp)/((u*u+ee*ee)*qo)*(1.0/2.0*sin(beta)*sin(beta)-1.0/6.0))+omega*omega*u*cos(beta)*cos(beta)/w
  gb     =      (1/w)*(omega*omega*a*a*q)/(sqrt(u*u+ee*ee)*qo)*sin(beta)*cos(beta)-
omega*omega*sqrt(u*u+ee*ee)*sin(beta)*cos(beta)/w
  gae    =      [gu,gb,0]
  R2     =      [[cos(phi)*cos(lambda),cos(phi)*sin(lambda),sin(phi)],$
[-sin(phi)*cos(lambda),-
sin(phi)*sin(lambda),cos(phi)],$
[-sin(lambda),cos(lambda),0]]
  R1     =      [[u*cos(beta)*cos(lambda)/(w*sqrt(u^2+EE^2)),-
1/w*sin(beta)*cos(lambda),-sin(lambda)],$
[u*cos(beta)*sin(lambda)/(w*sqrt(u^2+EE^2)),-
1/w*sin(beta)*sin(lambda),cos(lambda)],$
[sin(beta)/w,u*cos(beta)/(w*sqrt(u^2+EE^2)),0]]
  gs     =      R2#(R1#gae)
  gphi   =      -gs(0)*sin(alpha)+gs(1)*cos(alpha)
  gh     =      -gs(0)*cos(alpha)+gs(1)*sin(alpha)
  gnew(i) =      sqrt(gh^2+gphi^2)
ENDFOR
;      gnew=smooth(gnew,81,/edge_truncate)

END

```

A.4.10. Newtemperature.pro

PRO NEWTEMPERATURE,mmm,rrr,altres,length,altprof,sigma,fitbin,topbin,tmax,\$
gnew,density,TEMPERATURE,TEMPERROR,tempa,tempb

;Created by Leda Sox April 2014

```
TEMPERATURE = FLTARR(LENGTH)
TEMPA      = FLTARR(LENGTH)
TEMPB      = FLTARR(LENGTH)
TEMPERROR  = FLTARR(LENGTH)
ERRtest    = FLTARR(LENGTH)
H          = FLTARR(length) ;Pressure scale height = (RRR*T)/g
```

```
tmaxA = tmax+20.0
tmaxB = tmax-20.0
```

```
C1          = DOUBLE(DENSITY[TOPBIN]/DENSITY)
             ;RELATIVE DENSITY PROFILE FROM TOP
TEMPERATURE[topbin] = DOUBLE(tmax)
TEMPA[topbin]    = DOUBLE(tmaxA)
TEMPB[topbin]    = DOUBLE(tmaxB)
C3            = DOUBLE(ALTRES/(2.0*RRR*DENSITY(Topbin)))
UPPER         = DOUBLE(MMM*GNEW[TOPBIN]*DENSITY[TOPBIN])
INTEGRAL      = DOUBLE(0.0)
```

```
; templover = dblarr(N_elements(density)\
; tempintegral = dblarr(n_elements(density))
```

```
FOR J=TOPBIN-1, FITBIN,-1 DO BEGIN
  LOWER      = DOUBLE(MMM*GNEW[J]*DENSITY[J])
  INTEGRAL    = DOUBLE(INTEGRAL+(UPPER+LOWER)*C3)
  TEMPERATURE[J] = DOUBLE(C1[J]*(TEMPERATURE[topbin]+INTEGRAL))
  TEMPa[J]    = DOUBLE(C1[J]*(TEMPA[topbin]+INTEGRAL))
  TEMPb[J]    = DOUBLE(C1[J]*(TEMPB[topbin]+INTEGRAL))
  UPPER      = LOWER
  H[J]        = (RRR*TEMPERATURE[J])/(mmm*GNEW[J])
  TEMPERROR[J] = TEMPERATURE[J]^2.0*sigma[J]^2.0$
               +TEMPERATURE[TOPBIN]^2.0*sigma[TOPBIN]^2.0$
               *EXP(-2.0*(ALTPROF[TOPBIN]-ALTPROF[J])/7.0)
  ERRTEST[J]  =
  TEMPERATURE[J]^2.0*sigma[J]^2.0+TEMPERATURE[TOPBIN]^2.0$
               *sigma[TOPBIN]^2.0*EXP(-2.0*(ALTPROF[TOPBIN]-
```

```

ALTPROF[J])/H[J])
  TEMPERROR[J] = SQRT(TEMPERROR[J])
  ERRTEST[J] = SQRT(ERRTEST[J])
ENDFOR

FOR I=0,LENGTH-1 DO BEGIN
  IF (TEMPERATURE[I] EQ 0.0) THEN BEGIN
    TEMPERATURE[I] = !VALUES.F_NAN
  ENDIF
ENDFOR

FOR I=0,LENGTH-1 DO BEGIN
  IF (TEMPA[I] EQ 0.0) THEN BEGIN
    TEMPA[I] = !VALUES.F_NAN
  ENDIF
ENDFOR

FOR I=0,LENGTH-1 DO BEGIN
  IF (TEMPB[I] EQ 0.0) THEN BEGIN
    TEMPB[I] = !VALUES.F_NAN
  ENDIF
ENDFOR

;WRITECOL,'SCALEHEIGHT.TXT',ALTPROF,GNEW,TEMPERATURE,H
;WRITECOL,'TEMPERR.TXT',ALTPROF,TEMPERATURE,sigma,TEMPERROR

END

```

A.4.11. Mmmtemperature.pro

```

PRO MMMTEMPERATURE,mmm,rrr,altres,length,altprof,fitbin,topbin,tmax,gnew,$
    density,SIGMA,TEMPERATURE,TEMPERROR

```

;Written by: Leda Sox, 2015

```

TEMPERATURE = FLTARR(LENGTH)
TEMPERROR = FLTARR(LENGTH)

C1 = DOUBLE(DENSITY[TOPBIN]/DENSITY)
    ;RELATIVE DENSITY PROFILE FROM TOP
TEMPERATURE[topbin] = DOUBLE(tmax)
C3 = DOUBLE(ALTRES/(2.0*RRR*DENSITY(Topbin)))
UPPER = DOUBLE(MMM[topbin]*GNEW[TOPBIN]*DENSITY[TOPBIN])

```

```

INTEGRAL      = DOUBLE(0.0)

FOR J=TOPBIN-1, FITBIN,-1 DO BEGIN
  LOWER      = DOUBLE(MMM[J]*GNEW[J]*DENSITY[J])
  INTEGRAL    = DOUBLE(INTEGRAL+(UPPER+LOWER)*C3)
  TEMPERATURE[J] = DOUBLE(C1[J]*(TEMPERATURE[topbin]+INTEGRAL))
  UPPER      = LOWER
  TEMPERROR[J] = TEMPERATURE[J]^2.0*sigma[J]^2.0$
               +TEMPERATURE[TOPBIN]^2.0*sigma[TOPBIN]^2.0$
               *EXP(-2.0*(ALTPROF[TOPBIN]-ALTPROF[J])/7.0)
  TEMPERROR[J] = SQRT(TEMPERROR[J])
ENDFOR

FOR I=0,LENGTH-1 DO BEGIN
  IF (TEMPERATURE[I] EQ 0.0) THEN BEGIN
    TEMPERATURE[I] = !VALUES.F_NAN
  ENDIF
ENDFOR

END

```

A.5. Auxiliary IDL Code

The following programs are auxiliary to the temperature reduction algorithm, but are required to run the exact code given above. The `dataarray.pro` code combines all of the 2-minute profiles for the night into one array. It calls `readnewmcs.pro`. It must be run before the temperature algorithm to get the raw data files into the proper array format and saved as a `.sav` file to be input into `newreduction.pro`.

A.5.1. Dataarray.pro

```
PRO dataarray
```

```
;Written by: Leda Sox, 2014
```

```
length=14000
```

```
directory='c:\Users\Leda\IDLWorkspace83\Default\NewData\'
```

```

date = "
print,'Date in YYMMDD format?'
read,date
timestring = strcompress('20'+date,/remove_all)

toads =
dialog_pickfile(path=directory+timestring,get_path=pickedpath,/multiple_files)
numprof = n_elements(toads)
rawdata = dblarr(numprof,length)
data = dblarr(length,numprof)

readnewmcs,toads[0],lidardata
usulidar=lidardata

for i=1, numprof-1 do begin
    readnewmcs,toads[i],lidardata
    usulidar = [usulidar,lidardata]
endfor
rawdata = usulidar.data
data = rotate(rawdata,4)
DATA = FLOAT(DATA)

answer = "
print, 'Remove Profiles (y/n)?'
read, answer

goodprof = numprof
if (answer eq 'y') or (answer eq 'Y') then begin
    textfile = directory+timestring+'\'+timestring+'REMOVE.txt'
    OPENR,lun,textfile,/get_lun
    NLINES = FILE_LINES(TEXTFILE)
    goodprof = numprof-nlines
    print,'Number of good 2 min Profiles= ',goodprof
    remove = intarr(nlines)
    readf,lun,remove
    free_lun,lun
    for i=0,nlines-1 do begin
        index = remove(i)-1
        data(index,*) = !VALUES.F_NAN
    endfor
endif
if (answer eq 'n') or (answer eq 'N') then begin
    print,'Number of good 2 min Profiles= ',numprof
endif

```



```

if (goodprof lt 60) then answer='NO'
if (goodprof ge 60) then answer='YES'
print, 'More than 2 hours of data: ',answer
; PRINT,DATA(0,1825:1830),DATA(71,1825:1830)

save,data,filename=pickedpath+'\'+timestring+'data.sav'

END

```

A.5.2. Readnewmcs.pro

```

PRO readNEWmcs, input, lidardata

;Created by Leda Sox, April 2014

;-----
;This program is designed to read in the mcs files from the lidar system.
;-----

get_lun, lun1
openr,lun1,input ;Here we are opening the file passed to the read function

;datalength=SIZE(input)
;print,datalength
passlength=14000

headers = bytarr(256)
readu, lun1, headers

data = lonarr(passlength)
readu, lun1, data

lidardata = create_struct('headers',headers,'Data',Data)
close, lun1
free_lun, lun1

END

```

A.5.3. Dayofyear.pro

```
PRO DAYOFYEAR,Date,DOY,strdoy
```

```
;Created by Leda Sox, April 2014
```

```
Year = FIX(STRMID(Date,0,2))
Month = FIX(STRMID(Date,2,2))
Day = FIX(STRMID(Date,4,2))
;PRINT, YEAR, MONTH, DAY
```

```
IF (year eq '92') or (year eq '96') or (year eq '00') or (year eq '04') $
  or (year eq '12') or (year eq '16') then begin
  MD = [0,31,29,31,30,31,30,31,31,30,31,30,31]
ENDIF ELSE BEGIN
  MD = [0,31,28,31,30,31,30,31,31,30,31,30,31]
ENDELSE
```

```
monthtot = TOTAL(MD[0:Month-1])
;print, monthtot
intday = FIX(Day)
;print, intday
doy = monthtot+intday
;print, 'DOY= ',doy
strdoy = "
strdoy=strcompress(string(doy,FORMAT='(I03)'))

;print,strcompress(strdoy,/remove_all)

END
```

APPENDIX B

COPYRIGHT PERMISSIONS

Four figures in Chapter 2 of this required copyright permission from their sources. Chapter 5 was published by John Wiley and Sons in *Journal of Geophysical Research: Atmospheres* and also required permission from both the publisher and my coauthors for use in this dissertation. The following figures are copies of the copyright permissions granted by the publications' respective publishers and coauthors.

7/26/2016

RightsLink Printable License

**JOHN WILEY AND SONS LICENSE
TERMS AND CONDITIONS**

Jul 26, 2016

This Agreement between Leda Sox ("You") and John Wiley and Sons ("John Wiley and Sons") consists of your license details and the terms and conditions provided by John Wiley and Sons and Copyright Clearance Center.

License Number	3916721089333
License date	Jul 26, 2016
Licensed Content Publisher	John Wiley and Sons
Licensed Content Publication	Journal of Geophysical Research: Atmospheres
Licensed Content Title	Wind and temperature response of midlatitude mesopause region to the 2009 Sudden Stratospheric Warming
Licensed Content Author	Tao Yuan,B. Thuraiajah,C.-Y. She,A. Chandran,R. L. Collins,D. A. Krueger
Licensed Content Date	May 9, 2012
Licensed Content Pages	1
Type of use	Dissertation/Thesis
Requestor type	University/Academic
Format	Print and electronic
Portion	Figure/table
Number of figures/tables	1
Original Wiley figure/table number(s)	Figure 1
Will you be translating?	No
Title of your thesis / dissertation	RAYLEIGH-SCATTER LIDAR MEASUREMENTS OF THE MESOSPHERE AND THERMOSPHERE AND THEIR CONNECTIONS TO SUDDEN STRATOSPHERIC WARMINGS
Expected completion date	Aug 2016
Expected size (number of pages)	180
Requestor Location	Leda Sox 4405 Old Main Hill LOGAN, UT 84321 United States Attn: Leda Sox
Publisher Tax ID	EU826007151
Billing Type	Invoice
Billing Address	Leda Sox 4405 Old Main Hill LOGAN, UT 84321 United States Attn: Leda Sox

<https://s100.copyright.com/AppDispatchServlet>

1/5

Figure B.1. Copyright permission received for *Yuan et al.* [2012]. Permission is for use of Figure 2.3.

7/27/2016

RightsLink Printable License

**JOHN WILEY AND SONS LICENSE
TERMS AND CONDITIONS**

Jul 27, 2016

This Agreement between Leda Sox ("You") and John Wiley and Sons ("John Wiley and Sons") consists of your license details and the terms and conditions provided by John Wiley and Sons and Copyright Clearance Center.

License Number	3917161134310
License date	Jul 27, 2016
Licensed Content Publisher	John Wiley and Sons
Licensed Content Publication	Journal of Geophysical Research: Atmospheres
Licensed Content Title	A study of a self-generated stratospheric sudden warming and its mesospheric-lower thermospheric impacts using the coupled TIME-GCM/CCM3
Licensed Content Author	H.-L. Liu,R. G. Roble
Licensed Content Date	Dec 7, 2002
Licensed Content Pages	1
Type of use	Dissertation/Thesis
Requestor type	University/Academic
Format	Print and electronic
Portion	Figure/table
Number of figures/tables	1
Original Wiley figure/table number(s)	3
Will you be translating?	No
Title of your thesis / dissertation	RAYLEIGH-SCATTER LIDAR MEASUREMENTS OF THE MESOSPHERE AND THERMOSPHERE AND THEIR CONNECTIONS TO SUDDEN STRATOSPHERIC WARMINGS
Expected completion date	Aug 2016
Expected size (number of pages)	180
Requestor Location	Leda Sox 4405 Old Main Hill LOGAN, UT 84321 United States Attn: Leda Sox
Publisher Tax ID	EU826007151
Billing Type	Invoice
Billing Address	Leda Sox 4405 Old Main Hill LOGAN, UT 84321 United States

<https://is100.copyright.com/AppDispatchServlet>

1/5

Figure B.2. Copyright permission received for *Liu and Roble* [2002]. Permission is for use of Figure 2.5.

7/27/2016

RightsLink Printable License

**JOHN WILEY AND SONS LICENSE
TERMS AND CONDITIONS**

Jul 27, 2016

This Agreement between Leda Sox ("You") and John Wiley and Sons ("John Wiley and Sons") consists of your license details and the terms and conditions provided by John Wiley and Sons and Copyright Clearance Center.

License Number	3917160952190
License date	Jul 27, 2016
Licensed Content Publisher	John Wiley and Sons
Licensed Content Publication	Geophysical Research Letters
Licensed Content Title	Ionospheric signatures of sudden stratospheric warming: Ion temperature at middle latitude
Licensed Content Author	Larisa Goncharenko, Shun-Rong Zhang
Licensed Content Date	Nov 8, 2008
Licensed Content Pages	1
Type of use	Dissertation/Thesis
Requestor type	University/Academic
Format	Print and electronic
Portion	Figure/table
Number of figures/tables	1
Original Wiley figure/table number(s)	2
Will you be translating?	No
Title of your thesis / dissertation	RAYLEIGH-SCATTER LIDAR MEASUREMENTS OF THE MESOSPHERE AND THERMOSPHERE AND THEIR CONNECTIONS TO SUDDEN STRATOSPHERIC WARMINGS
Expected completion date	Aug 2016
Expected size (number of pages)	180
Requestor Location	Leda Sox 4405 Old Main Hill LOGAN, UT 84321 United States Attn: Leda Sox
Publisher Tax ID	EU826007151
Billing Type	Invoice
Billing Address	Leda Sox 4405 Old Main Hill LOGAN, UT 84321 United States Attn: Leda Sox

<https://s100.copyright.com/AppDispatchServlet>

1/5

Figure B.3. Copyright permission received for *Goncharenko and Zhang* [2008]. Permission is for use of Figure 2.6.

7/27/2016

RightsLink Printable License

**THE AMERICAN ASSOCIATION FOR THE ADVANCEMENT OF SCIENCE LICENSE
TERMS AND CONDITIONS**

Jul 27, 2016

This Agreement between Leda Sox ("You") and The American Association for the Advancement of Science ("The American Association for the Advancement of Science") consists of your license details and the terms and conditions provided by The American Association for the Advancement of Science and Copyright Clearance Center.

License Number	3917160596384
License date	Jul 27, 2016
Licensed Content Publisher	The American Association for the Advancement of Science
Licensed Content Publication	Science
Licensed Content Title	Stratospheric Harbingers of Anomalous Weather Regimes
Licensed Content Author	Mark P. Baldwin, Timothy J. Dunkerton
Licensed Content Date	Oct 19, 2001
Licensed Content Volume Number	294
Licensed Content Issue Number	5542
Volume number	294
Issue number	5542
Type of Use	Thesis / Dissertation
Requestor type	Scientist/individual at a research institution
Format	Print and electronic
Portion	Figure
Number of figures/tables	1
Order reference number	
Title of your thesis / dissertation	RAYLEIGH-SCATTER LIDAR MEASUREMENTS OF THE MESOSPHERE AND THERMOSPHERE AND THEIR CONNECTIONS TO SUDDEN STRATOSPHERIC WARMINGS
Expected completion date	Aug 2016
Estimated size(pages)	180
Requestor Location	Leda Sox 4405 Old Main Hill LOGAN, UT 84321 United States Attn: Leda Sox
Billing Type	Invoice
Billing Address	Leda Sox 4405 Old Main Hill LOGAN, UT 84321 United States

<https://s100.copyright.com/AppDispatchServlet>

1/6

Figure B.4. Copyright permission received for *Baldwin and Dunkerton* [2001]. Permission is for use of Figure 2.7.

7/27/2016

RightsLink Printable License

**JOHN WILEY AND SONS LICENSE
TERMS AND CONDITIONS**

Jul 27, 2016

This Agreement between Leda Sox ("You") and John Wiley and Sons ("John Wiley and Sons") consists of your license details and the terms and conditions provided by John Wiley and Sons and Copyright Clearance Center.

License Number	3917161368540
License date	Jul 27, 2016
Licensed Content Publisher	John Wiley and Sons
Licensed Content Publication	Journal of Geophysical Research: Atmospheres
Licensed Content Title	Connection between the midlatitude mesosphere and sudden stratospheric warmings as measured by Rayleigh-scatter lidar
Licensed Content Author	Leda Sox,Vincent B. Wickwar,Chad S. Fish,Joshua R. Herron
Licensed Content Date	May 11, 2016
Licensed Content Pages	10
Type of use	Dissertation/Thesis
Requestor type	Author of this Wiley article
Format	Print and electronic
Portion	Full article
Will you be translating?	No
Title of your thesis / dissertation	RAYLEIGH-SCATTER LIDAR MEASUREMENTS OF THE MESOSPHERE AND THERMOSPHERE AND THEIR CONNECTIONS TO SUDDEN STRATOSPHERIC WARMINGS
Expected completion date	Aug 2016
Expected size (number of pages)	180
Requestor Location	Leda Sox 4405 Old Main Hill LOGAN, UT 84321 United States Attn: Leda Sox
Publisher Tax ID	EU826007151
Billing Type	Invoice
Billing Address	Leda Sox 4405 Old Main Hill LOGAN, UT 84321 United States Attn: Leda Sox
Total	0.00 USD
Terms and Conditions	

TERMS AND CONDITIONS

<https://s100.copyright.com/AppDispatchServlet>

1/5

Figure B.5. Copyright permission received for Sox *et al.* [2016]. Permission is for use of the entirety of Chapter 5.

4405 Old Main Hill
 Logan, UT 84322
 (904)-599-2536
 leda.sox@gmail.com

November 16, 2016

Dear Chad Fish,

I am in the process of preparing my Ph.D. dissertation in Department of Physics at Utah State University. I am planning to submit it by December 2016. You were a co-author of my paper "Connection between the midlatitude mesosphere and sudden stratospheric warmings as measured by Rayleigh-scatter lidar, *J. Geophys. Res. Atmos.*, 121, 4627-4636, doi:10.1002/2015JD024374. I am requesting your permission to include the manuscript in its entirety in my dissertation. I will include acknowledgements of your contributions as an author to this manuscript as part of a footnote on the page of that chapter. In addition, a copy of this letter will be printed in an Appendix to my dissertation. Please indicate your approval of this request by signing in the endorsement below.

Thank you for your time and consideration.

Sincerely,
 Leda Sox

I hereby give my permission to Leda Sox to reprint the following manuscript in her dissertation:
 Sox, L., Wickwar, V. B., Fish, C., Herron, J. P. (2016), Connection between the midlatitude mesosphere and sudden stratospheric warmings as measured by Rayleigh-scatter lidar, *J. Geophys. Res. Atmos.*, 121, 4627-4636, doi:10.1002/2015JD024374.

Signed:



Date: Nov 19, 2016

Chad S. Fish
 Atmospheric and Space Technology Research Associates
 Boulder, CO

Figure B.6. Permission letter from C. S. Fish to use coauthored paper as Chapter 5.

4405 Old Main Hill
Logan, UT 84322
(904)-599-2536
leda.sox@gmail.com

November 16, 2016


Dear Dr. Josh Herron,

I am in the process of preparing my Ph.D. dissertation in Department of Physics at Utah State University. I am planning to submit it by December 2016. You were a co-author of my paper "Connection between the midlatitude mesosphere and sudden stratospheric warmings as measured by Rayleigh-scatter lidar, *J. Geophys. Res. Atmos.*, 121, 4627-4636, doi:10.1002/2015JD024374. I am requesting your permission to include the manuscript in its entirety in my dissertation. I will include acknowledgments of your contributions as an author to this manuscript as part of a footnote on the page of that chapter. In addition, a copy of this letter will be printed in an Appendix to my dissertation. Please indicate your approval of this request by signing in the endorsement below.

Thank you for your time and consideration.

Sincerely,
Leda Sox

I hereby give my permission to Leda Sox to reprint the following manuscript in her dissertation:
Sox, L., Wickwar, V. B., Fish, C., Herron, J. P. (2016), Connection between the midlatitude mesosphere and sudden stratospheric warmings as measured by Rayleigh-scatter lidar, *J. Geophys. Res. Atmos.*, 121, 4627-4636, doi:10.1002/2015JD024374.

Signed:  Date: Nov 17, 2016

Dr. Joshua P. Herron
Space Dynamics Laboratory
Logan, UT

Figure B.7. Permission letter from J. P. Herron to use coauthored paper as Chapter 5.

CURRICULUM VITAE

Leda Sox
(December 2016)

EDUCATION

- Dec 2016 PhD, Physics**
Utah State University, Logan, UT
Advisor: Vincent Wickwar
Dissertation title: Rayleigh lidar measurements of the mesosphere and thermosphere and their connections to sudden stratospheric warmings
- May 2010 BA, Mathematics-Physics**
BA, French
Agnes Scott College, Decatur, GA
Cum laude, Dean's List, Dean's Honors List
- Spring 2008 Study Abroad, Contemporary French Studies**
CIEE Paris Center for Critical Studies, Paris, France
- May 2006 High School Diploma**
St. Augustine High School, St. Augustine, FL
Ranked 7th, AP Scholar with Distinction, Cambridge AICE Diploma

RESEARCH EXPERIENCE

- Apr 2011- Jun 2016 Graduate Research Assistant**
Center for Atmospheric and Space Sciences (CASS), Logan, UT
-Developed, characterized, tested, operated and maintained next-generation high-power, large-aperture Rayleigh-scatter lidar (laser radar) system for ground-based active remote sensing of the atmosphere
-Overcame problems, issues and technical challenges to advance the Rayleigh lidar prototype system
-Led 1-year lidar data acquisition campaign which required quick turn-around of data products, real-time diagnosis of remote sensing system's performance, and analysis of science observations
-Provided analytical measurement performance analysis of the Rayleigh lidar system and its subsystems and developed methods for improving measurement capabilities during data campaign

- Competitively obtained funding for graduate research and conference travel (approx. \$70,000 total) and contributed to proposal efforts to obtain funding for USU Rayleigh lidar group's research projects (approx. \$36,000)
- Provided scientific support to Rayleigh lidar group and published research results in refereed journals and conference proceedings, presented results at numerous scientific conferences, science team meetings and workshops
- Coordinated the efforts of 6-8 graduate and undergraduate lidar operators, scientists and engineers in the completion of the 1-year data campaign

**Jun 2010-
Aug 2010**

Student Assistant

Lidar group, Electro-Optical Systems Laboratory
Georgia Tech Research Institute, Atlanta, GA

- Worked as part of a larger team as liaison between Agnes Scott College and GTRI to facilitate the completion of the strategic goals and objectives laid out in their Course Curriculum and Laboratory Improvement (CCLI) lidar grant awarded by the National Science Foundation (NSF)
- Operated a Rayleigh-Mie pulsed lidar system and differential absorption lidar (DIAL) system
- Contributed to proposal efforts by preparing lidar design and budget material for NASA CIPAIR grant (funded in 2010) to PI Peter Chen at Spelman College
- Mentored Agnes Scott College REU students on various projects using Rayleigh-Mie lidar

**Aug 2009-
May 2010**

Undergraduate Researcher

Physics Department, Agnes Scott College, Decatur, GA

- Performed novel research on characterizing pollen particles using the Eye-safe Atmospheric Research Lidar (EARL) at ASC
- Used the Rayleigh-Mie EARL system to study aerosols, clouds and atmospheric composition and their role in the Earth's climate system
- Led EARL operations from 2009-2010 and organized to day-to-night data campaigns

TEACHING EXPERIENCE

**2011-
Present**

Student Research Mentor

Atmospheric Lidar Observatory, CASS, Logan, UT

- Trained a rotating group of eight undergraduates to independently operate the high-power Rayleigh Lidar system

-Mentored the undergraduate research projects of Marcus Bingham, Chandler Griffith, David Barton, Rebecca Petrick, Ben Lovelady, Shayli Elliott and Bryant Ward

- Aug 2015-
Dec 2015** **Graduate Teaching Assistant, Physics I (PHYS 2210)**
Department of Physics, Utah State University, Logan, UT
-Led recitations and proctored exams for Physics for Scientists and Engineers I
-Overall instructor rating of 4.8/5.0 in student evaluation
- Fall 2013** **Graduate Teaching Assistant, Optics I**
Department of Physics, Utah State University, Logan, UT
-Designed and taught an Intro to Lasers and Laser Safety Lab course
- Aug 2011-
May 2012** **Instructor, Physics I & II Labs**
Department of Physics, Utah State University, Logan, UT
-Gave lectures on error analysis
-Instructed Intro Calculus-based Mechanics (2215) and Electromagnetics (2225) based lab experiments
-Graded lab reports
-Overall instructor rating of 4.3/5.0 in student evaluation
- 2006, 2008** **Math Learning Assistant and Course Tutor**
Department of Mathematics, Agnes Scott College, Decatur, GA
-Course-tutored for Calculus I and Pre-Calculus: attended classes and worked on homework with individual students
-Tutored Finite Math through Calculus II students in the Agnes Scott Math Learning Center
- Feb-May
2014** **Private Physics Tutor**
Utah State University, Logan, UT
- Feb-May
2006** **Private Pre-Calculus Tutor**
St. Augustine High School, St. Augustine, FL

PUBLICATIONS

Sox, L., Wickwar, V. B., Fish, C., Herron, J. P. (2016), Connection between the midlatitude mesosphere and sudden stratospheric warmings as measured by Rayleigh-scatter lidar, *J. Geophys. Res. Atmos.*, 121, 4627-4636, doi:10.1002/2015JD024374.

Sox, L., et al. (2016), First temperature results from a high-power, large-aperture Rayleigh lidar, *J. Geophys. Res. Atmos.*, *In prep.*

- Sox, L.**, et al. (2016), Simultaneous, collocated Rayleigh and sodium lidar temperature comparison, *J. Geophys. Res. Atmos.*, *In prep.*
- Wickwar, V. B., **Sox, L.**, et al. (2016), New high-power large aperture Rayleigh-scatter lidar, *Appl. Opt.*, *In prep.*
- Sox, L.**, Wickwar, V. B., Fish, C., Herron, J. P. (2015), Temperature Deviations in the Midlatitude Mesosphere During Stratospheric Warmings as Measured with Rayleigh-scatter Lidar, *EPJ Web of Conferences*, *119*, 13008, doi:<http://dx.doi.org/10.1051/epjconf/201611913008>.
- Wickwar, V. B., **Sox, L.**, Emerick, M. T., Herron, J. P. and Barton D. L. (2015), Early Observations with the Extremely Sensitive Rayleigh Lidar at Utah State University, *EPJ Web of Conferences*, *119*, 13007, doi:<http://dx.doi.org/10.1051/epjconf/201611913007>.
- Barton, D. L., Wickwar, V. B., Herron, J. P., **Sox, L.**, Navarro, L. A. (2015), Mesospheric neutral densities derived from Rayleigh lidar observations at Utah State University, *EPJ Web of Conferences*, *119*, 13006, doi:<http://dx.doi.org/10.1051/epjconf/201611913006>.

NON-REFEREED PUBLICATIONS

- Sox, L.**, Wickwar, V. B. (2015), Early Rayleigh-Scatter Lidar Temperature Measurements from the Lower Thermosphere, *Utah NASA Space Grant Consortium Fellowship Symposium Proceedings*, Salt Lake City, UT, USA, 12 May.
- Sox, L.**, Wickwar, V. B., Fish, C., Herron, J. P. (2014), Rayleigh Scatter Lidar Observations of the Midlatitude Mesosphere's Response to Sudden Stratospheric Warmings, *Utah NASA Space Grant Consortium Fellowship Symposium Proceedings*, Layton, UT, USA, 06 May.
- Sox, L.**, Wickwar, V. B., Herron, J. P. (2013), Middle Atmosphere Temperature Results from a New, High-powered, Large-Aperture Rayleigh Lidar, *Utah NASA Space Grant Consortium Fellowship Symposium Proceedings*, Salt Lake City, UT, USA, 05 May.
- Sox, L.**, Wickwar, V. B. (2012), Results from an Extremely Sensitive Rayleigh-scatter Lidar, *Rocky Mountain NASA Space Grant Consortium Fellowship Symposium Proceedings*, Logan, UT, USA, 09 May.

INVITED TALKS

Sox, L., (2015), Lidar Research from the Troposphere to the Thermosphere, Physics and Astronomy Department Colloquium, Agnes Scott College, Decatur, GA, USA, 17 Apr.

Sox, L., Wickwar, V. B., Fish, C., Herron, J. P., Emerick, M. T. (2013), Rayleigh Lidar Observations of the Midlatitude Mesosphere during Stratospheric Warming Events and a New Rayleigh-Mie-Raman Lidar at USU, Utah State University Physics Colloquium, Logan, UT, USA, 10 Sept.

Sox, L. and Wickwar, V. B. (2012), New Rayleigh-Scatter Lidar Research at USU, MLTI Waves and Dynamics at Polar Latitudes Workshop, Logan, UT, USA, 11 Oct.

Sox, L. and Wickwar, V. B. (2012), First Light with Upgraded ALO Rayleigh-scatter Lidar, Utah State University Physics Colloquium, Logan, UT, USA, 11 Sept.

PRESENTATIONS AND POSTERS

Sox, L., Wickwar, V. B., Yuan, T., and Criddle, N. R. (2016), Simultaneous, collocated Rayleigh and sodium lidar temperature comparison, Poster Presentation, CEDAR Workshop, Santa Fe, NM, USA, 22 Jun.

Wickwar, V. B., **Sox, L.**, Emerick, M. T., and Herron, J. P. (2016), Seasonal Temperatures from the Upper Mesosphere to the Lower Thermosphere Obtained with the Large, ALO-USU Rayleigh Lidar, Poster Presentation, CEDAR Workshop, Santa Fe, NM, USA, 22 Jun.

Price, J., Wickwar, V. B., **Sox, L.**, Emerick, M. T., Herron, J. P., Elliott, S., Ward, B., and Lovelady, B. (2016), Obtaining Continuous Observations from the Upper Stratosphere to the Lower Thermosphere Using the ALO-USU Rayleigh-Scatter lidar, Poster Presentation, CEDAR Workshop, Santa Fe, NM, USA, 22 Jun.

Sox, L., Wickwar, V. B., Yuan, T., and Criddle, N. R. (2015), Comparison of Coincident Rayleigh-Scatter and Sodium Resonance Lidar Temperature Measurements from the Mesosphere-Lower-Thermosphere Region, Poster Presentation, American Geophysical Union Fall Meeting, San Francisco, CA, USA, 16 Dec.

Sox, L., and V. B. Wickwar, (2015), Changing Atmospheric Composition and the Retrieval of Rayleigh Lidar Temperatures in the Lower Thermosphere, Poster Presentation, CEDAR Workshop, Seattle, WA, USA, 23 Jun.

Sox, L., Wickwar, V. B., Fish, C., and Herron, J. P. (2014), Effects of Major Sudden Stratospheric Warmings Identified in Midlatitude Mesospheric Rayleigh-Scatter Lidar Temperatures, Poster Presentation, American Geophysical Union Fall Meeting, San Francisco, CA, USA, 19 Dec.

Sox, L., Duly, T., and Emery, B. (2014), The National Science Foundation's Coupling, Energetics and Dynamics of Atmospheric Regions (CEDAR) Student Community, Poster Presentation, American Geophysical Union Fall Meeting, San Francisco, CA, USA, 17 Dec.

Sox, L., Wickwar, V. B., Fish, C., Herron, J. P., Emerick, M. T., Barton, D. L. (2014), Midlatitude Mesospheric Temperature Anomalies during Sudden Stratospheric Warmings and a New Rayleigh-Scatter Lidar at Utah State University, Physical Sciences Department Colloquium, Embry-Riddle Aeronautical University, Daytona Beach, FL, USA, 23 Oct.

Sox, L., Wickwar, V. B., Fish, C., Herron, J. P. (2014), Midlatitude Mesospheric Temperature during Major SSW Events as Observed with Rayleigh-Scatter Lidar, Poster Presentation, CEDAR Workshop, Seattle, WA, USA, 25 June.

Wickwar, V. B., **Sox, L.**, Barton, D. L., Herron, J. P. (2014), Emerick, M. T., Extremely Sensitive Rayleigh-Scatter Lidar at USU, Poster Presentation, CEDAR Workshop, Seattle, WA, USA, 25 June.

Sox, L., Wickwar, V. B., Fish, C., Herron, J. P. (2013), Temperatures in the Mid-Latitude Mesosphere during Sudden Stratospheric Warmings as Determined from Rayleigh Lidar Data. Poster Presentation, AGU Fall Meeting, San Francisco, CA, USA, 10 Dec.

Sox, L., Wickwar, V. B., Herron, J. P., Barton, D. L., Emerick, M. T. (2013), Ground-Based Observations with a Rayleigh-Mie-Raman Lidar from 15-120 km, Poster Presentation, Fall National Space Grant Meeting, Charleston, SC, USA, 18 Oct.

Wickwar, V. B., **Sox, L.**, Emerick, M. T., Herron, J. P. (2013), Midlatitude, Rayleigh-Mie-Raman Lidar for Observations from 15 to 120 km, Oral Presentation, IAGA 12TH Scientific Assembly, Merida, Yucatan, Mexico, 27 Aug.

Sox, L., Wickwar, V. B., Fish, C., Herron, J. P. (2013), The Mid-Latitude Mesosphere's Response to Sudden Stratospheric Warmings as Determined from Rayleigh Lidar Temperatures, Oral Presentation, IAGA 12TH Scientific Assembly, Merida, Yucatan, Mexico, 26 Aug.

Sox, L., Wickwar, V. B., Herron, J. P., Emerick, M. T. (2013), Rayleigh Lidar

Temperature Studies in the Upper Mesosphere and Lower Thermosphere, Poster Presentation, CEDAR Workshop, Boulder, CO, USA, 26 June.

Sox, L., Wickwar, V. B., Herron, J. P., Bingham, M. J., Petersen, L. W., Emerick, M. T. (2012), First Temperature Observations with the USU Very Large Rayleigh Lidar: An Examination of Mesopause Temperatures, Poster Presentation, AGU Fall Meeting, San Francisco, CA, USA, 04 Dec.

Sox, L., Wickwar, V. B., Herron, J. P., Bingham, M. J. (2012), Upgraded ALO Rayleigh Lidar and Its Improved Gravity Wave Measurements, Poster Presentation, CEDAR Workshop, Santa Fe, NM, USA, 27 June.

Sox, L., Wickwar, V. B., Herron, J. P., Bingham, M. J. (2012), Observations with the Most Sensitive Rayleigh-Scatter Lidar. Poster Presentation, Intermountain Graduate Research Conference, Logan, UT, USA, 05 Apr.

Sox, L., Wickwar, V. B., Herron, J. P., Bingham, M. J., Petersen, L. W. (2011), The World's Most Sensitive Rayleigh-Scatter Lidar, Poster Presentation, Joint CEDAR-GEM Workshop, Santa Fe, NM, USA, 28 June.

Sox, L. and Sullivan, A. C. (2010), Characterization of Pollen Particles Using LIDAR, Poster Presentation, Symposium on Undergraduate Research, Frontiers in Optics, Rochester, NY, USA, 25 Oct.

Sox, L., and Sullivan, A. C. (2010), LIDAR: Using Lasers to Investigate the World above Us, Poster presentation, Spring Annual Research Conference, Agnes Scott College, Decatur, GA, USA, 21 Apr.

Sox, L., (2010), Sketches from Memory: The Bande Dessinée as a Memoir, Oral presentation, Spring Annual Research Conference, Agnes Scott College, Decatur, GA, USA, 21 Apr.

UNDERGRADUATE-MENTEE PRESENTATIONS

Barton, D. L., Wickwar, V. B., **Sox, L.**, Herron, J. P. (2014), Seasonal Variations of Relative Densities Between 45 And 90 km Determined from USU Rayleigh Lidar Observations, Poster Presentation, CEDAR Workshop, Seattle, WA, USA, 25 June.

Barton, D. L., Wickwar, V. B., **Sox, L.**, Herron, J. P. (2013), The behavior of Neutral Densities between 45 and 90 km Determined from Rayleigh Lidar Observations above Logan, Poster Presentation, APS Four Corners Section Meeting, Denver, CO, USA, 18 Oct.

Barton, D. L., Wickwar, V. B., **Sox, L.**, Herron, J. P. (2013), Mesospheric Density Climatologies Determined at Midlatitudes Using Rayleigh Lidar, Poster Presentation, IAGA 12TH Scientific Assembly, Merida, Yucatan, Mexico, 27 Aug.

Griffith, C. (2013), LIDAR Temperature Observations related to Sudden Stratospheric Warmings, Student Showcase, Utah State University, Logan, UT, USA, 11 Apr.

SERVICE

2013-2015 Student Representative

Coupling, Energetics and Dynamics of Atmospheric Regions (CEDAR) Science Steering Committee (CSSC)

- Chosen by peers and confirmed by NSF officials to a 2-year term as Student Representative on the CSSC

-Served on a team of scientists and engineers to develop scientific goals, instrument requirements and measurement scenarios as well as suggest funding opportunities for the NSF's CEDAR and Aeronomy programs

-Participated in annual science working groups to identify key scientific thrusts and measurement needs of the upper atmospheric scientific community

-Proposed, organized and moderated a day-long tutorial workshop for students titled, "Aeronomy Instrumentation: Where does the data come from?"

Feb 2011 Science Fair Judge

Thomas Edison Charter School, Logan, UT

PROFESSIONAL DEVELOPMENT

Jul 2014 NSF Incoherent Scatter Radar Summer School

Arecibo Observatory, Arecibo, Puerto Rico

-2nd Place ISR Science Question presentation

-Group experiment conducted with the Arecibo ISR, which resulted in a successful observation of the He⁺ layer in the topside Ionosphere

Mar 2014 Science Communication Workshop

Utah State University, Logan, UT

Spring 2014 ELEC301x Discrete Time Signals and Systems

edX course

- Fall 2011** **INST 7930 College Teaching Seminar**
Utah State University, Logan, UT
- Aug 2010** **Atmospheric LIDAR Engineering**
Professional Education, Georgia Institute of Technology,
Atlanta, GA

PUBLIC OUTREACH

- 2012-2016** **USU Rayleigh lidar facility tours**
Atmospheric Lidar Observatory, CASS
Utah State University, Logan, UT
*-Gave impromptu and arranged tours of the facility and overview
of the science for hundreds of visitors since 2012*
- 2014, 2015** **“Lidar in a box/What is the Green Beam at USU?”**
Engineering Week Community Night, Utah State University,
Logan, UT
- May 2014** **USU Rayleigh lidar facilities tour to 120 middle school students**
Gaining Early Awareness and Readiness for Undergraduate
Programs (GEAR UP) summer program
- Feb 2014** **“Lidar in a box/What is the Green Beam at USU?”**
Science Unwrapped after events presentations, Utah State
University, Logan, UT
- Nov 2012** **“Lidar in a box”**
Science Unwrapped after events presentations, Utah State
University, Logan, UT
- Aug 2012** **“Atmospheric LIDAR”**
Intro to Space Flight and Engineering classes, St. Johns County
Aerospace Academy, St. Augustine High School/Embry Riddle
Aeronautical University, St. Augustine, FL
- Apr 2012** **“What do physicists do”**
11th grade English resource class, Mountain Crest High School,
Hyrum, UT
- Oct 2011** **“The Green Beam at USU”**
Science Unwrapped after events presentations, Utah State

University, Logan, UT

AWARDS AND FELLOWSHIPS

2011-2015	Fellow , Utah NASA Mountain Space Grant Consortium
2015	Scholarship , Keith Taylor Summer Research Scholarship, USU Physics Department
2013, 2015	Graduate Student Travel Award , USU School of Graduate Studies
2012, 2015	Travel Grant , USU Center for Women and Gender
2013	Scholarship , Gene Adams Scholarship, USU Physics Department
2012, 2013	Scholarship , Howard L. Blood Summer Research Scholarship, USU Physics Department
2013	Honorable Mention , NSF Graduate Research Fellowship
2006-2010	Letitia Pate Evans Scholarship , Agnes Scott College
2008	French Scholar's Award , ASC French Department
2006	100% Florida Bright Futures Scholarship

PROFESSIONAL MEMBERSHIPS

2014-	Earth Science Women's Network (ESWN)
2012-	Sigma Pi Sigma, National Physics Honor Society
2011-	American Geophysical Union (AGU)
2010-	Mortar Board, National Honor Society

ADDITIONAL EXPERIENCE

Spring	Senior Seminar Project
2010	French Department, Agnes Scott College, Decatur, GA <i>Thesis title: Sketches from Memory: The Bande Dessinée as a Memoir</i>

- Fall 2009
2010** **Educational Program Intern**
Alliance Française d'Atlanta, Atlanta, GA
-Assisted Educational director with public outreach and partnering organization events
-Prepared pedagogical documents and exercises for French language classes and workshops
-Aided course registration: publishing schedules online and working at the open house
- Summer
2009** **AmeriCorps Crew Member**
Utah Conservation Corps, Logan, UT
- Maintained trails and repaired fences in federal lands throughout Utah and Idaho
-Worked with the National Forest Service on the Uinta Basin Replacement Project
-Simultaneously took a course from Utah State University on Western Environmental Issues
- 2008, 2009** **Photo Editor**
The Profile, student newspaper, Agnes Scott College, Decatur, GA
- Fall 2008** **Editor-in-Chief**
Aurora, student literary magazine, Agnes Scott College, Decatur, GA
- Aug 2005-
May 2006** **Volunteer**
WFCF Community Radio Station, Flagler College, St. Augustine, FL
-Selected and edited new music for airplay that would be well received by the community